Thermogravimetric analysis of biomass-lignite blends for co-combustion

Lindsey, Benjamin Keith

Award date:
2006

Awarding institution:
University of Bath

THERMOGRAVIMETRIC ANALYSIS OF BIOMASS-LIGNITE BLENDS FOR CO-COMBUSTION

Benjamin Keith Lindsey

Doctor of Philosophy
University of Bath
Department of Chemical Engineering
May 2006

Copyright

ProQuest LLC
789 East Eisenhower Parkway
P.O. Box 1346
Ann Arbor, MI 48106-1346

Abstract

Co-firing biomass with coal in power stations reduces emissions of NO_x, SO_2 and the use of limited fossil carbon. However, different properties of biomass and coal affect furnace efficiency and performance. This thesis investigates the processes involved when coal and biomass are heated together. Biomass (olive kernels or forest residue) was blended with Ptolemais lignite, and sample weight (TG) recorded by thermogravimetric analysis, heating linearly to 1200 K under nitrogen (pyrolysis experiments) or air (oxidation experiments). Blends involving German lignite were also investigated, but gave inconsistent data. Using the Ptolemais lignite blends, a rule-of-mixtures model confirms that pyrolysis of a blend is a linear combination of activities of the original fuels, while oxidation is more complex. Decomposition processes were isolated from the weight-change rate (dTG) profiles using deconvolution with up to five Gaussian curves. Analysis of resulting TG and dTG data with a Prout-Tompkins nucleation kinetic model gave apparent activation energy and pre-exponential factors for the various decomposition processes, which were comparable to literature values. Combined with Gaussian parameters, these values were used to group peaks from all the blends, demonstrating the effect of blend ratio on decomposition. In air or nitrogen, processes that peak in rate below 600 K were due to biomass and exhibited constant activity as blend ratio increased. In nitrogen, reactions peaking above 600 K were linked with char condensation reactions common to both the original fuels and activity was again constant. Above 600 K in air, several trends in relative activity indicate heterogeneous char oxidation reactions ($e.g.\ C_{(s)} + O_{2(g)} \rightarrow CO_{2(g)}$) of certain active sites are inhibited by the presence of a co-fuel. The occurrence of new peaks suggest that blend oxidation involves new decomposition pathways, likely to be caused by volatile emissions of biomass blocking heterogeneous oxidation of lignite char. This represents a novel means of using TG data to observe the thermally activated interactions between materials within in a mixture.

Acknowledgements

Foremost, I would like to acknowledge the invaluable support and enthusiasm of my supervisor Dr. Tim Mays of the University of Bath, without whom this investigation would never have started. Also the ECSC project partners for their collaboration: Dr. Juri Riccardi and Dr. Nicola Rossi of Enel (Italy), Dr. Wilhelm Derichs of RWE Power (Germany), Dr. George Skodras of the Aristotle University of Thessaloniki (Greece) and Platon Pallis of the National Technical University of Athens (Greece). Fuel samples and complete funding for this project came from the European Coal and Steel Community (ECSC-7220-PR-131), for which I am exceptionally grateful. I also would like to thank the staff of the Department of Chemical Engineering at the University of Bath, for their advice and support as well as undergraduate students Takehiko Kano and Matthew Stanley for their excellent contributions on biomass pyrolysis and blend activity.

There are also many friends and relatives, who have given me so much support in recent years. My dear grandparents Margaret and Norman Hull, Jack Lindsey and my memory of Winifred Lindsey, for all of whom I have the greatest admiration and respect. My parents David and Judith, and my brother Oliver, who have each sustained me (financially and emotionally!) without question for too many years now, something I will never forget. To Edwige, for her love, her affection and her steadfast courage; with you, I am discovering a deep, happy companionship and I love you! To James Brown, The Chief, a true life-long friend. To Joanna and Mike for all their interest in my work. To Karen, Jack and Thomas, for amongst many other things, all the pictures, recipes and PC games that have sustained me for the last seven years! I also want to acknowledge all the friends I have made at university. Including (but by no means exclusively) Rachel Caley, Bethan Eggboro, Ruth Lawrence, Adele Murdock, Sarah and James Norwood, Toni Odunsi, Emma Sackett, Holly Shearer, Fernando Acosta, Dmitry Bavykin, Alex Brittan, Richard Bull, Brendan Darragh, Matt Edmunds, Phil Evans, Rodney Foo, Yong-Kyung Ly, Tim Metcalfe, Chin Chi Tai, Alex Shirley, Matthew Watt-Smith, Gang Yuan and all the other many wonderful people I have met along the way: thank you all!

Contents

Figures

Tables

Nomenclature

Symbols		
A	Pre-exponential factor	min^{-1}
α	Fraction of conversion	-
b	Blend ratio	-
β	Heating rate	$K\ min^{-1}$
c	Contribution to conversion (fraction)	-
E_{Act}	Activation energy	$J\ mol^{-1}$
G	Gibbs free energy	$J\ mol^{-1}$
γ	dTG area ≡ weight loss contribution	%wt.
H	Enthalpy	$J\ mol^{-1}$
k	Rate constant	-
L/HHV	Lower/higher heating value	$J\ kg^{-1}$
M_r	Molar mass	$g\ mol^{-1}$
m	Kinetic order parameter	-
N	Number of decomposition components	-
n	Kinetic order parameter	-
P	Pressure	Pa
R	Gas constant	$8.134\ J\ K^{-1}\ mol^{-1}$
t	Time	min
T	Temperature	K
T_{max}	Peak temperature	K
S	Entropy	$J\ K^{-1}$
V	Volume	l
w	Weight	mg
ω	Function of full width at half peak maximum ≡ activity range	K
%C	Carbon content	%wt.
%H	Hydrogen content	%wt.
%N	Nitrogen content	%wt.
%O	Oxygen content	%wt.
%S	Sulphur content	%wt.

Abbreviations

Ash	Ash content	%wt.
DSC	Differential Scanning Calorimetry	-
dTG	Weight change derivative (dTG/dT or $d\alpha/dt$)	%wt. K^{-1} or min^{-1}
dTG_{max}	Peak maximum rate	%wt. K^{-1} or min^{-1}
FC	Fixed carbon content	%wt.
FR	Forest Residue	-
GL	German Lignite	-
M	Moisture content	%wt.
OK	Olive kernels	-
PL	Ptolemais lignite	-
SEM	Scanning electron microscopy	-
TG	Sample weight percentage	%wt.
TGA	Thermogravimetric Analysis	-
VM	Volatile material content	%wt.

Subscript Identifiers

0	Initial value
Calc.	Calculated value
d	Displaced quantity
Exp.	Experimental value
FR/OK/PL/GL	Fuel type (see above)
F	Fluid point
f	Final value
H	Hemispheric deformation
i	Decomposition component identifier
ID	Initial deformation
Lit.	Literature value
T	Temperature point

Chapter 1 Introduction

1.1 Research Context

The use of biomass as a alternative to coal in energy conversion systems is increasingly attractive, considering the resulting advantages of reduced net CO_2 emissions, reduced emissions of NO_x and SO_2, reduced demands of finite fossil fuel reserves, avoidance of land fill, energy supply security (when considering the political influence of oil supply for example) and supply longevity. Unfortunately, most countries lack the fuel production capacity, the technology and the financial incentives to establish a significant biomass energy contribution at present. On the other hand, co-combustion, where coal and biomass are fired in the same furnace, retains many of benefits of the biomass, needs fewer changes to the energy infrastructure and can still encourage new biomass capacity. However, the lack of knowledge concerning the properties of biomass and biomass-coal blends, and their effect on the efficiency of coal-fired power stations remain, presenting a substantial barrier to development.

What has been established, are case studies of power stations co-firing mixtures of coal and biomass [Gayan *et al.* 2004] displaying a combination of constructive effects [Cliffe *et al.* 2001; Boylan *et al.* 2000; Battista *et al.* 2000] and some destructive effects [Dietl *et al.* 1999; Werther *et al.* 2000; Hupa 2005], depending on the operating conditions and fuel type. Also known are means of comparing the performance of coals and biomasses [van der Drift *et al.* 2001] under a multitude of laboratory and power station conditions. To lesser extents, the pyrolysis of pure fuels (especially of biomass) has been related to

its composition by way of a series of superimposed "peaks" in reaction activity [Alonso *et al.* 2001], while the pyrolysis of fuel blends under certain conditions is known to involve the cumulative decomposition of the parent fuels [Manya *et al.* 2003].

This investigation seeks to take established deconvolution [Katsikas *et al.* 2003] and kinetic analysis techniques [Varhegyi *et al.* 1997], previously developed for comparing the thermal decomposition of pure fuels, and apply them for the purpose of observing how mixed fuels interact when heated. By better understanding the sorts of interactions between the fuels, it might be possible to improve the understanding and operation of co-fired power stations.

1.2 Research Scope

This thesis presents the results of detailed research into the behaviour of fuel mixtures under closely controlled thermal conditions. The results described are part of a large series of experiments involving a suite of fuel samples. The mixtures are blends of coal and biomass, chosen for their co-firing potential in furnaces for heat and power generation. Olive kernels and forest residue were chosen as the biomass samples, while Ptolemais lignite was selected as the blend coal. A German lignite was also investigated, but due to apparent inter-sample variability did provide conclusive blend data.

Note that this is not an attempt to replicate the conditions of a power station furnace but is rather characterisation in laboratory conditions. These involve a temperature range of 350 to 1100 K, heating at 5 to 30 K min^{-1}; atmospheres of dry air or nitrogen, flowing at 3 or 30 ml min^{-1} (STP); fuel blends of zero to 100 %wt. (percent by weight) of biomass in coal at 20 %wt. increments; and samples analysed in batches of 1.0 to 60 mg. Conditions in power stations involve temperatures of between 973 and 1873 K (for fluidised bed and pulverised fuel furnaces respectively), while the heating rate experienced by fuel particles entering the combustion zone are also higher, at over 7,000 K min^{-1}. Furthermore, furnace fuel and air feed rates are also closely controlled

as the fuel-oxygen stoichiometry affects both fuel conversion efficiency and emissions of NO_x [Berkowitz, 1994].

Thermogravimetric analysis is used to record the sample weight as a function of time and temperature, from which the reactions that underpin the decomposition of the fuels and fuel blends are resolved. Kinetic parameters for the decomposition reactions are then compared to establish the effect of the fuel blend ratio on performance.

1.3 Dissemination

The contents of this thesis have been communicated on a number of occasions, to audiences with a number of research interests. Details of the investigation were regularly scrutinised at six-monthly project meetings as part of the ECSC contract, often highlighting the importance of the work to the energy industry. Several poster presentations were made concerning scientific aspects of the research, considering advances in the ability to separate blended fuel pyrolysis peaks and comparisons of peak profiles. These presentations were made at a number of international conferences, including the 13th International Congress on Thermal Analysis and Calorimetry in Sardinia in 2004 [Lindsey *et al.* 2004]; the Science Engineering and Technology Awards in the Houses of Parliament in 2004; and the 7th World Congress of Chemical Engineers in Glasgow in 2005 [Lindsey *et al.* 2005]. Appendix C contains posters and abstracts from these publications. Some results of this thesis have recently been submitted for publication in "Energy and Fuels".

1.4 Thesis Structure

This thesis is presented in six chapters. Chapter 2 summarises the background to the investigation, describing the reasons for the work; it introduces the areas of established theory the work includes, and presents a critical discussion of relevant published literature. Chapter 3 describes the experimental techniques employed, giving details of the equipment, the materials, and the analysis methodology. The important factors

affecting the accuracy and precision of the analysis are also considered. Chapter 4 describes the original experimental results providing observations of the data and indicating general trends. Chapter 5 presents a detailed analysis of the results, using a number of models to characterise and compare the thermogravimetric performance of pure and blended fuels. Chapter 6 draws together the conclusions of the present investigation, highlighting areas of novelty, but also limitations and therefore ideas for future work.

Chapter 2 Background

2.1 Introduction

It has recently been observed that co-firing of biomass and coal offers the "lowest risk, least expensive, most efficient and shortest term option for renewable based electrical power generation" [Baxter 2005]. Coal has been burned for power generation since the industrial revolution of the eighteenth century, while wood (a form of biomass) has been used for heat since pre-historic times. However, there has only been a limited interest in combining these two fuels in coal-fired power stations. Co-firing takes advantage of the sustainability and low emissions of biomass compared with coal, and of the high conversion efficiency and energy capacity when compared with dedicated biomass power stations [Hughes 2000]. However, the composition of a fuel strongly affects its mode of combustion, and given the stark differences between coal and biomass, we are just starting to understand how this influences their co-firing performance. This Section presents the basics of co-combustion, the types of fuel involved, their combustion chemistry, and gives a discussion of the analysis of fuel activity.

2.2 Motivations for using Co-Combustion

2.2.1 Emissions Reductions

The benefits of burning biomass cover a wide range of aspects and much has been written on the subject [Sorensen 2000; Tillman 2000; Sami *et al.* 2001; Demirbas 2003].

A notable benefit is a mean zero net carbon emissions where during growth, biomass reabsorbs as CO_2 the quantity of carbon released during combustion. This is in contrast to the release of carbon from fossil reserves, which with a recycling time of several hundred million years, contributes heavily to the greenhouse effect (Figure 2-1). According to Cannell [2003], in 2000, the UK released 147 million tonnes of organic carbon and CO_2 from fossil fuels. In a theoretical scenario involving the production of biofuels at the expense of all other UK agriculture, Cannell [2003] suggests the UK could reduce its carbon emissions by 30 to 70 million tonnes per year. In a more likely scenario involving the use of 50 percent of biomass at its current production rate, it is suggested that annual atmospheric carbon emissions could be reduced by between 3 and 5 million tonnes per year.

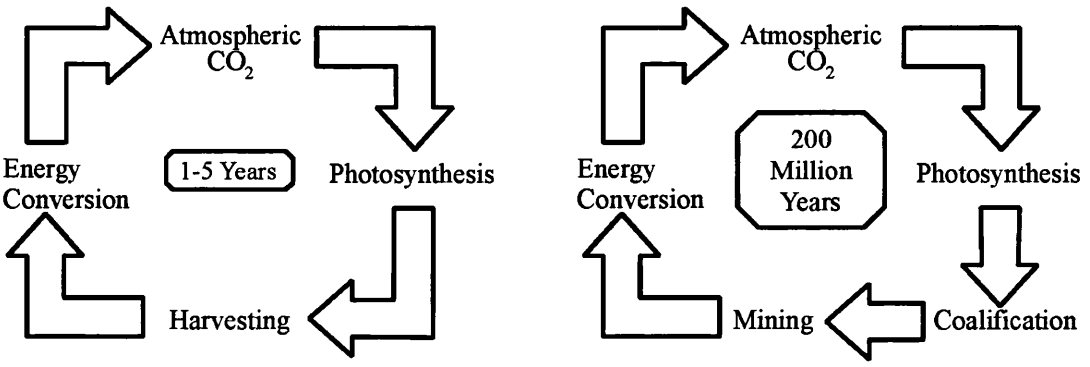

Figure 2-1: Schematic of the carbon cycles for (a) biomass and (b) fossil fuels

Also of importance are N_2O, NO_x and SO_2 emissions that contribute to acid rain and ozone depletion. Reduced emissions of these compounds during combustion of biomass, is primarily due to the lower fuel-nitrogen and fuel-sulphur levels compared to coal [Hein *et al.* 1998; Wang *et al.* 1999; Liu *et al.* 2002; Liu *et al.* 2002]. However, additional reactions linked to the composition of biomass can lead to reductions below

those caused by fuel ratio alone [Sami *et al.* 2001]. The chemistry of the emission of nitrogen and sulphur oxides, is discussed in Section 2.4.7 and 2.4.8 respectively. Indirectly, the use of large volumes of biomass in co-firing avoids their committal to landfill sites, avoiding the long-term atmospheric release of the greenhouse gas, methane [Sami *et al.* 2001; Demirbas 2003].

The UK government and EU members have set a number of targets relating to emissions levels. A detailed discussion of the politics involved would be beyond the scope of this investigation; however, the main incentives that concern co-firing are summarised in Table 2-1.

2.2.2 Energy Supply Security

As described in Section 2.2.1, the long recycling time for non-renewable fuels presents a significant drawback. Current global reserves of coal are estimated at 909 billion tonnes, which at current production rates suggests a predicted lifetime of between 101 years (for reserves in Pacific Asia) and 242 years (for reserves in Eurasia). Meanwhile, known global reserves of oil and natural gas have predicted lifetimes of 40 and 60 years respectively. In 2004, 32 percent (182 TWh) of UK electricity was generated by coal, with gas contributing 40.6 percent (425 TWh). Oil contributes around 31.8 percent (333 TWh) while combined renewable combustion technologies[1] contribute around 1.5 percent (10.5 TWh) [DTI 2005]. Clearly, biomass is not in a position to replace the fossil energy demand. In 2005, the estimated renewable contribution from co-firing was 516 MW, receiving around 10 percent of Renewables Obligation Certificates [Ofgem 2005] (Table 2-1).

However, through co-firing it is immediately possible to replace up to 10 percent of coal by energy content in most existing or power stations (more in new-build plant), considerably offsetting the demands on fossil fuels [DTI 2005].

---

(1) Includes: Wood, wood waste, agricultural waste, short rotation coppice, sewage gas and landfill gas.

Biomass is a diverse group of biologically derived materials that includes forestry wood waste, agricultural waste, and purpose grown fuel crops. Therefore, in comparison with coal coming from point sources, fuel production can be dispersed over large areas. Although transportation costs may initially make centralised (*i.e.* larger) power stations uneconomic [Werther *et al.* 2000], decentralisation from high-capacity power plants would improve energy security, both in terms of diversity of the fuel source, and in allowing energy production to be tailored to local needs and resources. The flexibility of domestically growing crops with optimum fuel properties would avoid the need to import fuels to meet a specification; coal burnt in the UK is almost entirely imported as most indigenous reserves contain excessive levels of sulphur.

Table 2-1: A summary of the main EU and UK incentives for use of renewable fuels and energy efficiency [PIU 2002; DTI 2003; DTI 2004; DTI 2005]

<table>
<tr><th>Incentive</th><th>Description</th></tr>
<tr><td>IPPC</td><td>Under the Integrated Pollution Prevention and Control Directive, power stations in the EU must obtain authorisation from a regulator, on the proviso of employing the Best Available Technology for reducing environmental impact</td></tr>
<tr><td>Renewables Obligation</td><td>Licensed UK electricity suppliers must generate electricity from a stated proportion of renewable sources, or pay a fine. RO certificates are awarded per MW generated from a list of renewable sources including landfill gas, wind, wave and biomass. Dedicated combustion, gasification and anaerobic digestion of biomass are eligible. Co-firing with biomass is also eligible for the fraction of energy generated by biomass, but only until 2016 while caps on a suppliers co-firing contribution will evolve to motivate increased biomass/coal fuel ratios until this time</td></tr>
<tr><td>LCPD</td><td>The Large Combustion Plant Directive establishes emissions limit values for new and existing power stations in the EU. For solid fuel stations (of over 300 MW) limits are:
<table>
<tr><th></th><th>Existing Plant</th><th>New Plant</th></tr>
<tr><td>SO_2 (mg Nm^{-3})</td><td>400</td><td>200</td></tr>
<tr><td>NO_x (mg Nm^{-3})</td><td>500</td><td>200</td></tr>
<tr><td>Dust (mg Nm^{-3})</td><td>50</td><td>30</td></tr>
</table>
Certain biomass types (including agricultural and forestry vegetable waste) are exempt from this legislation</td></tr>
<tr><td>Climate Change Levy</td><td>Industrial and commercial electricity consumers in the UK pay a levy of 4.3 £ MWh^{-1} unless they can prove attempts at efficient use of energy, or present a Levy Exemption Certificate costing 4.0 £ MWh^{-1}</td></tr>
<tr><td>Waste Incineration Directive</td><td>Sets and upholds operating conditions, technical requirements and emissions limits to prevent negative environmental effects through emissions to the air, surface and ground water, during incineration or co-incineration of waste</td></tr>
<tr><td>Other UK Targets</td><td>* Energy White Paper: Cut CO_2 emissions by 60 % by 2050
* Kyoto Protocol: Reduce greenhouse gas emissions to 12.5% below 1990 levels by 2008-12
* Climate Change Program: Cut carbon emissions by 15-25 Mt by 2020
* 10 % of electricity to come from renewable sources by 2010</td></tr>
</table>

In contrast to biomass-dedicated power stations, co-fired power stations would not be badly affected by the inconsistent biomass supply, such as that caused by the seasonal growth-harvest cycle, as power stations could still operate on coal alone [Demirbas 2003]. Further, the energy efficiencies for co-firing in existing power stations are much higher than biomass dedicated plants (14.8 and. 11.6 MJ kWh^{-1} respectively), a consequence of the smaller size of typical biomass boilers and the higher moisture levels involved [Hughes 2000].

2.2.3 Economic and Rural Development

Commercial co-firing means power stations could help develop local forestry and agricultural industries, cultivating a biofuel infrastructure that will not only benefit co-firing, but also a wide range of other biofuel technologies by generating an immediate and guaranteed demand [Tillman 2000]. Farmers around Yorkshire will appreciate this, having been contracted to grow willow coppice, for the ARBRE biomass-dedicated gasifier at Eggborough, later to be closed after financial difficulties [Van der Horst 2005].

Where biomass-processing costs are low, total fuel costs can be reduced [Hughes 2000; Sami *et al.* 2001]. There are also advantages for a producer of waste with fuel potential, the disposal of which would usually incur a cost; energy producers may charge a competitive gate-fee for biofuels (especially wet waste biofuels) and raise capital from the fuel before even burning it. The energy consumer will benefit where co-firing a biofuel with coal generates lower-cost energy than other renewable sources and with the emission reductions described, new-build coal power stations would not be made to install as expensive NO_x and SO_2 emissions control measures [Hughes 2000]. In a self-sustaining cycle, purchase of forest residues or wood fuels from regional or national forestry authorities could be used in the development and conservation of woodland and forest.

2.2.4 Established Technological Basis

Co-firing has been demonstrated for every boiler type, with every commercially significant coal type, and every major category of biomass [Baxter 2005]. At present biomass produces about 14 percent of the world's annual primary energy. However, there are suggestions that by 2050, biomass can provide 38 percent of the world's primary energy (including transport and domestic heating) and 17 percent of electricity [Demirbas 2004].

Small isolated businesses such as sugar plantations, timber mills, farms *etc.*, which produce combustible biomass waste as a matter of course, have used it as a source of energy in generating stations of up to 50 MWe [Arbon 2002]. It has been shown that in small percentages, biofuels may be almost directly substituted into existing fossil-fired power stations, a great advantage over other renewable energy sources such as wind and tidal energy that require a new energy infrastructure (*e.g.* [Hughes *et al.* 1998]). High initial investment costs (due to the economies of scale) and low thermal efficiencies frequently make small biomass dedicated power stations unattractive options, but co-combustion in new or existing coal-fired power stations has been shown to combine the best of both scales, especially in developed countries where personnel costs are high [Werther *et al.* 2000].

The differences between biomass and coal are illustrated below in Table 2-2 (p.11), and just as coals are blended for purposes of economy and performance [Nugroho *et al.* 2000], biomasses would facilitate combustion of a larger variety of coals in coal-dedicated power stations. Low NO_x and SO_x emissions from biomass permit higher nitrogen or sulphur coals to be used (Section 2.2.1). The inherently high volatile content of biomass enables clean burning, and higher rank coals with calorific contents but lower volatile content to be used without compromising flame stability. The large volatile emissions from biomass at relatively low temperatures also benefit more efficient gasification systems, while the high reactivity of biomass char ensures complete oxidation of the coal char.

Benefits also arise because of the coals presence, for example, where the heating value of a biomass is lower than that required to sustain auto-thermal combustion (20 MJ kg^{-}

[1]). In these circumstances, combining the biomass (such as sewage sludge with a heating value of only 11 MJ kg^{-1}) with a high heating value coal makes combustion possible [Biagini *et al.* 2002].

In terms of fuel supply, the UK currently produces around 30 million tonnes of combustible municipal solid waste per year (MSW, Section 2.3.3), of which 90 percent (27 million tonnes) is consigned to landfill. In the US, MSW is calculated as having a mean heating value 10.5 to 11.5 MJ kg^{-1}; from which it can be estimated that around 283 million GJ are being "wasted" in the UK per year [Demirbas 2004]. According to the DTI, UK electricity generation from MSW in 2000 was 840 GWh, rising to 971 GWh in 2004 [DTI 2005].

Table 2-3 summarises the experiences of co-firing with biomass in the UK. While only a few large-scale biomass dedicated power stations have been developed in the UK, most coal-fired powered stations have taken advantage of co-firing as a way of meeting the governments Renewables Obligation (Table 2-1).

Table 2-2: Comparison of the chemical characteristics of 11 coals and 17 biofuels. Daf indicates a dry, ash-free sample (Appendix A gives individual fuel data)

		Coal Mean	Biomass Mean	Coal Range	Biomass Range
C	(daf %wt.)	63.1	43.3	51.3-81.4	32.1-53
H	(daf %wt.)	4.6	5.4	2.9-5.8	3.8-6.7
O	(daf %wt.)	15.6	38.2	2.5-26.1	27-45.1
N	(daf %wt.)	1.0	0.7	0.6-1.5	0.1-1.4
S	(daf %wt.)	0.8	0.0	0.01-2.8	0-0.1
VM	(dry %wt.)	40.6	76.3	24.5-50.8	60.7-85.5
FC	(dry %wt.)	50.2	17.6	40.3-64	14.3-21.3
Ash	(dry %wt.)	9.2	6.4	3.3-18.2	0.5-22.9
Moisture	(as received %wt.)	27.8	25.0	3.3-57.1	10-53.3
HHV	(MJ kg^{-1})	22.9	16.2	17-31.6	10.4-21.4
VM/FC		0.8	4.5	0.4-1.2	3.3-5.9

Table 2-3: Instances of co-firing in the UK [DTI 2005]. Co-fuel information obtained by direct communication with the power station concerned

Power Station	Primary Fuel	Capacity (MWe)	Biomass co-fuel (Status)
Aberthaw B	Anthracite	1,489	Various (Commercial)
Cockenzie	High volatile Bituminous Coal	1,152	Wood (Commercial)
Cottam		1,970	Various (Commercial)
Didcot A		2,020	Wood (Commercial)
Drax		3,870	Various (Commercial)
Eggborough		1,960	Various (Commercial)
Ferrybridge C		1,955	Various (Commercial)
Fiddlers Ferry		1,961	Various (Commercial)
Ironbridge		970	Various (Commercial)
Kingsnorth		1,974	Various (Commercial)
Longannet		2,304	Waste Derived (Commercial)
Ratcliffe		2,000	Various (Commercial)
Rugeley		976	Various (Commercial)
Tilbury B		1,020	Wood (Commercial)
West Burton		1,932	Olive Cake (Trial)

2.3 Fuel Characteristics

2.3.1 Introduction

The ability to co-fire two fuels requires an extensive knowledge of the suitability of the fuel in terms of transport, preparation, boiler feeding, ignition [Grotkjaer *et al.* 2003], burnout, slagging, fouling, corrosion, and the particulate, gaseous and other waste products [Laursen *et al.* 2002]. Although the way a fuel behaves during combustion is covered in Section 2.4, all of these characteristics depend on the fuel composition, described in terms of its proximate and ultimate analysis in Sections 2.3.5 and 2.3.6 respectively. Biomass can also be divided into three significant pseudo-components: cellulose, hemicellulose and lignin, the nature of which are discussed in Section 2.3.7.

2.3.2 Coal vs. Biomass

Similarities between coal and biomass relate to their common origin – coal is fossilised biomass – while the differences relate to the many processes acting on the chemical and

physical properties of coal over the 200 million or so intervening years. Biomass exhibits all the variation in colour, texture, composition and density of modern organic matter, which Section 2.3.3 classifies in terms of renewable energy applications. In contrast, coal is a (usually) dense, (usually) black, and (usually) amorphous carbonaceous rock, derived from the sedimentation of decayed biomass in an anaerobic environment.

To compare their relative compositions, Table 2-2 presents data collated by the author for typical coals and biofuels. Relative to coal, biomasses contain higher volatile contents, lower levels of fixed carbon, more oxygen, less nitrogen and sulphur, more silica, potassium and calcium, less aluminium, iron and titanium, exhibit lower bulk densities and heating values, and wider ranges of ash and moisture. One significant difference between the two fuel types is the notable difference in the combustible phases, illustrated by the VM/FC ratio, meaning that in contrast to most coal, volatiles are a significant part of biomass combustion.

In terms of performance, biomass is more difficult to reduce in size than coal, results in pyrolysis at a lower temperature and produces char with a higher with oxygen content. Perhaps most importantly however it evolves volatile matter which although has a lower heating value than coals, makes a greater contribution to the fuels overall heating value due to biomasses very high volatile content. Volatiles contribute 70 percent of the total energy for biomass, compared with just 36 percent for coal [Quaak *et al.* 1999; Demirbas 2004].

2.3.3 Biofuels: Organic Renewable Energy

Biomass is classed as any "material of biological origin excluding material embedded in geological formations and transformed to fossil" [CEN/TS-14588:2004 2004]. In terms of energy generation, the varieties of biomass are extensive, so there is a need to define the subject of the present investigation. Renewable energy is a general term referring to energy of non-fossil origin and includes biofuels, waste fuels, hydro (tidal, wave, marine current and hydro storage), climatic power (on-shore and offshore wind, and solar) and geothermal power. Biofuels are derived from biomass for the purpose of

energy production. Waste fuels are original products of urban, industrial and commercial activity utilised for renewable energy. Table 2-4 differentiates a number of commonly used materials for the latter two categories. Poultry litter, sewage sludge, and meat and bone meal are in some references referred to as a waste fuel, and suffer from the legislative restrictions as such. However, it is the authors opinion they are biomass, in accordance with [CEN/TS-14588 2004]. These latter fuels are grouped as "wet waste biofuels", to contrast with solid/fibrous biofuels.

Table 2-4: Examples of fibrous and wet waste biofuels, and waste fuels. Fuel examples taken from the reference list

Biofuels		Waste Fuels
Fibrous Biofuels	Wet Waste Biofuels	
Sugar cane waste	Poultry litter	Landfill gas
Timber mill waste	Meat and bone meal	Coke oven gas
Short rotation coppice	Sewage sludge	Mine gas
Straw	Sewage digester gas	Stripped crude gas
Rice and coffee husks		Municipal solid waste
Nut shells		Refinery/plant flare gas
Forestry/arboriculture residue		Hazardous chemical waste
Palm oil and coconut residues		

2.3.4 Coal Formation and Classification

Coal is the fossilised remains of plant matter. Its formation begins with an accumulation of decomposing biomass in an anaerobic environment such as a riverbed, a swampland or a marine basin [Berkowitz 1994]. Initial anaerobic activity results in acidification of the deposits and peat is formed. Over several million years, the deposit is compacted by progressive layers of sedimentary overburden which, combined with geological heating brings about the maturation process that results in coal. Changes include the removal of moisture, volatile material, oxygen, hydrogen, nitrogen and sulphur; and a concentration of carbon and mineral matter. Figure 2-2a shows the maturation of coal as function of volatile content.

The youngest coal rank, lignite[2] is named after the most stable structure in biomass, lignin (Section 2.3.7). Lignites can contain between 63 and 79 percent carbon by weight (%C wt.), have a calorific value of 14.6 to 19.3 MJ kg^{-1} and are commonly used in power generation. The next rank of coal, sub-bituminous, contains 79 to 85 %C wt. and produces between 19.3 and 26.75 MJ kg^{-1}. It is used as a low sulphur alternative to higher rank coals. The next rank, bituminous coal, contains 85 to 92 %C wt. and generates between 24.4 and 32.5 MJ kg^{-1} it is commonly used in electricity generation and as a source of coke for the steel industry. The final rank, anthracite, is metamorphic as opposed to a sedimentary due to the high temperatures (> 720 K) required for the final stages of the coalification process. Anthracite contains over 92 %C wt., and generates more than 32.5 MJ kg^{-1}. The structures in Figure 2-3 describe the progressive increase in the aromatic content of coal as it matures, while the increasing occurrence of polyaromatic groups is described by Table 2-5.

For British and International Standards, coal maturity is determined by maceral analysis [BS-ISO-11760 2005]. Macerals are discrete carbonaceous remains of plant tissues and their decomposition products (Table 2-6). During coalification, the optical properties of macerals merge, and the proportion of the maceral group Vitrinite (calculated as the percentage mean random Vitrinite reflectance, $\%R_v$) is used to determine the coal's maturity. In coals of less than 87 %C wt., macerals exhibit distinct plant tissue features, while for coals of over 95 %C wt., only reflectance light microscopy can differentiate maceral types. Figure 2-2b describes the coal rank series as a function of $\%R_v$.

(2) For consistency with previous publications, the ASTM coal names are used.

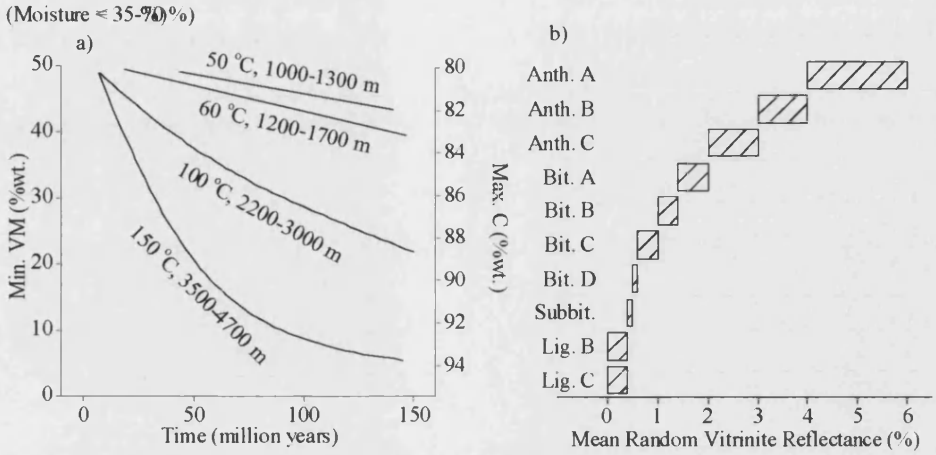

Figure 2-2: (a) Influence of time and heat on coal maturity as a function of volatile and carbon content; (b) Coal rank by Vitrinite measurement. [Berkowitz 1994; BS-ISO-11760 2005]

a)

b)

c)

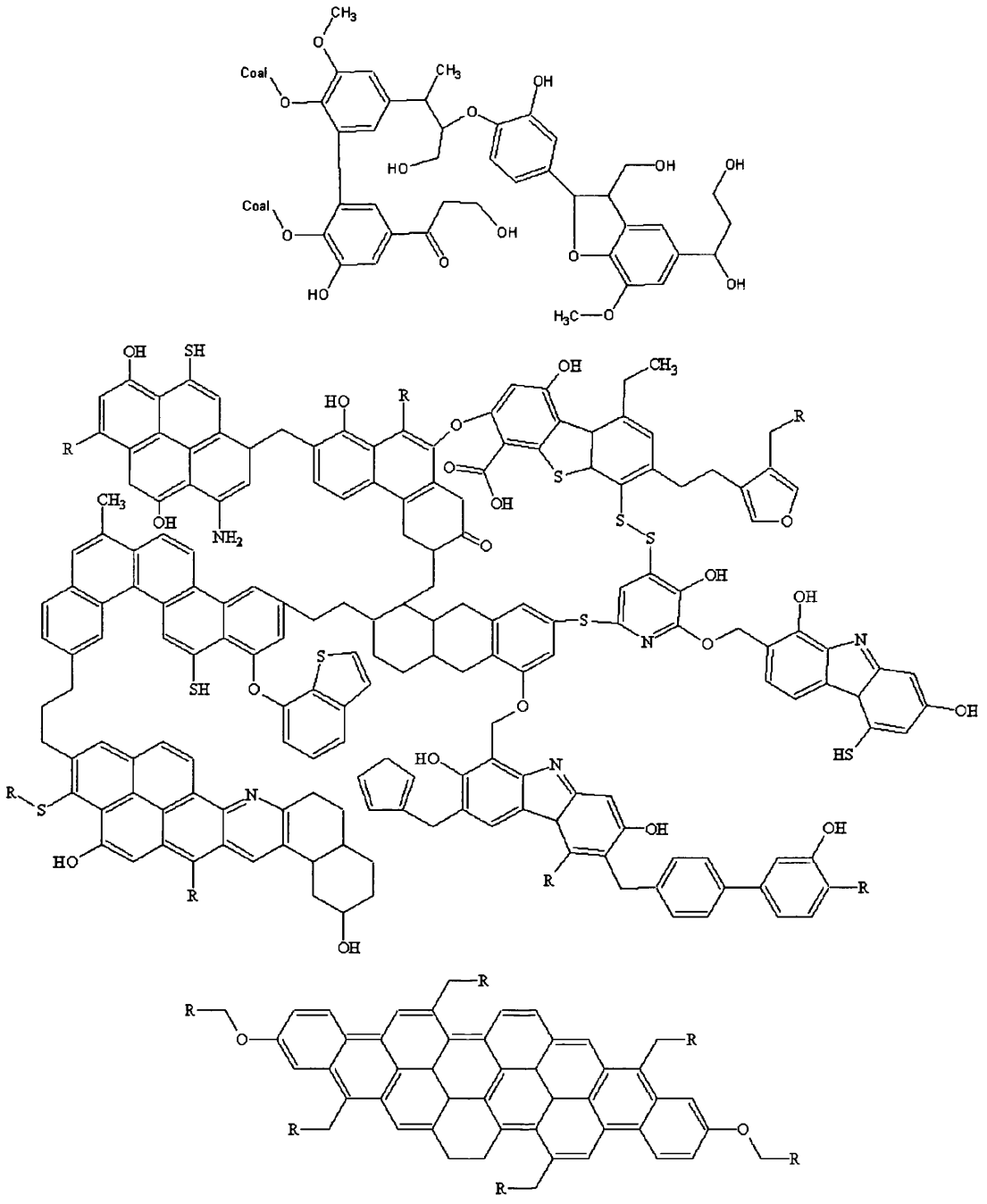

Figure 2-3: Model structure of fixed carbon content of (a) lignite, (b) bituminous coal and (c) anthracite (after [Berkowitz 1994])

Table 2-5: Aromatic composition of biomass and coal ranks [Tillman 2000]

Fuel	Number of rings per aromatic cluster (%)				Aromatic carbon (%C)
	1	2	3	4	
Woody biomass	100	-	-	-	20-25
Texas Lignite	42	26	21	11	46
Wyoming Subbit.	39	35	-	26	40
Illinois Bit.	8	50	36	8	60-70
Anthracite	Macromolecular				> 90

Table 2-6: Coal macerals and maceral groups as recognized by the International Committee for Coal Petrography [Berkowitz 1994]

Maceral Group	Macerals	Origin
Vitrinite	Collinite, tellinite	Humic gels, bark and cortical tissue
Exinite	Sporitite, cutinite, resinite, alginite	Spores, cuticles, resins, waxes and algal remains
Inertinite	Fusinite, sclerotinite	Carbonised woody tissue, fungal sclerotia and mycelia

2.3.5 Proximate Analyses

Four components of any fuel describe its proximate character, directly affecting its performance in a power station. These are moisture, volatile content, fixed carbon and ash, regularly quoted alongside its heating (calorific) value.

(i) Moisture

Moisture plays an important role in the combustion efficiency of a fuel. High moisture fuels such as peat or bagasse can choke bunkers and reduce milling efficiency, especially in pulverised fuel furnaces. The latent heat of evaporation also delays the release of volatile materials resulting in poor fuel ignition and low gas phase temperatures [Demirbas 2003]. Without pre-drying, large quantities of steam also mean the volumetric capacity of emissions reduction technologies must be increased.

There are several definitions for the moisture content of a sample. Ideally, only superficial moisture present in cracks and hollows, and physically adsorbed water in smaller micro-pores should be measured and as standard, water evolved through thermal decomposition above 420 K is ignored, particularly important in lower rank coals. Moisture is usually measured by heating a <60 mesh sample at between 380 and 385 K in nitrogen until constant mass is attained [BS-1016-104.1 1999].

In coal, moisture content decreases with increasing maturity. Although generally low, moisture in biomass can range from 10 to 60 %wt. depending on fuel type, season and pre-treatment, for example if a food product is recovered by freeze-drying, it also produces low moisture fuels.

(ii) Volatile Materials

Volatile content encompass the large range of products of non-oxidative processes and can include carbon dioxide, carbon monoxide, reaction water and a vast assortment of lighter hydrocarbons including tars that re-condense when cooled (Section 2.4.2). When released in an oxidising environment, volatile materials burn in the gas-phase (Section 2.4.5). Their proportion within the fuel affects the volume required for complete combustion, oxygen demand, oxygen availability to the char, mass/energy transfer processes and the ease of the fuels ignition [Berkowitz 1994]. Insufficient furnace volume results in incomplete combustion with raised levels of residual char, CO, hydrocarbons and polyaromatic hydrocarbons in the ash or undesirable gaseous emissions. This often culminates in downgrading the thermal capacity of a coal furnace where biomass is to be burnt.

Volatile content is measured by heating an air-dried, < 60-mesh sample out of contact with air at 1273 K for 7 minutes [BS-1016-104.3 1998].

As with moisture, volatile matter decreases with coal maturity. The volatile content of biomass is dependent on the biomass type, but is generally higher than coal. It is because of the volatile content and its ease of liberation from biomass, that ignition of biofuels is easier and occurs at lower temperatures than coal, giving more rapid but less controllable combustion [Sami *et al.* 2001].

(iii) Fixed Carbon Content

Fixed carbon content represents the fraction of the solid phase of a fuel that can oxidise if heated in air. In coal, this is the most important component as it represents the greater mass proportion of the fuel. By liberating more heat and hot gasses than the volatile phase per unit weight, it also represents the majority of the energy of coal [Berkowitz

1994]. Fixed-carbon content is calculated indirectly from the other proximate characteristics:

Equation 2-1: $$\%FC = 100\% - (\%Moisture + \%VM + \%Ash)$$

The importance of fixed carbon and comparisons between biomass and coal are discussed in Section 2.4.3.

(iv) Ash Content

Ash represents the fraction of the fuels solid phase that will not burn. In reality, a fuel does not contain ash, but mineral matter composed of inorganic minerals and complexes. Ash consists of the dehydration, decomposition and oxidation products of these compounds such as Equations 2-2 to 2-4 [Berkowitz 1994].

Equation 2-2: $$FeSO_4.nH_2O_{(s)} \rightarrow FeSO_{4(s)} + nH_2O_{(vap.)}$$

Equation 2-3: $$CaCO_{3(s)} \rightarrow CaO_{(s)} + CO_{2(g)}$$

Equation 2-4: $$FeS_{(s)} + 2O_{2(g)} \rightarrow FeSO_{4(s)}$$

Ash content is calculated as the mineral residue after a weighed sample has been heated gradually in air to 1188 ± 10 K [BS-1016-104.4 1998]. Although the ash content of biomass is generally low, the quantity is much more variable than for coal, as Table 2-6 illustrates. Some of the broad ranges of chemical processes of ash are considered in Section 2.4.6.

(v) Heating Value

The heating value of a fuel is amongst its most important properties, describing the amount of energy that can be released from the fuel. The two forms, higher and lower heating value (HHV and LHV respectively) represent the energy liberated with evolved moisture in condensed and vapour states [Sheng *et al.* 2005]. Typically, the experimental determination of heating value is performed using a bomb calorimeter [BS-1016-105 1992] where a sample is burned in excess oxygen in standard adiabatic conditions. However, this is a long and complex procedure so instead, estimations of HHV's may be calculated. The Dulong-Berthelot formula (Equation 2-5, giving the

HHV in kJ kg^{-1}) is an early example of such a calculation from ultimate composition data of a dry, ash-free coal sample [Berkowitz 1994]:

Equation 2-5: $$HHV = 1000.\begin{pmatrix} 35.6\%C + 116.22\%H - 11.09\%O \\ + 6.28\%N + 10.46\%S \end{pmatrix}$$

Sheng *et al.* [2005] describe other means of estimating the higher heating values for biofuel from proximate and ultimate analysis data, respectively:

Equation 2-6: $$HHV = 19.914 - 0.232\%Ash$$

Equation 2-7: $$HHV = 0.3259\%C + 3.4597$$

The accuracy of these techniques is not good however. When using Equation 2-6, Sheng *et al.* [2005] quote an mean absolute error of 3.78 %, while using carbon in Equation 2-7 gives a slightly better margin of error of 3.16 % comparing the calculated and actual HHV's for around 200 biomass samples.

2.3.6 Ultimate Analysis

Ultimate characterisation as described below provides information in terms of carbon and hydrogen, oxygen, nitrogen and sulphur content. These are less useful in a power station operation than the proximate properties; however, they are necessary for estimating emissions levels.

(i) Carbon and Hydrogen

A known mass of coal is burned at a temperature of 1623 K in a rapid current of oxygen, so that all the carbon is converted to carbon dioxide and all the hydrogen to water. Oxides of sulphur and chlorine are removed on silver gauze. Water is absorbed by magnesium perchlorate solution and the carbon dioxide by sodium hydroxide solution. A determination of moisture is carried out at the same time so the value for hydrogen may be corrected appropriately [BS-1016-6 1997].

(ii) Oxygen

Oxygen is typically accounted for by difference (Equation 2-8); accumulating the errors of the other elemental determinations.

Equation 2-8: $$\%O = 100\% - (\%C + \%H + \%N)$$

Other methods include passing pyrolysis gasses over carbon at 1373 K and estimating the resulting CO concentration gravimetrically, or by neutron bombarding the sample converting naturally occurring ^{16}O to ^{16}N, which decays with quantitative amounts of β-radiation.

(iii) Nitrogen

Nitrogen is classically determined by the Kjedahl-Gunning method [BS-1016-6 1997]. A known mass of the sample is heated with concentrated sulphuric acid and potassium sulphate, in the presence of a mixed catalyst (typically mercuric or selenium salt) to convert the nitrogen into ammonium sulphate. From this, ammonia released by steam distillation from alkaline solution is absorbed in boric acid and determined by titration with sulphuric acid. The formation and effect of nitrogen emissions from power stations are discussed in Section 2.4.7.

(iv) Sulphur

Total sulphur may be determined by the Eschka method for one-off analysis (*e.g.* ASTM D 3177) however the high temperature method [BS-1016-106.4.2 1996] is better for larger sample throughput. Here a known mass of the sample is burned in a stream of oxygen at a temperature of 1623 K. Aluminium oxide is added to prevent the retention of sulphur in the ash. The oxides of sulphur and chlorine are absorbed in neutral hydrogen peroxide and determined volumetrically, correcting for chlorine [BS-1016-8 1997]. For differentiation between the sulphate (SO_4^{2-}) and sulphite (*e.g.* FeS) forms of sulphur, the standard determination [BS-1016-106 1996] utilizes the differential solubility's of sulphate and pyrite in hydrochloric and nitric acids, such that each can be successively dissolved and determined directly. Classical determination of organic sulphur (*e.g.* thiol) was by difference between total and inorganic sulphur, while modern techniques use Scanning Electron Microscopy with Energy Dispersive X-Ray (SEM-

EDX) analysis for both the quantitative and qualitative organic sulphur content. The formation and effect of sulphur emissions from power stations are discussed in Section 2.4.8.

2.3.7 Fibrous Biomass Composition

The combustion and pyrolysis behaviour of fibrous biofuels is further dependent on three thermally active polymer components, cellulose, hemicellulose and lignin; as well as mineral matter and water [Orfao *et al.* 1999]. There is also an array of extractives including tannins and resins; however, their thermal influence is comparatively low.

The most common component, cellulose, is an unbranched polysaccharide chain composed of D-glucose monosaccharides (Figure 2-4). Cellulose is in turn surrounded by a matrix of hemicellulose, formed from units of glucose, mannose, galactose, arabinose and xylose (Figure 2-5). A hemicellulose polysaccharide consists of a backbone of monosaccharide units, from which monosaccharides extend at irregular intervals, which since they are not made to a framework are structurally amorphous. However, average compositions for some commonly isolated hemicellulose's are summarised in Table 2-7.

Table 2-7: Main polysaccharides structures of the plant cell wall and their composition [Lea et al. 1993]

Hemicellulose	Backbone monomer	Backbone linkage	Side-groups
Xylan	Xylose	1→4	Arabinose & glucuronic acid
Xyloglucan	Glucose	1→4	Xylosyl
Glucomannan	Mannose and Glucose	1→4	Galactose
Mannan	Mannose	1→4	-
Glucan	Glucose	1→4 and 1→3	-
Callose	Glucose	1→3	-

The final and least thermally active of the biopolymers is lignin, constructed from phenylpropanoid residues such as sinapyl alcohol (Figure 2-6). They are found in large deposits about vascular plant tissues, providing rigidity and resistance to degradation, notably in woody crops and mature grasses. The vast range of lignin compounds are ultimately defined by their insolubility in 72 percent sulphuric acid and lignin's inert

nature, caused by the high aromatic carbon content and low availability of oxygen, making them highly resistant to digestive enzymes.

Pastor-Villegas *et al.* [1998] describe the chemical and macromolecular changes involved during the pyrolysis of wood char. During carbonisation, cellulose microfibrils shrink to 83 percent their original length, accounting for most of biomass shrinkage partly through the high cellulose content of biomass and partly because lignin is largely aromatic and undergoes less shrinkage. Below 735 K, pyrolysis changes correlate with a thinning and shrinkage of the woody vessels and fibres.

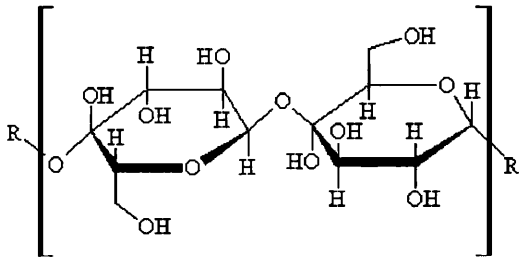

Figure 2-4: A cellulose repeating unit of two D-glucose units linked with a β(1→4) glycosidic bond (After [Lea et al.1993])

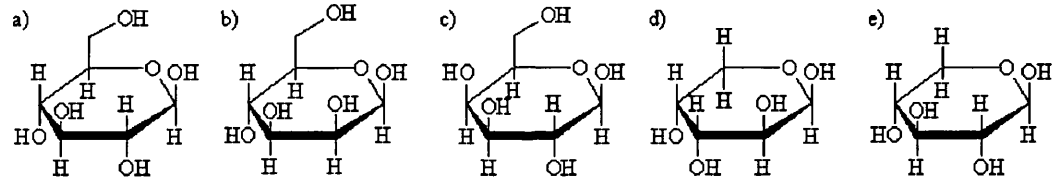

Figure 2-5: Monosaccharide units: a. β-D-glucose; b. β-D-mannose; c. β-D-galactose; d. β-L-arabinose; e. β-D-xylose (After [Lea et al.1993])

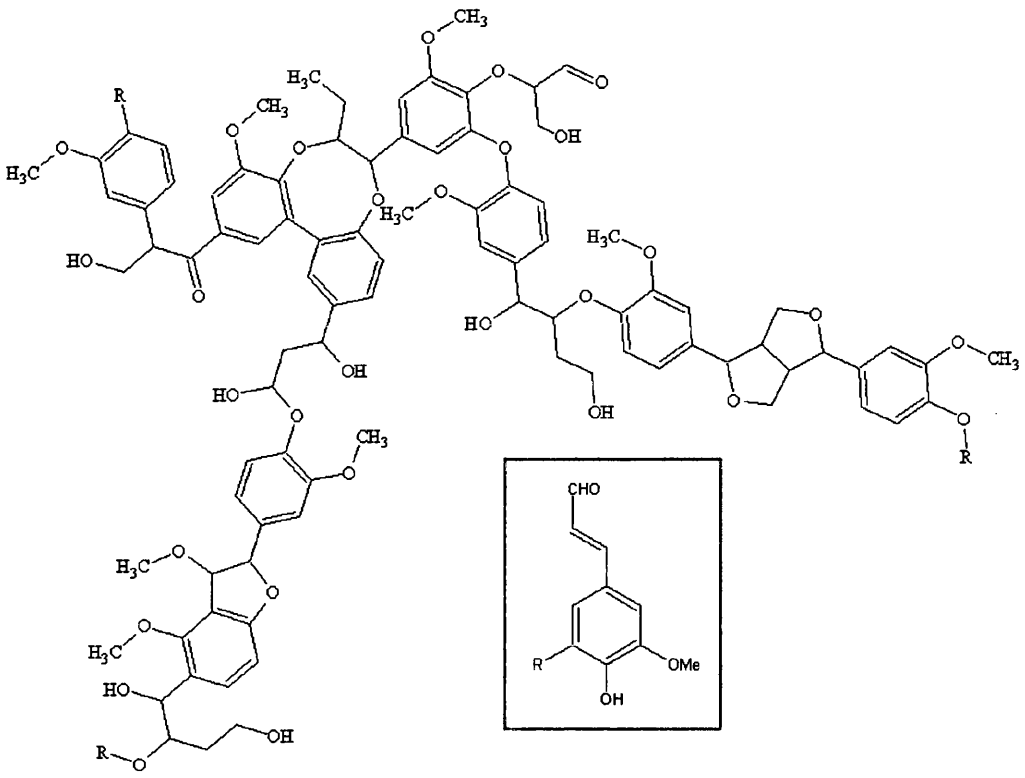

Figure 2-6: Model lignin structure, Inset: coniferaldehyde, an example of the phenylpropanoid residues found in lignin (After [Lea et al.1993])

2.4 Combustion Chemistry

2.4.1 Introduction

Before considering the effect of combining different fuels, combustion as a whole must be reviewed. The following Sections consider the chemistry involved when carbonaceous fuels burn, but the process can be summed up by a single global equation:

Equation 2-9: $\text{Char} + \text{Oxygen} \xrightarrow{\Delta} \text{Carbon Oxides}$

The efficiency at which this occurs is strongly influenced by the fuel composition described in Section 2.3, and the combustion conditions. In the present investigation, gasification and pyrolysis occur where oxygen is restricted or eliminated respectively, while oxidation and combustion occur where the rate of heating is controlled or excessive respectively.

2.4.2 Pyrolysis and Carbonisation

Pyrolysis is the precursor to combustion and involves the release of products in a slow vaporization process. Carbonisation refers to the reactions of the char. Aside from the char, there are three classes of pyrolysis product.

(i) Primary gaseous products formed by cracking of the aliphatic carbon structure and devolatilisation of functional groups to form CO, H_2, H_2S, and C_{1-2} hydrocarbons. Secondary de-alkylation of the tar as well as char condensation (carbonisation), involves the cyclisation, aromatisation and condensation reactions that lead to the chars pseudo-graphitic state (*e.g.* Figure 2-7, p. 28).

(ii) Low-temperature light tars produced below 973 K that includes phenols, methyl-substituted pyridines and olefins.

(iii) High-temperature tars produced from the dealkylation, dehydroxylation and condensation of light tars and chars above 973 K. Fractions range from lighter oils of benzene, toluene and xylene, to viscous mixtures of five-ring polycondensated aromatics.

During pyrolysis, chemically bound hydrogen is divided between carbon (forming gas or tar) and oxygen (forming water). Therefore, where a fuel exhibits high oxygen levels (*e.g.* biomass > lignite > anthracite) tar and oil yields are reduced, but against this, where hydrogen levels are high (*e.g.* biomass > lignite > anthracite), tar levels are also elevated [Berkowitz 1994]. Tar and gas compositions are also altered by the pyrolysis temperature and heating rate.

It is currently considered that heterogeneous reactions between residual char and the volatile material depend on the adsorption of the reagent to an active site, a reaction producing an intermediate complex, and the desorption of the species to the gas phase. This is also described in the five-stage process for oxidation in Section 2.4.3. These active sites for pyrolysis include cracks or edges in the char matrix that expose carbon atoms of a reduced stability; carbon in functional groups (*e.g.* CH_3) having a lower

activation energy than the surrounding graphite sheet; and heteroatoms (*e.g.* O, N or S) that induce irregularity and provide alternative activity pathways. The presence of certain mineral elements (K, Na, Mg) can also catalyse carbon reactions with CO_2, resulting in lower energy pathways for char oxidation.

Production of CO and H_2 increases with pyrolysis temperature while CO_2 production decreases so that above 1023 K, combustible gasses (CO, H_2 and CH_4) form 70 to 80 percent of biomasses pyrolysis gas volume. This highly reactive gas means that air-oxygen is often depleted during the pyrolysis stage (Section 2.4.5). This partially contributes to the fact that the majority of biomass weight loss occurs through rapid pyrolysis reactions, prior to char oxidation. For coal, where volatiles are less important in terms of volume and vigour, air oxygen depletion occurs in two stages: a small event for volatiles and a second more important event for char oxidation [Werther *et al.* 2000].

The pyrolysis onset temperatures depend strongly upon the fuel type and heating rate. Sami *et al.* [2001] quote research where for low heating rates (0.006 K min^{-1}) coal pyrolysis has been observed to begin between 623 and 673 K; for high heating rates (6,000 K min^{-1}) pyrolysis began at 1473 K; and at 1773 K for very high heating rates (600,000 K min^{-1}). However, delays due to heat transfer limitations are not discussed. This is a common observation for any reaction where heating rate, reaction rate, and rates of heat and mass transfer are important processes.

During pyrolysis, changes in the carbon, hydrogen and oxygen content of residual char are observed. Pastor-Villegas *et al.* [1998] described the chemical changes in wood char as it is heated in nitrogen to 1073 K. Carbon content increases to a maximum at around 973 K while oxygen and hydrogen decreases, levelling out at 1073 K. Quantifiable aromatisation of fixed carbon (Figure 2-7) begins before 673 K, with a peak in sample density at 1073 K indicating the limit of aromatisation. While heating to 1073 K, char porosity increases as volatile components (mostly tars) are removed from first meso- and macropores, (between 473 and 673 K) then micropores (between 673 and 1073 K) increasing surface area beyond the rate of char condensation. Above 1073 K, char porosity cannot be improved any further, as no volatile components remain. At this temperature, pore narrowing through straightening and ordering of the lingo-cellulose graphite layers, that began around 873 K, mean that when pore unblocking

becomes negligible (above 1073 K), pore narrowing and closure processes act to reduce char porosity. Zubkova [2005] investigated the macromolecular transformations of coal chars, including the effect of coal rank on the shrinkage (condensation) processes during the formation of coke.

Arenillas *et al.* [2003; 2004] describe the TG-MS-FTIR behaviour of a synthetic coal of known chemical structure to relate the pyrolysis emissions and TG behaviour of real coals with their chemical composition. Four pseudo-components to represent the carbonaceous matrix (phenol formaldehyde resin); semi-graphitic structures (3,4,9,10-perylenetetracarboxylic dianhrdride); pyridinic nitrogen (poly-4-vinylpyridine) and pyrrolic nitrogen (polyvinylpyrrolidone) were blended and cured to form the synthetic coal. Deconvolution of the dTG profile is used to isolate four reaction groups. After an initial moisture loss at 633 K, a weight-loss process at 743 K relates to CO_2 and H_2O emitted from labile carbonyl and hydroxyl moieties of the carbonaceous matrix. A process at 793 K relates to CO and phenol from the semi-graphitic pseudo-component, methane from the carbonaceous matrix, and small amounts of HCN and NO apparently from the pyridinic nitrogen. The fourth process with a peak maximum at 923 K, relates to emissions of H_2 and CO during char condensation of the carbonaceous matrix.

The pyrolysis mode depends on particle size and the volatile content of the fuel. Small particles and fuels of high volatile content can become shrouded by volatile gasses which can prevent oxygen reaching the char, whereas larger particles (> 80 μm) eject volatile materials in distinct jets [Sami *et al.* 2001].

Aside from beneficially reducing a biomass particles burnout time in pulverised fuel furnaces, this difference has important consequences for the fuel, air and heat distributions within a fluidised bed furnace. With over-bed feeding of biomass for example, the rapid ignition and combustion of biomass mean less of the heat reaches the bed, reducing the bed temperature. Even with in-bed feeding, the combustion rate for gasses in the interstitial spaces of the bed are reduced through a combination of deactivation of the combustible gasses, and the delay while combustible gas bubbles reach the bed surface where they burn rapidly [Werther *et al.* 2000].

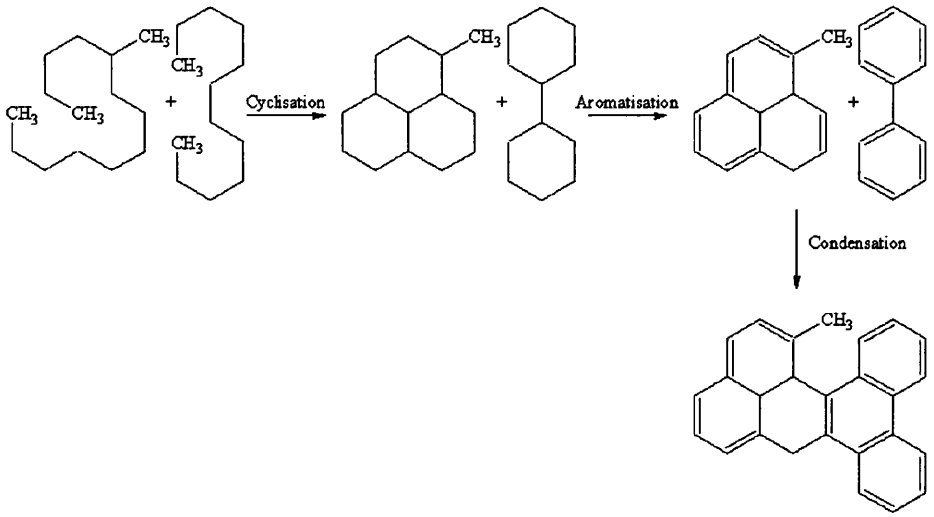

Figure 2-7: Stages in the formation of graphitic carbon (Adapted from Berkowitz [1994])

2.4.3 Heterogeneous Oxidation of the Char

Char ignition and oxidation arises in two modes. With heating rates or particle sizes of less than 60,000 K min^{-1} or 100 μm respectively, surface oxidation proceeds at a rate at least matching that of pyrolysis and combustion proceeds by a largely heterogeneous pathway. However, outside of these conditions, ignition becomes homogeneous as volatile gasses shroud the particle preventing char oxidation until volatile combustion is complete and the flame has been extinguished [Grotkjaer *et al.* 2003]. For small samples and single char particles, the rapid rate of homogeneous oxidation means that this restriction is only temporary and such char oxidation is generally unaffected [Sami *et al.* 2001], however the effect is more pronounced in boilers where the fuel supply is constant, or for fuels of large volatile content. The central processes of char oxidation are shown in Figure 2-8 (p. 30). Adsorption and desorption (steps 2 and 4 respectively) are generally quick compared with the other stages, meaning the overall reaction rate is either diffusion controlled (steps 1 and 5) or kinetically controlled (step 3) [Boonmee *et al.* 2005].

Chen *et al.* [1996] also look at the effect of coal rank (referring to the volatile content) and particle size on the homogeneous and heterogeneous oxidation, confirming that as coal rank increases, the preference for the heterogeneous decomposition pathway also

increases. For mid-rank coals, as the temperature rises, ignition and subsequent oxidation involves part-pyrolysis interrupted by char oxidation activity.

Oxygen mostly reaches the surface of the char as O_2, CO_2 or H_2O. Therefore, the dominant heterogeneous combustion reactions for char are [Sami *et al.* 2001] (with activation energies calculated at 700 K using Equation 2-33, p. 43):

Equation 2-10: $C_{(s)} + O_{2(g)} \rightarrow CO_{2(g)}$ $E_{Act,a} \sim 405.1\,kJ\,mol^{-1}$

Equation 2-11: $C_{(s)} + \frac{1}{2}O_{2(g)} \rightarrow CO_{(g)}$ $E_{Act,b} \sim 123.1\,kJ\,mol^{-1}$

Equation 2-12: $C_{(s)} + CO_{2(g)} \leftrightarrow 2CO_{(g)}$ $E_{Act,c} \sim 171.3\,kJ\,mol^{-1}$

Equation 2-13: $C_{(s)} + H_2O_{(vap.)} \leftrightarrow CO_{(g)} + H_{2(g)}$ $E_{Act,d} \sim 130.3\,kJ\,mol^{-1}$

Equation 2-14: $C_{(s)} + 2H_{2(g)} \leftrightarrow CH_{4(g)}$ $E_{Act,e} \sim 75.8\,kJ\,mol^{-1}$

However, the actual products of char oxidation are the subject of some controversy [Wang *et al.* 2003]. At ignition temperatures (600 to 700 K), oxidation reactions favour that described in Equation 2-10, however at typical combustion temperatures (1100 to 1200 K) the dominant oxidation reaction is that given by Equation 2-11. Reactions 2-10 and 2-11 are exothermic. The Boudouard reduction reaction of carbon with CO_2 (Equation 2-12) or the reactions with steam (Equation 2-13) are both endothermic and limited in free flowing air, however under boiler conditions, where oxygen levels are limited, pressures are low, or temperature exceed 4,000 K, they play a more significant role [Sami *et al.* 2001]. The hydro reaction (Equation 2-14) is common in gasification conditions, favouring lower temperatures.

In their study, Fu *et al.* [1997] describe the effect of temperature on Reactions 2-10, 2-11 and 2-12. They note that the overall char activation energy ($E_{Act,char}$), depends on the rates of the three reactions, and that at a single temperature $E_{Act,a}<E_{Act,b}<E_{Act,c}$. At high temperatures, Reactions 2-11 and 2-12 are faster than 2-10, so $E_{Act,char}$ is between $E_{Act,b}$ and $E_{Act,c}$. Conversely, at low temperatures, $E_{Act,char}$ is between $E_{Act,a}$ and $E_{Act,b}$.

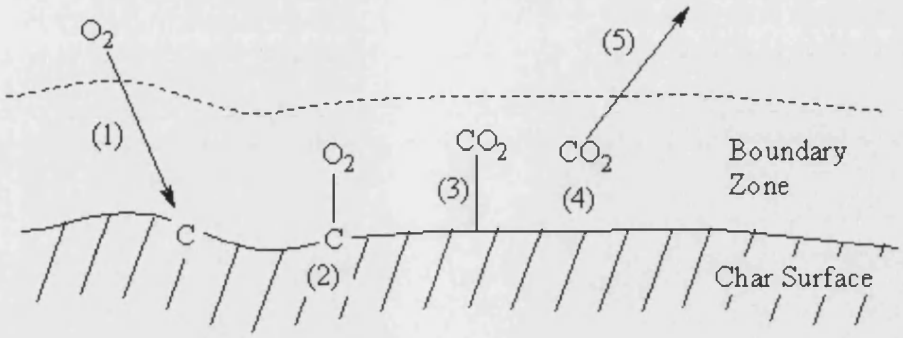

Figure 2-8: Processes governing a heterogeneous reaction. (1) Diffusion of oxidising species through the boundary layer to the particle surface; (2) Adsorption of the gas phase species at an active site; (3) Chemical reaction of the adsorbed species; (4) Desorption of the product; (5) diffusion of the gas phase products through the boundary layer

2.4.4 The Overlap between Heterogeneous Oxidation and Pyrolysis

Research into understanding the interaction between char oxidation and pyrolysis is driven by its influence on combustion systems. Gurgel-Veras *et al.* [1999] describe its effect on flame stability, particle temperature and fuel burnout efficiency. Gurgel-Veras *et al.* model the overlap between homogeneous oxidation and heterogeneous oxidation, considering the effects of particle size, ambient temperature, and oxygen concentration. Boonmee *et al.* [2005] describe the onset of heterogeneous oxidation of wood in relation to the surface temperature, and the role of kinetic and diffusion control mechanisms depending on the resistance of the char to oxidation. They identify a temperature of 637 K as being the transition temperature between kinetic and diffusion controlled activity.

Senneca *et al.* [2002a; 2002b] describe the importance of two conditions for heterogeneous ignition or decomposition by heterogeneous oxidation, that:

(i) The intrinsic kinetics of heterogeneous oxidation must be large in comparison to purely pyrolytic activity;

(ii) That the rate of inward diffusion of oxygen must exceed the outward flow of volatiles.

The degree to which these conditions are achieved is primarily dependent on the fuel (composition, morphology, dimension *etc.*), but also affected by the combustion conditions.

Senneca *et al.* describe three pathways when heating a sample in pyrolysis or oxidation conditions (Paths A, B and C; Figure 2-9). These are used to describe the relative reactions governing the oxidation or pyrolysis of a fuel. If the rate of pyrolysis exceeds the rate of oxidation, initial pyrolysis-type activity is similar in both conditions (Path A) and oxidation of the char (Path B) arises in a secondary peak (Figure 2-9a). Where the rate of oxidation dominates, oxidation (Path C) precedes pyrolysis (Path A) and discrete peaks for each condition are observed (Figure 2-9b). The third pathway (Figure 2-9c) is more complex. A high temperature peak is still observed relating to the oxidation of char (Path B), however Paths A and C compete for the volatile fraction. The resulting oxygen-prompted bond cleavage means that pyrolysis-type reactions occur at a lower temperature. Senneca *et al.* [2002] suggest that lingo-cellulosic biomass fuels fall into this latter category, with pyrolysis-type reactions occurring 20 to 30 K earlier when investigated in air.

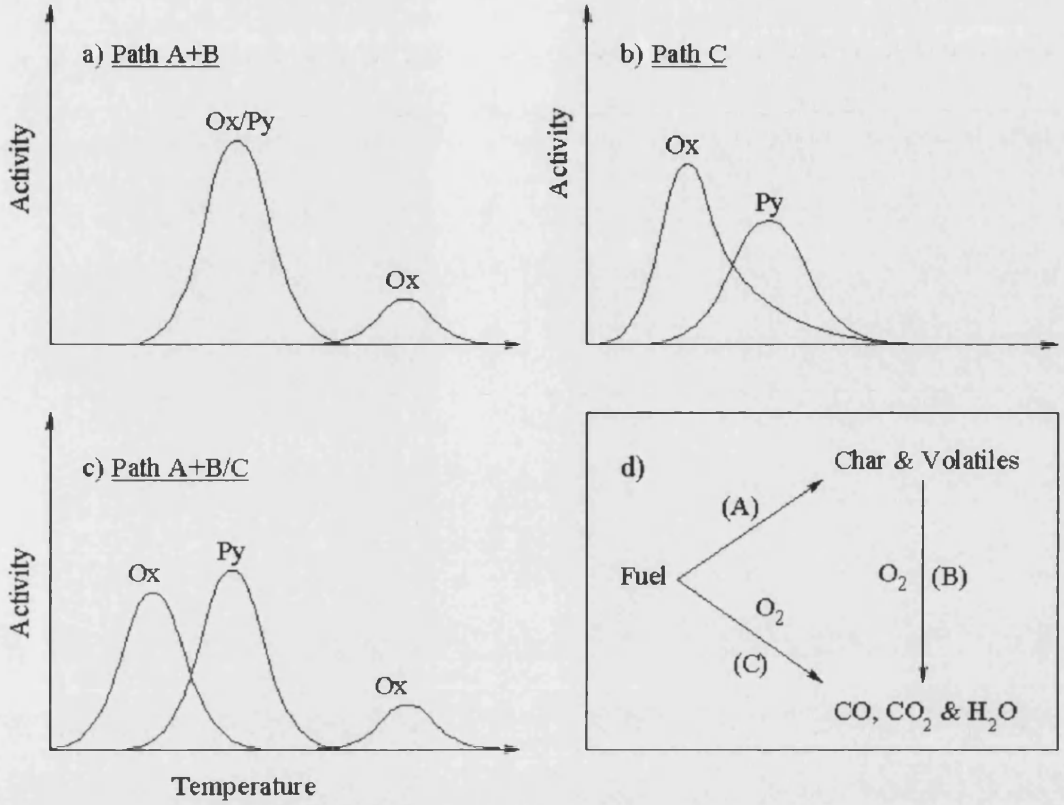

Figure 2-9: (a to c) Model describing three mechanisms for the reactions of heterogeneous oxidation (Ox) and pyrolysis (Py) of a fuel. (d) Comparison of mechanisms for the decomposition of a solid char (After Senneca et al. [2002a; 2002b])

2.4.5 Homogeneous Oxidation of Volatile Materials

Once volatile materials (Section 2.4.2) and the products of incomplete heterogeneous combustion (Section 2.4.3) are evolved from a fuel particle, those that are able (including CH_4, H_2 and CO) are oxidised in the gas phase. The most common reactions are therefore:

Equation 2-15: $$C_xH_y \xrightarrow{O_2} xCO_{2(g)} + \tfrac{y}{2} H_2O_{(g)}$$

Equation 2-16: $$2H_{2(g)} + O_{2(g)} \rightarrow 2H_2O_{(vap.)}$$

Equation 2-17: $$2CO_{(g)} + O_{2(g)} \rightarrow 2CO_{2(g)}$$

The rapid ignition and oxidation of volatile matter means large amounts of energy are released, resulting in a gas phase temperature significantly higher than that of the

particles [Demirbas 2003]. This effect is important when considering control of emissions (Section 2.4.7), and in designing burners and the boiler. The high gas phase temperatures bring the heat much closer to the burners [Sami *et al.* 2001]. The importance of homogeneous oxidation with biomass is evident when observing that volatiles represent around 70 percent of biomasses heat contribution, compared with just 36 percent for coal [Demirbas 2003]. Unfortunately, while gas phase chemistry has strong implications for emissions in char oxidation, the reactions are invisible to the thermogravimetric methods used in the present investigation.

2.4.6 Ash Chemistry

After the decomposition processes of devolatilisation (Section 2.4.2) and char oxidation (Section 2.4.3), any remaining chemistry involves the ash. There are a number of ash reactions, generally in excess of 850 K. Arvelakis *et al.* [2003] describe the TG and DTA decomposition profiles for a number of Mediterranean biomass ashes. Zheng *et al.* [2000] describe the thermal events for a sludge residue of the paper industry. Reactions occur between 873 and 1006 K relate to the decomposition of calcium carbonate (Equation 2-18), as well as several reactions involving the reduction, oxidation or chlorination of metals (Equations 2-19, 2-20, and 2-21 respectively). Oxides of Al, Ca, Si, Fe, Mg and Ti are less volatile and remain in the ash whereas Cd, Pb, Zn and Cu preferentially form chlorides, which are quickly volatilised [Zheng *et al.* 2000]. Weight losses between 1073 and 1323 K are caused by the melting and partial evaporation of alkali compounds, most notably potassium chlorides and carbonates.

Equation 2-18: $$CaCO_{3(s)} \xrightarrow{\Delta} CaO_{(s)} + CO_{2(g)}$$

Equation 2-19: $$M^{2+} \xrightarrow{Char/CO} M + CO_2$$

Equation 2-20: $$M + O_2 \rightarrow MO_x$$

Equation 2-21: $$M + Cl^- \rightarrow MCl_x$$

A significant problem for biomass is the significantly higher alkali metal content. Oxides of potassium and sodium are persistent in the ash, and strongly reducing its

softening temperature, resulting in a variety of side-reactions that lead to slagging, fouling, bed agglomeration and corrosion.

Slagging and fouling, which are respectively deposition of particles on the furnace walls and heat recovery surfaces, are a direct consequence of the ash in a molten state. Ash that has stuck to cooler surfaces traps more ash, reducing the heat transfer efficiency and inhibiting free gas flow. This may be overcome by enriching the fuel with alumina, CaO, MgO, dolomite or kaolin, to increase the ash softening temperature [Werther *et al.* 2000].

Quartz agglomerations of fluidised beds arise when bed material coagulates during reactions with sodium or potassium carbonates from the ash:

Equation 2-22:

$$2SiO_{2(s)} + Na_2CO_{3(s)} \rightarrow Na_2O.2SiO_{2(l)} + CO_{2(g)}$$
$$4SiO_{2(s)} + K_2CO_{3(s)} \rightarrow K_2O.4SiO_{2(l)} + CO_{2(g)}$$

Because of their relatively low melting points (1147 and 1037 K respectively), the eutectic products become sticky at furnace temperatures, significantly influencing fluidity and furnace performance. To avoid quartz agglomeration, ferric oxide additives are introduced, forming eutectic products with melting point of 1408 K (Equation 2-23).

Equation 2-23:

$$Fe_2O_{3(s)} + X_2O_{(s)} \rightarrow X_2Fe_2O_{4(s)}$$
$$Fe_2O_{3(s)} + X_2CO_{3(s)} \rightarrow X_2Fe_2O_{4(s)} + CO_{2(g)}$$

Such agglomeration with biomass ash is largely avoided by co-firing with coal, which have typically low alkali content. For example, 20 %wt. of coal in coffee husks reduces potassium levels from 43.8 to 13.5 %wt. of ash, with corresponding improvements to the performance [Werther *et al.* 2000].

Chemical corrosion of metal surfaces in the combustion system arises due to the dissolution of the ferrous oxides in the eutectic silicate mixtures described by Equation 2-24. The volatility of the alkali metals helps drive this process to the right [Werther *et al.* 2000]:

Equation 2-24:

$$K_2O_{(silicate)} + Fe_{(s)} \leftrightarrow FeO_{(silicate)} + K_{(s)}$$

The method for reduction of agglomeration also reduces the formation of corrosive molten silicates; however, the inherently high silica content of some biomass types (*e.g.* rice straw) still causes considerable boiler corrosion.

2.4.7 Nitrogen Emissions Pathways

The most important nitrogen species in emissions from coal power stations are NO, NO_2, N_2O and NH_3. These compounds damage respiratory tissue; cause acid rain and destruction of high-atmospheric ozone; promote formation of ground-level ozone; and contribute to photochemical smogs. Unfortunately global atmospheric inventories of these nitrogen pollutants are increasing at a rate of 0.2 – 0.4 percent per year [Liu *et al.* 2002].

Fuel nitrogen levels are generally lower in biomass than coal (Table 2-2), so partial or complete substitution of coals with biomass offers a means of cleaning up emissions. However, the levels are also greatly dependent on the complex nitrogen pathway that arises.

In a combustion furnace, nitrogen emissions have two origins:

(i) Oxidation of molecular air-nitrogen by molecular air-oxygen at temperature above 1,273 K (thermal-NOx)

(ii) From fuel-nitrogen as direct products or via intermediates involved in radical and oxidation reactions (Prompt-NOx). Winter *et al.* [1999] have described the complex reaction web for fuel-nitrogen (Figure 2-10)

In most pulverised fuel furnaces, conditions can support the thermal-NOx pathway. However, when firing with biomass, because of ash softening problems (Section 2.4.6), lower combustion temperatures mean the Prompt-NO_x pathway dominates.

On oxidation of the char, aromatic structures in the fuel form HCN, a direct precursor to N_2O (Equation 2-25); while amino or ammonium structures form NH_3 which decomposes to NO or N_2 (Equation 2-26) [Werther *et al.* 2000].

Equation 2-25: $HCN \xrightarrow{O} NCO \xrightarrow{NO} N_2O$

Equation 2-26: $NH_3 \longrightarrow NH_2,NH \begin{cases} \xrightarrow{O_2} NO \\ \xrightarrow[NO,OH]{} N_2 \end{cases}$

Emissions of N_2O or NO are inversely proportional to the nitrogen content of a fuel due to competition between reactions 2-27 and 2-28 [Winter *et al.* 1999]. Nitrogen rich fuels evolve high concentrations of NH_3, to the extent that it also acts as a reducing agent in a similar way to the Selective Non-Catalytic Reduction used in power stations.

Equation 2-27: $NH_{3(g)} + \frac{5}{4}O_{2(g)} \rightarrow NO_{(g)} + \frac{3}{2}H_2O_{(vap.)}$

Equation 2-28: $\frac{2}{3}NH_{3(g)} + NO_{(g)} \rightarrow \frac{5}{6}N_{2(g)} + H_2O_{(vap.)}$

Char also influences nitrogen emissions through direct reduction (Equations 2-29 and 2-30) and heterogeneous catalysis (Equation 2-31) [Liu *et al.* 2002].

Equation 2-29: $C_{(s)} + N_2O_{(g)} \rightarrow N_{2(g)} + CO_{(g)}$

Equation 2-30: $2C_{(s)} + 2NO_{(g)} \rightarrow N_{2(g)} + 2CO_{(g)}$

Equation 2-31: $CO_{(g)} + NO_{(g)} \xrightarrow{Char} N_{2(g)} + CO_{(g)}$

This reduction by char diminishes when changing from coal to biomass due to the lower fixed carbon content. However, the increase in volatile content improves char surface area and reactivity, which together with reduction zones for NO_x and N_2O formed by the rapid rate of biomass volatiles, overcomes any weakening in reactions 2-29 to 2-21 [Liu *et al.* 2002].

Chaiklangmuang *et al.* [2002] and Arenillas *et al.* [2002] describe partitioning of nitrogen between char and volatile products, observing that in pulverised fuel furnaces with short residence times, char products do not completely reduce the NO emissions. Fluidised bed furnace, where residence times where higher, gives sufficient time for the reduction reactions to reach equilibrium. Loeffler *et al.* [2002] describe the gas phase formation of NO and N_2O in a lab-scale fluidised bed, fed with methane as a source of CH radicals.

There are many observations that NO_x emissions of blends are not linearly proportional to fuel ratio. By co-firing with biomass, Liu *et al.* [2002] have reduced NO_x emissions by up to 34 %wt. compared with predicted values, while Ross *et al.* [2002] have recorded reductions of up to 49 percent compared with predicted values by blending coal with sawdust. By co-firing with binary coals of different rank, Rubiera *et al.* [2002a; 2002b] observe non-additive trends in NO emissions, which increase with the proportion of high volatile coal in the blend. Rubiera *et al.* suggest lower volatile fuels reduce the oxygen involved in volatile-N oxidation, so the efficiency of conversion of char-N increases.

Reduction of NO_x emissions from pf and cyclone furnaces by use of reactions 2-29 to 2-21 have been described by Zhang *et al.* [2002] using coal, and Harding *et al.* [2000] using biomass as a reburn fuel. In both cases, air stoichiometry is an important factor but with biomass, air ratios of 0.85 and a heat input of 15 percent from reburn fuel (wood) provide the greatest NO_x reduction of 50 to 60 percent in a cyclone boiler and 70 percent in a lab-scale reactor [Harding *et al.* 2000]. Harding *et al.* suggest that because of its low nitrogen and sulphur content and high volatile content, wood is an equivalent if not better reburn fuel than natural gas or coal. High levels of CaO, KOH and Fe_2O_3 (also associated with biomass) give ash similar catalytic properties in fluidised bed furnaces [Werther *et al.* 2000; Liu *et al.* 2002; Zhang *et al.* 2002].

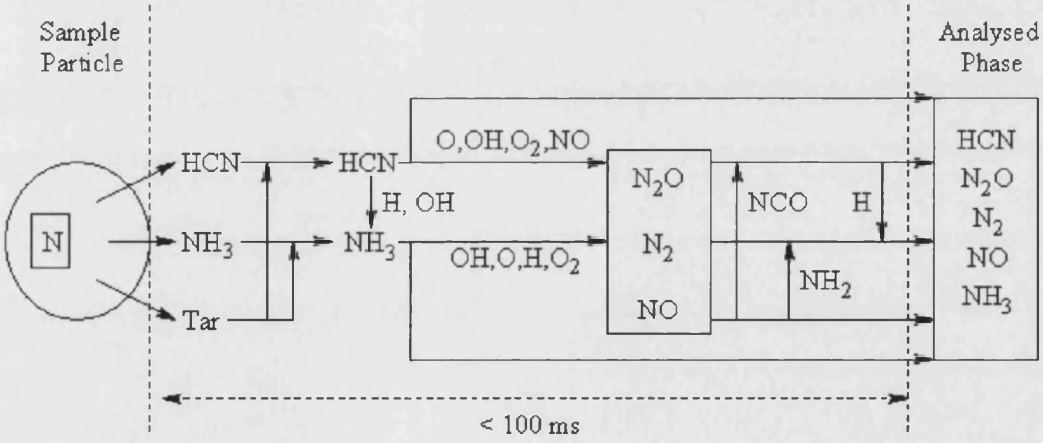

Figure 2-10: Reactions for fuel-N during the devolatilisation stage of fuel combustion [Winter et al. 1999]

2.4.8 Emissions of Sulphur Oxide Polyaromatic Hydrocarbons

Each year, 150 million tonnes of sulphur dioxide are discharged to the atmosphere by anthropogenic activities, and it is a significant contributor to air pollution in urban environments. As a primary pollutant, SO_2 is toxic to plants and animals, and weakens and corrodes plastics. Acid rains are produced from the dissolution of sulphur dioxide in rainwater (normally pH 5.6) to give sulphurous (H_2SO_3) and sulphuric (H_2SO_4) acids with a resulting pH of down to 2.0. Sulphur dioxide also forms sulphuric acid aerosols, which are transported over long distances, greatly distributing the effect. Acid rain causes the acidification of lakes, leaches nutrients from soils, and chemically weathers limestone buildings.

The low sulphur content of most biofuels leads to greatly reduced SO_2 emissions when co-fired with high sulphur coals. Furthermore, biomass tends to produce a highly alkaline ash (rich in Ca, K and P), which capture SO_2 from the evolved gasses. This effect has been observed for a wide range of solid biofuels, using pulverised fuel and fluidised bed combustors [Ohlsson 1994]. Sami *et al.* [2002] describe a comprehensive list of work concerning emissions from co-fired power stations. Where investigated, co-combustion often corresponds to significant reductions in SO_2 emissions, but the fuel type is important.

In an investigation of coal and refuse derived fuels in a cyclone combustor Ohlsson [1994] reports a reduction of 17 percent by weight from dedicated coal combustion under equivalent conditions. Ross *et al.* [2002] describe a 70 percent reduction in SO_2 when firing coal containing 37 percent of sawdust by weight in a 30 kW grate fired boiler with the energy/emissions ratios reduced by nearly 60 percent.

In addition to CO_2, emissions include carbon in organic compounds, including polyaromatic hydrocarbons (PAHs) and dioxins. These compounds are often extremely toxic, mutagenic and have been linked with immune system suppression in humans. Chagger *et al.* [1998] describes the formation of polychlorinated dibenzodioxins and polychlorinated dibenzodifurans (PCDDs and PCDFs) during biomass combustion, with formation favouring oxygen-lean conditions between 473 and 673 K. Banaee *et al.* [1995] describe how sulphur has a positive influence by limiting the formation of

chlorinated compounds (including PCDD/F) and thus the sulphur in coal has been shown lower their emissions during the combustion of municipal solid waste. This feature of co-combustion would benefit other high chlorine biomasses such as willow or construction timbers. Skodras *et al.* [2002] observe the reductions of SO_2 emissions when pure lignite is blended with natural wood, fibreboard (reconstituted wood), or power poles (waste wood), but although Skodras *et al.* measure levels of PCDD and PCDF, no correlation with sulphur is observed.

2.4.9 Decomposition of Biomass Components

The particular components of biomass have already been introduced (Section 2.3.7), and with respect to biomass it is the pathways for their thermal degradation that dictates the behaviour of the biomass, most notably pyrolysis of cellulose and lignin.

The importance of understanding the kinetics of char formation during biomass pyrolysis is highlighted by Wooton *et al.* [2004]. Firstly, in terms of the quantity and quality of products released from the char, but also in the possibility of secondary reactions between the pyrolysis or combustion products and the char surface. However, since the 1950's when the first kinetic models were suggested, there has been a steady succession of improved models. Antal *et al.* [1995] gave an extensive review of the details; however, the major stages are outlined below. One of the original cellulose kinetic models involves converting cellulose to an active cellulose intermediate (Figure 2-11a). This is described as the "Broido-Shafizadeh" model by Wooton *et al.* [2004] and the "Kilzer-Broido" model by Caballero *et al.* [1997]. It accounts for the high-energy initiation reaction observed in some experiments; however, it did not explain the various product ratios when different experimental conditions were used. Agrawal *et al.* (1988, as cited by [Capart *et al.* 2004]) suggest that at low temperatures, formation of the activated cellulose is in competition with a tar forming reaction (Figure 2-11b), reported to be a good fit for data with a range of heating rates [Caballero *et al.* 1997]. Later, the "Waterloo" model (Figure 2-11c, [Wooton *et al.* 2004]) similarly suggested that two reactions compete for the starting material, but dispensing with activated cellulose. The first reaction, de-polymerisation, favours rapid heating, and produces

low-DP (degree-of-polymerisation) cellulose. The alternative involves a suite of low temperature decomposition reactions including dehydration and elimination, yielding volatile compounds (water, CO, CO_2) and the highest yield of char. The low-DP cellulose will continue to depolymerise, resulting in levoglucosan and some char, or will undergo fragmentation yielding glycoaldehydes, volatile compounds and less char. Ash minerals (Na^+ and K^+) are shown to enhance the degree of fragmentation.

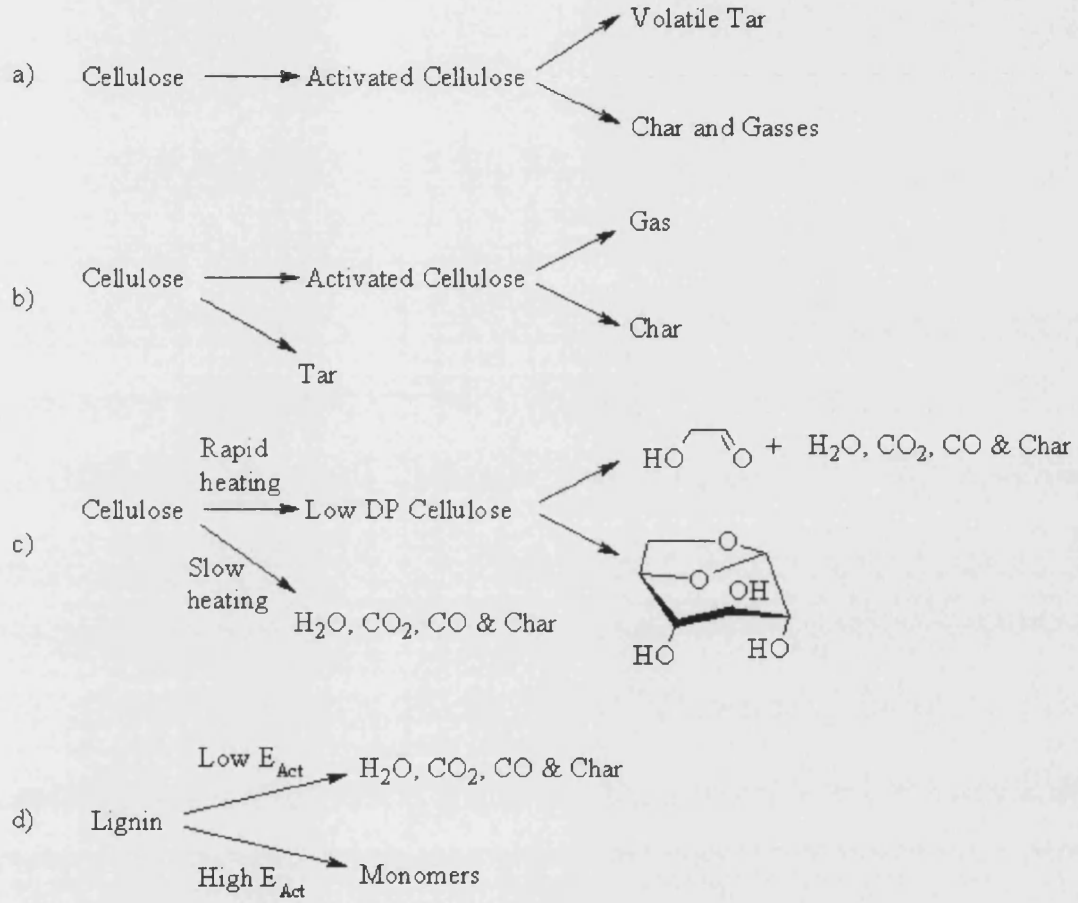

Figure 2-11: Cellulose degradation by (a) Briodo-Shafizadeh model, (b) Agrawal model (c) Waterloo model and (d) lignin degradation

Fisher *et al.* [2002] describe the pyrolytic behaviour and kinetics of holocellulose components (cellulose and hemicellulose) above 673 K, a temperature range that relates to the aromatisation of the char. Wooton *et al.* [2004] and McGrath *et al.* [2003] both describe the pyrolysis of cellulose using CPMAS-NMR (Cross Polarised Magic Angle Spinning Nuclear Magnetic Resonance) imaging. It was observed that increases in the aromatic nature of the char above 673 K correlated with only low weight changes

[McGrath *et al.* 2003], while the char concentrations of methyl, aliphatic, carboxyl, carbohydrate and phenolic carbon were all reduced [McGrath *et al.* 2003]. In the given conditions, hold time was not a factor, and polyaromatic hydrocarbon contents of the pyrolysis oil only increase with temperature. This observation is similar to that for the coalification process (Section 2.3.4).

Caballero *et al.* [1997] describe previous work concerning the pyrolysis characteristics of lignin polymers, which are considerably more complex than cellulose. First, the structure of lignin is not definite, making model compounds unsatisfactory. Further, methods of isolating lignin from biomass have strong effects on the lignins pyrolysis behaviour. Caballero *et al.* state that while some authors suggest a change in the mechanism with temperature, others suggest the change is related to the degree of conversion. Nevertheless, Antal (1983, cited by [Caballero *et al.* 1997]) suggests the decomposition is the result of two competitive pathways such as that in Figure 2-11d. Due to structural similarities, models devised for coal could also be applied to lignin [Caballero *et al.* 1997].

Jakab *et al.* [1997] investigated the chemical pathways for pyrolysis of wood lignins by thermogravimetric-mass spectroscopy. The dominant chemistry for lignin degradation starting at 593 K and peaking at 683 K is dominated by the scission of α and β-aryl-alkyl ether bonds yielding methylguaiacol and ethylguaiacol monomers. Liberation of water through the scission of alcoholic and phenolic hydroxyl groups at around 573 and 748 K are variable in T_{max} due to variation in the stabilities between compounds, however its formation is a significant contributor to the weight loss profile. Methane is liberated alkyl groups in lignin at 748 K, while phenolic methoxy groups produce methanol at 673 K and methane at 873 K. As with cellulose, lignin charring processes (involving aromatisation, condensation and macromolecular rearrangement, Section 2.4.2) then continue to liberate CO and H_2 up to 1229 K. Carbon dioxide is liberated from carbonyl groups, and formaldehyde is liberated from primary hydroxyl groups. Final char levels are inversely proportional to the concentration of hydroxyl and methoxy groups in the lignin.

Other discussions of the emission from various biomass types during pyrolysis are given by Wojtowicz *et al.* [2003], Ghetti, *et al.* [1996], Raveendran *et al.* [1996] and Bassilakis *et al.* [2001].

2.5 Kinetic Analysis by Thermogravimetry

2.5.1 Thermogravimetric Analysis

Thermogravimetric analysis (TG or TGA) combines an accurate microbalance with a computer-controlled furnace and is perhaps the original thermal analysis method. Used for measuring weight change reactions, residual mass, active thermal ranges, adsorption behaviour and reaction kinetics, the number of publications employing it increases every year. For more general information of the thermal analysis methods, techniques and the increasing number of applications, a review of literature is published periodically in Analytical Chemistry; maintained between 1988 and 2000 by the late Professor David Dollimore [Dollimore *et al.* 1998; 2000], with the most recent editions by Vyazovkin [2002].

2.5.2 Activation Energy, Temperature and the Rate of Reaction

Every dynamic chemical process has an associated energy of activation E_{Act}. This is the quantity of potential energy, above its ground state, that a chemical species must posses to be transformed. Equation 2-32 and Figure 2-12 describe the changes in enthalpy (H), entropy (S) and Gibbs free energy (G) at absolute temperature T.

Equation 2-32: $\Delta G = \Delta H - T.\Delta S$

Enthalpy is a measure of internal energy of a chemical bond, molecule or sample container and during an exothermic reaction (such as char oxidation by Equation 2-10), ΔH is negative. Entropy refers to the disorder of the system and since the second law of thermodynamics states that the order of an isolated system will never spontaneously increase, the overall ΔS is usually positive. The direction of a chemical change occurs

where there is a decrease in Gibbs free energy (ΔG in Figure 2-12a). Where reactions involve high temperatures, formation of gasses, or an increase in the number of molecules (*e.g.* A→B+C), $T.\Delta S$ will be large and ΔH can be small or even positive. Importantly, both of these circumstances are prevalent in the combustion process [Atkins 1998]. Activation energy (E_{Act}) is related in a linear fashion to the enthalpy of activation ($\Delta H^{\#}$), and the gas constant R (Equation 2-33) [Atkins 1998]. Figure 2-12b describes how for a number of molecules, the likelihood of a particular reaction occurring increases with temperature, due to changes in the distribution of energy.

Equation 2-33: $$E_{Act} = \Delta H^{\#} + 2RT$$

Where the temperature is sufficiently high, the population of molecules with sufficient energy means nearly all collisions lead to a reaction. In these cases, the reaction rate is diffusion-controlled – as opposed to activation controlled (Figure 2-12c, p.44).

The rate of a reaction can be related to the reagent concentration and thus the degree of conversion by a temperature dependent rate constant k. Thus, where f(α) is a rate law for the fraction of sample conversion α.

Equation 2-34: $$Rate = k.f(\alpha)$$

Here, conversion considers only the portion of the sample lost through reaction, so that for initial and observed sample weights of w_0 and w:

Equation 2-35: $$\alpha = \left({}^{w}/_{w_0} \right)$$

Table 2-8 describes a range of rate laws used in conjunction with TGA. For many reactions, the temperature dependence of k is given by the Arrhenius equation with activation energy E_{Act} and pre-exponential factor A:

Equation 2-36: $$k = A.\exp\left(-{}^{E_{Act}}/_{RT} \right)$$

Therefore, where dα/dt represents the rate of conversion with respect to time, by combining Equations 2-34 and 2-36 the standard equation for kinetic analysis is obtained:

Equation 2-37: $$d\alpha/dt = A.\exp\left(-{}^{E_{Act}}/_{RT} \right).f(\alpha)$$

These kinetic parameters, E_{Act} and A, are one objective of this investigation. They are indicative of the reactivity and thermo-kinetic character of fuels and are widely explored in the literature. The following Sections discuss some of the thermogravimetric techniques, and calculations applicable to the present investigation.

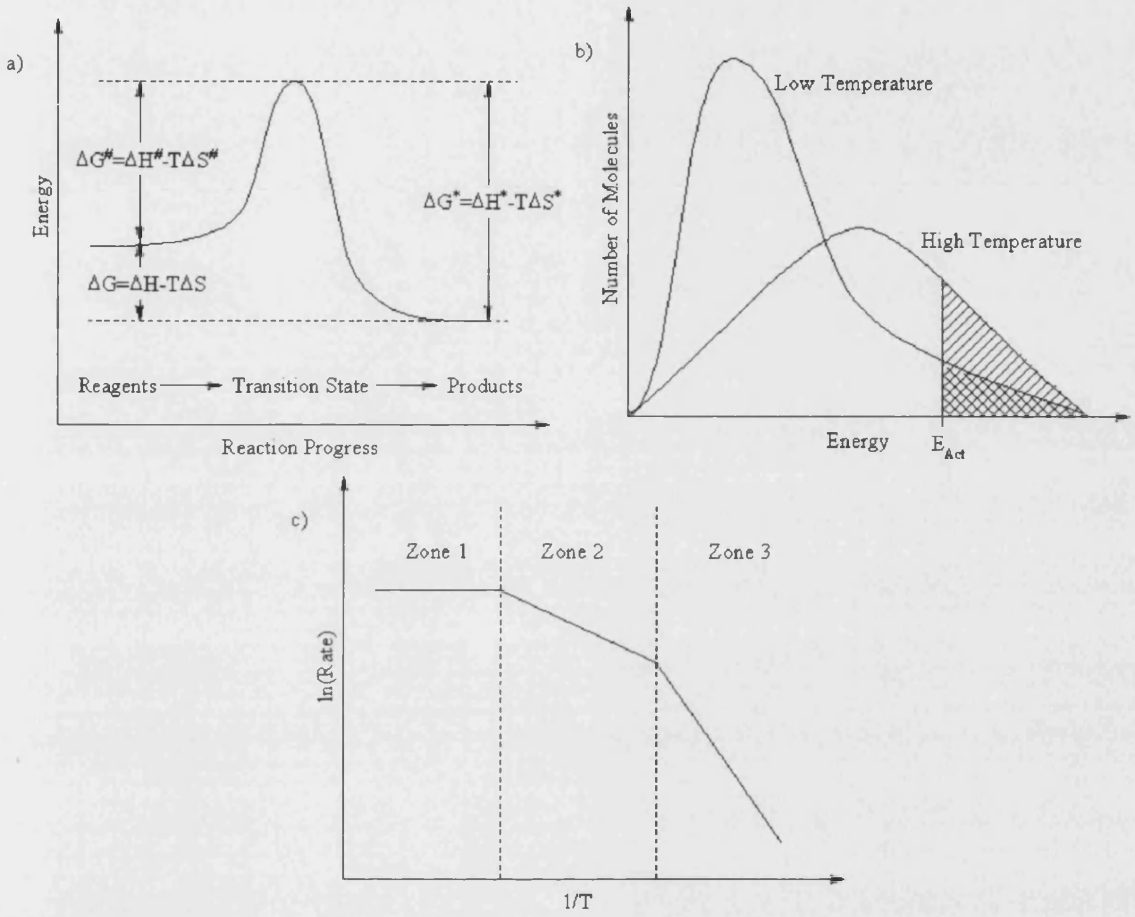

*Figure 2-12: Reaction kinetic schematics. (a) Changes in energy for a compound undergoing a reaction, # indicates an activation energy; * indicates the reverse reaction energy [Atkins 1998]. (b) The changes in molecular energy distributions with temperature; hatched areas describe the quantity of molecules where $E > E_{Act}$, at low (\\\\) and high (////) temperatures [Cotton et al. 1996]. (c) Effect of temperature on the controlling factors of a reaction, zones are described in the text*

Table 2-8: Commonly used derivative and integral expressions for solid thermal decomposition reactions

		$f(\alpha)=kt$	$g(\alpha)=1/k \cdot d\alpha/dt$
Net Reaction Order:	1st order reaction	$(1-\alpha)$	$-\ln(1-\alpha)$
	nth order reactions	$(1-\alpha)^n$	$[1/(n-1)][1-\alpha)^{n-1}$
Diffusion Mechanics:	Two-dimensional	$[-\ln(1-\alpha)]^{-1}$	$(1-\alpha)[\ln(1-\alpha)]+\alpha$
	Three-dimensional	$1.5[(1-\alpha)^{-1/3}-1]^{-1}$	$(1-2\alpha/3)-(1-\alpha)^{2/3}$
Nuclei-Growth:	Avrami-Erofeev	$n(1-\alpha)[-\ln(1-\alpha)]^{(n-1)/n}$	
	Prout-Tompkins	$(1-\alpha)^n\alpha^m$	

2.5.3 Comparison of Kinetic Analysis Techniques

Equation 2-37 describes the relationship between the temperature, sample weight and the rate of a reaction, three variables easily determined using thermogravimetry. Perhaps the most straightforward method is in the Friedman method, which uses the linearised form of Equation 2-36 giving Equation 2-38, where for a plot of $\ln[(d\alpha/dt)/f(\alpha)]$ against $1/RT$ gives a line with a slope and intercept of $-E_{Act}$ and $\ln[A]$ respectively.

Equation 2-38:
$$\ln\left[\frac{d\alpha/dt}{f(\alpha)}\right]=\ln[A]-\left(\frac{E_{Act}}{RT}\right)$$

However, the reliability of this approach has been questioned due to its dependence on derivative with respect to time. The method by Kissinger dispenses with it by observing that at T_{max}:

Equation 2-39:
$$\left[\frac{d}{dt}\left(\frac{d\alpha}{dt}\right)\right]_{T=T_{max}}=0$$

From this, Kissinger uses Equation 2-40, so that with heating rate of β, a straight line in a plot of $\ln(\beta/T_{max}^2)$ against $1/T_{max}$ gives a gradient of $-E_{Act}/R$.

Equation 2-40:
$$\ln\left(\frac{\beta}{T_{max}^2}\right)=\left(-\frac{E_{Act}}{RT_{max}}\right)+\text{Constant}$$

Nevertheless, use of Kissinger's technique requires a number of heating rates to avoid the large influence on E_{Act} of small errors in temperature when identifying the straight

line; Reynolds *et al.* [1997] indicate that a 1 K temperature error gives rise to a 1 kcal mol^{-1} deviation in E_{Act}.

Like Kissinger's, the Coats-Redfern approach also dispenses with the time variable, but by using a linear heating rate of $\beta = dT/dt$. Equation 2-41 illustrates this rearrangement of Equation 2-37:

Equation 2-41: $$d\alpha/f(\alpha) = A/\beta . \exp\left(-E_{Act}/RT\right).dT$$

Which is further rearranged to give:

Equation 2-42: $$\ln\left[\frac{g(\alpha)-g(0)}{T^2}\right] = \ln\left(AR/\beta E_{Act}\right) - E_{Act}/RT$$

From which, a plot of $\ln([g(\alpha)-g(0)]/T^2)$ against 1/T, gives E_{Act} and A from the gradient and intercept respectively. The various rate law functions (in terms of $f(\alpha)$ and $g(\alpha)$) are described in Table 2-8.

2.5.4 Measuring Kinetic Parameters by Thermogravimetry

The problems associated with the calculation of E_{Act} and A by thermogravimetric methods are illustrated in the introduction of Capart *et al.* [2004], who compare a range of kinetic models for cellulose decomposition. They refer to a number of contradictory instances where the activation energy of cellulose decomposition ranges from 100 to 250 kJ mol^{-1}. These problems are thought to arise due to a combination of inter- and intra-particulate heat transfer limitations; localised exo- and endothermic reactions; and the rate at which evolved product gases are removed, especially important when reactions are reversible. Such influences are dependent of sample size, heating rate, sweeping gas flow rates, furnace geometry and crucible design [Capart *et al.* 2004].

Further dispute arises in the rate law used. Staying with pyrolysis of cellulose, this is regularly defined as involving a first order kinetic reaction (Table 2-8) (*e.g.* [Antal Jr. *et al.* 1995; Varhegyi *et al.* 1997; Garcìa-Pèrez *et al.* 2001]). However, better fits to experimental data have been shown by using nuclei-growth models such as Prout-Tompkins or Avrami-Erofeev. Reynolds *et al.* [1997] determined that a 3-parameter

nucleation model (Prout-Tompkins nucleation with $n = 1$) was most suitable, giving A and E_{Act} values that describe a narrower peak than the first-order model. They suggest the latter may have appeared suitable in the past because of overlapping reactions making apparent cellulose activity appear wider and so suiting the first order profile. Similar peak narrowing is derived from A and E_{Act} parameters calculated by n^{th} order reactions where $n < 1.0$ (*e.g.* [Antal *et al.* 1980]).

Wilburn [2000] uses simulated data to describe the effect of superimposed reactions on the overall log plot, and thus the effect on the ability to estimate their kinetic parameters. Two superimposed peaks of equal dTG_{max} give two straight lines connected by a curve. However, two superimposed peaks of similar T_{max}, or unequal dTG_{max}, give entirely curved log plots, making the identification a straight line irrelevant.

2.5.5 Deconvolution of a dTG Profile

As Wilburn [2000] indicated, superimposed reactions of similar T_{max} dramatically reduces the suitable temperature range for the calculation of kinetic parameters. Brown *et al.* [2002] indicate that where multiple overlapping reactions contribute of overall conversion, data for each should be first isolated before separate kinetic analysis is carried out. The latter advises use of gas analysis to distinguish between different contributory processes; however, this may not be useful where two different reactions yield the same product.

The weight-loss rate (dTG) profile is often identified as multiple superimposed reactions, but obtaining the kinetic parameters for these reactions requires the TG and dTG data of each (Sections 2.5.3 and 2.5.4). Deconvolution is a means of first extracting the dTG data for each peak, which in turn can be used to calculate TG data.

Thermogravimetric data for polymer degradation is regularly deconvoluted as the thermal profiles can be easily interpreted, because of the straightforward chemistry. For example, Roeder *et al.* [2005] use deconvolution to observe the pyrolysis of blends of polypropylene with three additives using multiple Gaussian peaks noting that blend decomposition correlates with the ratio of blend components (Equation 2-47). Katsikas

et al. [2003] use deconvolution as a means of improving the Flynn-Wall method of kinetic analysis (Section 2.5.3) of poly(diisobutyl itaconate) by eliminating interferences of superimposed reactions. TG curves for different processes were reproduced from data deconvoluted from the recorded dTG curves using Lorentz functions.

Bujoreanu *et al.* [2002] use deconvolution to model the release of various forms of water (non-structured surface water, structured surface water, coordinated water, pore located water amongst others) from co-precipitated manganese ferrite powders, and to determine the kinetic behaviour of each loss. Li *et al.* [2005] also use deconvolution to improve kinetic studies, this time of amorphous carbon thin films. Here three Gaussian profiles were used to identify three superimposed decompositions, relating to two magnitudes of bonding energy, and graphite degradation. The T_{max} values for the isolated peaks were then used in the Kissinger method of evaluating activation energy (Section 2.5.3).

Direct reference to deconvolution in coal decomposition is rare. One reference in [Arenillas *et al.* 2004], comparing the dTG profiles of real and synthetic coals uses deconvolution to correlate weight-loss events with evolved compounds as determined by FTIR. Spectroscopy data can improve the accuracy of deconvolution if several compounds are evolved simultaneously [Slager *et al.* 2005].

2.5.6 Kinetic Analysis by TGA

To date, the analysis of fuels by thermogravimetric analysis has concentrated principally on their pyrolysis behaviour. Jones *et al.* [2005] describe the emissions from pyrolysis of blends of coal and biomass, using GC-MS analysis. Between them, Vamvuka *et al.* [2003], Kastanaki *et al.* [2002] and a similar paper by Vamvuka *et al.* [2003] have investigated co-pyrolysis with biomass (olive kernels, straw, forest residue and cotton residue), high-rank coals (Gottelborn coal), and low rank coals (Megalopolis and Ptolemais lignite). As all three papers come from the same laboratory and involve similar work, they will be discussed here together. The papers considered blends of 5, 10 and 20 %wt. biomass, using samples of 20 to 25 mg heating between 373 and 1223

K at 10 K min^{-1}, although Vamvuka *et al.* [2003] also report on 100 K min^{-1} heating rates, and a variety of particle sizes. All three papers however use a series of independent, parallel, first-order reactions to describe the decomposition of biomass, coal and blends alike. The reactions for biomass are attributed classically to cellulose, hemicellulose and lignin while coal pyrolysis is analogously observed as a number of pseudo-reactions of unknown chemical origin.

In all three papers, kinetic modelling of the reaction peaks was carried out by least-squares minimisation of the objective function (*O.F.*) between experimental and calculated rates of conversion:

Equation 2-43:
$$O.F. = \sum \left[\left(d\alpha / dt \right)_{Exp} - \left(d\alpha / dt \right)_{Calc} \right]^2$$

The calculated total rate of conversion is derived from Equation 2-37 (p.43), the association between kinetic parameters and coefficient for contribution to conversion (c) of N pseudo-components i:

Equation 2-44:
$$\left(d\alpha / dt \right)_{Calc} = \sum_{i=1}^{N} c_i \left(A_i . Exp\left(- E_{Act,i} / RT \right) . (1 - \alpha_i) \right)$$

The results of this analysis are summarised in Tables 2-9 and 2-10 for biomass and coal respectively. It shows that two coals displayed four reaction peaks while the third displayed five. Olive kernels, straw and cotton residue decomposition was identified as due to three pseudo-components, while straw featured a second hemicellulose reaction.

Since Vamvuka *et al.* [2003a; 2003b] reported data for a range of heating rates and particle sizes, the data range has been shown in Tables 2-9 and 2-10. This reveals there to be considerable variation in not only the kinetic parameters E_{Act} and A of each pseudo-component, which may be accounted for by heat or mass transfer limitations, but also in their apparent contribution to overall conversion, which is less understandable. It is suggested here therefore that this method of identifying the reaction profiles does not produce reliable kinetic parameters. Nevertheless, all the authors report they were able to use the kinetic parameters of the parent fuels to reproduce the rate of conversion profiles of fuel blends during pyrolysis.

Two other papers are noted here relating to the thermogravimetric co-pyrolysis of coal/biomass blends. Vuthaluru [2004] reports on the analysis of an Australian sub-bituminous coal blended with 10, 20, 30 and 50 %wt. proportions of wood waste or wheat straw. Up to three thermal events were highlighted in the TG profiles of the pure and blended fuels, and kinetic parameters were calculated for overall activity in each events temperature range. An n^{th} order reaction is used, where $f(\alpha) = (1-\alpha)^n$, so Equation 2-37 (p. 43) was re-written in the linear form as:

Equation 2-45: $$\ln\left(d\alpha/dt\right) = \ln\left(A/\beta\right) - \left(E_{Act}/RT\right) + n.\ln(1-\alpha)$$

Differentiation of this with respect to $\ln(1-\alpha)$ gives:

Equation 2-46: $$\frac{d\left(\ln\left[d\alpha/dt\right]\right)}{d\left(\ln[1-\alpha]\right)} = n - \left(E_{Act}/R\right).\frac{d\left(1/T\right)}{d\left(\ln[1-\alpha]\right)}$$

The straight line in a plot of $d(\ln[d\alpha/dt])/d(\ln[1-\alpha])$ against $d(1/T)/d(\ln[1-\alpha])$ therefore gives values of n and E_{Act} from its intercept and slope respectively. Vuthaluru observes that the char yields at a range of temperatures are linear with the biomass content of the blend, in agreement with typical suggestions that pyrolysis of two blended fuels proceed along independent pathways. However, the weight-loss contribution of the coal reaction also increases with biomass content, which suggests that although the reactions are not changed, inhibition occurs. Activation energies of 65 to 118 kJ mol^{-1} were obtained for the biomass processes, along with 183 kJ mol^{-1} for the coal process and 47 to 135 kJ mol^{-1} for the blend processes. Orders of reaction were calculated as 0.4 to 0.8 for the biomass processes, 1.07 for the coal process, and 0.21 to 1.6 for the blend processes. Processes of the 20 %wt. biomass blends exhibited the lowest values of E_{Act}.

Biagini *et al.* [2002] studies the TG profiles resulting from the pyrolysis of blends of between 15 and 60 %wt. pine sawdust or sewage sludge in high or low volatile coals. Experimental TG profiles of the blends were compared with profiles calculated by a "rule-of-mixtures"-type association, revealing the additive nature of the weight loss processes, so where b is the fraction of biomass in the blend:

Equation 2-47: $$\alpha_{Blend,T} = b.\alpha_{Biomass,T} + (1-b).\alpha_{Lignite,T}$$

This association means that during pyrolysis, in addition to solid phase decomposition of fuel components following independent devolatilisation pathways, the resulting char is not affected by liberated oxygenated species. There may be unobserved reactions between the coal and biomass volatile materials where pyrolysis peaks occupy similar temperature ranges. Kinetic analyses were performed using the Friedman method. Fushimi *et al.* [2003] look at the reactivity of chars from a selection of biomass derivative materials. They observe the activation energy of cellulose during pyrolysis ranges from 43 to 230 kJ mol^{-1}, as the heating rate decreases from 6000 to 60 K min^{-1}, while the activation energy of lignin rose from 22.9 to 52.8 kJ mol^{-1}. These variations were attributed to temperature gradients across the sample, due to limited heat-transfer. High heating rates that lead to explosive volatile emissions from a particle also reduce the possibility of re-polymerisation reactions that convert volatile materials back to char. As a result, formation of volatiles increases at the expense of char.

Table 2-9: Kinetic data for coal pseudo-components during pyrolysis [Kastanaki et al. 2002; Vamvuka et al. 2003a; 2003b]

		Reaction 1	Reaction 2	Reaction 3	Reaction 4	Reaction 5
Ptolemais Lignite	$\ln[A\ (min^{-1})]$	7.1	15.1 - 4.5	54.0	54.5	6.6
	E_{Act} (kJ mol^{-1})	46.8	98.6	65.2	439.6	75.2
	γ (%wt.)	14.2	7.5	10.1	1.1	11.1
Megalopolis Lignite	$\ln[A\ (min^{-1})]$	4.3 - 4.6	13.4	7.7 - 7.7	5.8	-
	E_{Act} (kJ mol^{-1})	32.4 - 34.1	89.6 - 89.7	65.2 - 65.4	75.1	-
	γ (%wt.)	13.8 - 14.5	6.2 - 6.9	6.0 - 6.6	8.9 - 16.1	-
Gottelborn Coal	$\ln[A\ (min^{-1})]$	27.7 - 31.3	14.4 - 32.2	0.6 - 14.5	2.1 - 27.2	-
	E_{Act} (kJ mol^{-1})	142.7 - 195.1	101.9 - 200.6	26.4 - 103.1	36.1 - 229.5	-
	γ (%wt.)	5.7 - 7.5	5.1 - 8.3	15.9 - 17.5	0.6 - 1.7	-

Table 2-10: Kinetic data for biomass pseudo-components during pyrolysis [Kastanaki et al. 2002; Vamvuka et al. 2003a; 2003b]

		Hemi-cellulose 1	Hemi-cellulose 2	Cellulose	Lignin
Olive Kernels	ln[A (min^{-1})]	18.6 - 21.3	-	32.2 - 42.8	3.1 - 7.5
	E_{Act} (kJ mol^{-1})	91.0 - 96.9	-	166.7 - 215.4	29.1 - 37.1
	γ (%wt.)	4.70 - 29.0	-	12.4 - 30.8	20.9 - 37.1
Straw	ln[A (min^{-1})]	25.5 - 25.4	-	46.3 - 46.3	3.5 - 3.7
	E_{Act} (kJ mol^{-1})	120.8 - 121.2	-	231.6 - 231.6	31.0 - 31.8
	γ (%wt.)	14.9 - 15.0	-	23.8 - 30.5	26.3 - 26.7
Forest Residue	ln[A (min^{-1})]	16.9 - 24.5	24.3 - 30.8	36.9 - 52.9	3.7 - 7.7
	E_{Act} (kJ mol^{-1})	81.60 - 112.2	124.6 - 155.4	198.9 - 286.9	33.6 - 41.7
	γ (%wt.)	4.50 - 41.4	16.7 - 24.9	15.8 - 36.0	19.7 - 32.3
Cotton Residue	ln[A (min^{-1})]	19.6 - 22.2	-	23.9 - 29.5	2.5 - 5.5
	E_{Act} (kJ mol^{-1})	93.10 - 105.9	-	124.6 - 151.9	28.1 - 31.9
	γ (%wt.)	8.90 - 14.4	-	34.5 - 35.8	25.1 - 29.6

Table 2-11: Pyrolysis activation energies (kJ mol^{-1}) for the component parts of several lignocellulosic materials from other publications

Hemicellulose	Cellulose	Lignin	Reference
-	197-238	-	[Antal Jr. *et al.* 1995]
188-267	210.0	-	[Fisher *et al.* 2002]
194-200	243-250	37-62	[Manya *et al.* 2003]
-	201.0	-	[Orfao *et al.* 1999]
98.0	-	-	[Font *et al.* 1991]
88.4	210.0	81.1	[Biagini *et al.* 2002]
106	226	114	[Branca *et al.*, 2004]

Examples for kinetic analysis for oxidation are less common. Branca *et al.* [2004] investigate the oxidation kinetics of two wood species. They identify three reaction peaks for the devolatilisation of wood with E_{Act} values of 106, 226 and 114 kJ mol^{-1} (Table 2-11) and a fourth reaction peak of char combustion, with an E_{Act} value of 183 kJ mol^{-1}. Lignins reactivity is reduced possibly because of the onset of oxidation.

2.6 Aims and Objectives

The benefits of co-combustion of coal and biomass have been demonstrated. The differences between biomass and coal and the existing means of characterising fuels have both been examined, as has the effect of the component parts. In some cases, the effects of combining fuels are favourable, in others unfavourable. An understanding of

the interaction between the fuels is lacking and thermogravimetric analysis, with associated kinetic study offers an opportunity to examine this synergistic chemistry. Knowledge of these processes may help in the selection of fuels and fuel blends, and the operation of boilers in terms of air needs, burner configuration, particle burnout, flame temperature and heat flow [Berkowitz 1994].

The aim of this investigation is to establish a means of observing the interactions between the biomass and lignite components of a blended fuel using TGA.

To do this, a series of fuels will be examined, in both pure and blended forms, and under both pyrolytic and oxidising conditions using thermogravimetry. The decomposition of the fuel will be analysed by a deconvolution method. Having reviewed the existing methodologies, an optimal kinetic model will be determined, and parameters pertaining to the kinetic character of each reaction will be calculated. These parameters will then be compared to observe the nature of interference between the reactions.

Chapter 3 Experimental Details

3.1 Introduction

This Section introduces the materials, instrumentation and experimental techniques employed in the investigation; with a focus on coal biomass blends. At the outset of this investigation, the TG-92 was in a considerable state of disrepair, so an important initial task was a full refurbishment, to restore the instrument to good working order. This involved several months of labour, coordinating with manufactures to determine what was required of the instrument, ordering the necessary parts and managing delivery and connection to water, air and gas services.

The use of Scanning Electron Microscopy is also presented as a means of visually clarifying interactions between the various fuel types, and changes in morphology.

3.2 Selection of Materials

3.2.1 ECSC Project 7220-PR-131 (CoalCombOptimisation)

The biomass and lignite samples employed in this investigation were part of a European project; they are not intended to be representative of UK fuels. Instead, they represent fuels commonly used in South/Central Europe and available in large quantities.

3.2.2 Lignite Samples

The German lignite, originating from RWE Rheinbraun, Köln, comes from Rhenish brown coal seams while the Greek lignites come from the Ptolemais basin of Western Macedonia. Lignite samples were supplied as lumps of up to 20 cm, but were ground to pass a 0.5 mm mesh before use. Proximate, ultimate and other chemical compositions of the lignites supplied by Aristotle University of Thessaloniki are given in Table 3-1.

3.2.3 Biomass Samples

Wood residues are the products of forestry management including wood chippings, sawdust and miscellaneous leaves, needles, bark and twigs while olive kernels are a by-product of the olive oil industry. It was not necessary to grind the biomass as a sufficient quantity of the delivered sample already passed the 0.5 mm mesh. Notably, the forest residue sample is made up of fibrous particles, while the olive kernels are more globular, and therefore similar to the crushed lignite.

3.2.4 Bio-Polymers

Cellulose microcrystalline powder and low-sulphonate Kraft lignin (Figures 3-1a and 3-1b) were both obtained from Sigma-Aldrich Co., USA, while the hemicellulose residues arabinose, xylose and galactose (Figures 3-1c to 3-1e) were obtained from Alfa-Aesar, all with D(+)-stereochemistry, and purity of > 98 %. Xylose and arabinose are fine colourless crystals, while galactose and cellulose are white powders. Lignin is a fine dark brown power.

3.2.5 Biomass-Lignite Blends

Fuel blends were prepared using proportions of fuel ranging from pure biomass to pure lignite in 20 percent increments by dry weight. Blends were prepared with total weights of 5 g, giving both sufficient sample for repeated analyses, and reducing the percentage

error of the measuring accuracy. Aliquots were measured to ± 0.5 mg, giving a 0.01 %wt. error for the blend ratio. However, possible due to their different geometries, forest residues did not evenly mix with the lignite and tended to rise to the top, and so to avoid inhomogeneous samples being analysed, vigorous stirring was required. Olive kernels were blended more evenly, and tended to remain blended.

Table 3-1: Proximate, ultimate and chemical analysis of the four fuels used in the present investigation

	Ptolemais Lignite[3]	German Lignite[1]	Olive Kernels[1]	Forest Residue[1]	Kraft Lignin[4]
Moisture (%wt.)					
As received	57.1	47.2	18.1	21.3	-
Proximate Analysis (%dry wt.)					
Volatiles	41.3	50.7	74.2	80.9	-
Fixed Carbon	40.5	44.6	22.7	17.6	-
Ash	18.2	4.7	3.1	1.5	~9.0[5]
Heating Value (MJ kg^{-1})					
LHV	22.36	28.57	28.05	27.13	-
HHV	23.24	29.72	29.87	28.82	-
Ultimate Analysis (%dry wt.)					
Carbon	50.1	64.2	51.6	51.0	35-45
Hydrogen	4.2	5.4	8.5	7.9	-
Nitrogen	1.5	0.7	1.1	0.3	-
Sulphur	0.6	0.0	0.0	0.0	4.0
Oxygen	25.4	25.0	35.7	39.3	-
Ash	18.2	4.7	3.1	1.5	-
Ash Analysis[6] (%ash wt.)					
CaO	13.38	18.62	25.20	34.02	-
Al_2O_3	3.40	0.93	10.01	4.16	-
Fe_2O_3	3.43	1.43	7.15	6.15	-
MgO	3.32	3.15	5.31	12.28	-
TiO_3	0.09	0.05	0.62	0.23	-
Na_2O	1.07	0.57	0.54	3.87	-

([3]) Fuel data supplied by the Aristotle University of Thessaloniki
([4]) Bio-polymer data supplied by Sigma-Aldrich
([5]) Impurities, including mineral matter
([6]) Excludes silica, typical range of which are 5 to 72.5 %ash wt. for coal and 1.5 to 39.5 %ash wt. for biomass [Seggiani 1999]

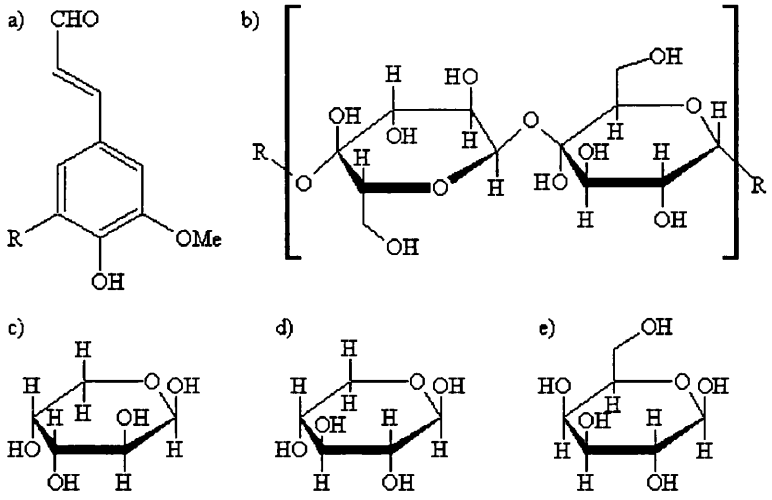

Figure 3-1: Structures of compounds used in the present investigation: (a) Low sulphonate lignin; (b) Cellulose; (c) Arabinose; (d) Xylose; (e) Galactose

3.3 Thermogravimetric Analysis

3.3.1 Instrumentation

The thermogravimetric analyser used in this work is a Setaram TG-92. Important properties of this instrument are given in Figure 3-2 and Table 3-2. It is an upright balance furnace, allowing measurement to 1873 K, where the sample is contained in a 170 µl alumina crucible, suspended in the vertical sample cavity of the furnace tube. The balance uses a null-point measurement mechanism to ensure that once the balance assembly is lowered into place, the sample is held at a constant position within the furnace, approximately 5 mm above the tip of the Type S (10%Pt-Rh/Pt) thermocouple. The furnace has an inductively wound graphite heating element, with an alumina tube enclosing the sample cavity. Argon is used as a shield gas, diffusing inward through joins in the furnace walls, and leaving through the sample cavity. This positive pressure protects the heating element from corrosion, oxidation and tarry deposits.

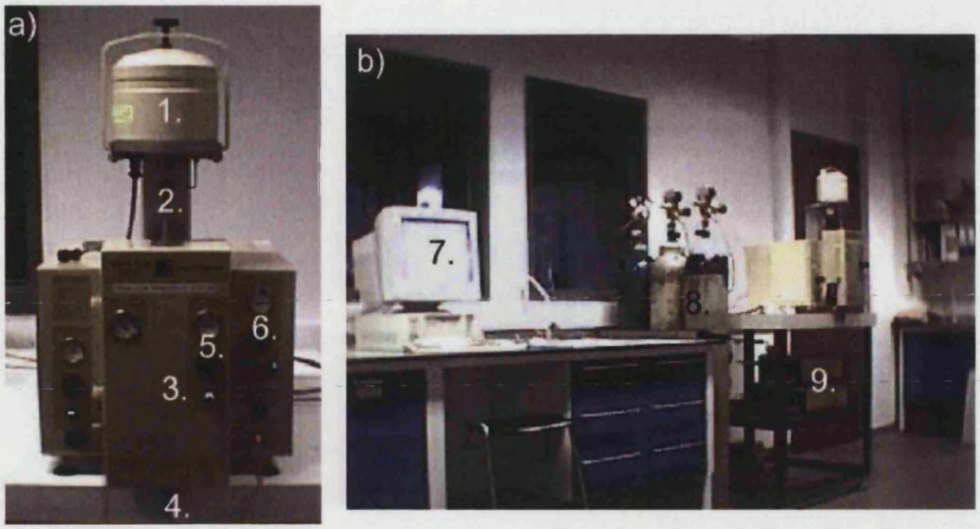

Figure 3-2: (a) Setaram TG-92 instrumental layout and (b) lab set-up. (1) Enclosed balance unit, (2) suspension mechanism, (3) furnace enclosure, (4) thermocouple, (5) furnace shield gas controls, (6) carrier gas controls, (7) computer, (8) gas supply cylinders, (9) TG and gas controller modules

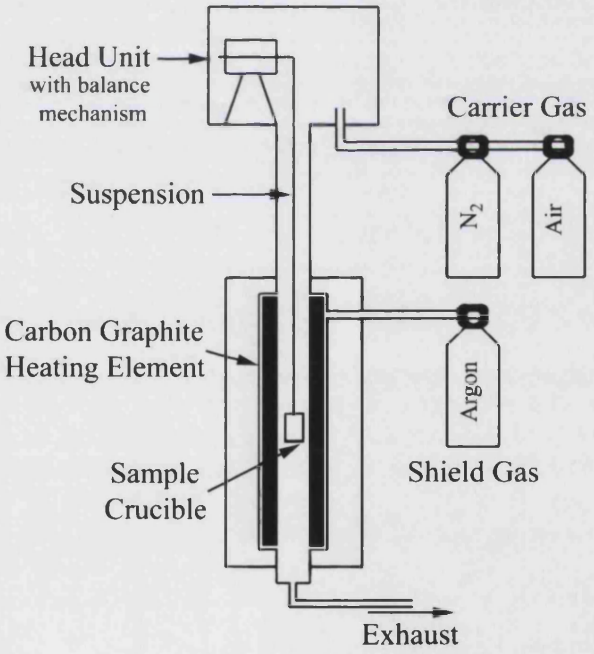

Figure 3-3: Schematic showing the gas connections of the TG-92 furnace (not to scale)

Table 3-2: Data for the Setaram TG-92 instrument and thermocouple

Furnace / Balance				Thermocouple	
Temperature Range (K)	Maximum Load (g)	Limit of Detection (μg)	Weight Range (mg)	Thermocouple Type S	Maximum Temp (K)
293 – 1873	35.0	0.03	± 200	Pt(10%)- Rh/Pt	1673

3.3.2 Weight Calibration

Weight change calibration, using a dynamic temperature method was conducted by heating dry calcium carbonate ($CaCO_3$, 35.41 mg, 100.09 g mol^{-1}) in nitrogen, between 300 an 1,300 K. The resulting weight loss profile due to emissions of CO_2, leaving lime (CaO, 56.08 g mol^{-1}) is given by Figure 3-4. The initial sample weight was used to predict molar yields of CaO and CO_2, and the resulting weights compared with observed data:

	$CaCO_{3(s)}$	$\xrightarrow{\Delta}$	$CaO_{(s)}$	+	$CO_{2(g)}$
Initial Weight	$35.41mg$				
⇒ Initial Moles	$0.353x10^{-3}$				
Mole Ratio	1	:	1	:	1
⇒ Predicted Moles			$0.353x10^{-3}$		$0.353x10^{-3}$
⇒ Predicted Weight			$19.84mg$		$15.56mg$
Measured Weight			$20.13mg$		$15.28mg$
⇒ Deviation			−1.4%		+1.8%

The error margin for overall weight-loss measurement is therefore ± 1.8 percent of the sample weight. This error is small compared to the overall sample weight loss (described in Chapter 4 and amounting to up to 80 percent of sample weight), although more significant for some of the isolated sample reactions introduced in Section 5.5, where contributions to sample weight loss can be less than 10 percent of the sample weight.

3.3.3 Temperature Calibration

Sample temperature was calibrated by the fusion point method. This involved arranging a fusible link of sample metal wire between the last suspension link and a crucible containing an inert metal weight to overcome surface tension effects (Figure 3-5). The sample wires were composed of indium (M.pt: 430 K), lead (M.pt: 600 K), aluminium (M.pt: 933 K) and copper (M.pt: 1,356 K), to cover the temperature range of the present investigation. The sample was heated in nitrogen to avoid formation of metal oxides, and at a rate of 20 K min^{-1}. At the metals fusion point, a weight change was detected as the metal weight fell away.

Figure 3-6a, gives the combined TG profiles of the sample metals. The main fusion event, accounting for over 90 percent of total weight lost in most cases, occurs over a few degrees. The result was a linear relationship (R^2 = 0.999), between experimental and literature fusion temperatures (Figure 3-6b). The gradient of 1.0 indicates the observed temperature to be consistently 1.70 K lower than the actual temperature. This may be a consequence of impurities in the metal; the inert weight causing the link to give-way when soft but not melted; or simply a temperature gradient between thermocouple and sample. Nevertheless, the negligible difference and the linearity of the plot indicate the good accuracy of the thermocouple in measuring the sample temperature over the full temperature range.

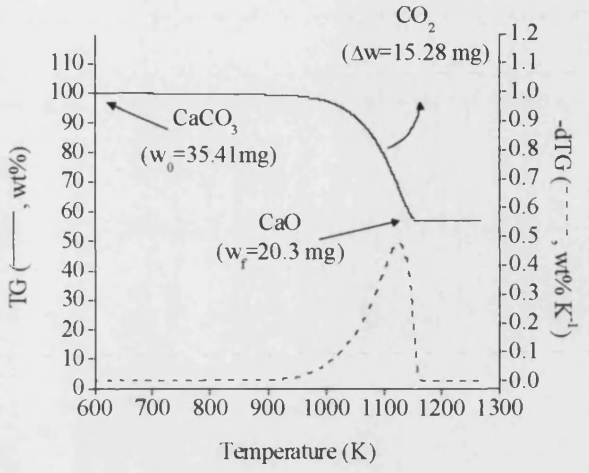

Figure 3-4: Weight calibration of the TGA using 35.41 mg of calcium carbonate, heating at 20 K min^{-1} under flowing nitrogen

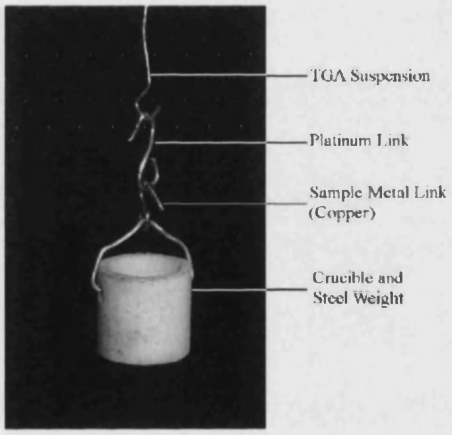

Figure 3-5: Arrangement of the crucible and suspension wires for verification of the temperature by a fusion point method

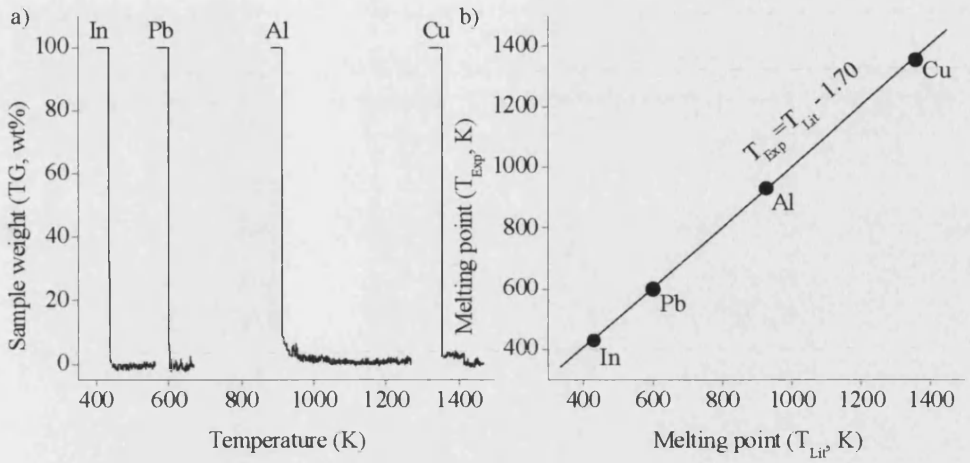

Figure 3-6: Melting point temperature calibration of the Setaram TG-92 instrument using indium, lead, aluminium and copper; (a) TG profile for the sample metals heated at 20 K min^{-1} under nitrogen; (b) Comparison of observed (T_{Exp}) and literature (T_{Lit}) melting points

3.3.4 Software Calculation of the Derivative Thermogravimetric Value

It is probable that the Setsoft software calculates the derivative thermogravimetric value from the thermogravimetric value by calculating the slope of the latter using Equation 3-1. Here the dTG at data point *i* (dTG_i) is given by the thermogravimetric and temperature values (*TG* and *T* respectively), up to *j* points symmetrically adjacent to data point *i*, where $n = 1,2,\ldots j$.

Equation 3-1:

$$dTG_n = \frac{\sum_{n=1}^{j}[TG_{i+n} - TG_{i-n}]}{\sum_{n=1}^{j}[T_{i+n} - T_{i-n}]}$$

3.3.5 Experimental Variables

Work was conducted to determine the effect of heating rate, carrier-gas flow rate, sample size and particle sizes on the TG and dTG profiles for oxidation of pure olive kernels, pure Ptolemais lignite and a blend of 60 %wt. olive kernels in Ptolemais

Lignite (%wt.$_{OK/PL}$). Pyrolysis was also evaluated using pure Ptolemais lignite. Table 3-3 describes the range of experimental conditions employed. Results are described in Sections **4.2** and **4.4**.

Table 3-3, Matrix of experiments for evaluation of the experimental technique during variation of (a) heating rate, sample size range and carrier gas flow rate and (b) sample particle size. X = experiment

a)	Heating rate (K min^{-1})	Sample Size Range (mg) 1-5	25-30	35-40	45-50
Low flow-rate, (3 ml min^{-1})	5		X		
	10		X		
	20	X	X	X	X
	30		X		
High flow-rate, (30 ml min^{-1})	30		X		

b)	Olive kernel particle size (mm) <0.1	0.1-1.0	1.0-1.4	1.4-2.0
20 K min^{-1}, 25-30mg, Low flow-rate	X	X	X	X

3.3.6 Oxidation

Oxidation experiments were carried out in flowing dry air (M_r = 29 g mol^{-1}) with a flow rate of 3 ml min^{-1} (STP).

3.3.7 Pyrolysis

Pyrolysis experiments were carried out in oxygen-free nitrogen (N_2 > 99.998 %vol.) with a flow rate of 3 ml min^{-1} (STP). A purge phase of two hours at 298 K, with the sample in place was included to remove oxygen from the system before the experiment was started.

3.3.8 Buoyancy Effect

Because of the furnace design, the effect of buoyancy on experimental TG results must be considered. The Archimedes principle states that the buoyancy force acting upwards

on a submerged body is equal to the downwards force that would result from the weight of fluid that has been displaced by the object. The result of unbalanced forces is that when a body displaces a volume of fluid weighting less or more than the body does, the body it will sink or rise accordingly. In the TGA, as the air is heated its density decreases, so the weight of the displaced air volume decreases and so does the resulting buoyancy force. The result is that the sample apparently gains weight with increasing furnace temperature.

The effect of changing buoyancy forces may be calculated by rearranging the ideal gas law to give Equation 3-2, relating the displaced gas weight w_d, volume V_d (~ 700 µl for the sample, crucible and suspension), atmospheric pressure P (1.01 x10^5 Pa), the molar mass of air M_r (29 g mol^{-1}) , temperature T and molar gas constant R. Figure 3-7 compares Equation 3-2 with the typical control experiment using an inert material (alumina) with the approximate volume of the sample. This comparison reveals an excellent match between the two datasets, with the slight deviation of around 0.05 mg between 450 and 600 K likely to be due to contaminants on the crucible. This "weight" profile was subtracted from the experimental data of the investigation as a matter of routine to provide true sample weight information.

Equation 3-2:
$$w_d = \frac{PV_dM_r}{RT}$$

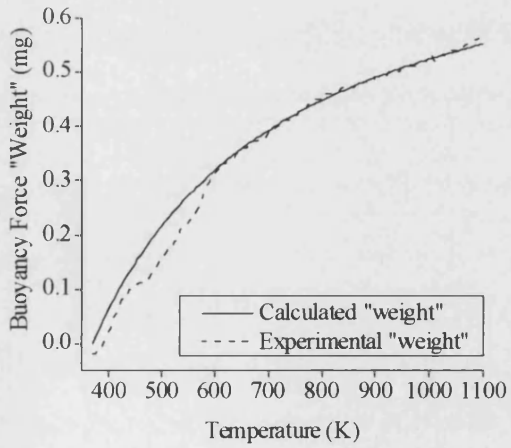

Figure 3-7: Comparison between the weight of displaced air calculated by Equation 3-2, and an experiment using powdered alumina (β = 10 K min^{-1}, air)

3.4 Material Characterisation by Scanning Electron Microscopy

3.4.1 Instrumentation

The instrument used for SEM analysis was a JEOL JSM-6310 scanning electron microscope based at the University of Bath. It features a cryogenic stage for studying hydrated frozen specimens. The backscattered electron micrographs presented in this thesis were taken on a dedicated PC.

3.4.2 Methodology

Original and thermally treated samples (either carbonised under N_2 or oxidised to varying degrees under air, see Sections 3.3.6 and 3.3.7) were analysed by SEM. They were then attached to the sample disk using a carbon-based paste; adhesive tapes were inadequate at retaining the sample. The sample was then frozen by submerging in liquid nitrogen slush at 93 K. The ice was then sublimed on the microscope stage at 193 K to remove frost. The sample was sputter coated in the microscope at 93 K. This gave a fine layer of gold to enhance conductivity. Backscattered electron images were taken with operating voltages of 10 to 15 kV depending on the sample qualities. Images were taken at magnifications between ×50 and ×5,000. Results of the SEM analysis are discussed in Section **4.5**.

Chapter 4 Experimental Results

4.1 Introduction

This chapter presents the data produced by the experimental analysis of the fuel samples. Preliminary investigative work established the effect of experimental conditions on the oxidation (Section 4.2) and the pyrolysis (Section 4.4) of pure and blended fuels. Once the optimal conditions of analysis had been decided, work began to characterise and compare the behaviour of the pure and blended fuels. Finally, morphological changes after various thermal treatments were observed by scanning electron microscopy (Section 4.5).

4.2 TG Analysis Reproducibility

Sample variability of both coal and biomass samples are a direct consequence of the highly variable nature of the sample composition, on both macro and microscopic scales. The thermal activity of plant material is dependent of the cellular materials, the plant tissues, the plant species and the crop season (not to mention sample pre-treatment history), while two coal samples from the same seam can vary in both maceral and mineral composition. Furthermore, the any variability is compounded by the small sample sizes employed by the TGA.

To identify the degree of sample variability, multiple thermogravimetric profiles for several of the samples are presented in Figure 4-1. Standard error values for up to five data series were calculated by Equation 4-1 (where $y_{T,s}$ is the data value at temperature T of series s and n_y is the combined number of data points from all series).

Equation 4-1:
$$S.E. = \sqrt{\frac{\sum_{T=350}^{1100}(y_{T,1} - y_{T,2})^2}{(n_y - 1)n_y}}$$

While pyrolysis profiles were accurately reproduced (Figures 4-1a and 4-1b), oxidation reproducibility was more variable (Figures 4-1c and 4-1d), where German lignite exhibits a larger standard error than Ptolemais lignite.

Figures 4-1e and 4-1f compare the deviation for the TG profiles of replicate experiments for 60 $\%wt._{FR/PL}$ and 50 $\%wt._{FR/GL}$. Forest residue-Ptolemais lignite blend oxidation reproducibility is reasonable, with a standard error value of 1.01 %wt. (Figures 4-1e). The only significant deviation arising between 710 and 720 K occurs through a difference is magnified by the combination of the large dTG_{max} and the narrowness of the implied reaction. However, a similar level of reproducibility could not be attained for similar German lignite blends (Figure 4-1f), where a standard error of 5.88 %wt. is observed. The result was that even with a large number of repeated analyses of the same German lignite blend; results were so variable that reliable conclusions could not be made.

There are several reasons for this variability of the German lignite data. The German lignite was already extremely finely ground when received, while the Ptolemais lignite sample received was very coarse. This meant the particle size of the Ptolemais lignite could be closely controlled through subsequent grinding, while the German lignite particle size could not be regulated. As shown in Section 4.3.4, particle size has a strong influence on sample activity where small particle sizes (< 0.1 mm) are involved. This may also explain the narrower, higher dTG_{max} of the German lignite, compared with that of the Ptolemais lignite (Figure 4-2, p. 76).

The German lignites fineness would increase the particles surface area making them more reactive. Enhanced activity of these particles may stimulate activity in the biomass, with the result that the blend homogeneity – and thus the degree of lignite-biomass particle contact – alters the dTG profile.

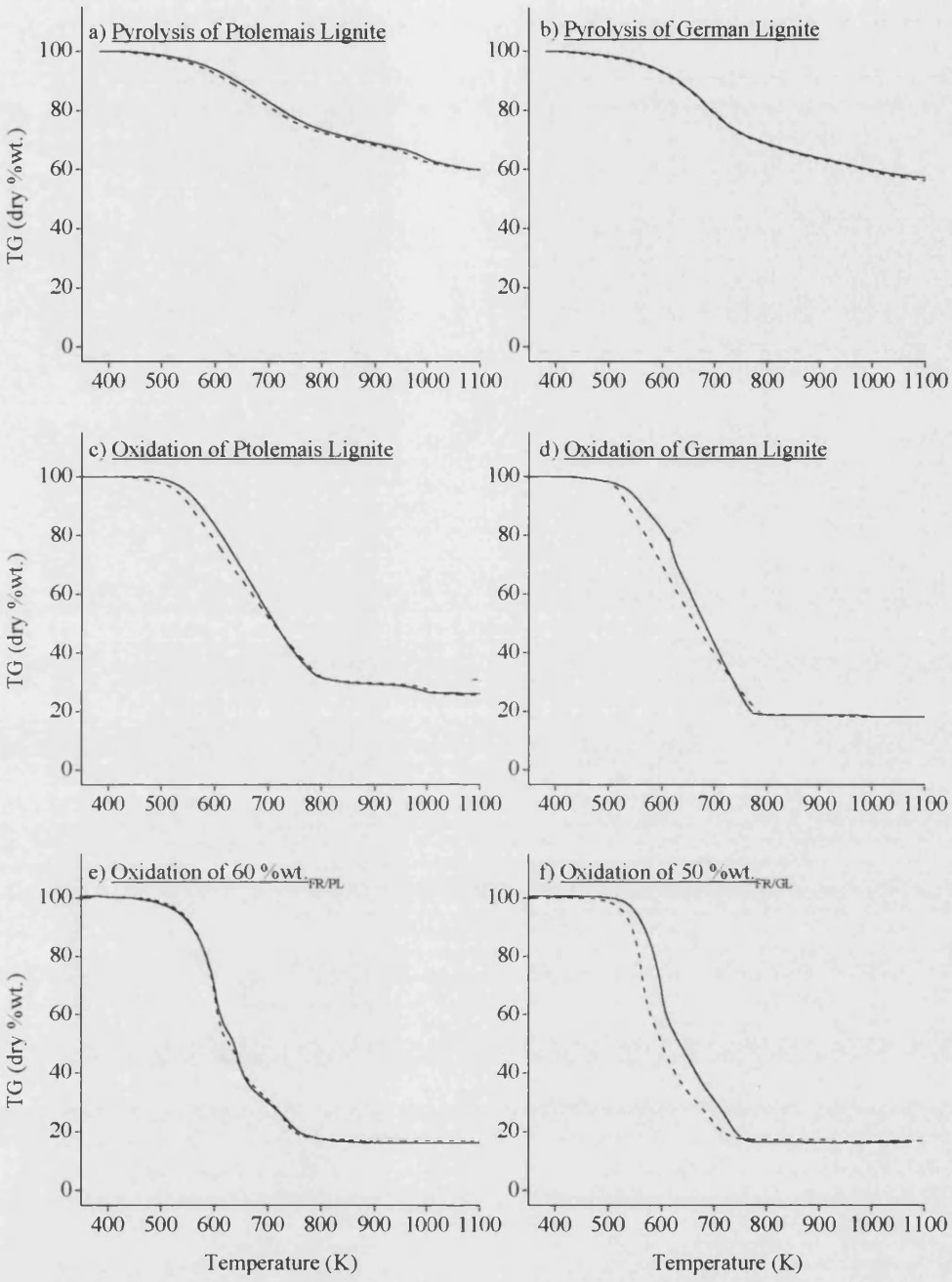

Figure 4-1: Comparison of duplicate experimental TG data. (a) Pyrolysis of Ptolemais lignite (S.E. = 0.50 %wt. K^{-1}); (b) Pyrolysis of German lignite (S.E. = 0.21 %wt.); (c) Oxidation of Ptolemais lignite (S.E. = 1.59 %wt.); (d) Oxidation of German lignite (S.E. = 3.31 %wt.); (e) Oxidation of 60 %wt.$_{FR/PL}$ blend (S.E. = 1.01 %wt.); (f) Oxidation of 50 %wt.$_{FR/GL}$ (S.E. = 5.88 %wt.)

4.3 Oxidation Experiments

4.3.1 Effect of Heating Rate

Figure B-1 (Appendix B) describes the effect of changing the heating rate (using 5, 10, 20 and 30 K min^{-1}) during the oxidation of Ptolemais lignite. The first 100 K of activity, between 480 and 580 K, is comparable for all experiments in terms of both total weight loss (TG) and the rate of weight-change (dTG). After 580 K, the 20 and 30 K min^{-1} profiles deviate from the peak shape of the 5 and 10 K min^{-1} experiments. It is likely that lower heating rates allow TG processes to advance at their intrinsic reaction rate, with no competition for oxygen or energy.

However, with higher heating rates, reaction progress is dictated by the rate of heat and mass transfer, accounting for the limited apparent reactivity and the linear region. The reaction first proceeds at its own rate until oxygen is depleted, it then proceeds at a lower restricted by the rate of inward diffusion of oxidising species. To compensate for the restricted rate of reaction, increases in heating rate elevate the burnout temperature from 700 K when β = 5 K min^{-1} to 800, 950 or 1000 K when β = 10, 20 or 30 K min^{-1} respectively. This would mean that reactions at 775 K (observed for β = 5 K min^{-1}) were obscured at higher heating rates, and furthermore that reactions at 950 K are shifted to higher temperatures due to competition between reactions for oxygen. It is possible that for heating rates above 30 K min^{-1}, the reactions at 950 K may also be obscured.

As with the lignite, for all the heating rates the onset of weight loss of olive kernels (Figure B-2) is also constant at 450 K. Between 650 and 1000 K, the dTG profiles also involve similar changes as the lignites, with a progressive increase of burnout temperature with heating rate. It is noticeable that above 10 K min^{-1}, TG processes exhibit linear profiles of limited reaction rates as described above. However, the profile of the primary TG process between 450 and 650 K is equal for all the experiments, suggesting a strong independence from any restrictive processes. This independence is analogous to that for lignite up to 580 K. Reactions in this range relate to

devolatilisation, which is independent of oxygen transfer to the fuel surface, and contributes a higher weight percentage of biomass than lignite. However, olive kernels also exhibit a second peak at 700 K for all heating rates, although obscured at lower heating rates. The presence and constancy of the peak at the onset of the linear region, is suggestive of a reaction that is independent of mass or heat transfer restrictions. Alternatively, the peak for 20 or 30 K min^{-1} experiments may relate to the same reaction as the linear weight-loss region, representing the point at which oxygen stoichiometry drops below unity before the reactive component is depleted. For biomass, oxygen diffusion may be further compromised by the additional homogeneous oxidation of volatile materials, using up oxygen before it reaches the char surface.

As shown in Figure B-4, a blend of the fuels containing 60 percent by weight of olive kernels in Ptolemais lignite (60 $\%wt._{OK/PL}$) exhibits certain properties of the parent fuels. For example, decomposition involves three prominent peaks at 550, 600 and 750 K corresponding with olive kernels, lignite and olive kernels respectively. The first peak remains constant for all heating rates while at lower heating rates the 600 K peak is significantly narrower than that of pure lignite. For the upper heating rates, both the latter peaks resolve into a single linear profile as observed previously; however, the burnout temperatures are 50 to 100 K lower than for analogous pure fuel experiments.

4.3.2 Effect of Initial Sample Weight

Figures B-3, B-5 and B-6 show the effect of increasing the initial weight of Ptolemais lignite, olive kernels and the blend (60 $\%wt._{OK/PL}$) of their respective dTG profiles. For Ptolemais lignite, weight loss (not counting moisture) begins at around 480 K. For samples of 1 to 5 mg, there is a principal reaction peak at 620 K, followed by two smaller reactions at 800 and 960 K. For samples of 25 to 50 mg, the rate loss reaches a maximum at around 550 K, followed by a flat tailing in rate, which ends abruptly at between 950 and 1100 K depending on the initial sample weight.

Unlike the heating rate experiments, when initial sample weight is increased the devolatilisation of olive kernels (550 K, Figure B-5) displays a reduction in width and increase in dTG_{max}. The cause of this increase in the rate of devolatilisation is not clear.

Olive kernels do however demonstrate the difference between large (> 5 mg) and small (< 5 mg) sample sizes observed for lignite, as well as the progressive lowering in reaction rate and increase in burn-out temperature of the linear region with increasing initial sample weight. The shifting of the 950 K TG process as the previous reactions burn-out temperature increases is possibly caused by non-gravimetric endothermic reactions (such as ash softening or melting) between these two events that compete with the TG process for energy.

While in Figure B-2a (olive kernels, β = 5 K min^{-1}) there are two dTG peaks at 750 K, Figure B-5a (olive kernels, w_0 = 1-5 mg), with the peak at 750 K displays a single broad peak. This lack of detail, due to the inability of the instrument to resolve the small weight changes at the higher heating rate in Figure B-5a suggest slightly larger samples should be use to obtain more detailed data.

The fuel blend profiles are again comparable to the parent fuels, and similar effects as the initial sample weight is increased (Figure B-6).

4.3.3 Effect of Carrier Gas Flow Rate

Figures B-7, B-8 and B-9 describe the dTG profiles for Ptolemais lignite, olive kernels and the 60 %wt.$_{OK/PL}$ blend respectively under low (3 ml min^{-1}) and high (30 ml min^{-1}) carrier gas flow rates. They demonstrate that increasing the flow rate, which increases the availability of oxygen to the reaction zone, prompts more rapid reaction for the non-oxidation processes, demonstrated by the higher dTG of the linear region and earlier burnout temperatures, typically by around 150 K. The increase in the rate of devolatilisation (the flow of 30 ml min^{-1} produces narrower peaks with higher dTG_{max} values) may be caused by the elevated rates of homogeneous oxidation, liberating energy for further reactions, and reducing the concentration of volatile materials in the gas phase.

4.3.4 Effect of Particle Size

The effect of particle size on the profile for dTG was measured for olive kernels (Figure B-10). Particle size does not affect profile shape as strongly as other conditions, however the rate of devolatilisation is strongly enhanced when dust (d < 0.1 mm) is analysed, giving a narrower peak (550 K) with a higher dTG_{max}. It also manifests as a single peak, where devolatilisation peaks for the larger particles exhibit shoulders at 580 K. This may be caused by the higher surface area to volume ratio of the dust, eliminating any internal temperature gradients, enabling pyrolysis reactions to proceed in a single event and improving mass transfer within the particle.

4.3.5 German and Ptolemais Lignites

Figure 4-2 below compares the TG and dTG profiles for Ptolemais lignite and German lignite 1 under oxidising conditions. The TG profiles (Figure 4-2a) show the majority of both lignites weight (~ 60 %wt.) is lost between 550 and 750 K; losses above this (up to 1100 K) amount to less than 10 percent by weight. There are a number of common features to the lignites dTG profiles (Figure 4-2c and 4-2d). Both feature their main oxidation maxima at 650 K with a shoulder at around 600 K suggesting multiple processes and both include a secondary oxidation reaction between 750 and 800 K. By contrast, dTG_{max} of German lignite (Figure 4-2d) is higher than Ptolemais lignite (Figure 4-2c), while German lignite peaks are also narrower, making the 600 K shoulder more prominent. Ptolemais lignite features a small decomposition reaction at 950 K, while the only reactivity above 800 K in the German lignite is a significantly smaller reaction peak at 900 K. The intrinsic variability of the German lignite blends (Section 4.2 p.66) however, mean the analysis of blends by this method is inappropriate.

4.3.6 Olive Kernels and Forest Residue

The weight loss profiles for olive kernels and forest residue are shown in Figure 4-2b. Both fuels display activity between 500 and 750 K, representing around 90 percent loss by weight. Between 750 and 1100 K, losses amount to less than 5 percent by weight.

By comparing the dTG profiles (Figure 4-2e and 4-2f), weight loss is observed to occur in two distinct stages. The first occurs between 500 and 625 K, peaking at 600 K for forest residue and 580 K for olive kernels. This is a significant reaction for the forest residue, illustrated by the large dTG_{max} and slightly greater weight loss in this temperature range. The second stage occurs between 650 and 750 K, peaking at around 730 K for both fuels. Both fuels display similar profiles in this stage. Above 780 K, the calcination peak of ash at 950 K is the only significant activity, a greater for olive kernels than for forest residue.

4.3.7 Fuel Comparison: Biomass and Coal Oxidation

A comparison of the profiles for the lignite and biomass fuel groups (Figure 4-2) identifies some of their key differences. The common weight-loss onset temperatures indicate that similar pyrolysis reactions precede the dominant oxidation processes of each fuel. But while the active temperature ranges are similar (between 500 and 800 K), lignite oxidation gives a single thermal process peaking at 650 K, perfectly between the two biomass oxidation processes at 600 and 700 K. Lignites loose less mass through oxidation than biomass because of greater ash content; respectively 35 and 10 percent by weight is ash. The reactivities of the two fuels (in terms of dTG_{max}) are similar, and the primary peak of olive kernels at 600 K, exhibits a similar dTG_{max} to German lignite (~ 0.7 %wt. K^{-1}). Under these conditions, forest residue and Ptolemais lignite represent the upper and lower reactivity extremes.

4.3.8 Ptolemais Lignite Blends with Olive Kernels and Forest Residues

Figure 4-3 compares the thermogravimetric oxidation profiles for the blends of olive kernels with Ptolemais lignite. Analogous profiles for forest residue blends are given in Figure 4-4. They reveal that with the majority of weight loss is between 500 and 800 K, with overall losses at 1100 K arising in a regular order that increases with the biomass content of the blend. This pattern is more regular for blends with forest residues, than with olive kernels. There are also similarities with the parent fuels. The dTG profiles each exhibit three discrete maxima, the T_{max} values of which are comparable to those of

the parent fuels (lignites at 650 K, and biomass at 600 and 700 K). Differences arise however in terms of the blend peaks at 600 K which are notably narrower than that of the Ptolemais lignite (Figure 4-2c), especially clear in the low biomass (20 $\%wt._{OK/PL}$) profiles of Figure 4-3e. Furthermore, the 950 K ash reaction of Ptolemais lignite is missing from the blend profiles, even where the comparable reaction of the olive kernels (Figure 4-2e) appears in the higher biomass content profiles of Figures 4-3b and 4-3c. At this stage, the only other notable effect of combining the fuels is the loss of the sharp peak for olive kernels at 700 K, which although present in the 80 and 60 $\%wt._{OK/PL}$ blends (Figures 4-3b and 4-3c), is not present in either the 40 or 20 $\%wt._{OK/PL}$ blends (Figures 4-3d and 4-3e). This may be a consequence of the weight change becoming marginal as the lignite content increases, or that the reaction has been changed by components of Ptolemais lignite.

4.3.9 Oxidation Temperature Ranges

Figure 4-5 describes the changing active temperatures ranges during oxidation of the blends as their respective biomass content increases. They reveal that while the temperature at which activity begins (T_{Onset}) remains relatively constant, the burnout temperature ($T_{Burnout}$) decreases with decreasing lignite content. Onset and burnout are determined as the temperatures at which the dTG first exceeds 0.03 %wt. K^{-1} for more than 5 K, then drops back below 0.03 %wt. K^{-1} until 1100 K. These thresholds were decided upon to separate actual activity from the background noise. The changes observed are caused by the increasing concentration of biomass with progressively lower amounts of material for heterogeneous oxidation. The rapid drop in burnout between zero and 20 $\%wt._{OK/PL}$ (Figures 4-5a and 4-5b) indicates the lower level of ash activity within in the blends, compared with that of pure Ptolemais lignite.

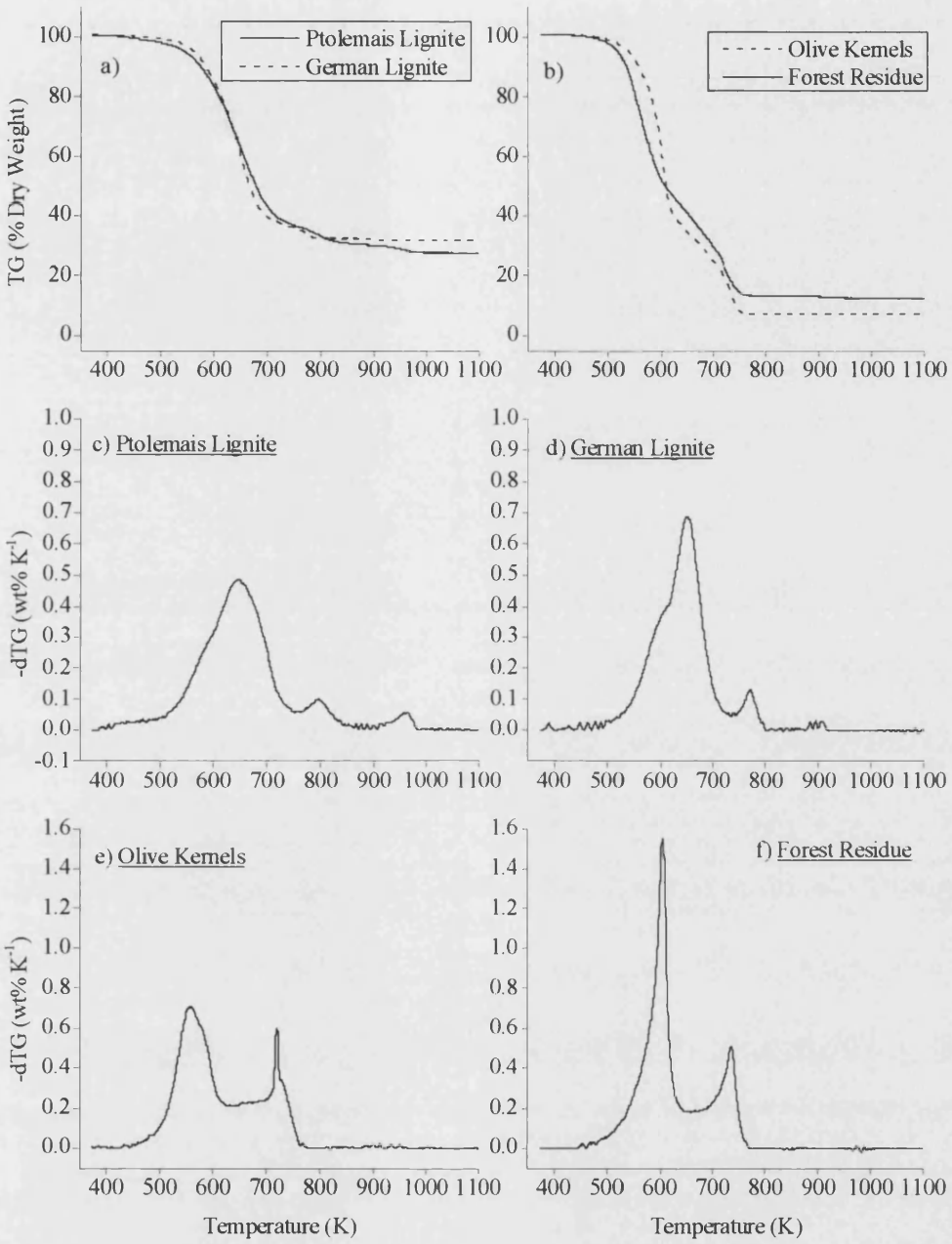

Figure 4-2: Comparison of (a-b) TG and (c-f) dTG profiles for the oxidation of Ptolemais lignite, German lignite, forest residue and olive kernel. (β: 10 K min^{-1}; w_0: 5-10 mg; air flow: 3 ml min^{-1})

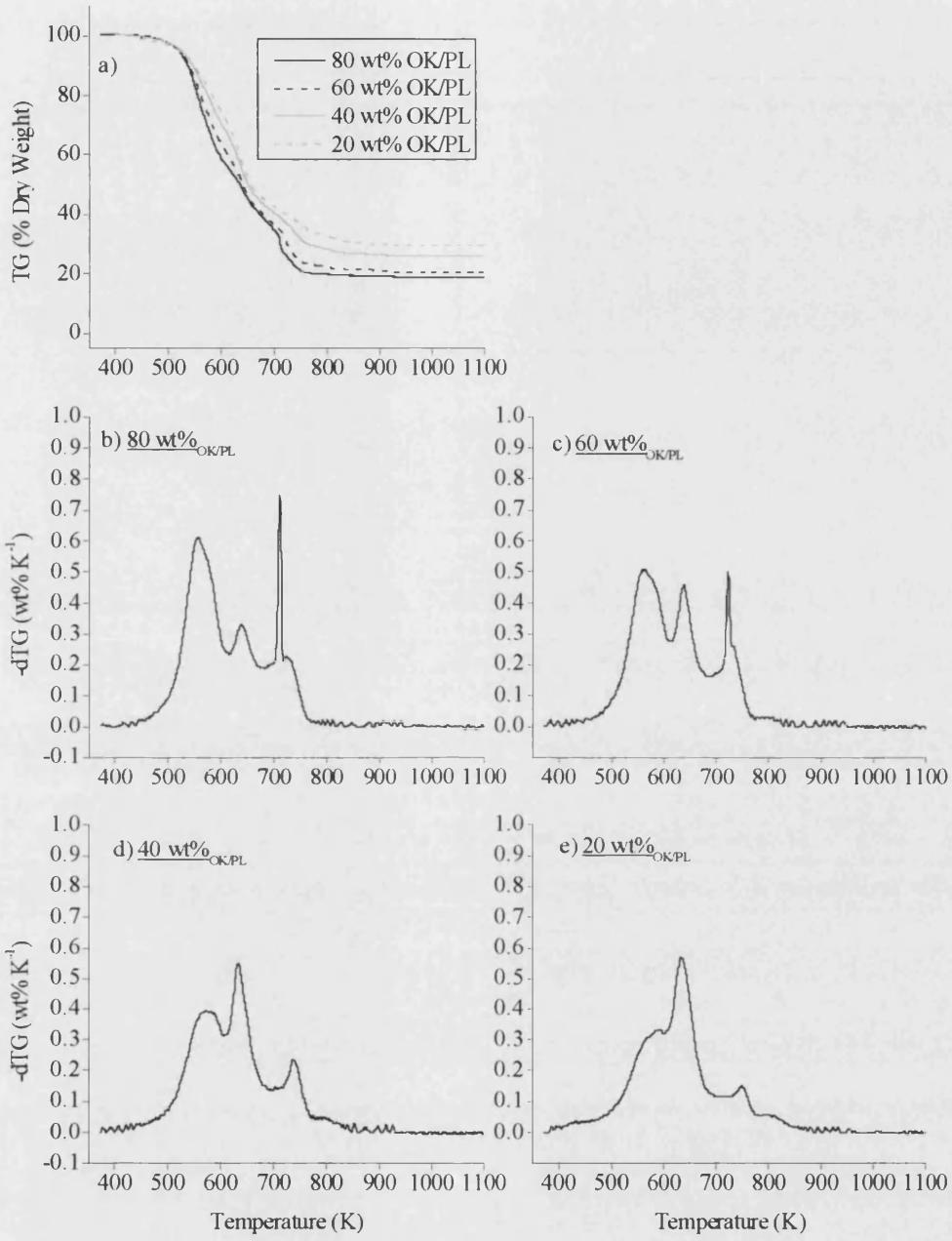

Figure 4-3: Comparison of (a) TG and (b-e) dTG thermogravimetric profiles for the oxidation of blends of Ptolemais lignite (PL) with olive kernels (OK). (β: 10 K min^{-1}; w_0: 5-10 mg; air flow: 3 ml min^{-1})

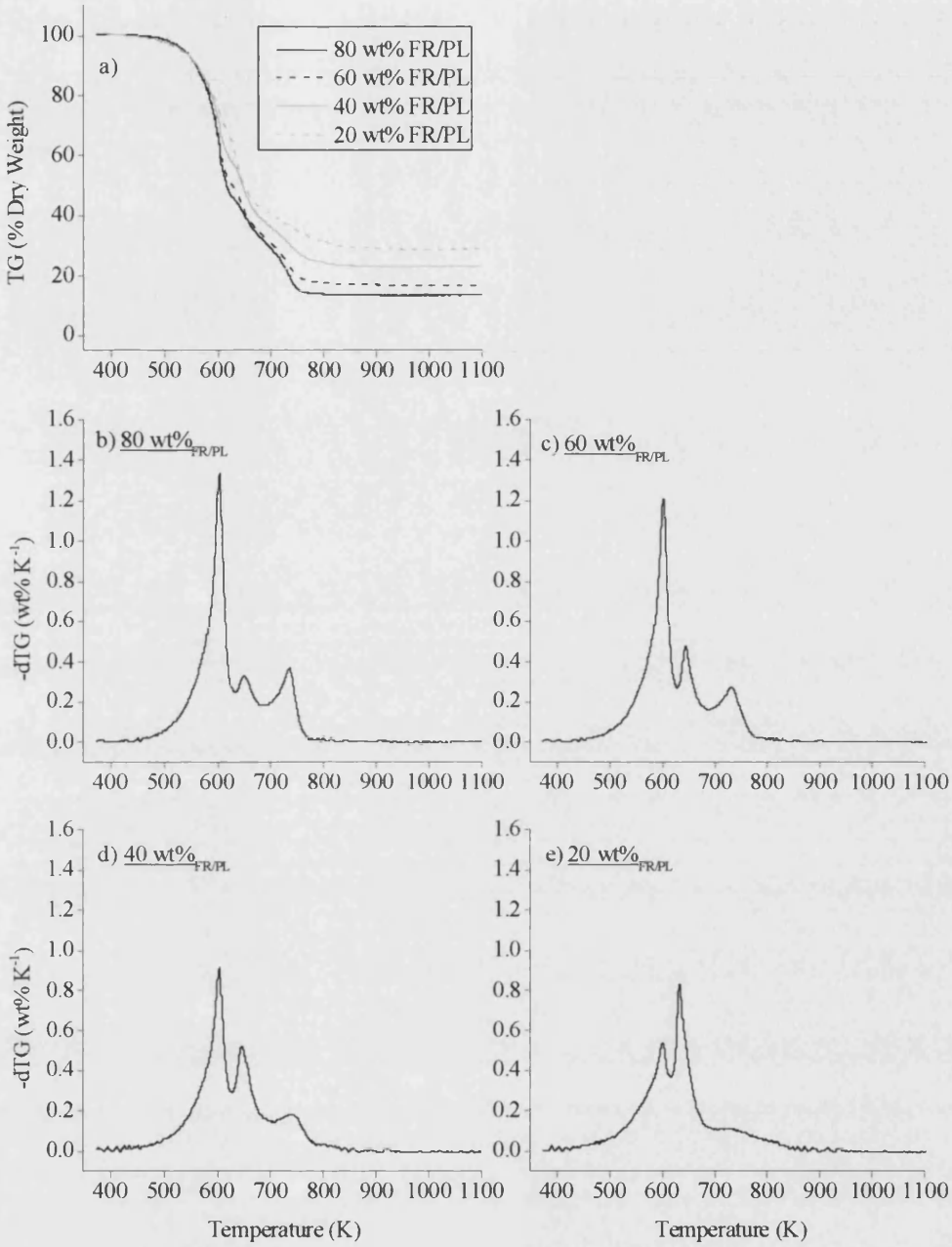

Figure 4-4: Comparison of (a) TG and (b-e) dTG thermogravimetric profiles for the oxidation of blends of Ptolemais lignite with forest residues (FR). (β: 10 K min^{-1}; w_0: 5-10 mg; air flow: 3 ml min^{-1})

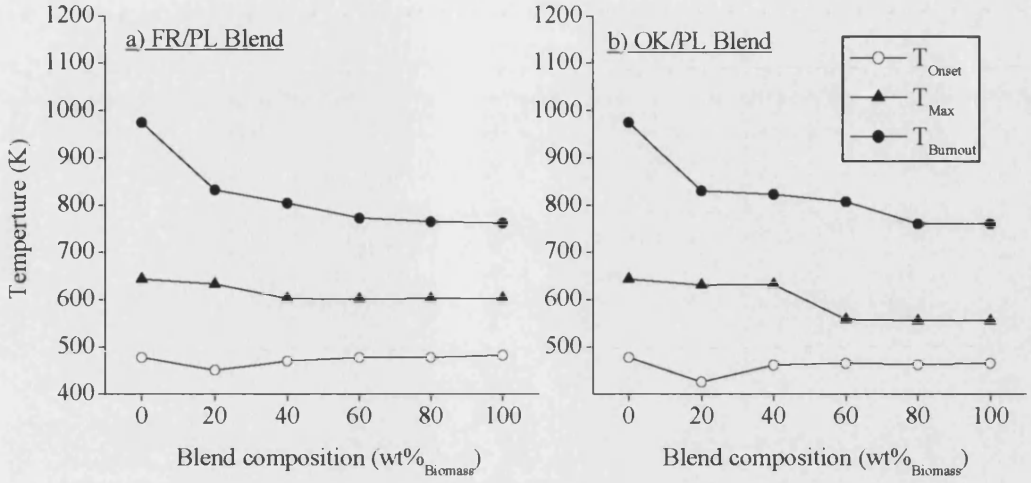

Figure 4-5: Comparison of thermally active ranges for oxidation of the biomass/lignite blends. (T_{Onset}: dTG > 0.03 %wt. K^{-1}, T_{max}: temperature of highest dTG. $T_{Burnout}$: dTG < 0.03 %wt. K^{-1})

4.4 Pyrolysis Experiments

4.4.1 Effect of the Experimental Variables

The dTG profiles of Figures B-11 to B-13 (Appendix B) reveal that pyrolysis is largely independent of sample size, heating rate and gas flow rate, with only small variations in the peak temperature of the second process. This agrees with observations that pyrolysis is a thermally mediated reaction and so independent of mass transfer kinetics. The noise of the profile appears to increase for the 1-5 mg sample (Figure B-13a), this may be caused by the magnitude of weight changes observed for this sample size approaching the noise level of the instrument. Therefore, without modification to the instrument, pyrolysis reactions where lignites in particular exhibit small weight changes, larger sample sizes should be used.

4.4.2 Tailing Phenomena

Tailing of profiles above 1000 K (Figure 4-6), when all the main reactions have been completed, was observed during the pyrolysis of all samples. The apparatus is sealed and under positive pressure, reducing the chance of air leaking into the furnace and the nitrogen carrier gas as a purity of 99.998 %, however it may by that trace levels of oxygen in the carrier gas or the argon shield gas have led to low levels of char oxidation. Werther *et al.* [2000] suggest that pyrolytic changes above 1000 K relate to graphitisation of the fixed carbon; structural and chemical condensation reactions; loss of thermally unstable oxygen groups (*e.g.* ether moieties) and progressive straightening and rearrangement of graphitic sheets into regular stacked layers, (Section 2.4.2). Section 2.4.6 also describes the ash changes occurring in this temperature range, which also contribute small mass changes.

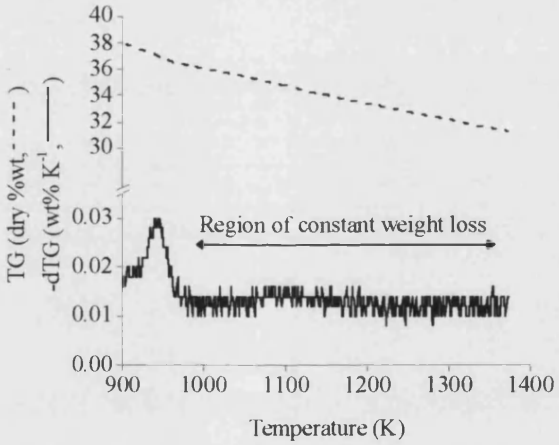

Figure 4-6: High temperature pyrolytic behaviour of olive kernels, comparing weight loss (TG) and weight loss rate (-dTG) profiles between 650 and 1375 K. (β: 5 K min^{-1}; w_0: 5-10 mg; nitrogen flow rate: 3ml min^{-1})

4.4.3 German and Ptolemais Lignites

Compared with the oxidation profiles, the weight loss of lignites under pyrolysis conditions is significantly lower (Figures 4-7c to 4-7d), exhibiting dTG_{max} values of less than 0.2 %wt. K^{-1}. However, the activity is distributed of a much broader range, from

400 to over 1100 K. As described above, an important fact of pyrolysis is that under linear heating conditions the char does not reach a stable weight, indicating that condensation reactions are sustained. By 1100 K however, lignites retain around 60 percent by weight as char, with a rate of weight loss maintained at 0.012 %wt. K^{-1}. That the activity between 400 and 500 K not observed in air (Section 4.3.5), suggests the latter may remove a small amount of reactive material during drying, which is not removed when dried under nitrogen. Peak between 600 and 700 K (Figures 4-7b to 4-7c) are slightly higher and more pronounced for German lignite than Ptolemais lignite. These peaks appear to be superimposed over lower-level activity, sustained for the full temperature range. Ptolemais lignite retains the reaction at 950 to 1000 K, observed previously (Section 4.3.5) as the calcination of $CaCO_3$ in the ash. The fact that this reaction is also present in these pyrolysis experiments confirms it to be a non-oxidation reaction.

In comparison with the oxidation experiments, the principal pyrolysis peak matches with the peak in oxidation, with differences in T_{max} of around 50 K. For both lignites, the oxidation rate exceeds pyrolysis rate until they exchange between 700 and 850 K Pyrolysis then continues beyond 1100 K at around 0.012 %wt. K^{-1} (discussed above in Section 4.4.2).

4.4.4 Olive Kernels and Forest Residue

Pyrolysis activity of the biomass is dominated by a pronounced weight-loss event between 500 and 650 K (Figures 4-7e and 4-7f). This process results in a 50 percent weight-loss, with the forest residue peak at 600 K, just after olive kernels. Olive kernels also display a significantly lower reactivity than forest residues, with dTG_{max} values of 0.7 and 1.2 %wt. K^{-1} respectively. The primary pyrolysis event coincides well with the primary oxidation event of biomass (Section 4.3.6). After 600 K, the rate of pyrolysis significantly weakens reaching a constant level by around 800 K. The shape of dTG profile between 600 and 800 K (Figures 4-7e and 4-7f) is suggestive of a low-reactivity process similar to lignite pyrolysis (Figures 4-7b and 4-7c). Above 800 K, the rates of pyrolysis for both biomass types are fractionally higher their rates of oxidation resulting

in the previously observed failing in weight loss. The lower dTG in this region when compared with lignite is predictable due to the lower char content of biomass.

4.4.5 Fuel Comparison: Biomass and Coal Pyrolysis

While the comparison of the oxidation profiles of the two fuel types identified their relative ash contents, a comparison of their pyrolysis profiles clearly illustrates the differences in terms of the combustible material involved. While biomass quickly evolves large quantities of volatile materials, losing up to 50 percent of its weight by 650 K, lignite undergoes a slower change, with a maximum somewhere around 700 K, illustrative of the large quantities of fixed carbon involved. Biomass also exhibits a fixed carbon component, with weight loss between 800 and 1100 K sustained at 0.01 %wt. K^{-1}, similar to lignite, although the residual mass percentage by 1100 K is significantly lower.

4.4.6 Ptolemais Lignite Blends with Olive Kernels and Forest Residue

Profiles describing the thermogravimetric activity of blends of Ptolemais lignite and olive kernels are given in Figure 4-8. Profiles for blends with forest residues are given in Figure 4-9. Pyrolysis of the blends is driven by biomass processes, accounting for losses by 600 K of between 25 and 55 weight percent for forest residue blends, and between 20 and 40 weight percent for the olive kernel blends, increasing with biomass content. Weight losses between 600 and 1100 K are less dependent on blend ratio, as both biomass and lignite contribute to activity in this range. This is demonstrated in the dTG profiles where relatively between 650 and 900 K the blends follow similar trends, starting around 0.1 %wt. K^{-1} and tailing to 0.01 %wt. K^{-1}. In the olive kernel blends (Figures 4-8b to 4-8e), activity above 900 K alludes to the ash reactions described in Section 2.4.6, culminating in a small peak at 950 K in the 80 $\%wt._{OK/PL}$ blend.

4.4.7 Pyrolysis Temperature Ranges

Figure 4-10 compares the active ranges for pyrolysis, determined by the technique described previously (Section 4.3.9). For the Ptolemais lignite blends (Figures 4-10a and 4-10b) there is a progressive decrease in the final reaction temperature, but a gradual increase in onset temperature as the biomass content increases. Interestingly T_{max} varies very little for the blends, and equates well to that of biomass, indicating lignite does not influence this activity in pyrolysis of the blends. There is a sharp change reduction in the burnout temperature between 60 and 80 $\%wt._{FR/PL}$ (Figure 4-10a), likely to be due to the lignite ash reaction noted before becoming insignificant in the blends.

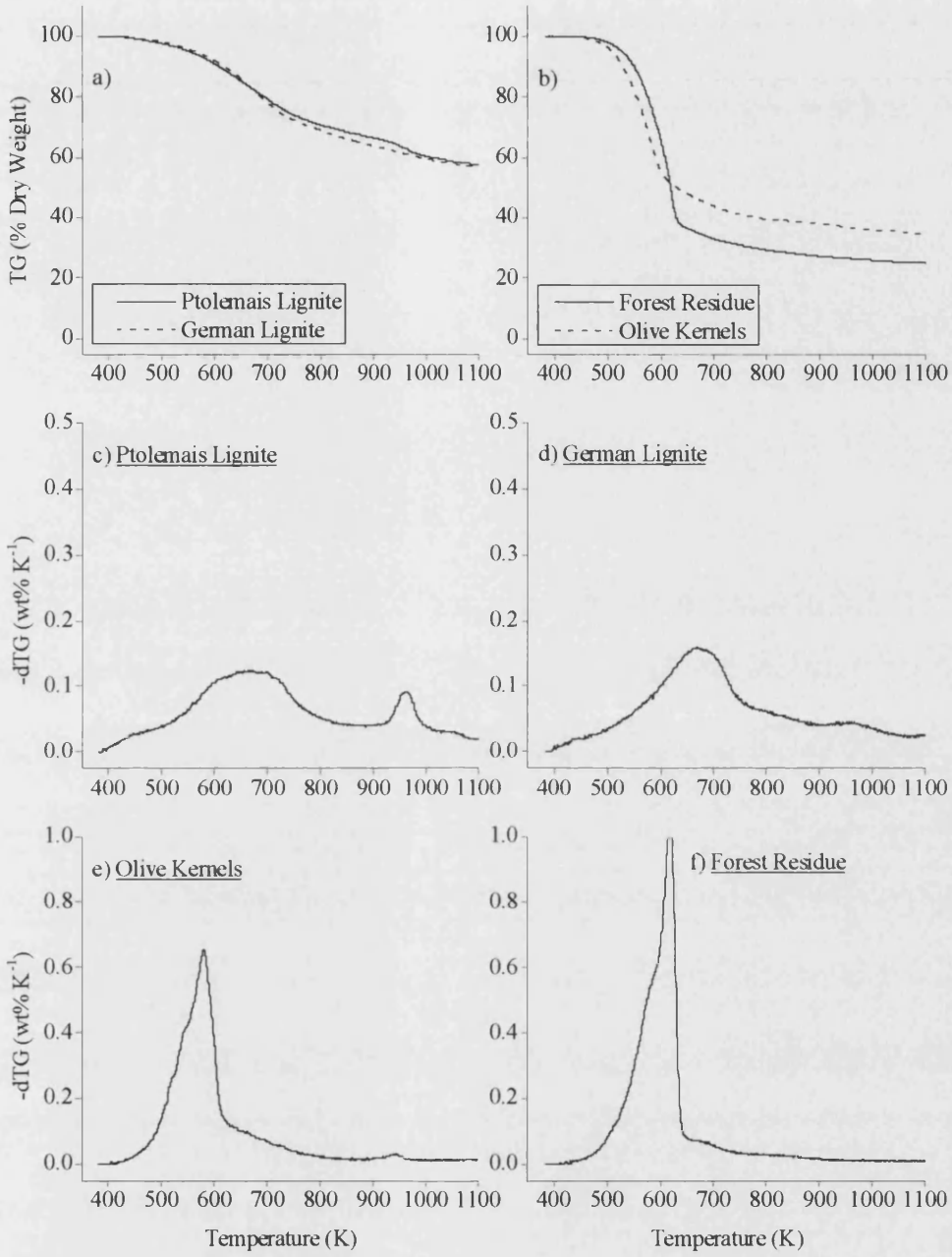

Figure 4-7: Comparison of (a-b) TG and (c-f) dTG profiles for the pyrolysis of Ptolemais lignite and German lignites, forest residue and olive kernels. (β: 5 K min^{-1}; w_0: 5-10 mg; nitrogen flow rate: 3 ml min^{-1})

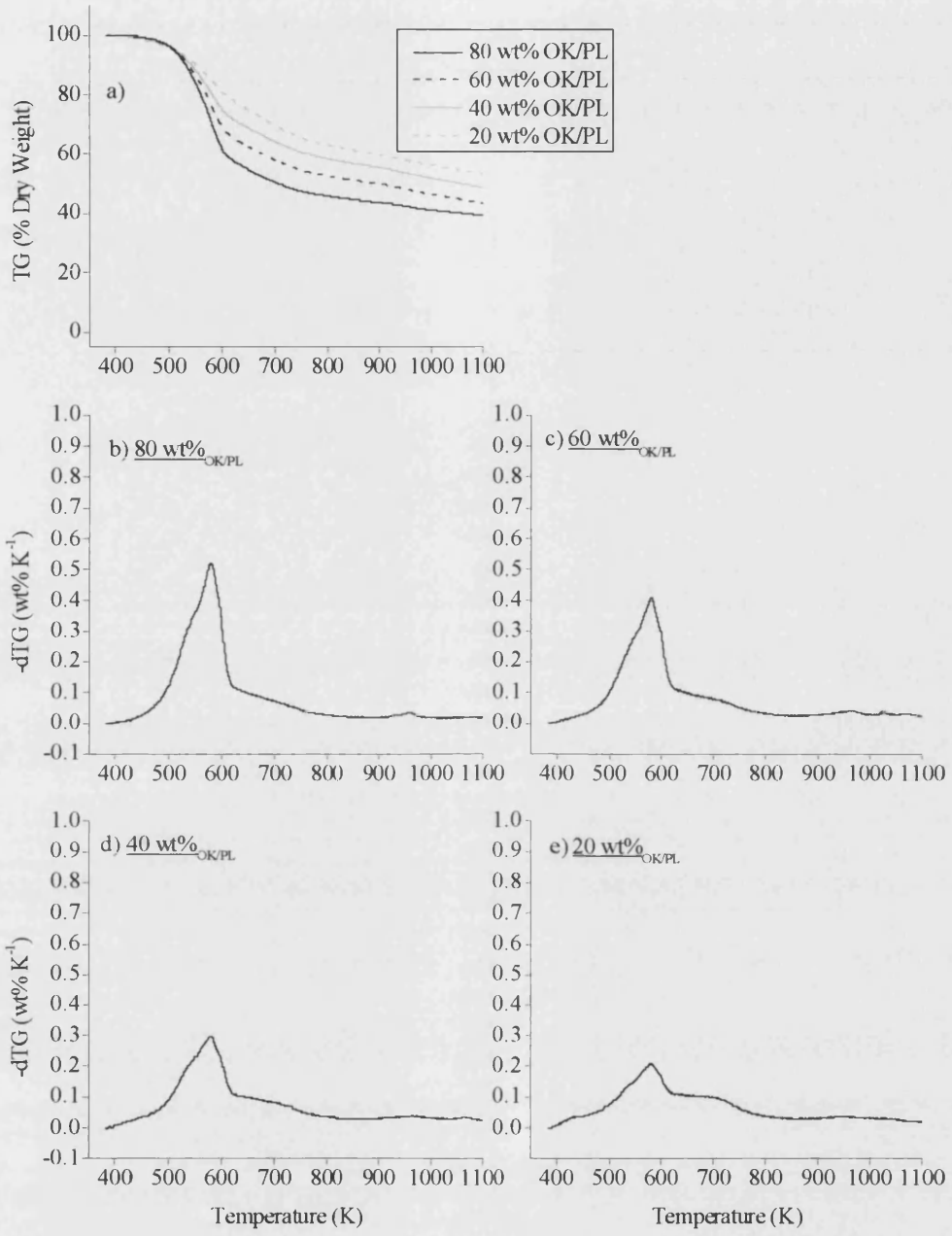

Figure 4-8: Comparison of (a) TG and (b-e) dTG profiles for the pyrolysis of blends of Ptolemais lignite with olive kernels. (β: 5 K min^{-1}; w_0: 5-10 mg; nitrogen flow rate: 3 ml min^{-1})

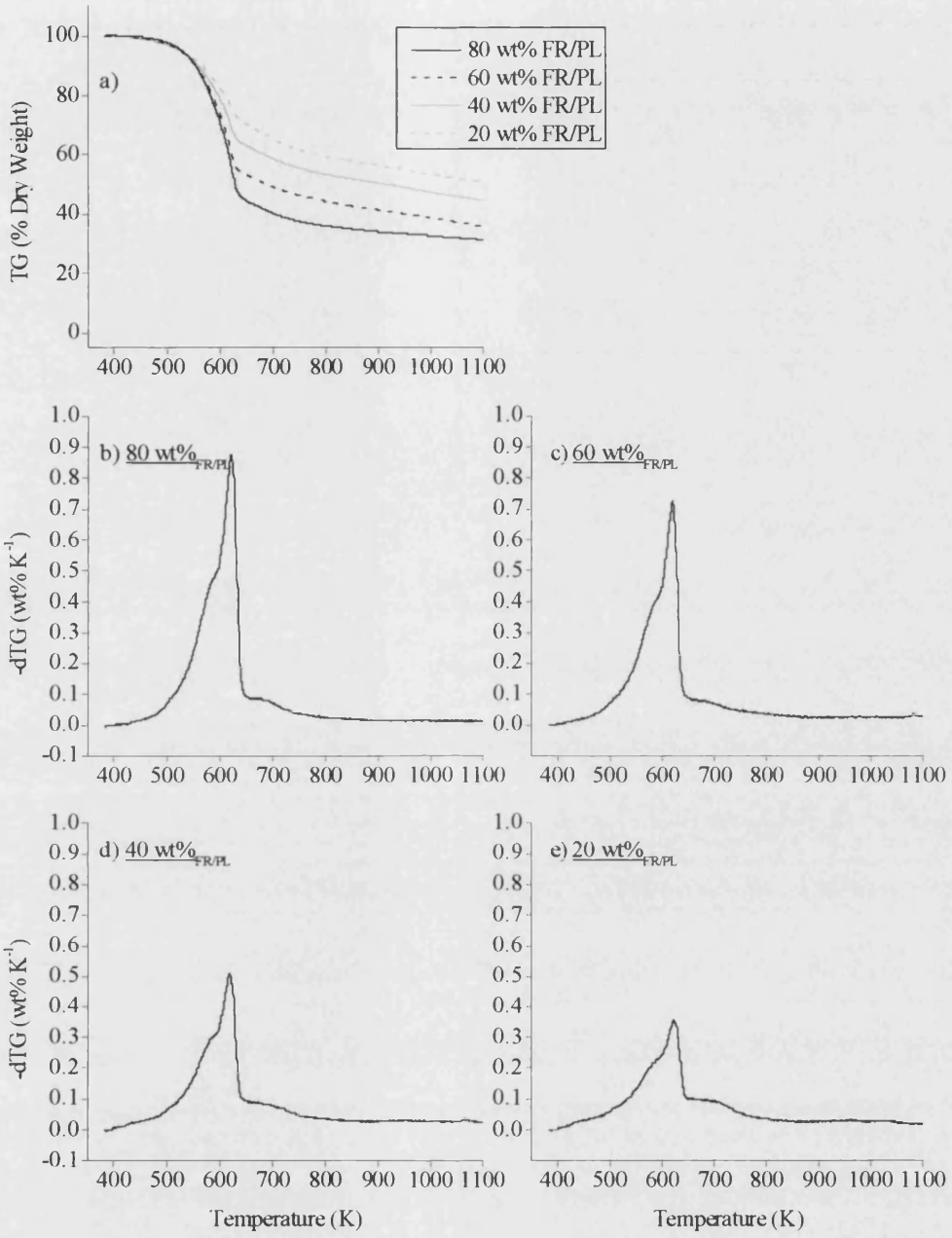

Figure 4-9: Comparison of (a) TG and (b-e) dTG profiles for the pyrolysis of blends of Ptolemais lignite with forest residue. (β: 5 K min^{-1}; w_0: 5-10 mg; nitrogen flow rate: 3 ml min^{-1})

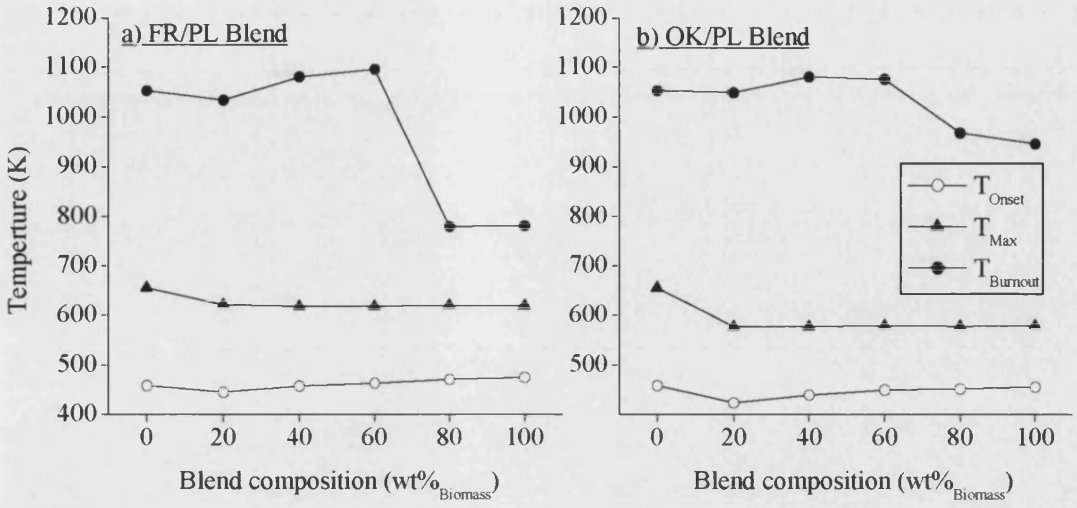

Figure 4-10: Comparison of thermally active ranges for pyrolysis of the biomass/lignite blends. (T_{Onset}: $dTG > 0.03$ %wt. K^{-1}, $T_{max} = dTG_{max}$. $T_{Burnout}$: $dTG < 0.03$ %wt. K^{-1})

4.5 Scanning Electron Microscopy

Scanning electron images were taken of the samples in a raw state, as well as pyrolysed and ashed samples prepared as described in Sections 3.3.6 and 3.3.7. The back-scattered electron images (BEI) are given in Figure 4-11, and discussed where relevant in subsequent Sections. In general they reveal that pyrolysis at the heating rates used in the present investigation has little effect on the structure. Lignites display a slight shrinkage, with an increase in surface detail (Figures 4-11a and 4-11c), while biomass demonstrates even less change, with the structure of tissues in the raw fuels still visible after pyrolysis. Figures 4-11b and 4-11d illustrate the persistence of lignin-rich xylem tissues in olive kernels, before and after pyrolysis. This might be expected, as it is only with high heating rates (above 5000 K s^{-1}) that pyrolysis has been shown to cause considerable morphological changes as the char melts and boils [Cetin *et al.* 2004; Lorenz *et al.* 2000]. Oxidation has a greater effect and ash residues of lignites (Figure 4-11e) and biomass (Figure 4-11f) display a range of new textures resulting from various fusion, fluidity and recrystallisation processes.

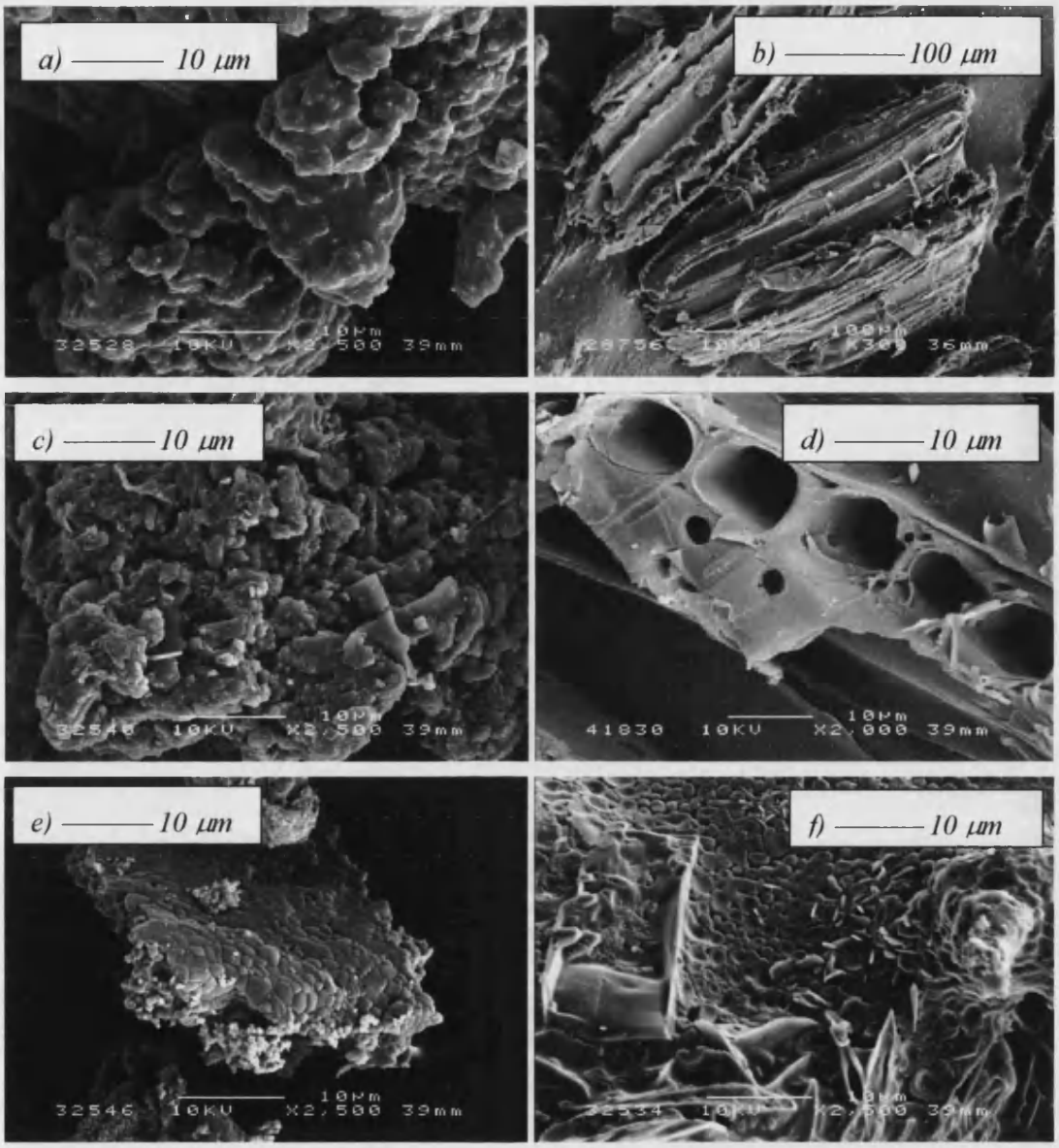

Figure 4-11: Scanning electron micrographs of (a) Ptolemais lignite as received, (b) Ptolemais lignite char, (c) Ptolemais lignite ash, (d) olive kernels as received, (e) olive kernel char (f) olive kernel ash

Chapter 5 Analysis and Discussion of Results

5.1 Introduction

The data produced by thermogravimetric analysis of the original and blended fuels are presented in Chapter 4; TG and dTG profiles were compared and initial observations made concerning their relative degrees of reactivity. The following Sections investigate the data more closely, using models first described in Section 2.5, and newly devised analytical approaches to better define the characteristics of the pure and blended fuels in terms of the reactions and interactions of the component parts. Section 5.2 considers the oxidation and pyrolysis of the principal biomass active components, and their blends. Sections 5.3 and 5.5 explain the use of global rule-of-mixtures models and more detailed deconvolution to predict the shape of the thermogravimetric profiles, and then observe differences. Section 5.4 uses SEM to observe the changes in the morphology of the char particles during oxidation. Section 5.6 uses deconvolution data to calculate the apparent kinetic parameters, describe the chemical reactions involved in the thermal degradation, and investigate how they change with the blend composition.

5.2 Thermal Analysis of Biomass Pseudo-Components

5.2.1 Introduction

This Section describes the thermal activity of blends of synthetic biomass components in pure and blended forms, under pyrolysing and oxidising conditions. The optimal conditions described previously had not been established, and comparatively large sample sizes were used without pre-drying. Nevertheless, the results serve well in illustrating the differences in reactivity of the various pseudo-components.

5.2.2 Oxidation and Pyrolysis of Cellulose

The pyrolysis and oxidation profiles of cellulose are given in Figures 5-1 and 5-2 (p. 92 and 93) respectively. Reactions between 550 and 650 K result in a loss of around 75 %wt. under both conditions, although activity is considerably larger during oxidation than pyrolysis (dTG_{max} = 3.7 and 1.9 %wt. K^{-1} respectively). This increase for the oxidising atmosphere may be driven by heat liberated during homogeneous oxidation, however it also supports suggestions by Seneca *et al.* [2002a; 2002b], where some pyrolysis-like reactions are prompted by mild oxidation. As a result, devolatilisation reactions occur around 20 K earlier in the oxidising atmosphere. Above this, there is no further activity for pyrolysis, while oxidation displays a second peak (T_{max} = 700 K) giving rise to a loss of around 10 %wt (Figure 5-2b).

The locations of these peaks and the effects of changing the atmosphere are comparable to those of the biomass samples observed in Chapter 4, indicating the appropriateness of describing biomass decomposition in terms of these components.

5.2.3 Oxidation and Pyrolysis of Lignin

Both pyrolysis and oxidation of lignin – dTG profiles of which are given in Figures 5-1e and 5-2f respectively – display a number of common features. Compared with

cellulose, activity in both conditions is considerably lower, dominated by a loss of around 25 %wt. between 500 and 700 K. The similarities of this activity for both conditions suggest devolatilisation occurs before heterogeneous oxidation. Profiles in Figures 5-1a and 5-2a also imply that activity between 700 and 900 K results in a greater weight loss through pyrolysis, than through oxidation.

The thermal activity of lignin is also unique above 900 K, when oxidation leads to a sudden loss of around 40 %wt., followed by a small gain of between 2 and 5 %wt. This appears to be an oxidative reaction as the pyrolysis profiles indicate only a slight weight loss process around 975 K. The convoluted oxidation dTG profile between 1000 and 1200 K here suggest several processes arise, with weight loss and weight gain effects. These reactions may involve fixed carbon, since even original lignin contains large amounts of aromatic carbon. Uptake of oxygen by aromatic moieties might be ruled out because the weight-gain processes (*i.e.* negative peaks in Figure 5-2) occur after the weight-loss processes. However, the method of lignin extraction may have introduced inorganic contaminants such as (K_2O or Ca) which are shown to be reactive in this temperature range (Section 2.4.6).

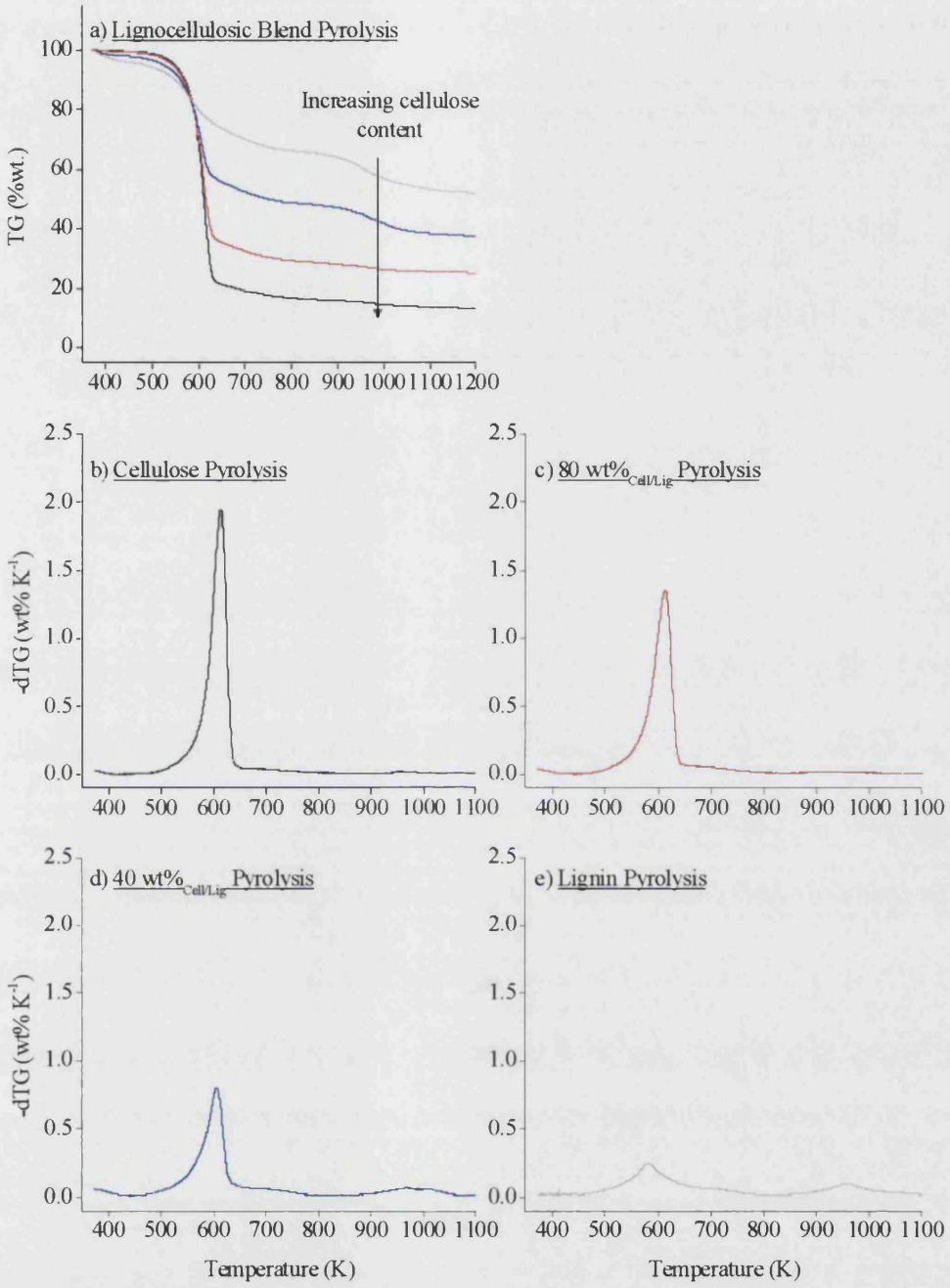

Figure 5-1: Pyrolysis of lignocellulose blends. (a) TG profiles; (b-e) dTG profiles for pure cellulose, blends of 80 and 40 %wt. cellulose in lignin and pure lignin. (β: 20 K min^{-1}; w_0: 25-30 mg; N_2 flow: 3 ml min^{-1})

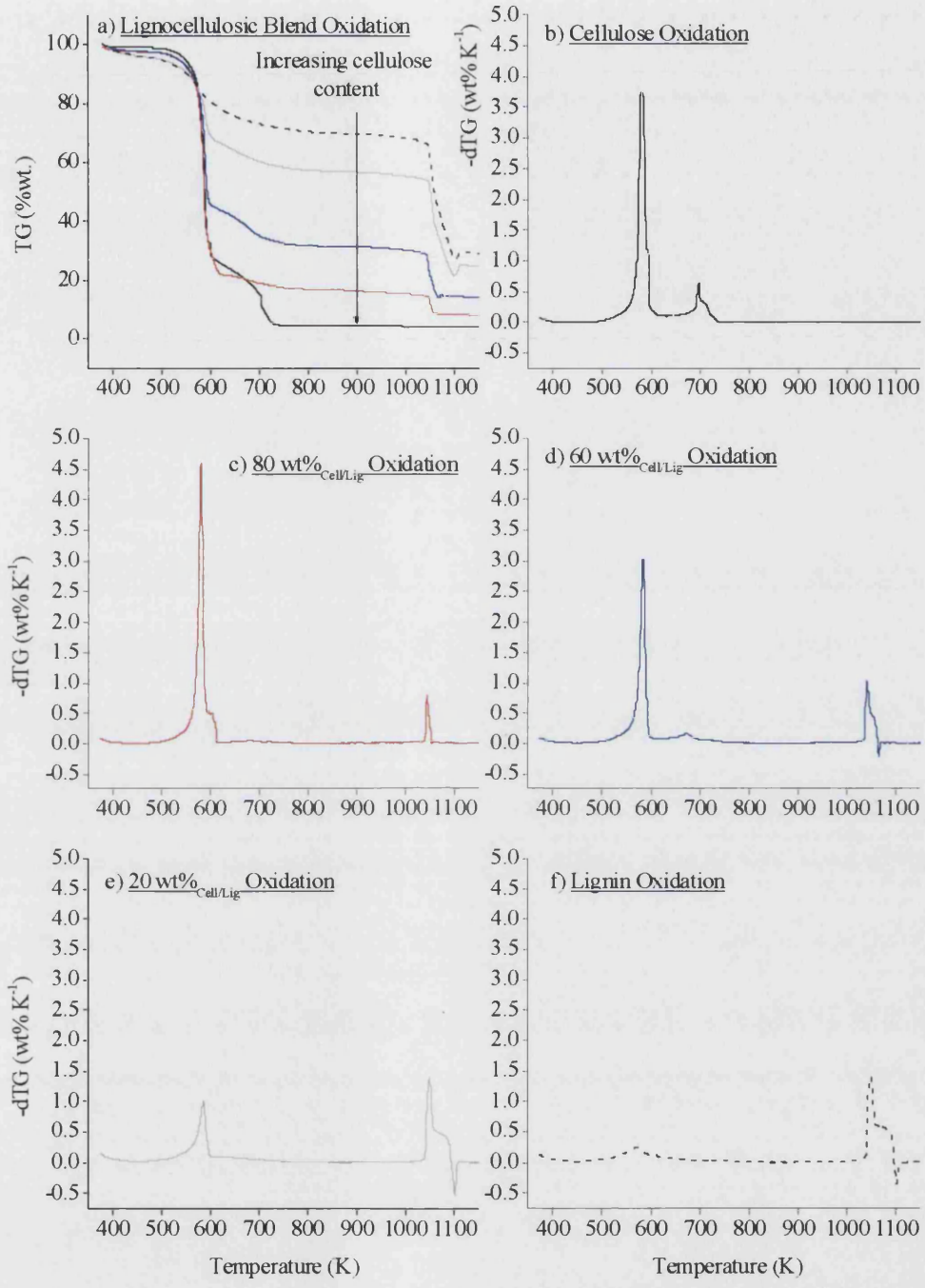

Figure 5-2: Oxidation of lignocellulose blends: (a) TG profiles; (b-e) dTG profiles for pure cellulose, blends of 80 and 40 %wt. cellulose in lignin and pure lignin. (β: 20 K min^{-1}; w_0: 25-30 mg; air flow: 3 ml min^{-1})

5.2.4 Oxidation and Pyrolysis of the Lignocellulose Blends

Profiles of dTG in Figures 5-1c to 5-1d, and 5-2c to 5-2e describe the pyrolysis and oxidation (respectively) of blends of cellulose and lignin. Typically, weight loss increases with the cellulose content, as char formation reactions (during pyrolysis) or ash yield (during oxidation) become less important. Char oxidation (Figure 5-1) reactions between 650 and 750 K also increases in peak activity (dTG_{max}) as the cellulose content increases.

5.2.5 Oxidation of Hemicellulose

Analysis of the hemicellulose monomers has revealed the effect of the chemical composition on thermogravimetric activity. Figure 5-3 illustrates the oxidation activity of arabinose, xylose and galactose. As with cellulose, oxidation activity is exclusively between 480 and 800 K, with a loss of nearly 100 %wt. indicating a negligible mineral content. Arabinose and xylose are geometric isomers, and consequently reveal almost identical TG and dTG profiles consisting of two peaks at 480 and 720 K, with further various activities in between. Dehydration involving labile hydroxyl groups (*e.g.* Figure 5-4a) would leave carbon double bonds. March [1992] describes an elimination reaction for allylic ethers (Figure 5-4b) occurring at 430 °C (~700 K) coinciding with peaks in activity in Figures 5-3b and 5-3c.

Galactose (Figure 5-3d) is a geometric isomer of glucose, of the cellulose monomer. But as a monomer, the activity of galactose also differs from cellulose (Figure 5-2b). Because of the additional CH_2OH, galactose also has a different profile to other hemicellulose compounds. This difference may explain the extra peak in activity at 550 K with the elimination of methanol (Figure 5-4c).

Higher temperature activity for galactose is also shifted to 790 K, compared with 720 K for galactose and arabinose. Possibly, the enol ether formed from galactose in Figure 5-4c represents a more stable intermediate to the open chain compounds produced from ring splitting reaction of arabinose and galactose in Figure 5-4b.

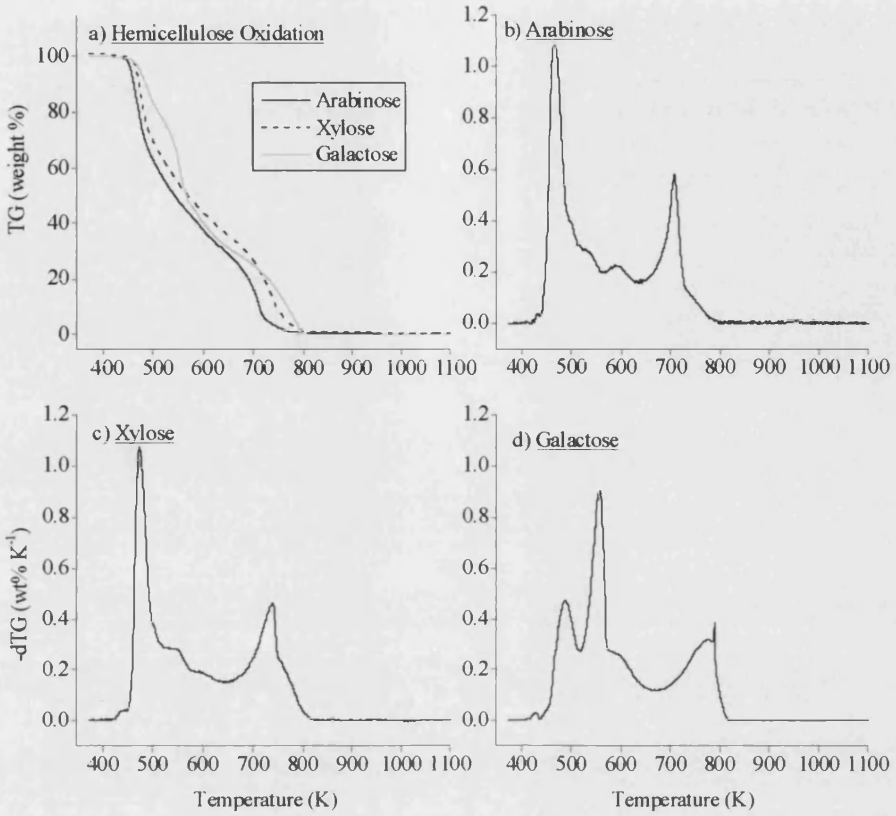

Figure 5-3: (a) TG and (b-d) dTG profiles for the oxidation of three hemicellulose compounds. (β: 20 K min^{-1}; w_0: 25-30 mg; air flow: 3 ml min^{-1})

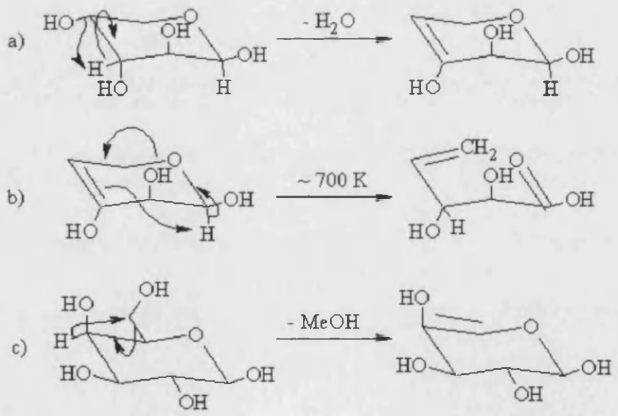

Figure 5-4: Suggested decomposition reactions for hemicellulose compounds: (a) Dehydration of arabinose, suggested as causing the dTG peak at 500 K; (b) Reaction for hemicellulosic compounds around 700 K, similar to a reaction for allylic ether groups given by March [1992]; (c) Methanol elimination, suggested to part of the activity of galactose

5.3 The Rule of Mixtures Model

5.3.1 Methodology

Initial attempts to predict the TG and dTG profiles of the pyrolysis and oxidation of blended fuels were based on the assumption of independent reaction pathways. This would produce an additive weight-loss profile, where features of the two fuels are in proportion to their mass fraction in the blend. There have been several instances of using this sort of model during the pyrolysis of biomass [Antal Jr. *et al.* 1995], binary coal blends [Peralta *et al.* 2002] and coal-biomass blends [Biagini *et al.* 2002; Vuthaluru 2004], however no known work compares the results of oxidation conditions.

The rule of mixtures model uses Equation 2-47, introduced in Section 2.5.6. Here α represents fraction of conversion (it may be replaced with a dTG value) at temperature T for the blend, biomass or lignite as per subscript; and b is the weight fraction of biomass in the blend.

Equation 2-47: $$\alpha_{Blend,T} = b.\alpha_{Biomass,T} + (1-b).\alpha_{Lignite,T}$$

This model arises regularly in materials science, where the physical properties of mixtures, solutions or composites are predicted from the ratio of the properties of the components.

5.3.2 Rule of Mixture Model for Pyrolysis

Profiles for the pyrolysis of the olive kernels-Ptolemais lignite blends are given in Figure 5-5 (p. 99), while profiles for the pyrolysis of forest residue blends are given in Figure 5-6 (p. 100). They both demonstrate a good match between calculated and experimental profiles, indicating overall activity is additive of the original fuels. Standard error values of the TG profiles 0.73 %wt. for olive kernel blends and 1.03 %wt. for the forest residue blends, indicating olive kernel blends to be a better fit to the model, however all these values fall within the sample variability ranges observed in Section 4.2. The deviation for forest residue indicates an underestimation of the rate

before 630 K and an overestimation after 630 K, most apparent for the 20 $\%wt._{FR/PL}$ blend. One possibility is that the difficulty of producing a homogeneous forest residue blend (linked in Section 3.2.5 to the fibrous nature of forest residue particles) results in an excess of lignite in the crucible. This excess would reduce the weight-loss at low temperatures, and increase weight-loss at high temperatures. Such an error might be avoided in future by weighing the sample components directly into the crucible.

On this basis, olive kernels appear to have been accurately measured; however, there remains a small discrepancy between 600 and 950 K, where the more weight is lost from the blends than predicted (Figure 5-5a). At 950 K, a reaction of pure lignite is absent from the experimental profiles and consequentially the deviation between profiles disappears. Figures 5-5b to 5-5e show that the rate of pyrolysis of the olive kernel blends is higher than predicted between 400 and 600 K, offsetting two overestimations in activity around 650 and 980 K and by 1000 K resulting in similar TG profiles.

5.3.3 Rule of Mixture Model for Oxidation

The oxidation of the olive kernel-Ptolemais lignite blend, modelled using the rule-of mixtures method is illustrated by Figure 5-7 while TG and dTG profiles for the forest residue-Ptolemais lignite blends are given in Figure 5-8. Root mean squared error values of the TG profiles of 2.07 %wt. for olive kernel blends and 1.96 %wt. for forest residue blends firstly indicate forest residue blends to be a marginally better fit, but also highlights the poorer fit of the model to oxidation experimental data when compared with pyrolysis. Onset and burnout temperatures are accurately predicted, as is the shape of the initial peak (T_{max} = 580 K), associated below with the pyrolytic activity of biomass. Between 650 and 800 K however, the model and experimental profiles vary considerably. There is an underestimation of the maxima for lignite activity (T_{max} = 650 K), accompanied by significant narrowing of the peak. The higher temperature biomass reaction (T_{max} = 720 K in Figure 4-3, p. 77) is shifted to 750 K and becomes more pronounced for blends of lower biomass content (*i.e.* Figures 5-7d and 5-7e p. 101).

Reactions of pure lignite around T_{max} = 950 K are also absent from the experimental profiles from the blends.

The effect is that while weight loss is underestimated before 700 K (*e.g.* Figure 5-7a), weight loss is overestimated after 700 K, culminating in an underestimation of the residual ash yield. This weight deviation increases with lignite content, up to 6.1 %wt. for olive kernel blends and 8.1 %wt. for the forest residue blends. The extra residual weight, plus the absence of the lignite reaction at 950 K, may relate to the ash composition of the two samples. Biomass contains elevated concentrations of calcium carbonate ($CaCO_3$) implied by the levels of lime (CaO), in Table 3-1, (p. 56). Calcium carbonate undergoes calcination at 950 K (Equation 5-1). Calcium has also been shown to catalyse char oxidation reactions, and is likely to be responsible for increasing the overall rate of all oxidation profiles [Zhang *et al.* 2003].

Equation 5-1: $$CaCO_{3(s)} \Leftrightarrow CaO_{(s)} + CO_{2(g)}$$

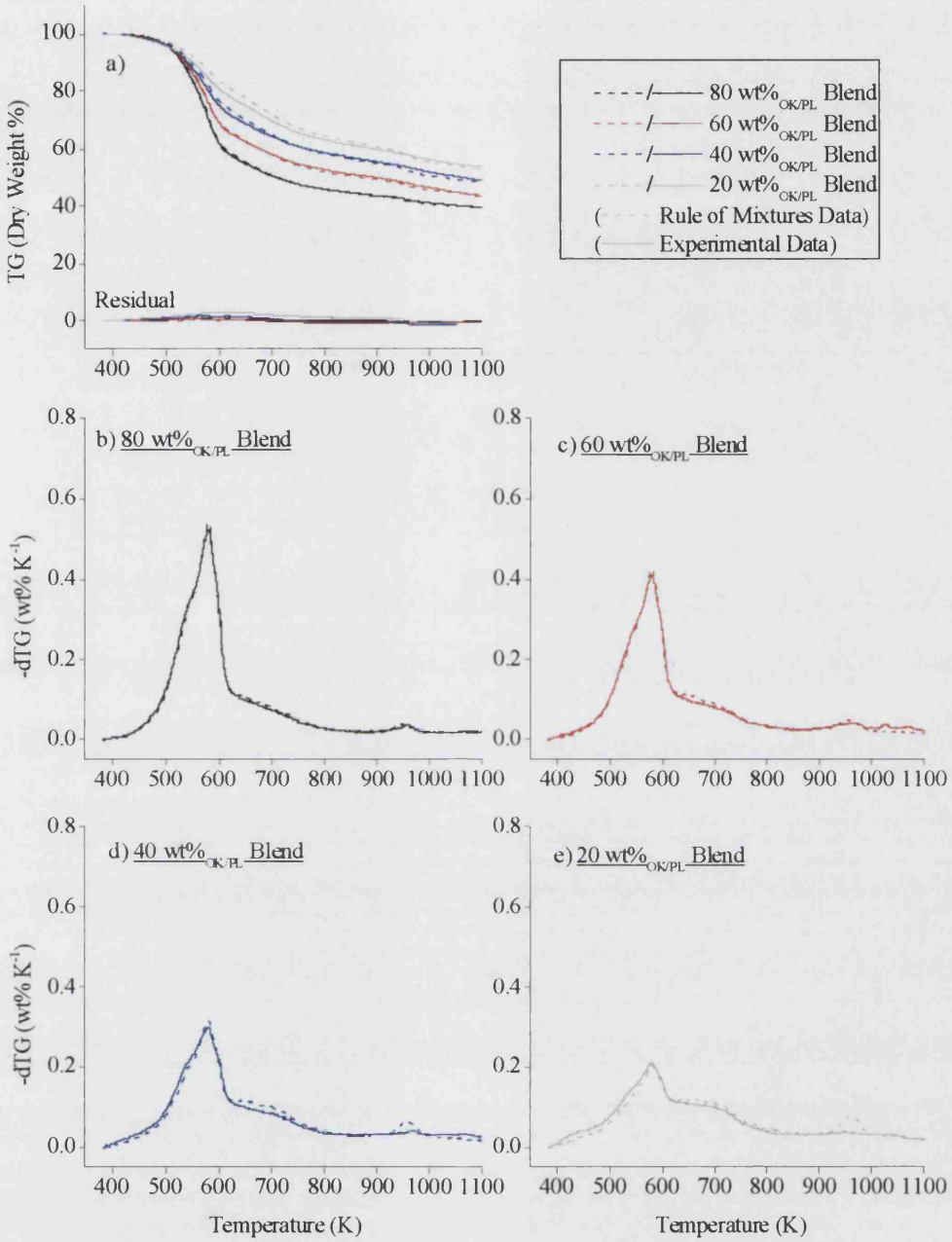

Figure 5-5: Comparison of experimental data and rule of mixtures model data for the pyrolysis of olive kernels in Ptolemais lignite. (a) Thermogravimetric profiles with residual data. (b-e) Derivative thermogravimetric profiles. (β: 10 K min^{-1}; w_0: 5-10 mg; N_2 flow: 3 ml min^{-1})

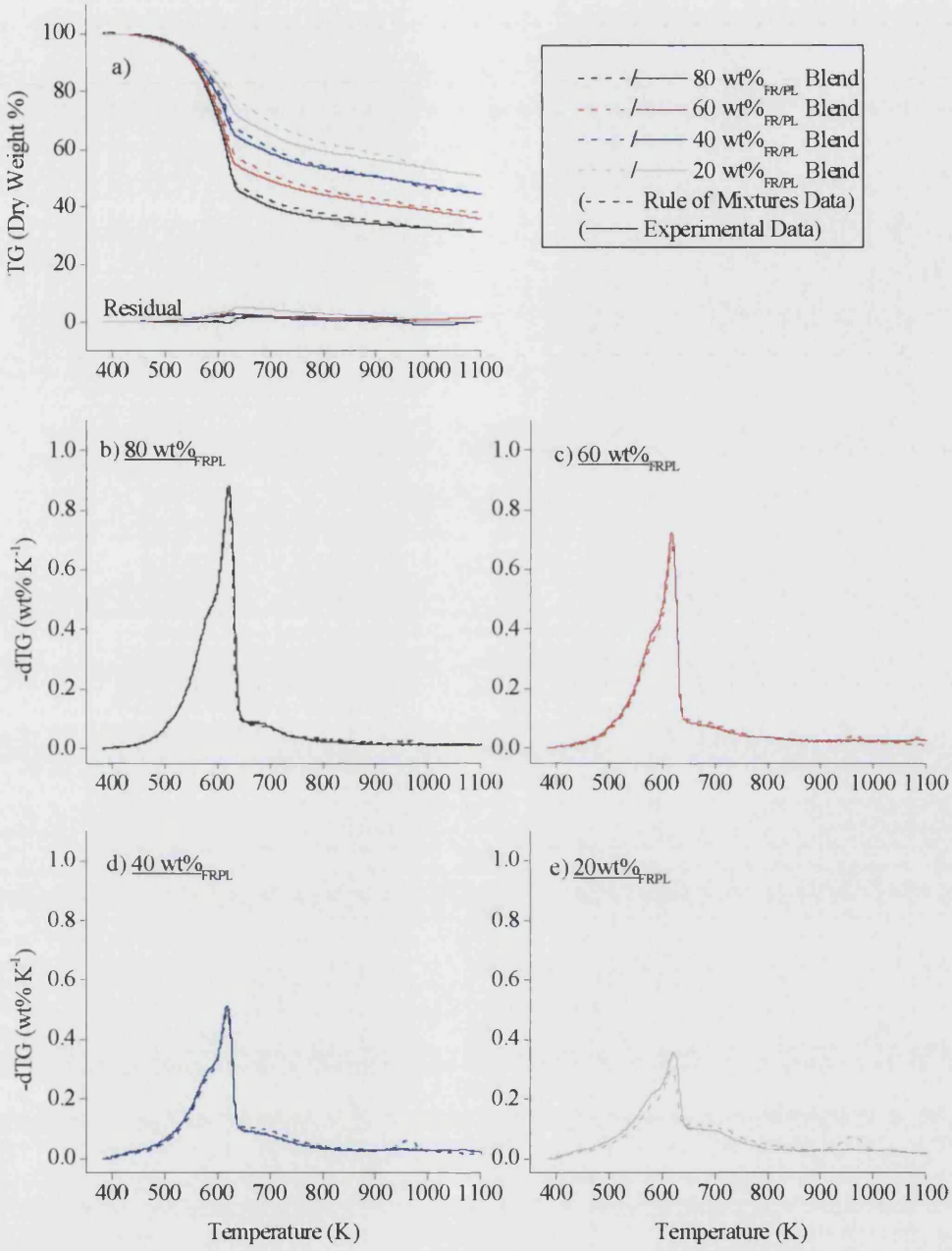

Figure 5-6: Comparison of experimental data and rule of mixtures model data for the pyrolysis of forest residues in Ptolemais lignite. (β: 10 K min^{-1}; w_0: 5-10 mg; N_2 flow: 3 ml min^{-1})

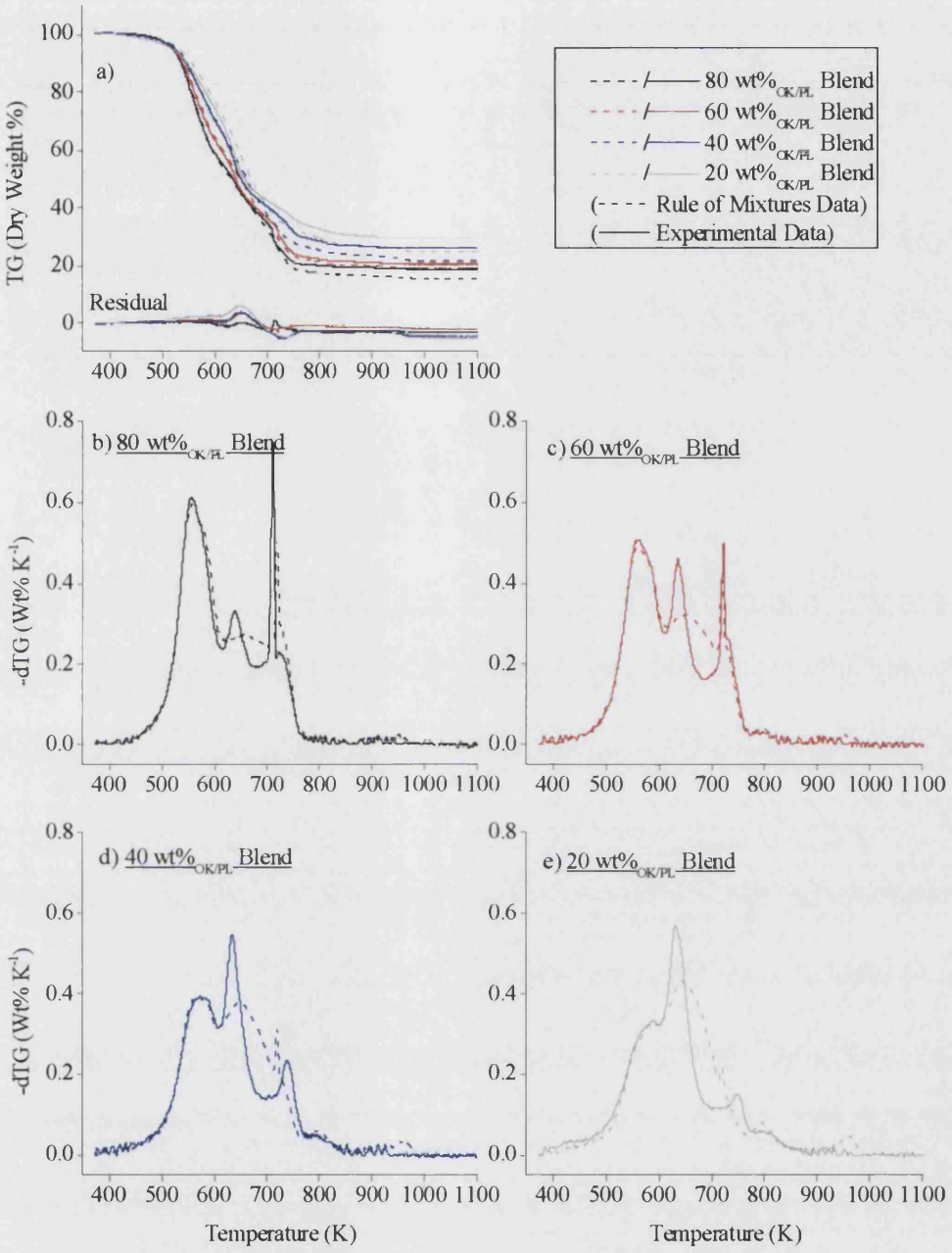

Figure 5-7: Comparison of experimental data and rule of mixtures model data for the oxidation of olive kernels in Ptolemais lignite. (a) Thermogravimetric profiles with residual data. (b - e) Derivative thermogravimetric profiles. (β: 10 K min^{-1}; w_0: 5-10 mg; air flow: 3 ml min^{-1})

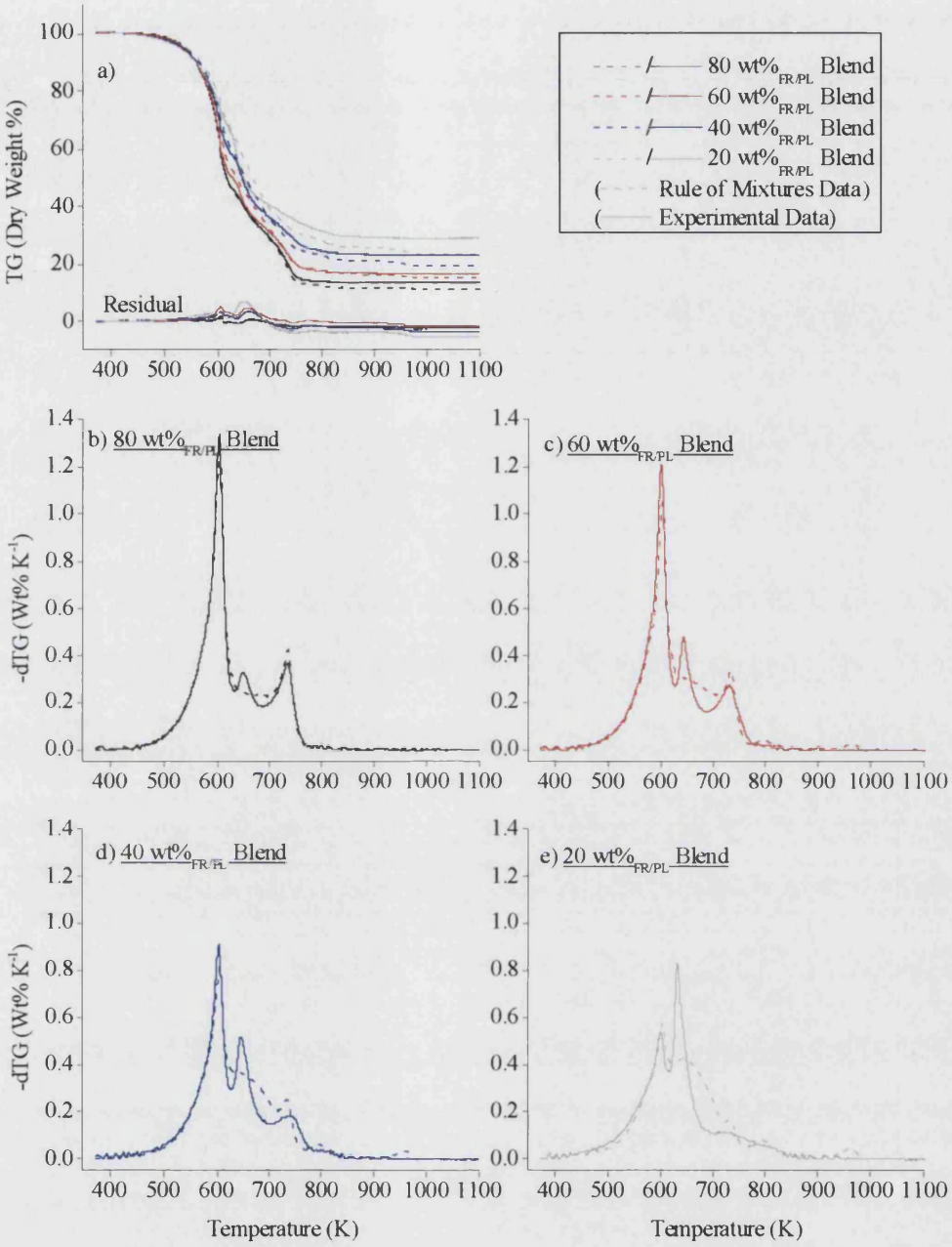

Figure 5-8: Comparison of experimental data and rule of mixtures model data for the oxidation of forest residues in Ptolemais lignite. (β: 10 K min^{-1}; w_0: 5-10 mg; air flow: 3 ml min^{-1})

5.4 SEM Analysis of Partially Oxidised Blends

The difference between model and experimental profiles of oxidation experiments prompted analysis of the sample surface using scanning electron microscopy. Figure 5-9 displays representative images of the stages of oxidation of the 20 %wt.$_{OK/PL}$ blend, with samples produced by heating in air in the TGA at 20 K min^{-1} to 542, 610, 720 and 741 K, attaining samples of 75, 50, 30 and 27 %wt. respectively.

Particle structures comparable to the original samples (Figures 5-9a and 5-9b) are observed in the 75 %wt. sample (Figure 5-9c) however in the 50 %wt. sample, many particles appeared to be stuck together, and a representative image is shown in Figure 5-9d. The 30 and 27 %wt. samples display particles with assorted textures (Figures 5-9e and 5-9f), and as observed for the pure materials, no features distinctive of their origin. The sticking may be due to a softening of the ash although even biomass-borne ash usually has a higher melting point. Nevertheless, it coincides with the significant deviation in weight-loss observed for the rule-of-mixtures model (Section 5.3.3). While it is not conclusive, this coincidence might allude to the mechanisms during blend oxidation (described in Figure 5-10):

1. < 550 K: Particles decompose separately, with the minor deviation from the ROM model a consequence of volatile-char interaction;

1. 550 – 700 K: Additional weight-loss occurs when close particle contact increases the opportunity for solid-solid interactions;

2. 700 K: The two fuel types become increasingly agglomerated, with further oxidation of fixed carbon, net weight-loss is however less than the model predicts, due to capture of emissions (*e.g.* SO_2) by the ash

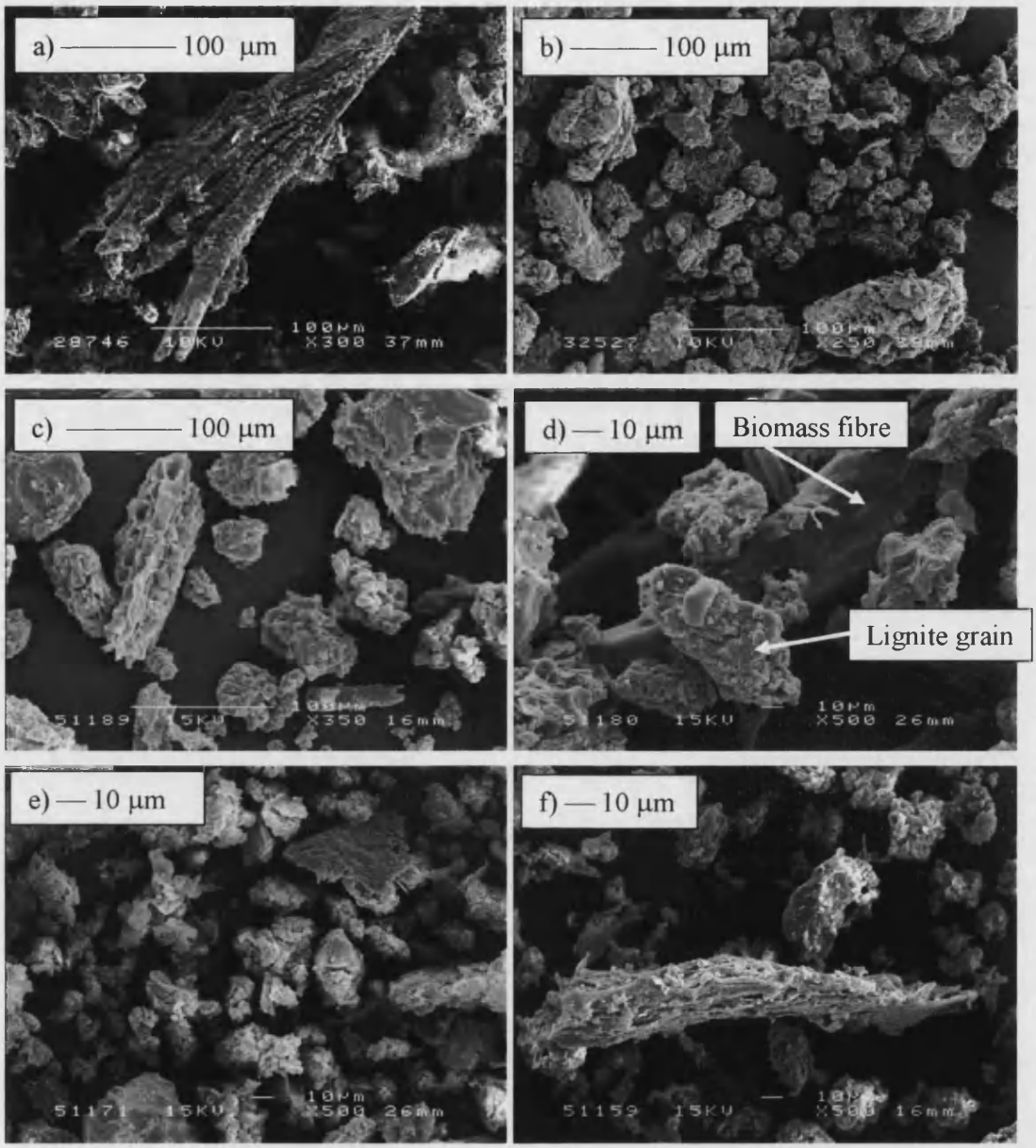

Figure 5-9: Back-scattered electron images from SEM analysis of (a) original olive kernels, (b) original Ptolemais lignite, and (c-f) products of partial oxidation of the 20 %wt.$_{OK/PL}$ blend to 75, 50, 30 and 27 % weight respectively

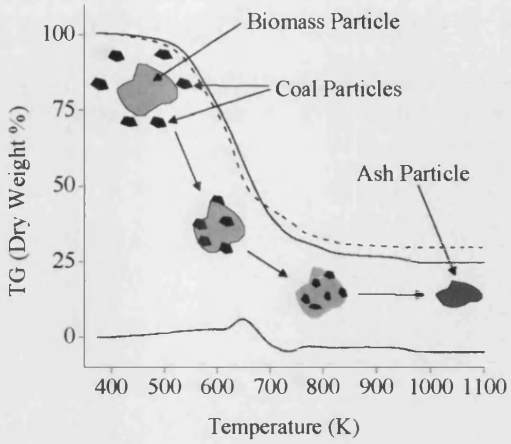

Figure 5-10: Oxidation sequence suggested by rule-of mixtures model and particle interactions observed by SEM for the 20 %wt.$_{OK/PL}$ blend TG oxidation profile. (β: 10 K min^{-1}; w_0: 5-10 mg; air flow: 3 ml min^{-1})

5.5 Deconvolution of the Derivative Thermogravimetric Data

5.5.1 Methodology

Deconvolution methods were introduced in Section 2.5.5. However, a few additional words about the methodology used in the present investigation are required.

It has been established with the rule-of-mixtures model (Section 5.3) that while the pyrolysis profile of a fuel blend is equal to the weighted sum of its component fuels, when a blend is oxidised, changes occur in the fuels intrinsic reactions that prevent the profile being predicted in the same way. This Section uses deconvolution of the dTG profiles to separate these intrinsic reactions, firstly so that changes in T_{max} and weight-loss contributions of each reaction can be observed; but more importantly to provide TG data from which the kinetic parameters of individual reactions may be calculated (Section 5.6).

Derivative thermogravimetric data in terms of dTG/dT (%wt. K^{-1}) was used so that when dTG was plotted against temperature, the area under the curve gave a sample

weight percentage. Deconvolution was carried out using the comprehensive plotting and data-analysis software, Origin 7.0. The procedure involved importing the data, heuristically initialising T_{max} points and the number of peaks, and then allowing the software to optimise peak parameters by least squares fitting, using the Levenburg-Marquard method of chi-square reduction.

As described, Lorentz and Gaussian curves have been mentioned in literature as options in deconvolution of dTG data. Figure 5-11a compares the peak shapes of the profiles, defined by Equation 5-2 for Lorentz profiles and Equation 5-3 for Gaussian profiles. Figure 5-11a demonstrates how with the same parameters, the extremes of the Lorentz profile extend beyond the range of the Gaussian profile. The parameters of peak area (percentage weight-loss contribution, γ), peak width (ω, a function of the peaks full width at half peak maximum, FWHM), and the modal temperature (T_{max}) are described in Figure 5-12. The baseline dTG value (dTG_0) is redundant in the present investigations as baseline activity is zero. Gaussian profiles consistently gave a better fit to the reaction profiles, as indicated by the smaller standard error values given in Figure 5-11. Analogous parameter errors for the Lorentz profile were 20 to 80 percent larger. The Lorentzian profile gave the least satisfactory fit for smaller peaks (Figure 5-11e). This is in agreement with published deconvolution work (*e.g.* [Li *et al.* 2005]) where Gaussian peaks are used. Kinetic analysis of cellulose pyrolysis was also improved when narrower peak models were used. Conesa *et al.* [2001] advises the nucleation law in preference of the first-order rate law in the calculation of kinetic parameters for this reason.

Equation 5-2:
$$dTG = dTG_0 + \left[2\gamma/\pi\right]\left[FWHM/4(T - T_{max})^2 + (FWHM)^2\right]$$

Equation 5-3:
$$dTG = dTG_0 + \left[\gamma/\left(\omega\sqrt{\pi/2}\right)\right].Exp\left[-2(T - T_{max})^2/\omega^2\right]$$

The results of Gaussian deconvolution of the oxidation and pyrolysis profiles for all blends are given in Sections 5.5.2 and 5.5.3.

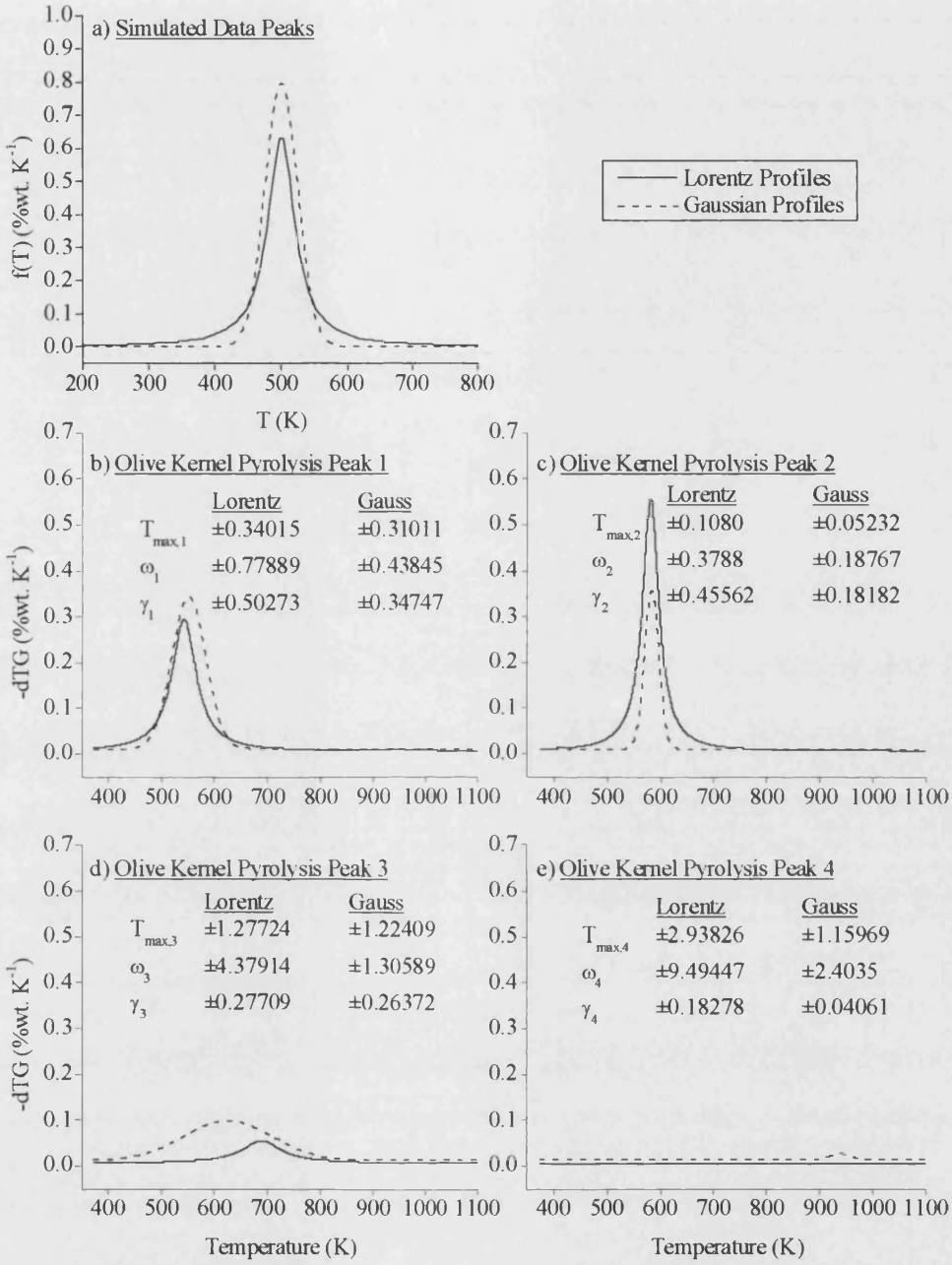

Figure 5-11: Comparison of Lorentz and Gaussian profiles for dTG data. (a) Using peak parameters of T_{max}=500 K, γ=50 %wt. and FWHM=20 K. (b-e) Deconvolution of olive kernel pyrolysis profiles using four peaks, giving the standard error margins of each parameter

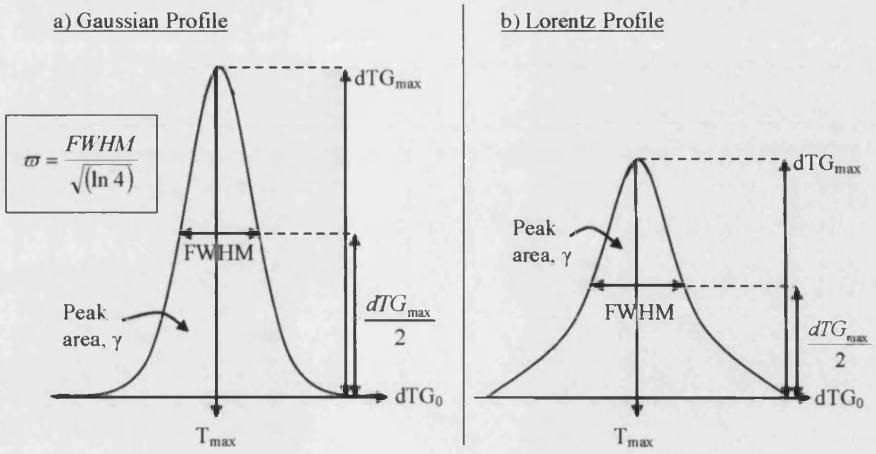

Figure 5-12: Peak parameter definitions for (a) Gaussian and (b) Lorentz Profiles as used in the present investigation

5.5.2 Deconvolution of the Pyrolysis Profiles

Pyrolysis profiles are generally more straightforward than the oxidation profiles (Section 5.5.3), with fewer reaction peaks and less ambiguous relationships between reactions for the blends and pure fuels. The deconvolution of the profiles of olive kernels and Ptolemais lignite (Figures 5-13a and 5-13f respectively) identify the differences during the devolatilisation of the two fuel types. Biomasses display two (olive kernels) or three (forest residue, Figure 5-14a) peaks between 500 and 650 K, followed by a low activity process peak extending to 800 K. This latter peak covers a similar temperature range to the main peak of lignite, which is in turn superimposed over extremely low activity extending beyond 1100 K. The final process peak of lignite (T_{max} = 960 K) is analogous to a process peak of olive kernels.

Deconvolution of the profiles from pyrolysis of the blends required four or five peaks. Figures 5-13b to 5-13e give the results of deconvolution of the olive kernel-Ptolemais lignite blends. They indicate two peaks between 500 and 650 K, matching peaks of pure olive kernels (Figure 5-13a). Forest residue blends (Figures 5-14b to 5-14e) also display peaks in this temperature range, similar to the pure forest residue (Figure 5-14a). Remaining activity of the olive kernel blends, involves two peaks in activity at 650 and 1000 K respectively.

Parameters of the isolated reaction peaks for pyrolysis, along with their standard errors are given in Table 5-1 (p.116; also illustrated on page 131). Standard error margins are between 0.01 and 1 % for T_{max} values, between 1 and 19 % for weight-loss contributions, and between 0.3 and 8 % for the peak width parameter. Error in the parameters may be linked with the unsuitability of the Gaussian profile, for example if the dTG profile of a reaction was asymmetrical. However, as determined in Section 3.3.2, the error margin of the TGA instrument amounts to ± 1.8 %wt. While only a few reaction peaks exhibit an area below this value (e.g. Peak 4 of the olive kernels), it makes up a significant part of the area for a number of other peaks (e.g. Peaks 2 and 4 of the OK/PL blends. This may indicate times where peak area is not an accurate indicator of a reactions contribution to sample weight loss.

5.5.3 Deconvolution of the Oxidation Profiles

Four peaks best fitted the oxidation data of olive kernel and forest residue (Figures 5-15a and 5-16a respectively) and both biomass samples display peaks at 590 K, a broad reaction at 680 K and a smaller peak at 730 K. However, while forest residue exhibits two peaks around 600 K, olive kernels exhibit two peaks around 720 K. Deconvolution of the oxidation profile of lignite is illustrated in Figure 5-15f. Ptolemais lignite displays four reaction peaks with T_{max} values of 600, 675, 800 and 900 K. Figures 5-15b to 5-15e give the deconvoluted profiles of the olive kernel-Ptolemais lignite blends during oxidation, and reveal the decompositions involve four or five reaction peaks, only some of these however are recognisable as belonging to either of the pure fuels.

Table 5-2 (p.117) compares the peak parameters and standard error values for deconvolution of the oxidation profiles. The error margins are mostly narrower than for pyrolysis, with a few exceptions. Errors vary from zero to 0.4 % for T_{max}, 0.5 to 8.0 % for weight-loss contribution, with the exception of a reaction in the 40 $\%wt._{FR/PL}$ blend; and 0.5 to 4.0 % for the activity range, with the exception of two of the forest residue blends. As with the pyrolysis reactions, a number of oxidation peaks exhibit an area below that of the instrumental accuracy for sample weight determination (1.8 %wt.;

Section 3.3.2). This includes a number of the higher temperature reactions isolated from the profiles of Ptolemais lignite and its blends, where peaks areas fall between 0.4 and 2 %wt. The implication is that these may be spurious weight loss events; however, their reproducibility (Section 4.2) indicates that they are accurately portrayed.

The high peak for forest residues around 600 K (Figure 5-16a) is characteristic of the cellulose and hemicellulose components undergoing pyrolysis (Section 5.2). The relative peak sizes indicate forest residues contain a larger quantity of these compounds than olive kernels (Figure 5-15a). The peak of olive kernels around 720 K is typical of decomposition of hemicellulose at higher temperatures. Extensive devolatilisation from these biomass carbohydrates, may explain why the oxidation reactions around 600 and 675 K feature similar T_{max} values as the lignite, but narrower peaks and higher activities (dTG_{max}) in the blends than in the pure Ptolemais lignite. The effect of volatile materials inhibiting char oxidation is discussed in Sections 2.4.2 and 2.4.3. This change is also observed in the forest residue blends (Figure 5-16 p.115). From deconvolution alone, it is not clear which lignite reaction has been affected, but if volatile material are obstructing the flow of oxygen, it is possible the char also undergoes carbonisation-type reactions in the reducing atmosphere.

Oxidation reactions once the devolatilisation subsides (*e.g.* the 600 and 675 K peaks of Ptolemais lignite, Figure 5-15f) are likely to involve different active sites undergoing competition between complete and incomplete oxidation reactions of char carbon, Equation 2-10 and Equation 2-11 respectively (p. 29) [Hayhurst 1998; Li 2001]. These reactions are shown to have activation energies of 405.1 kJ mol^{-1} and 123.1 kJ mol^{-1} respectively.

The balance between the modes of oxidation is dependent on a number of factors. Hayhurst *et al.* [1998] look at the effects of temperature and suggest that Reaction 2-10 dominates oxidation up to 1000 K. However, the surface chemistry and morphology of the char are also important. The presence of labile or peripheral carbon (*i.e.* reactive function groups or carbon at the edge of a graphite sheets) increases the quantity of carbon removed by Reaction 2-11, while the availability of oxygen, in pores for example, will limit Reaction 2-10.

These differences are also likely to account for differences in biomass activity. SEM analysis reveals the morphology of biomass and lignite to be considerably different, with a large occurrence of pits, cracks and pores in the biomass, compared with the more compacted lignite (Section 4.5). Furthermore, the greatly reduced aromatic carbon content of biomass compared with lignite (Sections 2.3.3 and 2.3.4) will reactivity during heterogeneous oxidation.

These higher temperature oxidation peaks change with biomass content, depending on which fuel each reaction originates. Where olive kernels are the majority fuel (*i.e.* profiles in Figures 5-15b and 5-15c), an additional peak around 700 K is similar to the activity of hemicellulose (Section 2.4.9), while the area of peaks around 650 K increase with lignite content. However, the changes of other peaks are more subtle, such the very broad peaks of the olive kernel blends, with T_{max} values of 610 K. Subsequent Sections will resolve these subtleties, and establish correlations between the pure and blended fuel peaks.

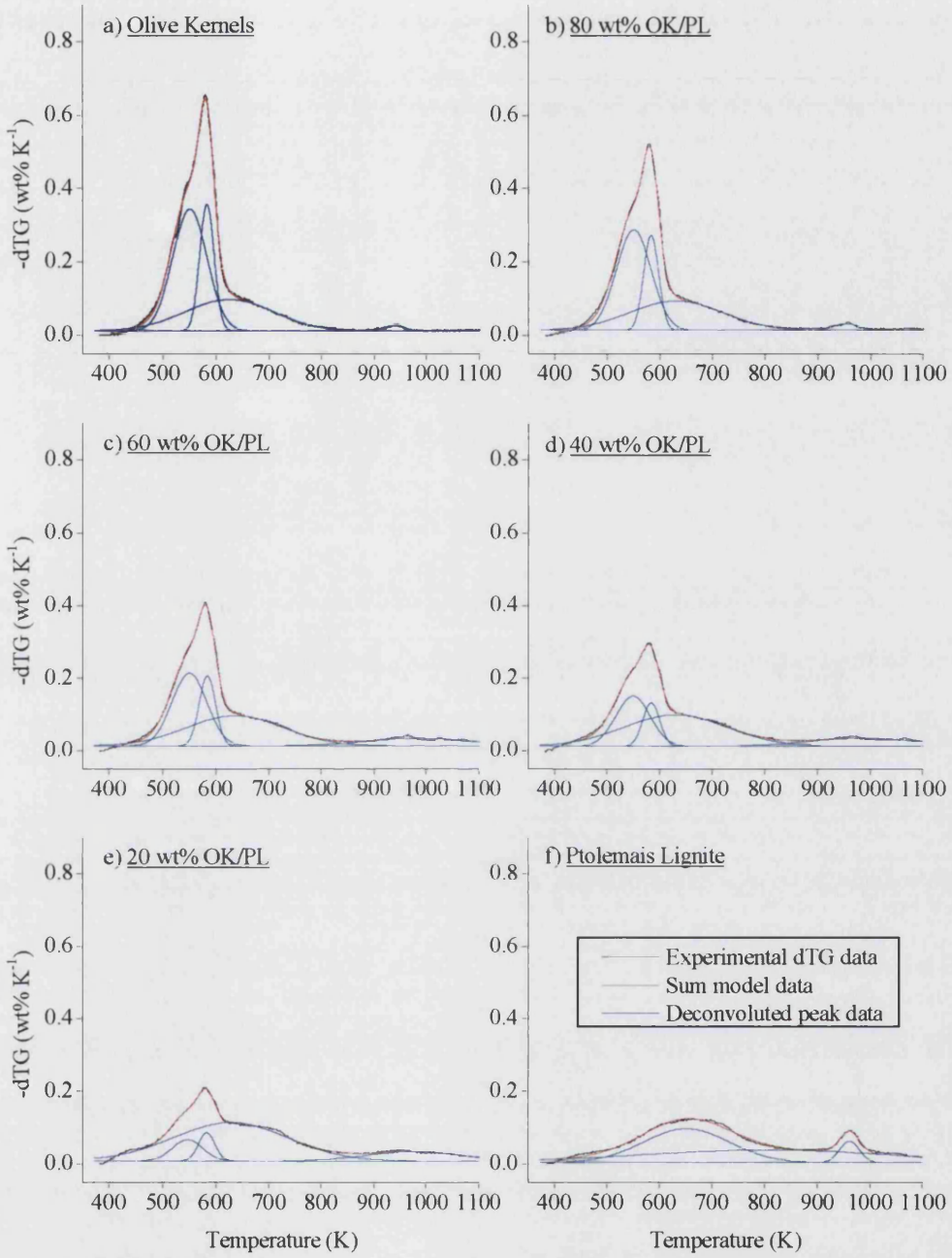

Figure 5-13: Gaussian deconvolution of the pyrolysis dTG profiles of olive kernel and Ptolemais lignite blends and pure fuels using multiple peaks. (β: 10 K min^{-1}; w_0: 5-10 mg; N_2 flow: 3 ml min^{-1})

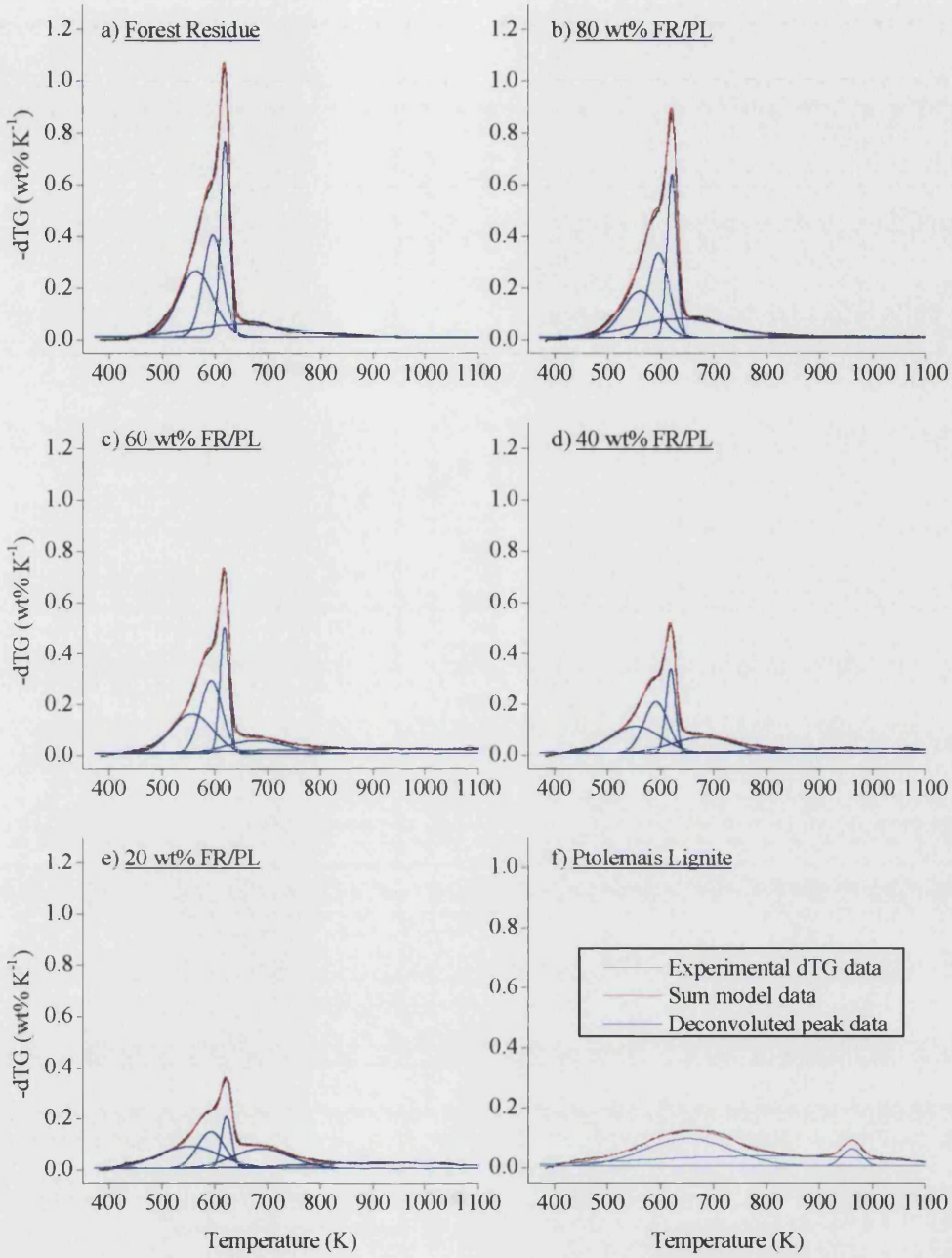

Figure 5-14: Gaussian deconvolution of the forest residue/Ptolemais lignite blend dTG pyrolysis profiles using multiple peaks. (β: 10 K min^{-1}; w_0: 5-10 mg; N_2 flow: 3 ml min^{-1})

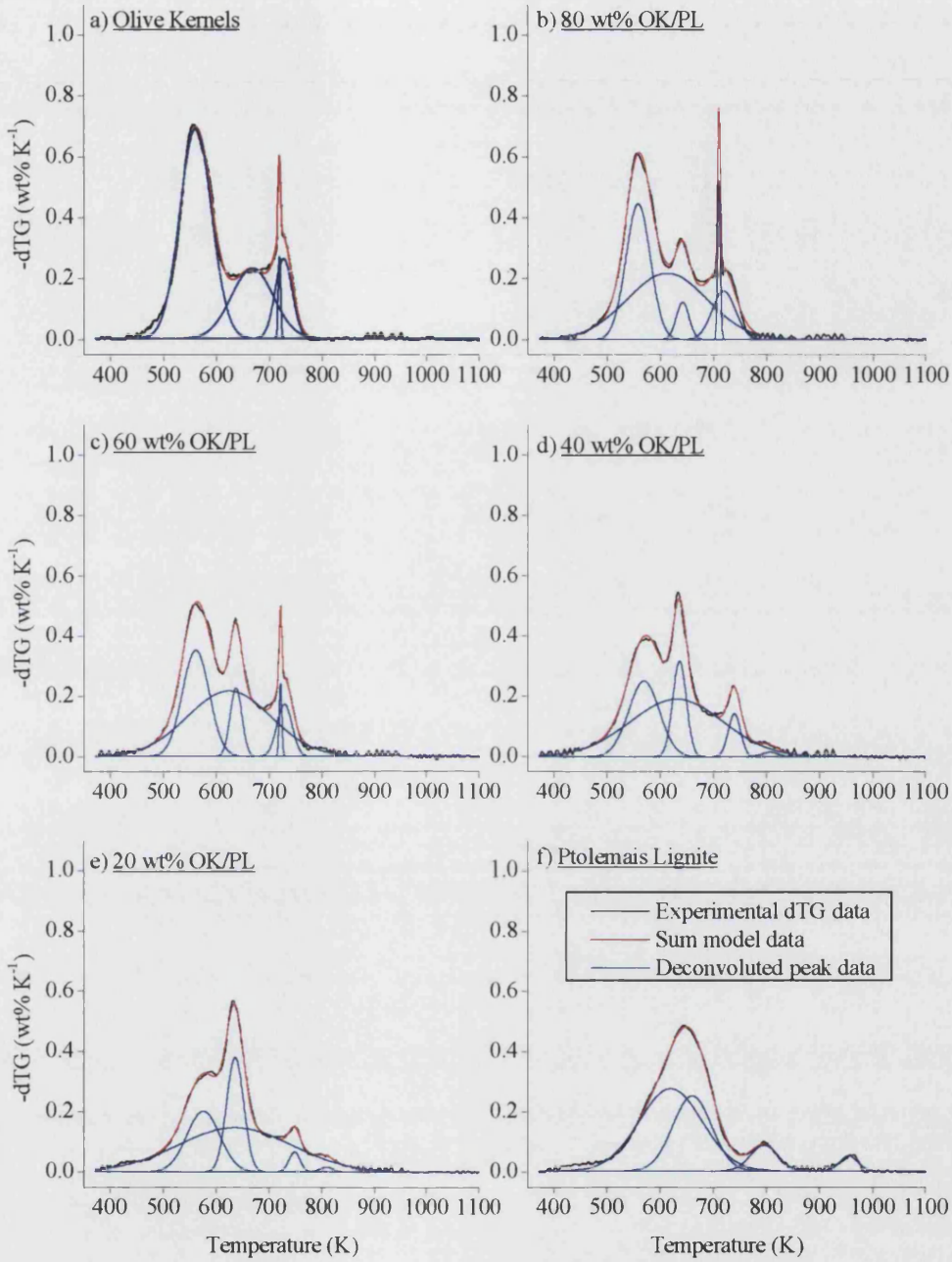

Figure 5-15: Gaussian deconvolution of the oxidation dTG profiles of olive kernel and Ptolemais lignite blends and pure fuels using multiple peaks (β: 10 K min^{-1}; w_0: 5-10 mg; air flow: 3 ml min^{-1})

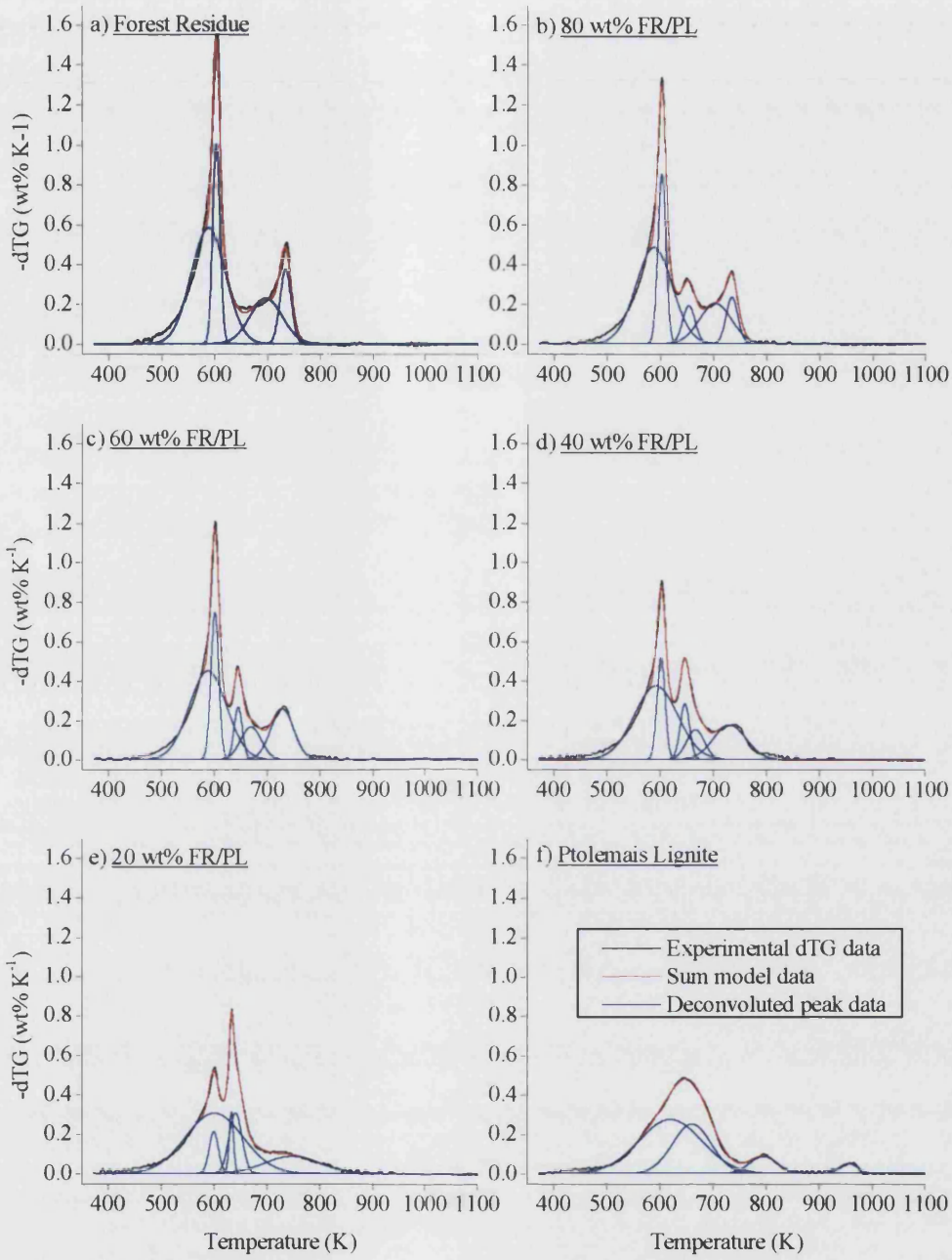

Figure 5-16: Gaussian deconvolution of the forest residue/Ptolemais lignite blend dTG oxidation profiles with multiple peaks (β: 10 K min^{-1}; w_0: 5-10 mg; air flow: 3 ml min^{-1})

Table 5-1: Pyrolysis peak parameters. Standard errors (Equation 4-1, p.67) in brackets

Sample	Peak 1	Peak 2	Peak 3	Peak 4
T_{max} (K)				
OK	550.57 (±0.31)	582.64 (±0.05)	624.91 (±1.22)	937.98 (±1.16)
FR	563.18 (±3.59)	596.21 (±0.53)	619.04 (±0.04)	651.24 (±4.54)
PL	651.55 (±0.39)	802.4 (±2.87)	961.3 (±0.21)	-
20 %wt.$_{OK/PL}$	547.05 (±1.99)	582.73 (±0.29)	628.36 (±0.54)	977.12 (±1.15)
40 %wt.$_{OK/PL}$	549.55 (±0.83)	584.11 (±0.13)	630.57 (±0.88)	985.78 (±1.41)
60 %wt.$_{OK/PL}$	550 (±0.55)	583.66 (±0.08)	635.64 (±1.09)	985.4 (±1.51)
80 %wt.$_{OK/PL}$	550.38 (±0.37)	583.39 (±0.07)	631.08 (±1.21)	953.73 (±0.95)
20 %wt.$_{FR/PL}$	551.14 (±5.68)	592.6 (±0.51)	621.99 (±0.05)	688.35 (±2.78)
40 %wt.$_{FR/PL}$	552.71 (±5.48)	591.37 (±0.46)	618.98 (±0.04)	681.5 (±4.16)
60 %wt.$_{FR/PL}$	556.37 (±4.54)	592.9 (±0.43)	617.87 (±0.03)	678.76 (±4.12)
80 %wt.$_{FR/PL}$	560.83 (±5.65)	595.88 (±0.42)	637.81 (±3.12)	621.09 (±0.04)
Weight-loss Contribution, γ (%wt.)				
OK	26.82 (±0.35)	11.74 (±0.18)	18.02 (±0.26)	0.73 (±0.04)
FR	20.98 (±2.5)	18.62 (±2.59)	16.35 (±0.49)	11.05 (±0.49)
PL	18.86 (±0.19)	20.72 (±0.66)	2.73 (±0.03)	-
20 %wt.$_{OK/PL}$	4.02 (±0.29)	2.89 (±0.24)	28.18 (±0.14)	5.7 (±0.1)
40 %wt.$_{OK/PL}$	11.28 (±0.33)	4.83 (±0.23)	21.45 (±0.19)	5.98 (±0.13)
60 %wt.$_{OK/PL}$	16.36 (±0.34)	7.38 (±0.21)	18.94 (±0.23)	4.96 (±0.12)
80 %wt.$_{OK/PL}$	22.62 (±0.33)	9.24 (±0.19)	18 (±0.24)	1.17 (±0.04)
20 %wt.$_{FR/PL}$	12.26 (±1.18)	9.13 (±0.69)	4.83 (±0.11)	10.21 (±0.64)
40 %wt.$_{FR/PL}$	12.55 (±0.52)	11.68 (±1.01)	7.49 (±0.16)	9.4 (±0.75)
60 %wt.$_{FR/PL}$	15.32 (±1.84)	15.13 (±1.6)	10.59 (±0.24)	7.25 (±0.48)
80 %wt.$_{FR/PL}$	14.63 (±2.76)	16.21 (±2.73)	15.71 (±0.47)	14.31 (±0.4)
Activity Range, ω (K)				
OK	64.37 (±0.44)	27.15 (±0.19)	166.57 (±1.31)	40.09 (±2.4)
FR	65.66 (±3.08)	37.75 (±1.89)	17.23 (±0.18)	185.62 (±4.17)
PL	162.52 (±0.98)	485.88 (±9.18)	37.36 (±0.45)	-
20 %wt.$_{OK/PL}$	55.48 (±2.46)	30.07 (±0.83)	215.53 (±0.79)	176.54 (±2.67)
40 %wt.$_{OK/PL}$	65.01 (±0.98)	32.1 (±0.55)	197.05 (±1.01)	204.93 (±3.61)
60 %wt.$_{OK/PL}$	64.96 (±0.7)	30.52 (±0.34)	181.34 (±1.24)	187.29 (±3.75)
80 %wt.$_{OK/PL}$	65.68 (±0.51)	28.45 (±0.25)	177.64 (±1.36)	49.7 (±1.98)
20 %wt.$_{FR/PL}$	116.18 (±4.95)	51.23 (±1.48)	19.17 (±0.2)	107.72 (±2.92)
40 %wt.$_{FR/PL}$	94.48 (±4.5)	46.17 (±1.5)	18.07 (±0.16)	117.4 (±5.25)
60 %wt.$_{FR/PL}$	78.43 (±3.72)	42.22 (±1.58)	17.12 (±0.16)	114.88 (±5.21)
80 %wt.$_{FR/PL}$	65.38 (±4.95)	39.63 (±2.17)	173.52 (±2.91)	18.16 (±0.18)

Table 5-2: Oxidation peak parameters. Standard errors (Equation 4-1, p.67) in brackets

Sample	Peak 1	Peak 2	Peak 3	Peak 4	Peak 5
T_{max} (K)					
OK	561.08 (±0.12)	667.77 (±0.65)	718.9 (±0.05)	726.7 (±0.17)	-
FR	588.06 (±0.23)	603.19 (±0.04)	696.79 (±0.88)	733.62 (±0.14)	-
PL	619.77 (±2.02)	660.23 (±0.35)	795.16 (±0.46)	955.18 (±0.43)	-
20 %wt.$_{OK/PL}$	575.98 (±0.23)	635.93 (±0.07)	635.38 (±0.68)	748.09 (±0.2)	809.48 (±0.93)
40 %wt.$_{OK/PL}$	569.19 (±0.15)	635.91 (±0.07)	630.85 (±0.95)	739.33 (±0.12)	806.66 (±1.38)
60 %wt.$_{OK/PL}$	561.39 (±0.09)	637.3 (±0.07)	624.25 (±0.55)	721.28 (±0.03)	728.64 (±0.13)
80 %wt.$_{OK/PL}$	557.92 (±0.10)	641.49 (±0.19)	612.47 (±0.99)	710.00 (±0.02)	718.95 (±0.24)
20 %wt.$_{FR/PL}$	599.96 (±0.69)	598.94 (±0.10)	632.41 (±0.05)	640.17 (±0.16)	747.30 (±1.57)
40 %wt.$_{FR/PL}$	592.12 (±0.54)	601.62 (±0.05)	646.43 (±0.21)	666.41 (±2.66)	730.90 (±0.62)
60 %wt.$_{FR/PL}$	587.44 (±0.44)	600.5 (±0.04)	644.73 (±0.15)	668.8 (±1.41)	727.83 (±0.49)
80 %wt.$_{FR/PL}$	587.54 (±0.28)	602.39 (±0.04)	653.16 (±0.28)	703.49 (±1.11)	734.61 (±0.2)
Weight-loss Contribution, γ (%wt.)					
OK	51.79 (±0.21)	22.84 (±0.54)	1.55 (±0.04)	10.58 (±0.36)	-
FR	47.29 (±0.30)	17.37 (±0.15)	17.36 (±0.5)	9.78 (±0.35)	-
PL	40.09 (±1.69)	22.48 (±1.61)	5.4 (±0.11)	2.03 (±0.05)	-
20 %wt.$_{OK/PL}$	15.61 (±0.17)	15.18 (±0.1)	39.18 (±0.2)	1.69 (±0.04)	0.46 (±0.05)
40 %wt.$_{OK/PL}$	18.12 (±0.25)	10.14 (±0.09)	41.82 (±0.25)	4.09 (±0.08)	0.54 (±0.09)
60 %wt.$_{OK/PL}$	22.33 (±0.19)	6.27 (±0.08)	43.12 (±0.27)	1.45 (±0.02)	6.193 (±0.07)
80 %wt.$_{OK/PL}$	25.46 (±0.24)	3.71 (±0.15)	41.08 (±0.49)	3.39 (±0.03)	8.83 (±0.25)
20 %wt.$_{FR/PL}$	41.22 (±0.50)	4.63 (±0.09)	3.15 (±0.08)	9.3 (±0.19)	11.09 (±0.32)
40 %wt.$_{FR/PL}$	38.02 (±0.47)	9.84 (±0.13)	6.22 (±0.82)	6.31 (±1.20)	13.39 (±0.25)
60 %wt.$_{FR/PL}$	39.66 (±0.45)	13.96 (±0.16)	5.15 (±0.43)	7.96 (±0.89)	13.9 (±0.29)
80 %wt.$_{FR/PL}$	41.45 (±0.32)	16.05 (±0.15)	5.6 (±0.29)	15.27 (±0.37)	6.41 (±0.27)
Activity Range, ω (K)					
OK	59.87 (±0.21)	78.93 (±1.91)	4.6 (±0.10)	32.09 (±0.53)	-
FR	64.82 (±0.39)	13.82 (±0.10)	60.91 (±1.60)	20.89 (±0.43)	-
PL	117.45 (±1.06)	72.18 (±1.43)	50.75 (±0.88)	32.89 (±0.87)	-
20 %wt.$_{OK/PL}$	61.99 (±0.52)	31.95 (±0.14)	214.12 (±1.25)	20.67 (±0.47)	24.2 (±2.28)
40 %wt.$_{OK/PL}$	57.51 (±0.41)	25.5 (±0.16)	175.05 (±1.52)	22.88 (±0.33)	29.81 (±3.72)
60 %wt.$_{OK/PL}$	50.47 (±0.24)	21.93 (±0.19)	158.12 (±0.74)	4.76 (±0.07)	28.39 (±0.27)
80 %wt.$_{OK/PL}$	45.59 (±0.26)	24.15 (±0.60)	150.52 (±1.13)	5.21 (±0.04)	44.27 (±0.74)
20 %wt.$_{FR/PL}$	108.2 (±0.75)	17.53 (±0.25)	8.15 (±0.13)	24.33 (±0.28)	101.91 (±2.36)
40 %wt.$_{FR/PL}$	81.12 (±0.70)	15.23 (±0.14)	17.59 (±0.70)	33.32 (±3.71)	60.91 (±1.14)
60 %wt.$_{FR/PL}$	70.48 (±0.56)	14.94 (±0.11)	15.48 (±0.53)	38.29 (±3.42)	43.01 (±0.79)
80 %wt.$_{FR/PL}$	68.56 (±0.42)	15.08 (±0.10)	23.44 (±0.72)	60.37 (±1.43)	21.83 (±0.53)

5.6 Kinetic Analysis of the Isolated Peaks

5.6.1 Methodology

Estimated derivative thermogravimetric data for identical were first converted to weight data using integration using the trapezoid rule. The large number of data points in a profile (> 2000) mean this is a suitably accurate method. So for dTG_i is the rate of weight loss at temperature T_i we have:

Equation 5-4:
$$TG = \left[\frac{(T_2 - T_1)}{2.(dTG_1 + dTG_2)} \right]$$

It is standard procedure to calculate kinetic parameters using dTG in terms of dα/dt where α is fraction conversion and t is time. Therefore, it was necessary to convert dTG/dT to $d\alpha/dt$ and TG to α, to simplify future calculations:

Equation 5-5:
$$\frac{d\alpha}{dt} = \left(\frac{dTG}{dT}\right)\left(\frac{\beta}{100\%}\right)$$

Equation 5-6:
$$\alpha = \left(\frac{TG}{100\%}\right)$$

Log plots of ln[(dα/dt)/f(α)] against $1/RT$ where f(α) was the rate law (*e.g.* Figure 5-17), were then made for each peak of each blend, under each condition. Three rate laws, discussed in Section 2.5.3, were tested: first order, n^{th} order, and Prout-Tompkins nucleation model; examples of which using the first peak of olive kernel pyrolysis are given in Figure 5-17. The Prout-Tompkins model gave the most reliable straight line, although the fit of the n^{th} order model could be slightly improved by assuming a high value for the order of reaction (around 20).

Brown [1997] presents a summary of the Prout-Tompkins nuclei growth model, originally applied to the autocatalytic degradation of potassium permanganate [Prout, Tompkins, 1944]. In an isothermal plot of conversion α against time, the model gives a sigmoid plot. As the model contains both α and (1- α), it is influenced by both reagent and product concentrations, with m and n describing the relative importance of rate acceleration and deceleration respectively. Figure 5-18 (from Brown [1997]) describes

the effect of changing the m and n values, showing firstly that the profile becomes narrower as m or n → 1, and secondly that α → 0.5 (the point of inflection) as m → n.

Brown [1997] describes *m* as being between zero and 1.0, while Conesa *et al.* [1995] apply the Prout-Tompkins equation to the pyrolysis of cellulose, finding the lowest variation coefficient (with a percentage error of 1.77 %) of 10 kinetic models with *n* and *m* values of 0.3 and 1.38 respectively. Thus, the values determined as optimal for the present investigation (n = 1.0 and m = 1.3) are within the previously published range.

The generic rate law plot given in Figure 2-12c (p. 44) identifies the rate controlling factors of a reaction with increasing temperature. It identifies an upper temperature threshold where the true reaction rate is limited as temperature increases, first by the rate of diffusion through the internal pore structure, and later by diffusion of oxygen through the gas stream. Hustad *et al.* [1991] identified temperature thresholds of 620 K and 1020 K respectively for the kinetics of char oxidation, however, in the present study thresholds are more specific to the decompositions of individual sample components, and so are based on boundary conditions for conversion of $0.1\alpha_{max}$ to $0.5\alpha_{max}$. This is within that identified by Brown [1997] for conversion of ~ $0.05\alpha_{max}$ to $0.95\alpha_{max}$ as being the optimal linear range of the Prout-Tompkins model. Figure 5-19 illustrates the range of the present investigation for the first reaction peak of olive kernel pyrolysis. The boundary conditions exclude data from the first 1 %wt. of conversion, where d(dα/dt)/dt approaches zero and the rate law becomes unusable. While the upper threshold, excluding data above where $T = T_{max}$, means the change in line gradient brought about by diffusion limitations are avoided [Wang *et al.* 2003].

Straight lines in the log plot provide pre-exponential factor and activation energy from the y-intercept and gradient respectively (Equation 2-38):

$$\ln\left[\left(d\alpha/dt\right)/f(\alpha)\right] = \ln[A] - \left(E_{Act}/RT\right)$$

$$y = \ln\left[\left(d\alpha/dt\right)/f(\alpha)\right],\ x = \left(1/RT\right)$$

$$\Rightarrow \text{Intercept} = \ln[A]$$

$$\Rightarrow \text{Gradient} = -E_{Act}$$

The calculated values, along with literature comparisons are described in Section 5.6.2. Determining changes in the decomposition reactions requires analogous peaks from the different samples to be grouped together. This was done by performing cross-plots to observe trends in the calculated parameters. Sections 5.6.2 to 5.6.5 discuss the results and trends of this analysis.

The results of the kinetic calculations for olive kernel and Ptolemais lignite samples (pure and blended) are given in Tables 5-3 and 5-4.

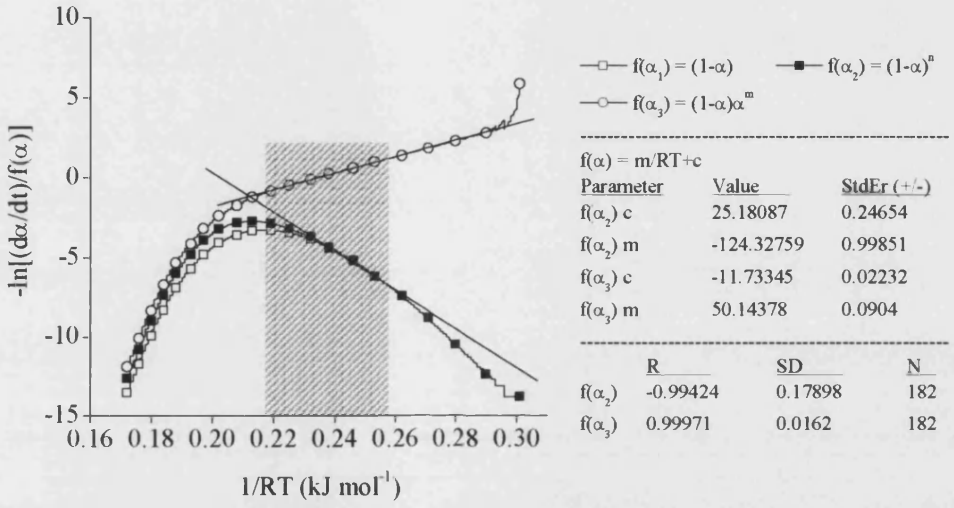

Figure 5-17: Comparison of log plots obtained by three rate-law models where n = 2.0 and m = 1.3. Properties of the linear fits are given for the n^{th} order ($f(\alpha_2)$) and P-T ($f(\alpha_3)$) models. The range of fitting (described in Figure 5-19) is illustrated by the shaded area. Data is taken from the first peak of olive kernel pyrolysis

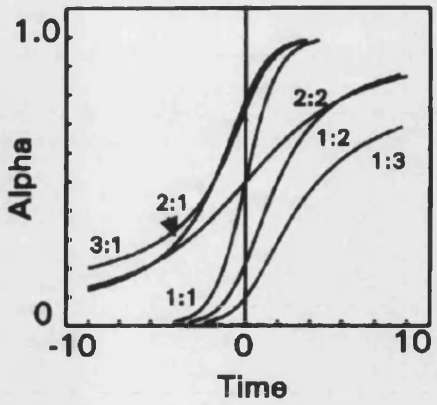

Figure 5-18: Example α-time plots of the sigmoid profiles given by the Prout-Tompkins model for different values of m and n (given as m:n (from [Brown 1997])

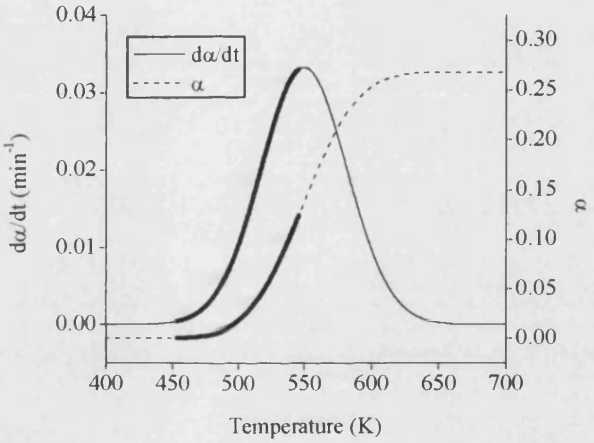

Figure 5-19: Illustrating the optimal range (in bold) of thermogravimetric data used in the calculation of kinetic parameters. Data taken from the first peak of olive kernel pyrolysis

5.6.2 Analysis of Cross-Plots

The cross-plots described in this section are a novel method, devised by the author, for comparing parameters of the isolated reaction peaks. In addition to the present example, it would also be suitable for revealing trends of other parameters, where other experimental variables are being changed (*e.g.* oxygen partial pressure, sample pre-treatment *etc.*). The aim is to identify group reactions of a similar mechanism, or

chemical process. Peaks of the pure and blended fuels were grouped using a cross-plot method comparing peak properties (T_{max}, peak area and peak width) with activation energy. The outcome for the oxidation and pyrolysis of the olive kernel blends are shown in Figures 5-20 and 5-21 respectively[7]. Initial groups were assigned where peak parameters fell in a localised area, as with most pyrolysis reactions. Figure 5-20a illustrates this, comparing E_{Act} and T_{max}. In several cases (*e.g.* group E of Figure 5-20b), peak parameters exhibit trends in activation energy, peak parameter, or both. These trends complicate the grouping procedure; however, this also identified the interdependent reactions.

In the analysis of the olive kernel blends, pyrolysis reactions were divided into six groups labelled A to F (Figure 5-20), while oxidation reactions were divided into eight groups labelled A to H (Figure 5-21).

Pyrolysis groups A and C are comparable to biomass reactions, while group B is common to both pure fuels (Figure 5-20). Groups E and F fall in a similar temperature range, however the large width differences of several peaks give them a significantly higher activation energy so two groups are used. One reaction of lignite (group D) is absent from the other samples.

Of the oxidation reactions, two groups (B and H) involve peaks comparable to lignite, while three groups (A, E and F) contain peaks comparable to olive kernels (Figure 5-21). Group C only contains blend reactions, while groups D and H are only observed in the pure fuels. Overall, there is a positive correlation between T_{max} and activation energy (Figure 5-21a), and an exponential relationship between activation energy and peak area (Figure 5-21b) and peak width (Figure 5-21c).

(7) Comparable plots for the forest residue blends are given in Figures 5-26 and 5-27 respectively. Discussion in Sections 5.6.2 to 5.6.6 will focus on the olive kernel blends; a comparison with the forest residue blends is given in Section 5.6.7.

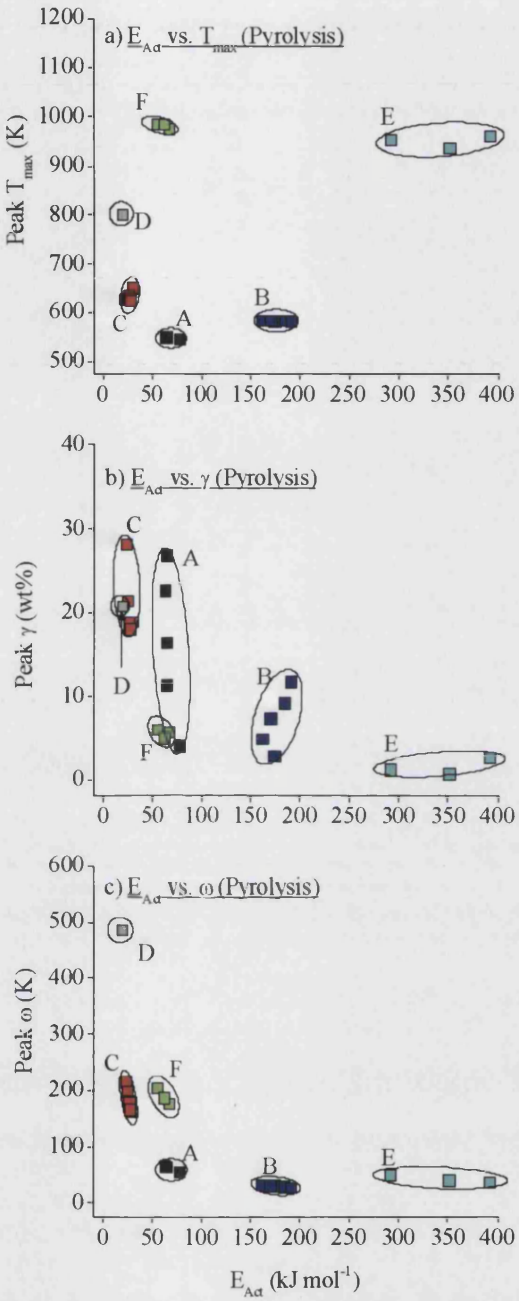

Figure 5-20: Cross-plots of pyrolysis E_{Act} against (a) T_{max}, (b) γ and (c) ω, for each peak of the olive kernel-Ptolemais lignite pure and blended fuels. (Group A = ■, Group B = ■, Group C = ■, Group D = ■, Group E = ■, Group F = ■, Group G = □ and Group H = ■)

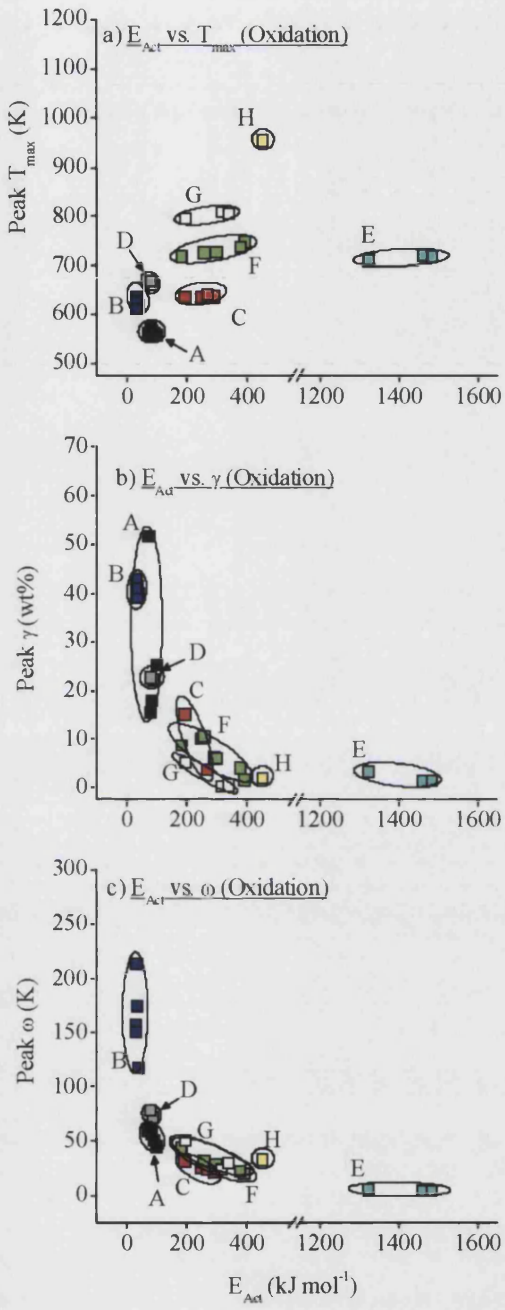

Figure 5-21: Cross-plots of oxidation E_{Act} against (a) T_{max}, (b) γ and (c) ω, for each peak of the olive kernel-Ptolemais lignite pure and blended fuels. (Group colour codes given in Figure 5-20 p.123)

5.6.3 Activation Energy Values

The close correlation between activation energy and pre-exponential factor (the compensation effect described in Section 5.6.6), means patterns for activation energy are replicated by the pre-exponential factor. Therefore, the discussion below applies to both. Activation energies for the pyrolysis and oxidation of the olive kernel-Ptolemais lignite blends are listed in Tables 5-3 and 5-4 respectively.

The low error margins for activation energies given indicate that the nucleation kinetic model results in a suitable linear section to the log plot. In most cases, standard errors of kinetic parameters from the present investigation are between 0.05 % and 0.3 % of the activation energy and the pre-exponential factor respectively (Table 5-3). An exception to this is the oxidation peak of olive kernels (*e.g.* 20 $\%wt._{OK/PL}$, Peak 5), where the error is around 3 %. This error arose where the peaks narrowness reduced the regularity of data points. This meant the boundary conditions described in Section 5.6.1 could only be applied approximately.

Literature data for the oxidation of raw fuels is rare, although coal char oxidation has been quoted with activation energies of between 100 and 300 kJ mol^{-1} (*e.g.* [Boonmee *et al.* 2005]). It, matching certain values observed in the lignites and some fuel blends in the present investigation is more likely however that the lower activation energy reactions (between 20 and 150 kJ mol^{-1}) represent the evaporation of low and medium molecular weight species, including tars, especially where comparable reaction groups are observed in both oxidising and pyrolysis conditions.

Table 5-3: Pyrolysis kinetic parameters for the olive kernel-Ptolemais lignite blend series'. Standard errors (Equation 4-1, p.67) in brackets

Sample	Peak 1	Peak 2	Peak 3	Peak 4
Activation Energy (kJ mol^{-1})				
OK	63.83 (±0.05)	191.69 (±0.63)	27.19 (±0.04)	351.15 (±0.97)
PL	29.14 (±0.05)	18.44 (±0.05)	392.24 (±0.88)	-
20 $\%wt._{OK/PL}$	77.44 (±0.05)	174.66 (±0.4)	22.66 (±0.04)	67.13 (±0.12)
40 $\%wt._{OK/PL}$	64.00 (±0.04)	162.65 (±0.31)	24.12 (±0.03)	54.59 (±0.14)
60 $\%wt._{OK/PL}$	63.71 (±0.03)	170.65 (±0.38)	25.73 (±0.04)	61.35 (±0.17)
80 $\%wt._{OK/PL}$	62.72 (±0.03)	184.21 (±0.57)	26.49 (±0.05)	291.77 (±0.75)
Pre-Exponential Factor (ln[min^{-1}])				
OK	14.6 (±0.01)	39.25 (±0.63)	6.67 (±0.01)	44.3 (±0.13)
PL	6.81 (±0.01)	5.29 (±0.01)	48.67 (±0.11)	-
20 $\%wt._{OK/PL}$	17.06 (±0.01)	35.44 (±0.09)	6.15 (±0.01)	9.45 (±0.02)
40 $\%wt._{OK/PL}$	14.46 (±0.01)	33.08 (±0.07)	6.26 (±0.01)	7.96 (±0.02)
60 $\%wt._{OK/PL}$	14.48 (±0.01)	34.83 (±0.08)	6.4 (±0.01)	8.66 (±0.02)
80 $\%wt._{OK/PL}$	14.34 (±0.01)	37.64 (±0.12)	6.56 (±0.01)	36.42 (±0.1)

Table 5-4: Oxidation kinetic parameters. Standard errors (Equation 4-1, p.67) in brackets

Sample	Peak 1	Peak 2	Peak 3	Peak 4	Peak 5
Activation Energy (kJ mol^{-1})					
OK	69.61 (±0.19)	77.13 (±0.04)	255.58 (±0.79)	1481.5 (±15.46)	-
PL	38.03 (±0.03)	83.88 (±0.07)	191.91 (±0.35)	447.63 (±1.6)	-
20 $\%wt._{OK/PL}$	74.66 (±0.03)	30.35 (±0.54)	191.59 (±0.48)	386.94 (±3.27)	312.26 (±9.82)
40 $\%wt._{OK/PL}$	79.26 (±0.05)	32.11 (±0.5)	244.86 (±0.81)	375.24 (±1.24)	336.58 (±0.32)
60 $\%wt._{OK/PL}$	89.16 (±0.14)	27.29 (±0.15)	289.66 (±1.14)	1460.2 (±15.17)	294.24 (±0.98)
80 $\%wt._{OK/PL}$	98.16 (±0.2)	28.11 (±0.14)	266.21 (±0.72)	1323.0 (±14.15)	178.46 (±0.36)
Pre-Exponential Factor (min^{-1})					
OK	15.62 (±0.04)	14.71 (±0.01)	245.38 (±2.6)	42.12 (±0.13)	-
PL	8.63 (±0.01)	16.02 (±0.01)	29.10 (±0.06)	55.76 (±0.21)	-
20 $\%wt._{OK/PL}$	16.09 (±0.01)	36.13 (±0.09)	7.91 (±0.13)	61.02 (±0.54)	44.87 (±1.49)
40 $\%wt._{OK/PL}$	17.22 (±0.01)	45.9 (±0.16)	8.03 (±0.12)	60.28 (±0.21)	49.06 (±0.05)
60 $\%wt._{OK/PL}$	19.5 (±0.03)	53.99 (±0.22)	6.81 (±0.04)	241.03 (±2.54)	48.13 (±0.17)
80 $\%wt._{OK/PL}$	21.5 (±0.05)	49.17 (±0.14)	7.03 (±0.04)	221.99 (±2.41)	29.93 (±0.06)

5.6.4 Pyrolysis Reaction Trends

Figure 5-22 and Figure 5-23b illustrate the trends of peak parameter and activation energy with blend composition for the olive kernel-Ptolemais lignite blend series under pyrolysis conditions. All the samples involve two or three reactions with activation energies between 10 and 100 kJ mol^{-1}. Furthermore, biomass and the blends exhibit reactions with activation energies of between 100 and 200 kJ mol^{-1}, while the 80 and

100 $\%wt._{OK\text{-}PL}$ blends exhibit reactions with activation energies of between 300 and 350 kJ mol^{-1}.

The activation energies of pyrolysis groups A and B (comparable with those in Table 2-10), and the strong positive trend in peak area with the biomass content (Figure 5-22e) indicate they are most likely to be the decompositions of hemicellulose and cellulose respectively.

Group C is much broader than the former two, and is present in all samples. It may represent the decomposition reactions of the char. In biomass, this is mostly due to lignin (Section 2.3.7). The blends would contain more char because of the high fixed carbon content of lignite, which would explain the increase in peak area of group C with lignite content (Figure 5-22e). The activation energy of this group (E_{Act} = 30 kJ mol^{-1}) is a close match for literature values given in Section 2.5.6, for the decomposition of lignin.

Peaks with activation energies of 30 to 60 kJ mol^{-1} (with T_{max} = 610 to 720 K) were observed by Alonso *et al.* [2001] during the pyrolysis of 30 different coals, coinciding with pyrolysis group C of the present investigation. However, other peaks described by Alonso *et al.* with activation energies of 120 to 180 kJ mol^{-1} (T_{max} = 950 to 1050 K) and 130 to 250 kJ mol^{-1} (T_{max} = 690 to 740 K), do not correlate with those observed here. This may be through model or experimental differences, since Alonso *et al.* used n^{th} order kinetic models and heating rates of 25 K min^{-1}.

As discussed in Section 2.4.9, Arenillas *et al.* [2003; 2004] studied the pyrolysis reactions of a synthetic coal. Between 740 and 790 K, two peaks in TG activity were linked with emissions of CO_2 and H_2O from carbonyl and hydroxyl groups, and CO and phenol from the condensed char. These reactions coincide with group D in the present investigation, so although this shows that deconvolution has not resolved each individual pyrolysis reaction, group D is likely to include the condensation and aromatisation processes of fixed carbon.

Groups E and F (T_{max} = 950 K) are similar to those observed by Arenillas *et al.* [2003; 2004] releasing H_2 and CO, and attributed to the aromatisation of fixed carbon.

Gopalakrishnan *et al.* [1996] describes the decomposition of calcium carbonate to lime (CaO) at around 973 K. Lime catalyses the oxidation of fixed carbon [Wu *et al.* 2005]. In the present investigation, lime from the biomass may therefore catalyses the oxidation of the lignite char, resulting in the products observed by Arenillas *et al.* Such catalysis would also explain the large reduction in activation energy between pyrolysis groups E and F (Figure 5-23b).

Table 5-5: Assignment of dTG peaks identified by deconvolution, to the pyrolysis groups of the olive kernel-Ptolemais lignite blends

Group	Suggested Reaction
A	Hemicellulose pyrolysis (Biomass and blends)
B	Cellulose pyrolysis (Biomass and blends)
C	Lignin/fixed carbon condensation (All fuels)
D	Fixed carbon condensation (Lignite only)
E	$CaCO_3 \rightarrow$ CaO or H_2/CO from char (Blends only)
F	$CaCO_3 \rightarrow$ CaO or H_2/CO from char (Pure fuels only)

5.6.5 Oxidation Reaction Trends

Figures 5-22 and 5-23a illustrate the trends of peak parameter and activation energy with blend composition for the olive kernel-Ptolemais lignite blend series under oxidation conditions. Plots in Figure 5-23a show that most oxidation energies fall between 20 and 450 kJ mol^{-1}, although the 60, 80 and 100 $\%wt._{OK/PL}$ blends also exhibit extremely high-energy reactions of between 1300 and 1500 kJ mol^{-1}.

The weight-loss contribution of group A is strongly reduced with the introduction of lignite, demonstrated by the rapid reduction in peak area between 80 and 100 $\%wt._{OK/PL}$ of Figure 5-22b. The apparent activation energy of the group does not change (Figure 5-23a) suggesting it is not competing with simultaneous reactions, so it is likely the active component is being removed by an earlier process. Group C for example, exhibits a decrease in peak area with increasing biomass content, similar in proportion to group A. Oxidation group A is similar to pyrolysis peaks A and B described in Section 5.6.4, so may also represent a devolatilisation reaction. Section 2.4.2 describes how volatile material blocks the flow of oxygen to the char surface. Reducing the biomass content would also reduce the quantity of volatile material in the vapour phase,

so more oxygen would be able to reach the char surface, altering the apparent activity of the oxidation reaction groups.

Oxidation groups B, F and G share a number of similarities in terms of activation energy range and peak properties, as well as similar group trends with biomass content. The T_{max} values remain stable at 620, 750 and 800 K for B, F and G respectively while their activation energies occur between 130 and 400 kJ mol^{-1}. This covers the energy range for the main oxidation reactions of carbon (Reactions 2-10 and 2-11, p.29) [Fu *et al.* 1997]. It may be assumed that the decomposition of a fuels fixed carbon component involves a combination of these reactions. The observed activation energy for the group would therefore become smaller if conversion by Reaction 2-11 increased (*i.e.* conversion by Reaction 2-10 decreased).

Using the trends in Figure 5-23a therefore, as the blend biomass content increases, conditions mean active components of oxidation groups B and G favour the higher energy pathway (Reaction 2-10) while active components of group F favour the low energy pathway (Reaction 2-11). Fuel factors influencing the preference for each of these reactions are discussed in Section 5.5.3.

Groups B and G have their highest peak areas in biomass and lignite respectively (Figure 5-22b). Group B involves the narrow peaks around T_{max} 610 K of Figures 5-15b to 5-15e. Their arrangement, just after the pyrolysis-type peak of group A has subsided, and also just after the T_{max} of group C – suggested below to relate to a non-oxidative char reaction – make it possible that group B represents the first possible char oxidation reactions once the shield of volatile materials from the previous reactions, has been removed. Although Senneca *et al.* [2000b] describe the synergy between pyrolysis and oxidation reactions in an oxidative environment, they do not consider this shielding phenomenon in their model (Figure 2-9).

Oxidation group C exhibits similar activation energies, T_{max} and peak width values (Figures 5-23a, 5-22b and 5-22c respectively) to pyrolysis group C (Figures 5-23b, 5-22e and 5-22f respectively). Oxidation group C might represent char reduction reactions occurring while the particles are shielded by volatile materials. It would be absent from the pure biomass as fixed carbon levels are low; Liang *et al.* [2000] show

that heterogeneous oxidation only occurs in biomass after pyrolysis is complete, because of the large and highly active.

Because of its location, group E is also likely to represent an oxidation reaction, and its T_{max} value suggests it may be the oxidation of a hemicellulose component, observed in Figure 5-3 (p. 95). The extremely high apparent activation energy may be caused by inhibition of the active group until strong heating and access to oxygen result in a very rapid (narrow) and highly active (a large dTG_{max}) reaction. Alternatively, it may have been caused by sudden heating from a strongly exothermic reaction in the olive kernels. The localised rise in heating rate, and disparity in temperature between probe and sample, and would result in a false peak shape and an inaccurate estimation of the reaction kinetics.

Table 5-6: Possible assignment of dTG peaks identified by deconvolution, to the oxidation groups of the olive kernel-Ptolemais lignite blends

Group	Suggested Reaction
A	Devolatilisation (Biomass and blends)
B	C → CO_2/CO (Blends only)
C	Char pyrolysis-type reactions (Lignite and blends)
D	C → CO_2/CO (Pure fuels only)
E	C → CO_2/CO (Sharp, misplaced reaction?)
F	C → CO_2/CO (Biomass and blends, cellulose)
G	C → CO_2/CO (Lignite and blends)
H	$CaCO_3$ → CaO + CO_2

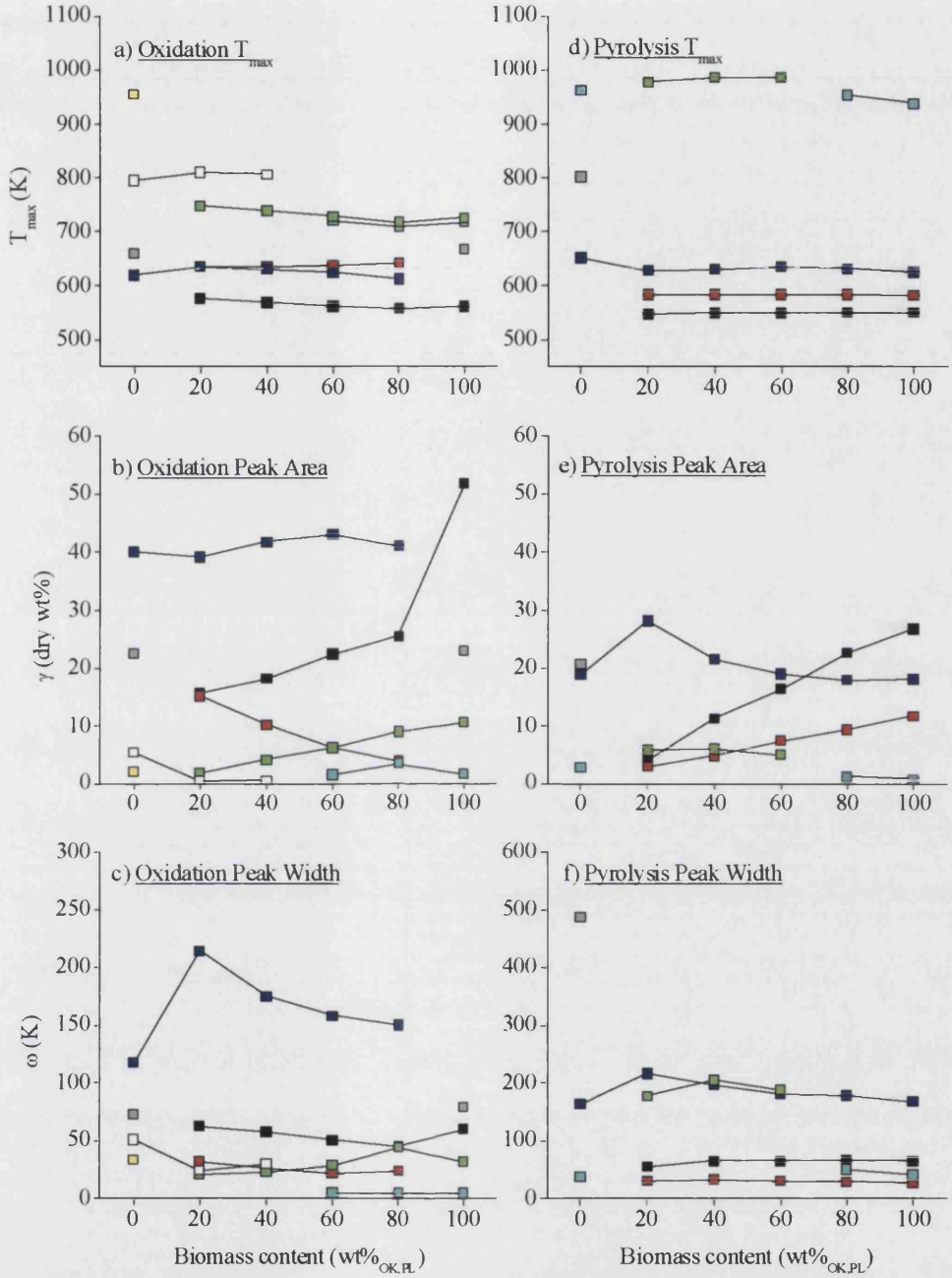

Figure 5-22: Variation of peak parameters T_{max}, γ and ω with blend composition for (a-c) oxidation and (d-f) pyrolysis of the olive kernel-Ptolemais lignite blend. (Group colour codes given in Figure 5-20 p.123)

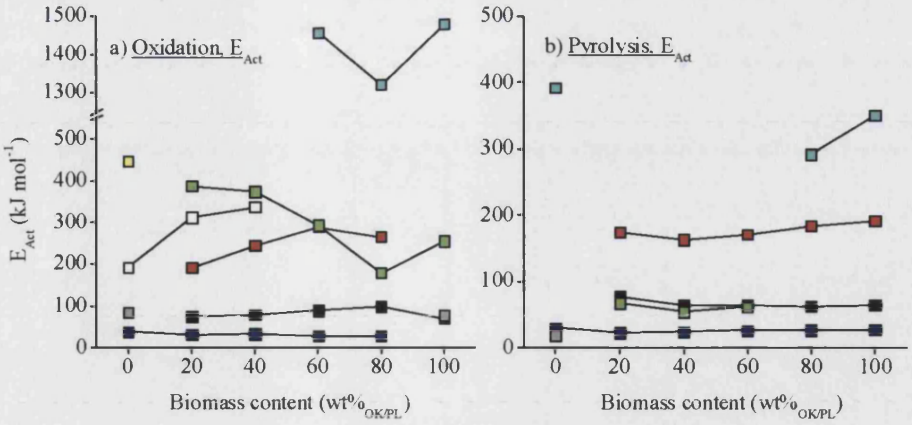

Figure 5-23: Activation energy variation with blend composition for (a) oxidation (b) pyrolysis of the olive kernel-Ptolemais lignite blends and pure fuels. (Group colour codes given in Figure 5-20 p. 123)

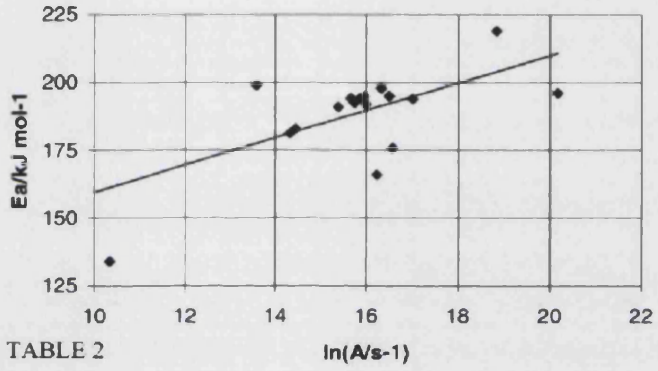

Figure 5-24: Compensation plot from [Brown et al. 2000] using data from the decomposition of $CaCO_3$ and various kinetic analysis procedures (slope =0.501 kJ mol^{-1}, intercept = 109.6 kJ mol^{-1}, r^2 = 0.48)

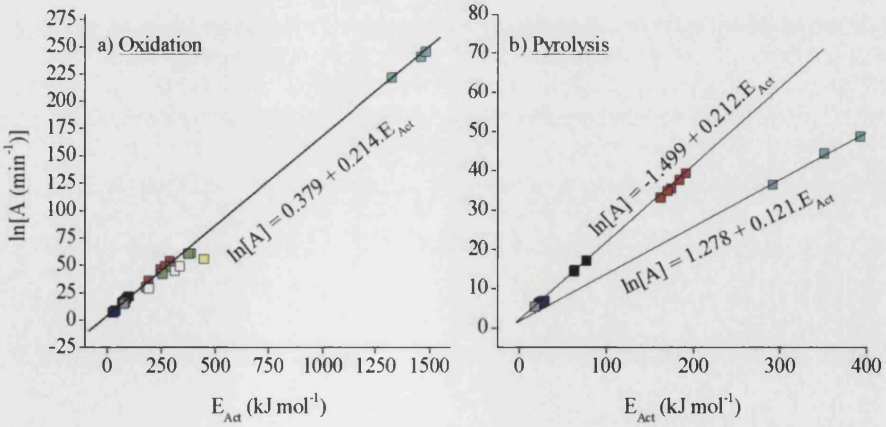

Figure 5-25: Compensation plots for the (a) oxidation and (b) pyrolysis of olive kernel-Ptolemais lignite blends. (Group colour codes given in Figure 5-20 p. 123)

5.6.6 The Compensation Effect

Comparisons between the calculated kinetic parameters A_i and $E_{i,Act}$ for reaction i are often made that suggest an apparent compensation effect between the parameters. The cause and implication of the effect is presently the subject of much debate in the literature [Brown *et al.* 2000; Budrugeac 2000; Brown *et al.* 2002; Wu *et al.* 2005]. Compensation plots typically use a linear equation of the form in Equation 5-7 where a and b are the y-intercept and gradient respectively. Figures 5-24 and 5-25 describe the results for Brown *et al.* [2000] and the present investigation respectively, this comparison is generally seen a measure of the quality of experimental consistency.

Equation 5-7: $$\ln[A_i] = a + bE_{i,Act}$$

In fact, the standard error values of a are sufficient (± 1.41 K) to suggest that $a = 0$, leaving a much simpler linear association of

Equation 5-8: $$\ln[A_i] = bE_{i,Act}$$

Brown *et al.* [2002] give an extensive discussion of whether the phenomenon has mathematical or physical origin, with reference to observations of an earlier publication [Brown *et al.* 2000]. In the 2002 paper, Brown *et al.* concluded that "true" compensation trends might be used to identify incorrect computational procedures, including improper use of power law exponents (*e.g.* n and m) or the appropriate range of α, and the use of an incorrect conversion model, f(α). The occurrence of true compensation trends were also discussed by Budrugeac *et al.* [2005], stating that changes in heating rate, also give rise to false compensation effects. True compensation effects arise between related reactions when using modified reagents or environments. The precise definition of "modified environment" is not given (it is presumed to mean the atmospheric conditions: $[O_2]$, pressure, pH *etc.*), but it appears that as long as the original sample, heating rate and subsequent calculations are constant, compensation trends can be used to observe accurate experimental methods.

Wu *et al.* [2005] attribute the strong compensation trend they observe to the heterogeneous coal structure, with active sites exhibiting a continuous range of energy levels. They describe the positive correlation between the apparent E_{Act} and pre-

exponential factor in terms of the degree of char condensation. Sites of high activation energy include char of more extensive aromatisation than areas with less aromatisation, which exhibit lower activation energies. As a result, where a higher energy site is activated, there are more carbon atoms in the locality to be at least partially activated, and the pre-exponential factor (also called the frequency factor) is increased. Where condensation is less extensive, activation energy is lower, but so is the carbon atom density, and therefore so is the pre-exponential factor.

In the present investigation, linear correlations are observed between the log pre-exponential factors and activation energy as noted in the literature. Two gradients are observed amongst the reactions in the present investigation. Most reactions exhibit a gradient of 0.21 ± 0.02 kJ mol^{-1}, similar to those observed by Wu *et al.* [2005] for the oxidation reactions of coal char. However, two reactions during pyrolysis involve significantly lower gradients of 0.12 kJ mol^{-1}. If the effect of char condensation on the compensation trend as described above is true, it may be that during the pyrolysis of the olive kernel-Ptolemais lignite blends, certain reactions are being retarded, resulting in a higher apparent activation energy. This may occur if there is competition between reactions for heat. Alternatively, it may be that the apparent activation energies are accurate, but the pre-exponential factor is falsely low. Wu *et al.* [2005] relate this parameter to the number of reactive sites being activated at a given temperature, suggesting that the number of active sites for these reactions has been reduced. It is not clear what might cause this, however it may be that active sites are being involved in competitive iso-gravimetric side reactions, and so alter the proportion available to react at their usual temperature.

5.6.7 Forest Residue Blend Activity

Figures 5-26 to 5-30, and Tables 5-8 and 5-9 describe results of kinetic analysis of the forest residue blends. Although the oxidation trends are not as clear as for the blends with olive kernel, under pyrolysis conditions similar trends are apparent.

Forest residue pyrolysis reactions were divided into six groups (A to F). Groups A to C contains biomass and blend reactions with approximately constant T_{max} values of 550,

600 and 610 K, and activation energies of around 45, 110 and 310 kJ mol^{-1}. The three groups also display increasing weight loss contributions of 12-22, 10-20 and 4-16 %wt. respectively. In literature, these three groups are linked to pyrolysis reactions of biomass and the activation energy of group B observed in the present investigation is a close match to literature values for hemicellulose in Table 2-10. However, the low activation energies of group A suggest this peak relates to weight loss through evaporation processes while the high activation energies of group C are more likely to relate to bond breaking reactions of a less volatile functional group.

Group D contains biomass, blends and lignite reactions, and exhibits values of T_{max} (630 to 690 K), weight loss contribution (10 to 20 %wt.) and activation energy (30 to 50 kJ mol^{-1}) that share no trend with biomass content of the blend. It may be therefore that these reactions (like group C of the olive kernel blends) represent the combined lignite char/biomass lignin condensation reactions.

Group E contains lignite and blend reactions, which exhibit decreasing trends in T_{max} and weight loss contribution, but constant activation energy levels. Although the chemistry of the reactions cannot yet be identified, this group represents the activity of a component of lignite not observed in biomass.

Group F contains the single lignite reaction observed at high temperature during the deconvolution (Section 4.3.5). Its absence from any of the biomass-containing samples means this activity of the reagents have been suppressed, or become involved in an earlier process. For example, it may have become involved in the reactions of group E, resulting in this group's higher apparent activation energy. With olive kernels, a comparable peak was observed, identified as either the calcination of calcium carbonate to lime, or graphitisation of the fixed carbon.

As Figure 5-28 shows, trends are less apparent in the forest residue blend oxidation reactions, however 8 groups (A to H) have been suggested here according to T_{max}, and peak area cross plot correlations with activation energy (Figure 5-29). Group A contains biomass, blends and lignite reactions with a constant T_{max} of around 600 K, and activation energy that increases from 40 to 50 kJ mol^{-1} as biomass content increases. Contribution to mass loss from group A increases once the biomass content exceeds 50

%wt. of the blend. As with the olive kernels, this low temperature loss is likely to be devolatilisation reactions of the biomass holocellulose fraction.

The apparent activation energies of Groups B to G make it possible for them all to represent the oxidation of carbon from different regent species using a combination of Reactions 2-10 and 2-11. Oxidation group C of forest residues (which shows a larger range in activation energy) is only present in the blends, in a similar way to group B of the olive kernel blends. It was suggested that this may be caused by the graphitisation of the char while oxygen is excluded by the volatile emissions. Group H identifies a reaction of Ptolemais lignite alone. The peak properties of forest residue blend pyrolysis group F match this group exactly, strongly indicating them both to represent the calcination activity described above.

Table 5-7: Possible assignment of dTG peaks identified by deconvolution, to reactions of the forest residue-Ptolemais lignite blends

Condition	Group	Suggested Reaction
Oxidation	A	Devolatilisation (Biomass and blends)
	B	Char pyrolysis-type reactions (Lignite and blends)
	C	C → CO_2/CO (Blends only)
	D	C → CO_2/CO (Pure fuels only)
	E	C → CO_2/CO (Biomass and blends)
	F	C → CO_2/CO (Biomass and blends)
	G	C → CO_2/CO (Lignite and blends)
	H	$CaCO_3$ → CaO + CO_2 (Lignite only)
Pyrolysis	A	Holocellulose pyrolysis (Biomass and blends)
	B	Hemicellulose pyrolysis (Biomass and blends)
	C	Holocellulose pyrolysis (Biomass and blends)
	D	Fixed carbon condensation (All fuels)
	E	Fixed carbon condensation (Lignite only)
	F	$CaCO_3$ → CaO (Lignite only)

Table 5-8: Pyrolysis kinetic parameters. Standard errors (Equation 4-1, p.67) in brackets

Sample	Peak 1	Peak 2	Peak 3	Peak 4
Activation Energy (kJ mol^{-1})				
FR	66.11 (±0.03)	140.47 (±0.36)	340.17 (±1.92)	26.11 (±0.05)
PL	29.14 (±0.05)	18.44 (±0.05)	392.24 (±0.88)	-
20 $\%wt._{FR/PL}$	33.61 (±0.05)	100.07 (±0.08)	314.7 (±1.24)	55.55 (±0.09)
40 $\%wt._{FR/PL}$	40.97 (±0.05)	111.73 (±0.15)	329.74 (±1.51)	49.6 (±0.09)
60 $\%wt._{FR/PL}$	52.12 (±0.04)	123.53 (±0.23)	344.5 (±1.76)	50.86 (±0.09)
80 $\%wt._{FR/PL}$	66.47 (±0.03)	133.55 (±0.29)	312.13 (±0.68)	26.89 (±0.05)
Pre-Exponential Factor (ln[min^{-1}])				
FR	14.74 (±0.01)	28.44 (±0.08)	65.44 (±0.38)	6.23 (±0.01)
PL	6.81 (±0.01)	5.29 (±0.01)	48.67 (±0.11)	-
20 $\%wt._{FR/PL}$	8.36 (±0.01)	20.5 (±0.02)	59.97 (±1.24)	10.57 (±0.02)
40 $\%wt._{FR/PL}$	9.72 (±0.01)	22.89 (±0.03)	63.26 (±0.3)	9.68 (±0.02)
60 $\%wt._{FR/PL}$	11.96 (±0.01)	25.21 (±0.05)	66.29 (±0.35)	9.86 (±0.02)
80 $\%wt._{FR/PL}$	14.78 (±0.01)	27.07 (±0.06)	6.51 (±0.01)	59.77 (±0.13)

Table 5-9: Oxidation kinetic parameters. Standard errors (Equation 4-1, p.67) in brackets

Sample	Peak 1	Peak 2	Peak 3	Peak 4	Peak 5
Activation Energy (kJ mol^{-1})					
FR	70.68 (±0.15)	396.81 (±2.61)	115.1 (±0.11)	400.19 (±1.51)	-
PL	38.03 (±0.03)	83.88 (±0.07)	191.91 (±0.35)	447.63 (±1.6)	-
20 $\%wt._{FR/PL}$	39.31 (±0.02)	318.83 (±1.41)	728.02 (±5.61)	261.63 (±0.97)	74.00 (±0.05)
40 $\%wt._{FR/PL}$	55.59 (±0.03)	364.07 (±1.78)	370.08 (±1.69)	206.22 (±0.5)	128.74 (±0.14)
60 $\%wt._{FR/PL}$	64.67 (±0.08)	368.64 (±2.23)	419.04 (±2.18)	179.49 (±0.41)	187.38 (±0.44)
80 $\%wt._{FR/PL}$	66.45 (±0.09)	365.31 (±2.22)	283.04 (±0.88)	118.7 (±0.1)	386.72 (±1.4)
Pre-Exponential Factor (min^{-1})					
FR	15.21 (±0.03)	78.27 (±0.53)	20.39 (±0.02)	65.00 (±0.25)	-
PL	8.63 (±0.01)	16.02 (±0.01)	29.10 (±0.06)	55.76 (±0.21)	-
20 $\%wt._{FR/PL}$	9.06 (±0.00)	63.05 (±0.29)	36.68 (±0.08)	48.68 (±0.19)	12.79 (±0.01)
40 $\%wt._{FR/PL}$	12.22 (±0.01)	71.88 (±0.36)	67.97 (±0.32)	36.93 (±0.09)	21.65 (±0.14)
60 $\%wt._{FR/PL}$	14.05 (±0.02)	73.01 (±0.46)	77.12 (±0.41)	32.19 (±0.08)	31.13 (±0.08)
80 $\%wt._{FR/PL}$	14.41 (±0.02)	72.21 (±0.45)	51.51 (±0.17)	20.8 (±0.02)	62.68 (±0.23)

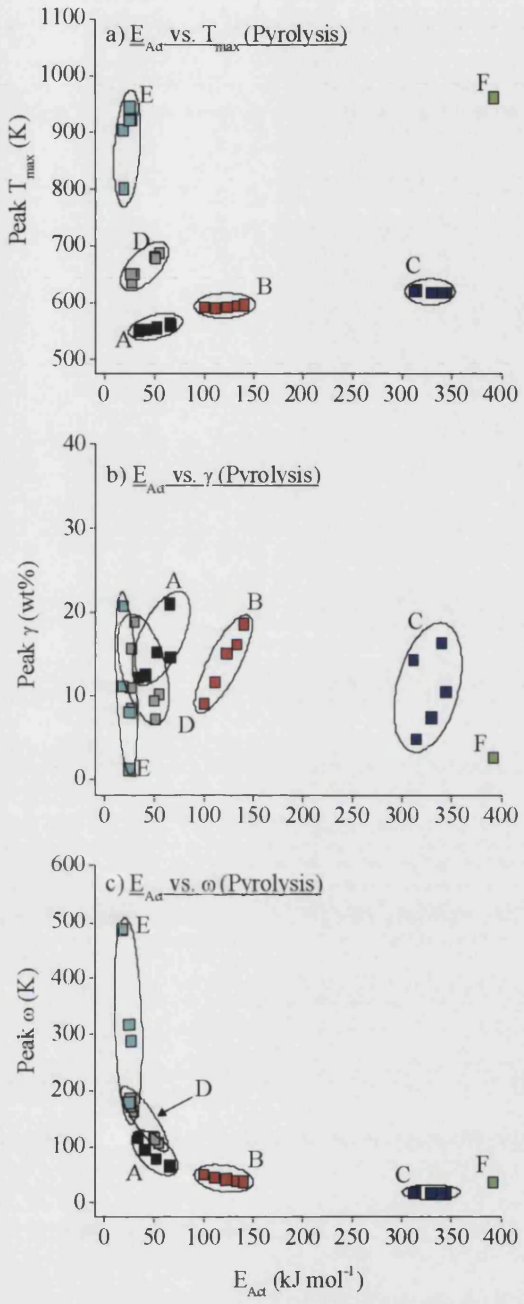

Figure 5-26: Cross-plots of pyrolysis E_{Act} against (a) T_{max}, (b) γ and (c) ω of the forest residue-Ptolemais lignite pure and blended fuels. (Group colour codes given in Figure 5-20 p.123)

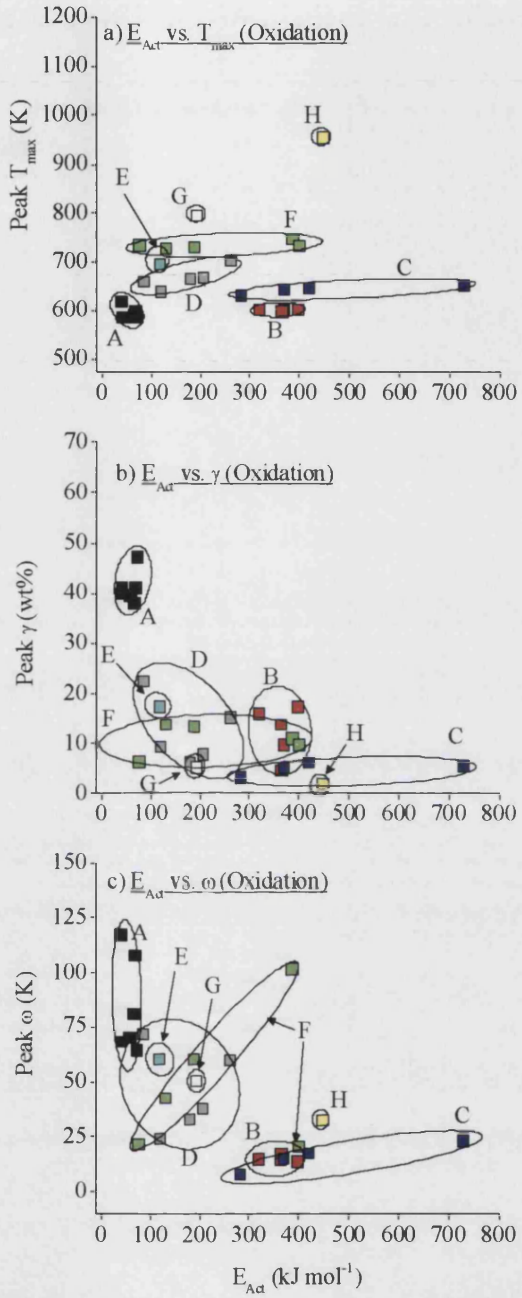

Figure 5-27: Cross-plots of oxidation E_{Act} against (a) T_{max}, (b) γ and (c) ω of the forest residue-Ptolemais lignite pure and blended fuels. (Group colour codes given in Figure 5-20 p.123)

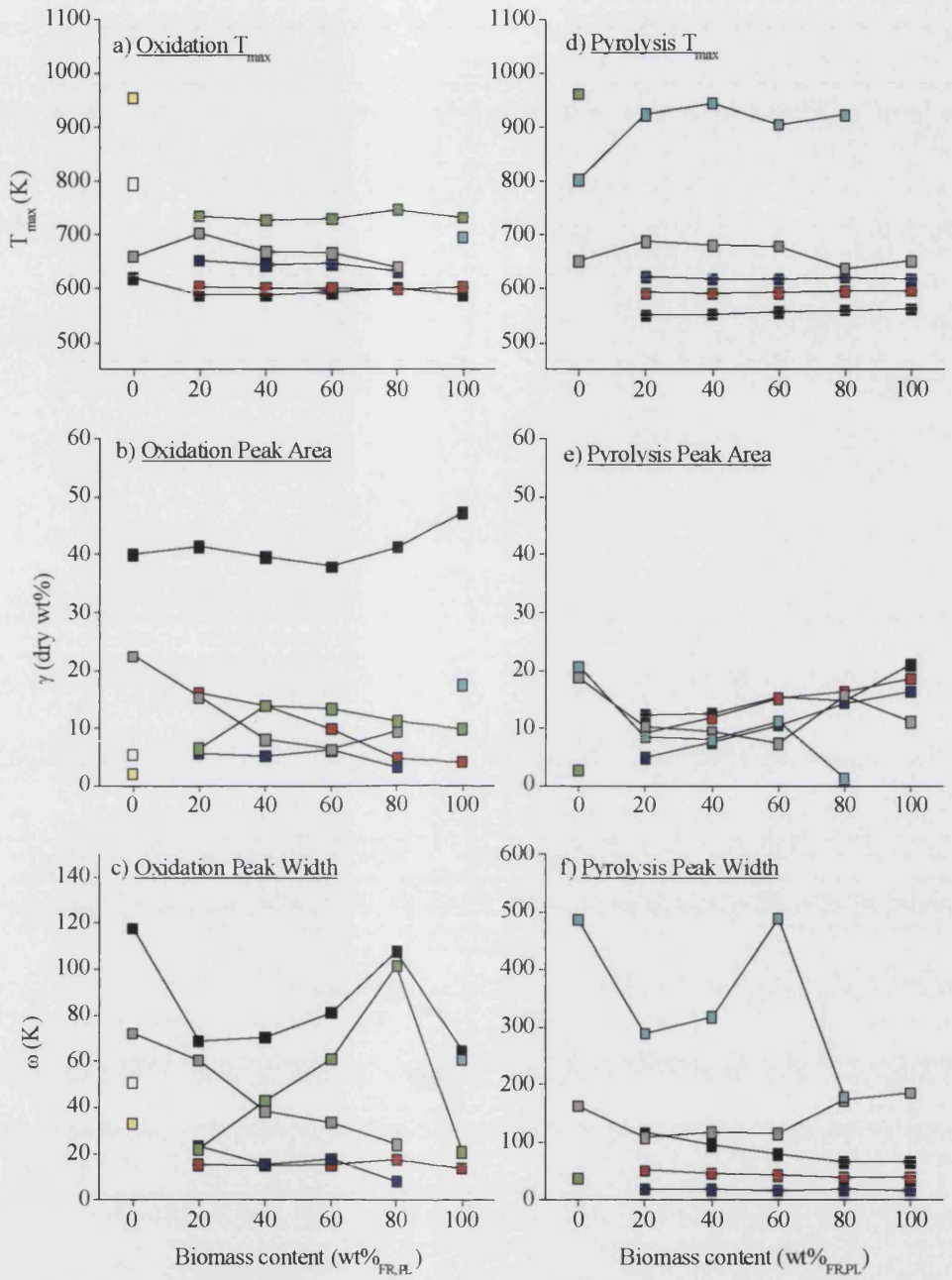

Figure 5-28: Variation of peak parameters T_{max}, γ and ω with blend composition for (a-c) oxidation and (d-f) pyrolysis of the forest residue-Ptolemais lignite blend. (Group colour codes given in Figure 5-20 p.123)

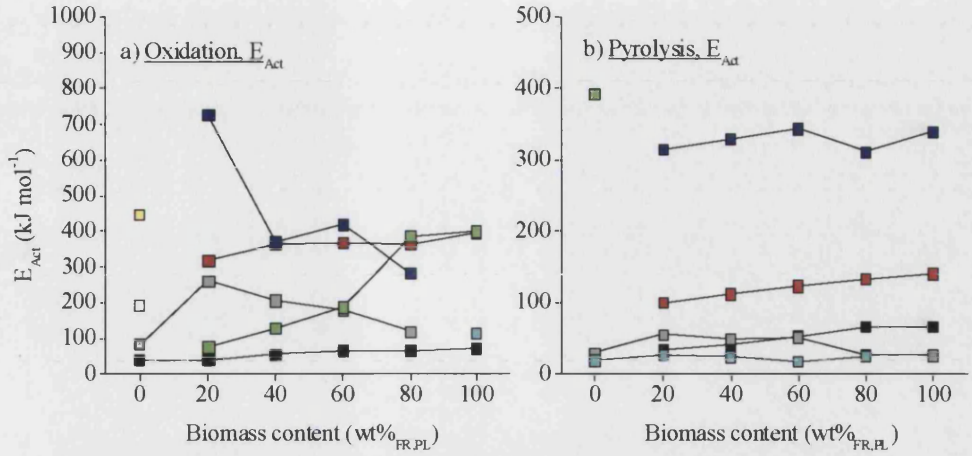

Figure 5-29: Variation of peak activation energy with blend composition for (a) oxidation (b) pyrolysis of the forest residue-Ptolemais lignite blends. (Group colour codes given in Figure 5-20 p.123)

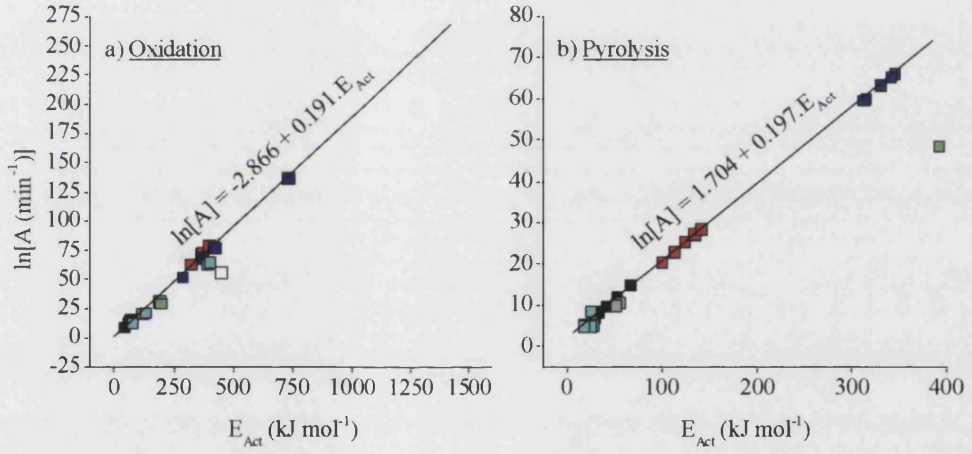

Figure 5-30: Compensation trends of ln[A] and E_{Act} for peaks in (a) oxidation and (b) pyrolysis reaction for the forest residue-Ptolemais lignite blends. (Group colour codes given in Figure 5-20 p.123)

Chapter 6 Concluding Remarks

6.1 Overall Conclusions

The objective of this investigation was to quantify the interactions between various blended fuels subjected to a linear heating. Knowledge of such interactions is useful in comparing blends, and understanding their performance when burned in coal-fired power stations.

This investigation covered the following work:

1. Pure and blended samples of biomass and lignite were linearly heated from 400 to 1100 K in inert (nitrogen) or oxidising (air) conditions to obtain weight (TG) and rate of weight-change (dTG) profiles. The fuel blends consisted of olive kernels or forest residue with Ptolemais lignite.

2. Using a rule-of-mixtures (ROM) model, deviations in the blends profiles from a cumulative weight-loss profile calculated from the profiles of the pure fuels were observed. This analysis confirmed that the activity during fuel blend pyrolysis is cumulative, with deviations of less than one weight percent of the component fuels. Low-temperature oxidation reactions of the blends are also cumulative of the component fuels; however once devolatilisation has subsided, remaining fuel blend oxidation is not cumulative and significant differences in activity arise, with the result that during oxidation a deviation of up to 10 weight percent of the predicted sample TG is observed. These differences result in

noticeable changes to the dTG profiles, and an overall underestimation of the sample TG. The deviation was significantly larger for the forest residue-Ptolemais lignite blends compared with the olive kernel blends.

3. Using scanning electron microscopy partially oxidised blend chars showed that at the point of maximum deviation between ROM calculated profiles and experimental profiles, particles of biomass and lignite adhere to one another. A mechanism for the oxidation process is suggested which includes the sticking phenomenon, around 650 K.

4. Rate of weight-loss profiles were deconvoluted into a series of discrete processes, using multiple Gaussian profiles, provided data that described each processes weight-loss contribution (γ), modal temperature (T_{max}), peak rate (dTG_{max}) and activity range (ω). During pyrolysis olive kernels and forest residue displayed four process peaks each, Ptolemais and German lignite's displayed three and two peaks respectively and the blends displayed five peaks each. During oxidation, five process peaks were fitted to the biomass and blend profiles, and four peaks were fitted to the lignite profiles.

5. Numerical integration of the deconvoluted dTG data gave TG profiles for each intrinsic process. A Prout-Tompkins nucleation kinetic model was applied to the TG and dTG data to calculate the apparent kinetic parameters of activation energy (E_{Act}) and pre-exponential factor (A) for each process. Kinetic parameters and weight-loss contributions of biomass pyrolysis are a close to those of the biomass pseudo-components of cellulose, hemicellulose and lignin.

6. Comparisons of all five parameters by a cross-plot method revealed their trends and similarities, depending on the process, fuel type and conditions. Using these trends, processes were grouped appropriately. During pyrolysis a blend series (includes lignite, blends and biomass) displayed six process groups, while during oxidation eight process groups were observed. Within the groups, parameters were compared with blend ratio and thus the effect of blend composition on the activity of the intrinsic reactions is observed.

From this investigation, the following general conclusions have been made:

1. Combining a Gaussian fit of the dTG data and the Prout-Tompkins nucleation type kinetic model with a values of n = 1.0 and m = 1.3, gives a reasonable approximation of the reaction profile and activities of the decomposition reactions for the fuel combinations investigated.

2. Devolatilisation reactions in both pyrolysis conditions and during low temperature devolatilisation, are largely unaffected by the presence of a co-fuel, with positive trends in weight-loss contribution and constant activation energies.

3. Where pyrolysis processes of char condensation are similar for the two pure fuels, whereupon they amalgamate to form a single group in the blends, of which weight-loss contributions are generally constant with changing blend ratio.

4. Oxidation processes are strongly modified in the presence of a co-fuel. This may be due to volatile materials shielding oxygen from the particles surface, inhibiting char oxidation reactions.

5. Once homogeneous oxidation of volatile materials is complete, remaining char (not reacted in pseudo-pyrolysis type reactions), combusts in a vigorous event.

6. Many of the apparent activation energies for oxidation fall between the intrinsic activation energies of the two key carbon oxidation reactions. Previous work has shown that apparent activation energies for char oxidation are a ratio of these intrinsic reactions, which compete over a range of temperatures. It is likely that the oxidation dTG peaks isolated here represent the decomposition of different fixed carbon active sites.

7. Changing the blend composition appears to influence the balance between Reactions 2-10 and 2-11 for this decomposition; as biomass content increases some processes increasingly involve Reaction 2-10 (their apparent activation energies increase); while other processes increasingly involve Reaction 2-11 (their apparent activation energies decrease).

8. High temperature reactions of the lignite and of olive kernels are probably related to the decomposition of calcium carbonate.

6.2 Recommendations for Future Work

This is a list of suggestions for future work, following the completion of the present investigation:

1. Use gas analysis (*e.g.* FT-IR) to observe the effect of blending on emissions, most notably the CO/CO_2 ratios. Profiles of product concentration can also be deconvoluted in conjunction with the TG profiles.

2. Carry out analysis of other fuel blends (especially considering other lignites and other grades of coal) to establish the reliability of the deconvolution and data analysis techniques identified by this work, for a range of fuel combinations.

3. Carry out analysis of pre-charred blends by TGA to observe any occurrence of interactions between char emissions.

4. Carry out a more thorough investigation of the particle-sticking phenomenon involving more stages of partial oxidation to observe the process fully. Analysis of the discrete particles (*e.g.* SEM-SIMS) would also identify their chemical nature and prove their fuel origin.

5. Heat and mass-transfer processes prevent deconvolution of dTG profiles using higher heating rates. However, TG analysis might be carried out on blends pre-charred at higher heating rates. Wire mesh reactors in particular can attain heating rates comparable to a power station. Deconvolution of the TG data would describe the persistence of reactive species in the blend char as oxidation proceeds.

6. Carry out investigation of links between the variation of reactions as observed in the present work, and the performance of power stations such as NO_x, SO_2 and

CO_2 emissions levels, the occurrence of unburnt fuel and ash fouling and overall energy economy.

7. Use TGA characterisation to correlate properties of a blend with key furnace performance data, such as gas phase temperature, ash composition, levels of slagging and fouling, efficiency of fuel conversion and NO_x or SO_2 emissions.

Chapter 7 References

Alonso, M.J.G., A.G. Borrego, D. Alvarez, W. Kalkreuth and R. Menendez (2001). *"Physicochemical transformations of coal particles during pyrolysis and combustion."* Fuel 80: 1857-1870.

Annamalai, K., B. Thien and J. Sweeten (2003). *"Co-firing of coal and cattle feedlot biomass (FB) fuels, Part 2: Performance results from 30 kW (100,000) BTU/h laboratory scale boiler burner."* Fuel 82: 1183-1193.

Antal Jr., M.J. and G. Varhegyi (1995). *"Cellulose Pyrolysis Kinetics: The Current State of Knowledge."* Industrial Engineering and Chemical Research 34: 703-717.

Antal, M.J., H.L. Friedman and F.E. Rogers (1980). *"Kinetics of cellulose pyrolysis in nitrogen and steam."* Combustion Science and Technology 21: 141-152.

Arbon, I.M. (2002). *"Worldwide use of biomass in power generation and combined heat and power schemes."* Processes of the Institution of Mechanical Engineers Part A: Journal of Power and Energy 216: 41-58.

Arenillas, A., R. Backreedy, J.M. Jones, J.J. Pis, M. Pourkashanian, F. Rubiera and A. Williams (2002). *"Modelling of NO formation in the combustion of coal blends."* Fuel 81: 627-636.

Arenillas, A., C. Pevida, F. Rubiera and J.J. Pis (2003). *"Comparison between the reactivity of coal and synthetic coal models."* Fuel 82: 2001-2006.

Arenillas, A., C. Pevida, F. Rubiera, R. Garcia and J.J. Pis (2004). *"Characterisation of model compounds and a synthetic coal by TG/MS/FTIR to represent the pyrolysis behaviour of coal."* Journal of Analytical and Applied Pyrolysis 71: 747-763.

Arvelakis, S., H. Gehrmann, M. Beckmann and E.G. Koukios (2003). *"Studying the ash behaviour of agricultural residues using thermal analysis."* Journal of Thermal Analysis and Calorimetry 72: 1019-1030.

Atkins, P.W. (1998). Physical Chemistry (6th Edition). John Wiley and Sons, London.

Banaee, J. and R.A. Larson (1995). *"Co-combustion of a chlorinated polymer with high-sulphur coals and other polymeric materials: Inhibition of the formation of chlorinated benzenes."* Waste Management 15: 609-614.

Battista Jr., J.J., E.E Hughes and D.A. Tillman (2000). *"Biomass co-firing at Seward Station."* Biomass and Bioenergy 19: 419-427.

Bassilakis, R., R.M. Carangelo and M.A. Wojtowicz (2001). *"TG-FTIR analysis of biomass pyrolysis."* Fuel 80: 1765-1786.

Baxter, L. (2005). *"Biomass-coal co-combustion: opportunity for affordable renewable energy."* Fuel 84: 1295-1302.

Berkowitz, N. (1994). An Introduction to Coal Technology (2nd Edition). Academic Press Inc, New York.

Biagini, E., F. Lippi, L. Petarca and L. Tognotti (2002). *"Devolatilisation rate of biomasses and coal-biomass blends: an experimental investigation."* Fuel 81: 1041-1050.

Boonmee, N. and J.G. Quintiere (2005). *"Glowing ignition of wood: the onset of surface combustion."* Proceedings of the Combustion Institute 30: 2303-2310.

Boylan, D., V. Bush and D.I. Bransby (2000). *"Switch Grass co-firing: pilot scale and field evaluation."* Biomass and Bioenergy 19: 411-417.

Branca, C. and C. Di Blasi (2004). *"Global intrinsic kinetics of wood oxidation."* Fuel 83: 81-87.

Brown, M.E. (1997). *"The Prout-Tompkins rate equation in solid-state kinetics."* Thermochimica Acta 300: 93-106.

Brown, M. E. and A. K. Galwey (2002). *"The significance of 'compensation effects' appearing in data published in 'computational aspects of kinetic analysis': ICTAC project 2000."* Thermochimica Acta 387: 173-183.

Brown, M.E., M. Maciejewski, S. Vyazovkin, R. Nomen, J. Sempere, A. Burnham, J. Opfermann, R. Strey, H.L. Anderson, A. Kemmler, R. Keuleers, J. Janssens, H.O.

Desseynh, C.R. Li, T.B. Tangi, B. Roduit, J. Malek and T. Mitsuhashi (2000). *"Computational aspects of kinetic analysis Part A: The ICTAC kinetics project-data, methods and results."* Thermochimica Acta 355: 125-143.

BS-1016-6 (1997). *"Methods for Analysis and Testing of Coal and Coke: Ultimate Analysis of Coal."* British Standards Institute.

BS-1016-8 (1997). *"Methods for Analysis and Testing of Coal and Coke: Chlorine in Coal and Coke."* British Standards Institute.

BS-1016-104.1 (1999). *"Methods for Analysis and Testing of Coal and Coke. Proximate Analysis: Determination of Moisture Content of the General Analysis Test Sample."* British Standards Institute.

BS-1016-104.3 (1998). *"Methods for analysis and testing of coal and coke. Proximate analysis: Determination of volatile matter content."* British Standards Institute.

BS-1016-104.4 (1998). *"Methods for Analysing and Testing Coal and Coke. Proximate Analysis: Determination of Ash."* British Standards Institute.

BS-1016-105 (1992). *"Methods for Analysis and Testing of Coal and Coke. Determination of Gross Calorific Value."* British Standards Institute.

BS-1016-106.4.2 (1996). *"Methods for Analysis and Testing of Coal and Coke. Ultimate Analysis of Coal and Coke: Determination of Total Sulphur Content (High Temperature Combustion Method)."* British Standards Institute.

BS-1016-106.5 (1996). *"Methods for Analysis and Testing of Coal and Coke. Ultimate Analysis of Coal and Coke: Determination of Forms of Sulphur in Coal."* British Standards Institute.

BS-ISO-11760 (2005). *"Classification of Coals."* British Standards Institute.

Budrugeac, P. (2000). *"On the evaluation of the thermal lifetime of polymeric materials which exhibit a complex mechanism of thermal degradation consisting of two successive reactions."* Polymer Degradation and Stability 67: 271-278.

Bujoreanu, V.M., L. Frangu and E. Segal (2002). *"Kinetic investigation on the dehydration of co precipitated mixed oxide powders."* Journal of Thermal Analysis and Calorimetry 68: 787-801.

Caballero, J.A., J.A. Conesa, R. Font and A. Marcilla (1997). *"Pyrolysis kinetics of almond shells and olive stones considering their organic fractions."* Journal of Analytical and Applied Pyrolysis 42: 159-175.

Cannell, M.G.R. (2003). *"Carbon sequestration and biomass energy offset: theoretical, potential and achievable capacities globally, in Europe and the UK"* Biomass and Bioenergy 24: 97-116.

Capart, R., L. Khezamia and A.K. Burnham (2004). *"Assessment of various kinetic models for the pyrolysis of microgranular cellulose."* Thermochimica Acta 417: 79-89.

Cetin, E., R. Gupta and B. Moghtaderi (2004). *"The effect of pyrolysis pressure and heating rate on radiata pine char structure and apparent gasification reactivity."* Fuel 84: 1328-1334.

CEN/TS-14588:2004 (2004). *"Solid biofuels: Terminology, definitions and descriptions."* European Committee for Standardisation.

Chagger, H.K., A. Kendall, A. McDonald, M. Pourkashanian and A. Williams (1998). *"Formation of dioxins and other semi-volatile organic compounds in biomass combustion."* Applied Energy 60: 101-114.

Chaiklangmuang, S., J. Jones, M. Pourkashanian and A. Williams (2002). *"Conversion of volatile-nitrogen and char-nitrogen to NO during combustion."* Fuel 81: 2363-2369.

Chen, Y., S. Mori and W.P. Pan (1996). *"Studying the mechanisms of ignition of coal particles by TG-DTG."* Thermochimica Acta 275: 149-158.

Cliffe, K.R. and S. Patumsawad (2001). *"Co-combustion of waste from olive oil production with coal in a fluidised bed."* Waste Management 21: 49-53.

Conesa, J.A., J.A. Caballero, A. Marcilla and R. Font (1995). *"Analysis of different kinetic models in the dynamic pyrolysis of cellulose."* Thermochimica Acta 254: 172-192.

Conesa, J.A., A. Marcilla, J.A. Caballero and R. Font (2001). *"Comments on the validity and utility of the different methods for kinetic analysis of thermogravimetric data."* Journal of Analytical and Applied Pyrolysis 58-59: 617-633.

Cotton, F.A., G. Wilkinson and P.L. Gaus (1996). Basic Inorganic Chemistry (3rd Edition). John Wiley & Sons, New York.

Demirbas, A. (2002). *"Fuel characteristics of olive husk and walnut, hazelnut, sunflower, and almond shells."* Energy Sources 24: 215-221.

Demirbas, A. (2003). *"Sustainable co-firing of biomass with coal."* Energy Conversion and Management 44: 1465-1479.

Demirbas, A. (2004). *"Combustion characteristics of different biomass fuels."* Progress in Energy and Combustion Science 30: 219-230.

Dietl, R., and W. Schmidt (1999). *"Technical large-scale test of biomass co-combustion in a lignite-fired power-plant."* VGB Power Tech 4: 60-64.

Dollimore, D. and S. Lerdkanchanaporn (1998). *"Thermal Analysis."* Analytical Chemistry 70: 27R-35R.

Dollimore, D. and P. Phang (2000). *"Thermal Analysis."* Analytical Chemistry 72: 27R-36R.

DTI (2003). *"Energy White Paper: Our Energy Future - Creating a low carbon economy."* Department of Trade and Industry, London.

DTI (2004). *"First Annual report on the implementation of the Energy White Paper."* Department of Trade and Industry, London.

DTI (2005). *"Best Practice Brochure: Co- Firing of Biomass (Main Report) Report No. COAL R287 DTI/Pub URN 05/1160."* Department of Trade and Industry, London.

DTI (2005). *"Digest of the United Kingdoms Energy Statistics."* Department of Trade and Industry, London.

Fisher, T., M. Hajaligol, B. Waymack and D. Kellogg (2002). *"Pyrolysis behaviour and kinetics of biomass derived materials."* Journal of Analytical and Applied Pyrolysis 62: 331-349.

Font, R., A. Marcilla, E. Verdú and J. Devesa (1991). *"Thermogravimetric kinetic study of the pyrolysis of almond shells and almond shells impregnated with $CoCl_2$."* Journal of Analytical and Applied Pyrolysis 21: 249-264

Fu, W.B., B.L. Zhang and S.M. Zheng (1997). *"A relationship between the kinetic parameters of char combustion and the coal's properties."* Combustion and Flame 109: 587-598.

Fushimi, C., K. Araki, Y. Yamaguchi, A. Tsutsumi (2003). *"Effect of heating rate on gasification of biomass, Part 1: Reactivity of char."* Industrial Chemical Engineering Research 42: 3922-3928.

Gayan, P., J. Adanez, L.F. de Diego, F. Garcia-Labiano, A. Cabanillas, A. Bahillo, M. Aho and K. Veijonen (2004). *"Circulating fluidised bed co-combustion of coal and biomass."* Fuel 83: 277-286.

Garcia-Perez, M., A. Chaala, J. Yang and C. Roy (2001). *"Co-pyrolysis of sugarcane bagasse with petroleum residue, Part 1: thermogravimetric analysis."* Fuel 80: 1245-1258.

Ghetti, P., L. Ricca and L. Angelini (1996). *"Thermal analysis of biomass and corresponding pyrolysis products."* Fuel 75: 565-573.

Gopalakrishnan, R. and C.H. Bartholomew (1996). *"Effects of CaO, high-temperature treatment, carbon structure and coal rank on intrinsic char oxidation rates."* Energy & Fuels 10: 689-695

Grotkjaer, T., K. Dam-Johansen, A.D. Jensen and P. Glarborg (2003). *"An experimental study of biomass ignition."* Fuel 82: 825-833.

Gurgel-Veras, C.A., J. Saastamoinen, J.A.C. Jr and M. Aho (1999). *"Overlapping of the devolatilisation and char combustion stages in the burning of coal particles."* Combustion and Flame 116: 567.

Harding, N.S. and B.R. Adams (2000). *"Biomass as a re-burning fuel: a specialized cofiring application."* Biomass and Bioenergy 19: 429-445.

Hayhurst, A.N. and M.S. Parmar (1998). *"Does solid carbon burn in oxygen to give the gaseous intermediate CO, or produce CO_2 directly? Some experiments in a hot bed of sand fluidised by air."* Chemical Engineering Science 53: 427-438

Hein, K.R.G. and J.M. Bemtgen (1998). *"EU clean coal technology - co-combustion of coal and biomass."* Fuel Processing Technology 54: 159-169.

Hughes, E. (2000). *"Biomass cofiring: economics, policy and opportunities."* Biomass and Bioenergy 19: 457-465.

Hughes, E. and D.A. Tillman (1998). *"Biomass cofiring: status and prospects 1996."* Fuel Processing Technology 54: 127-142.

Hupa, M. (2005). *"Interaction of fuels in co-firing in FBC."* Fuel 84:1312-1319

Hustad, J.E., D. Vareide and O.K. Sonju (1991). *"Burning rates of coke particles in the freeboard above a fluidised bed reactor."* Combustion and Flame 85: 232-240.

Jakab, E., O. Faix and F. Till (1997). *"Thermal decomposition of milled wood lignins studied by thermogravimetry/mass spectrometry."* Journal of Analytical and Applied Pyrolysis 40-41: 171-186.

Jones, J.M., M. Kubacki, K. Kubica, A.B. Ross and A. Williams (2005). *"Devolatilisation characteristics of coal and biomass blends."* Journal of Analytical and Applied Pyrolysis 73: 197-206.

Kastanaki, E., D. Vamvuka, P. Grammelis and E. Kakaras (2002). *"Thermogravimetric studies of the behaviour of lignite-biomass blends during devolatilisation."* Fuel Processing Technology 77-78: 159-166.

Katsikas, L. and I. Popovic (2003). *"Improvement to the Flynn-Wall method of determining apparent activation energies of the thermal degradation of polymers."* Journal of Physical Chemistry 107: 7522-7525.

Laursen, K. and J.R. Grace (2002). *"Some implications of co-combustion of biomass and coal in a fluidized bed boiler."* Fuel Processing Technology 76: 77-89.

Li, C. and T.C. Brown (2001). *"Carbon oxidation kinetics from evolved carbon oxide analysis during temperature-programmed oxidation."* Carbon 39: 725-732

Liang, X.H. and J.A. Kozinski, (2000). *"Numerical modelling of combustion and pyrolysis of cellulosic biomass in thermogravimetric systems."* Fuel 79: 1477-1486.

Lea, J.L. and R.C. Leegood (1993). Plant Biochemistry and Molecular Biology. John Wiley & Sons, New York.

Li, Y. Q., L.H. Zhang and H. Gong (2005). *"Dynamic thermal degradation studies on amorphous carbon thin films."* Journal of Thermal Analysis and Calorimetry 79: 677-683.

Lindsey, B.K. and T.J. Mays (2004). *"Thermogravimetric Analysis of The Carbonisation of Biomass-Coal Blends."* Book of Abstracts, 13th International Congress of Thermal Analysis and Calorimetry, Chia Laguna, Sardinia; 12th-19th September 2004. p. 367.

Lindsey, B.K. and T.J. Mays (2005). "Thermogravimetric Analysis of the C-Carbonisation of Biomass-Lignite Blends." Book of Abstracts, 7th World Congress of Chemical Engineering Glasgow, Scotland; 10th-14th July 2005. p. 410.

Liu, D.C., T. Mi, B.X. Shen, B. Feng and F. Winter (2002a). *"Reducing N_2O Emission by Co-Combustion of Coal and Biomass."* Energy & Fuels 16: 525-526.

Liu, D.C., C.L. Zhang, T. Mi, B.X. Shen and B. Feng (2002b). *"Reduction of N_2O and NO emissions by co-combustion of coal and biomass."* Journal of the Institute of Energy 75: 81-84.

Loeffler, G., C. Wartha, F. Winter and H. Hofbauer (2002). *"Study on NO and N_2O Formation and Destruction Mechanisms in a Laboratory-Scale Fluidized Bed."* Energy & Fuels 16: 1024-32.

Lorentz, H., E. Carrea, M. Tamura and J. Haas (2000). *"The role of surface structure development in pulverised fuel combustion."* Fuel 79: 1161-1172.

Manya, J.J., E. Velo and L. Puigjaner (2003). *"Kinetics of Biomass Pyrolysis: a Reformulated Three-Parallel-Reactions Model."* Industrial Engineering and Chemical Research 42: 434-41.

March, J. (1992). Advanced Organic Chemistry; Reactions, Mechanisms and Structure (4th Edition). John Wiley & Sons, New York.

McGrath, T.E., W.G. Chan and M.R. Hajaligol (2003). *"Low temperature mechanism for the formation of polycyclic aromatic hydrocarbons from the pyrolysis of cellulose."* Journal of Analytical and Applied Pyrolysis 66: 51-70.

Nugroho, Y.S., A.C. McIntosh and B.M. Gibbs (2000). *"Low-temperature oxidation of single and blended coals."* Fuel 79: 1951-1961.

Ofgem (2005). *"The Renewables Obligation: Ofgem's second annual report."* Office of gas and Electricity Markets, London.

Ohlsson, O. (1994). *"Results of combustion and emissions testing when co-firing blends of binder-enhanced densified refuse-derived fuel (p-RDF) pellets and coal in a 440 MWe cyclone fired combustor, Volume 1: Test Methodology and Results, Subcontract Report No. DE94000283."* Argonne National Laboratory, Argonne.

Orfao, J.J. M., F.J.A. Antunes and J.L. Figueiredo (1999). *"Pyrolysis kinetics of lignocellulosic materials - three independent reactions model."* Fuel 78: 349-358.

Pastor-Villegas, J., C.J. Duran-Valle, C. Valenzuela-Calahorro and V. Gomez-Serrano (1998). *"Organic chemical structure and structural shrinkage of chars prepared from rockrose."* Carbon 36: 1251-1256.

Peralta, D., N.P. Paterson, D.R. Dugwell, R. Kandiyoti (2001). *"Coal blend performance during pulverised-fuel combustion: estimation of relative reactivity's by a bomb-calorimeter test."* Fuel 80: 1623-1634

PIU (2002). *"The Energy Review."* The Cabinet Office - Performance and Innovations Unit, London.

Prout, E.G. and F.C. Tompkins (1944). *"Thermal decomposition of potassium permanganate."* Transactions of the Faraday Society 40: 488-498.

Quaak, P., H. Knoef and H. Stassen (1999). Energy from Biomass: A Review of Combustion and Gasification Technologies. The World Bank, Washington D.C.

Raveendran, K., A. Ganesh and K.C. Khilar (1996). *"Pyrolysis characteristics of biomass and biomass components."* Fuel 75: 967-998.

Reynolds, J.G. and A.K. Burnham (1997). *"Pyrolysis decomposition kinetics of cellulose-based materials by constant heating rate micropyrolysis."* Energy & Fuels 11: 88-97.

Roeder, J., R.V.B. Oliveira, D. Becker, M.W. Gonçalves, V. Soldi and A.T.N. Pires (2005). *"Compatibility effect on the thermal degradation behaviour of polypropylene blends with polyamide 6, ethylene propylene diene copolymer and polyurethane."* Polymer Degradation and Stability 90: 481-487.

Ross, A.B., J.M. Jones, S. Chaiklangmuang, M. Pourkashanian, A. Williams, K. Kubic, J.T. Andersson, M. Kerst, P. Danihelka and K. D. Bartle (2002). *"Measurement and prediction of the emission of pollutants from the combustion of coal and biomass in a fixed bed furnace."* Fuel 81: 571-582.

Rubiera, F., Arenillas, A., Pevida, R, Garcia and J.J. Pis (2002a). *"Modification of combustion behaviour and NO emissions by coal blending."* Fuel Processing Technology 77-78: 111-117.

Rubiera, F., Arenillas, A., Pevida, R, Garcia, J.J. Pis, K.M. Steel and J.W. Patrick (2002b). *"Coal structure and reactivity changes induced by chemical demineralisation."* Fuel Processing Technology 79: 273-279.

Sami, M., K. Annamalai and M. Wooldridge (2001). *"Co-firing of coal and biomass fuel blends."* Progress in Energy and Combustion Science 27: 171-214.

Seggiani, M., (1999). *"Empirical correlation of the ash fusion temperatures and temperature of critical viscosity for coal and biomass ashes."* Fuel 78: 1121-1125

Senneca, O., C. Riccardo, S. Masi, and P. Salatino (2002a). *"A thermogravimetric study of non-fossil solid fuels. Part 1 Inert pyrolysis."* Energy & Fuels 16: 653-660.

Senneca, O., C. Riccardo and P. Salatino (2002b). *"A thermogravimetric study of non-fossil solid fuels. Part 2 Oxidative pyrolysis and char combustion."* Energy & Fuels 16: 661-668.

Shafizadeh, F. and Y. Sekiguchi (1984). *"Oxidation of chars during smouldering combustion of cellulosic materials."* Combustion and Flame 55: 171-179.

Sheng, C. and J.L.T. Azevedo (2005). *"Estimating the higher heating value of biomass fuels from basic analysis data."* Biomass and Bioenergy 28: 499-507.

Skodras, G., P. Grammelis, P. Samaras, P. Vourliotis, E. Kakaras and G.P. Sakellaropoulos (2002). *"Emissions monitoring during coal waste wood co-combustion in an industrial steam boiler."* Fuel 81: 547-554

Slager, T.L. and F.M. Prozonic (2005). *"Simple methods for calibrating IR in TGA/IR analyses."* Thermochimica Acta 426: 93-99.

Sorensen, B. (2000). Renewable Energy. Academic Press.

Storm, C., H. Rudiger, H. Spliethoff and K.R.G. Hein (1999). *"Co-pyrolysis of coal/biomass and coal/sewage sludge mixtures."* Journal of Engineering for Gas Turbines and Power 121: 55-63.

Tillman, D.A. (2000). *"Biomass co-firing. The technology, the experience and the combustion consequences."* Biomass and Bioenergy 19: 365-84.

Vamvuka, D., E. Kakaras, E. Kastanaki and P. Grammelis (2003a). *"Pyrolysis characteristics and kinetics of biomass residuals mixtures with lignite."* Fuel 82: 1949-1960.

Vamvuka, D., N. Pasadakis and E. Kastanaki (2003b). *"Kinetic modelling of coal/agricultural by-product blends."* Energy & Fuels 17: 549-558.

Van der Drift, A., J. van Doorn and J.W. Vermeulen (2001). *"Ten residual biomass fuels for circulating fluidised-bed gasification."* Biomass and Bioenergy 20: 45-56.

Van der Horst, D. (2005). *"UK biomass energy since 1990: the mismatch between project types and policy objectives."* Energy Policy 33: 705-716.

Varhegyi, G., J. Antal, M. Jerry, E. Jakab and P. Szabo (1997). *"Kinetic modelling of biomass pyrolysis."* Journal of Analytical and Applied Pyrolysis 42: 73-87.

Vuthaluru, H.B. (2004). *"Investigations into the pyrolytic behaviour of coal/biomass blends using thermogravimetric analysis."* Bioresource Technology 92: 187-195.

Vyazovkin, S. (2002). *"Thermal Analysis."* Analytical Chemistry Symposia Series 74: 2749-2762.

Wang, J., H. Liu, J. Lu, D. Liu, X. Xia and L. Ma (1999). *"Emission control during co-combustion of coal and biomass in a fluidised bed combustor."* Developments in Chemical Engineering and Mineral Processing 7: 501-511.

Wang, H., B.Z. Dlugogorski and E.M. Kennedy (2003). *"Coal oxidation at low temperatures: oxygen consumption, oxidation products, reaction mechanism and kinetic modelling."* Progress in Energy and Combustion Science 29: 487-513

Werther, J., M. Saenger, E.U. Hartge, T. Ogada and Z. Siagi (2000). *"Combustion of agricultural residues."* Progress in Energy and Combustion Science 26: 1-27.

Wilburn, F.W. (2000). *"Kinetics of overlapping reactions."* Thermochimica Acta 354: 99-105.

Winter, F., C. Wartha and H. Hofbauer (1999). *"NO and N_2O formation during the combustion of wood, straw, malt waste and peat."* Bioresource Technology 70: 39-49.

Wojtowicz, M.A., R. Bassilakis, W.W. Smith, Y. Chen, R.M, Carangelo (2003). *"Modelling the evolution of volatile species during tobacco pyrolysis."* Journal of Analytical and Applied Pyrolysis 66: 235-261.

Wooten, J.B., J.I. Seeman and M.R. Hajaligol (2004). *"Observation and characterisation of cellulose pyrolysis intermediates by ^{13}C CPMAS NMR. A new mechanistic model."* Energy & Fuels 18: 1-15.

Wu, H., X. Li, J.I. Hayashi, T. Chiba and C.Z. Li (2005). *"Effects of volatile/char interactions on the reactivity of chars from NaCl-loaded Loy Yang brown coal."* Fuel 84: 1221-1228.

Zhang, B.J., W.W. Shi and W.B. Fu (2002). *"Effects of fuel characteristics on the NO reduction during the reburning with coals."* Fuel Processing Technology 79: 93-106.

Zhang, L., A. Sato, Y. Nimomiya and E. Sasaoka (2003). *"In-situ desulphurisation during combustion of high-sulphur coals added with sulphur capture sorbents."* Fuel 82: 255-266.

Zheng, G. and J.A. Kozinski (2000). *"Thermal events occurring during the combustion of biomass residue."* Fuel 79: 181-192.

Zubkova, V.V. (2005). *"Some aspects of structural transformations taking place in organic mass of Ukrainian coals during heating, Part 1: Study of structural transformations when heating coals of different caking capacity."* Fuel 84: 741-754.

Appendix A Collected Sample Characteristics

Table A-1: Comparison of the proximate characteristics for 11 coal and 17 biofuel samples [Storm et al. 1999; Tillman 2000; Sami et al. 2001; Demirbas 2002; Ross et al. 2002; Annamalai et al. 2003]

	VM (dry %wt.)	FC (by difference, dry %wt.)	Ash (dry %wt.)	Moisture (ar %wt.)	HHV (MJ kg^{-1})	VM/FC
Coal						
Black Thunder, PRB	43.4	49.3	7.3	29.2	17.0	0.9
Utah White Oak,	42.8	48.5	8.8	10.6	22.0	0.9
Pennsylvania Upper Freeport	24.5	61.4	14.1	7.5	23.0	0.4
Illinois #6	40.3	51.7	8.5	12.3	22.4	0.8
Polish Wujek	32.7	64.0	3.3	3.3	31.6	0.5
Low S Wyoming	44.7	48.3	7.1	22.8	21.4	0.9
Gottelborn	33.9	57.0	9.1	-	-	0.6
Ptolemais Lignite	41.4	40.3	18.2	57.1	-	1.0
German Lignite I	50.8	44.5	4.7	47.2	-	1.1
German Lignite II	50.6	43.1	6.3	45.2	-	1.2
German Lignite III	41.8	44.5	13.7	42.5	-	0.9
Biomass						
Switch grass	76.7	14.3	9.0	15.0	12.6	5.4
Alfalfa stalks	76.1	17.5	6.5	10.5	13.6	4.4
Barley straw	68.9	20.9	10.3	-	17.3	3.3
Wheat straw	71.3	19.8	8.9	21.0	17.5	3.6
Sugarcane bagasse	73.8	15.0	11.3	53.3	17.3	4.9
Olive pits	78.7	18.2	3.2	-	21.4	4.3
Rice husks	60.7	17.8	22.9	10.0	13.5	3.4
Peach pits	79.1	19.9	1.0	-	20.8	4.0
Sawdust	84.6	14.4	1.1	34.9	10.4	5.9
Urban wood waste	75.9	18.1	5.9	30.8	11.1	4.2
Eucalyptus	82.5	16.9	0.5	41.0	19.4	4.9
Poplar	82.3	16.4	1.3	33.1	19.4	5.0
Olive Kernel	71.7	21.3	6.7	10.9	-	3.4
Forest Residue	85.5	15.2	0.5	14.3	-	5.6

Table A-2: Comparison of the ultimate characteristics for 11 coal and 17 biofuel samples [Storm et al. 1999; Tillman 2000; Sami et al. 2001; Demirbas 2002; Ross et al. 2002; Annamalai et al. 2003]

	C (daf %wt.)	H (daf %wt.)	O (by difference, daf %wt.)	N (daf %wt.)	S (daf %wt.)
Coal					
Black Thunder, PRB	51.3	2.9	10.5	0.7	0.4
Utah White Oak,	63.5	4.4	12.2	0.9	0.6
Pennsylvania Upper Freeport	69.1	4.0	2.5	1.2	2.1
Illinois #6	66.0	4.4	5.7	1.4	2.8
Polish Wujek	73.0	4.9	20.2	1.3	1.6
Low S Wyoming	54.1	3.4	13.1	0.8	0.4
Gottelborn	81.4	5.6	10.6	1.5	1.0
Ptolemais Lignite	52.8	4.6	23.0	1.4	0.1
German Lignite I	64.2	5.4	25.1	0.7	<0.01
German Lignite II	61.4	5.6	26.1	0.6	<0.01
German Lignite III	57.4	5.8	22.5	0.6	<0.01
Biomass					
Switch grass	39.7	5.0	31.8	0.7	0.2
Alfalfa stalks	40.6	5.2	36.0	1.8	0.1
Barley straw	39.9	5.3	43.8	1.3	-
Wheat straw	43.2	5.0	39.4	0.6	0.1
Sugarcane bagasse	44.8	5.4	39.6	0.4	0.0
Olive pits	48.8	6.2	43.5	0.4	<0.01
Rice husks	34.9	5.5	38.9	0.1	-
Peach pits	53.0	5.9	39.1	0.3	0.1
Sawdust	32.1	3.9	28.2	0.3	0.0
Urban wood waste	33.2	3.8	27.0	1.0	0.1
Eucalyptus	48.3	5.9	45.1	0.2	<0.01
Poplar	48.5	5.9	43.7	0.5	<0.01
Olive Kernel	48.8	6.3	36.8	1.4	<0.01
Forest Residue	50.6	6.7	41.7	0.4	<0.01

Appendix B Thermogravimetric Profiles

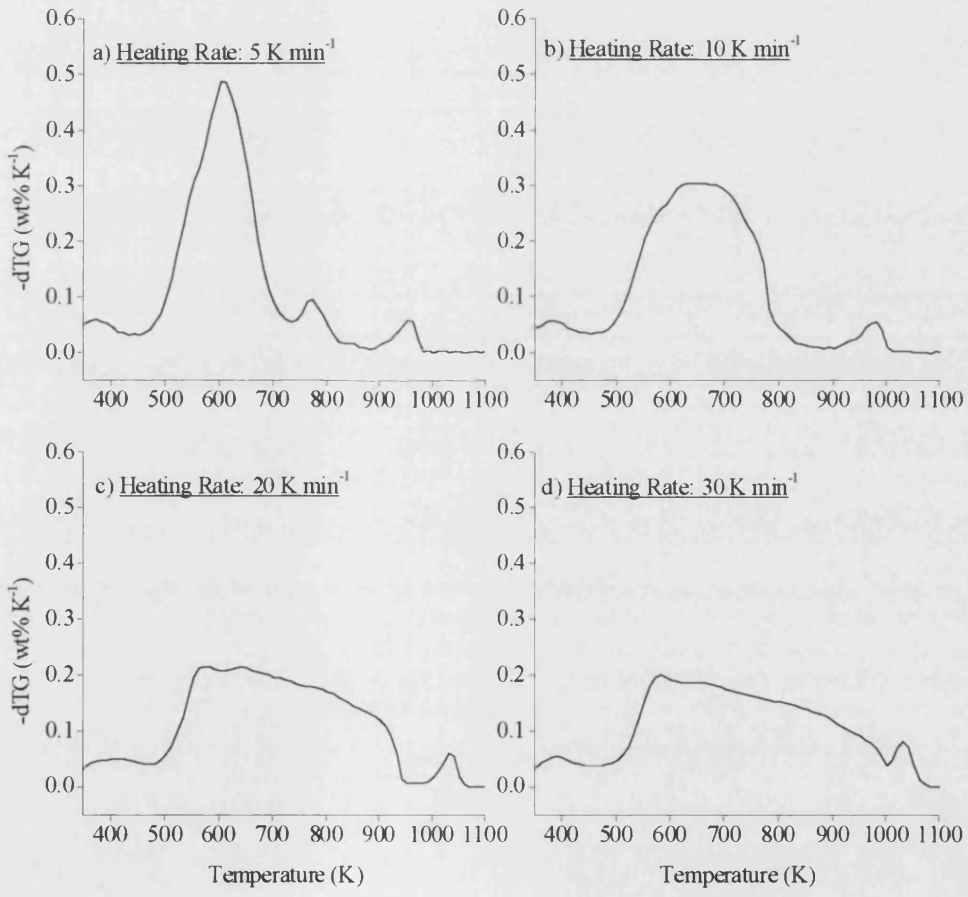

Figure B-1: Rate of weight-loss during oxidation of Ptolemais lignite with various heating rates. (β: 5, 10, 20 or 30 K min^{-1}; w_0: 25-30 mg; air flow: 3 ml min^{-1})

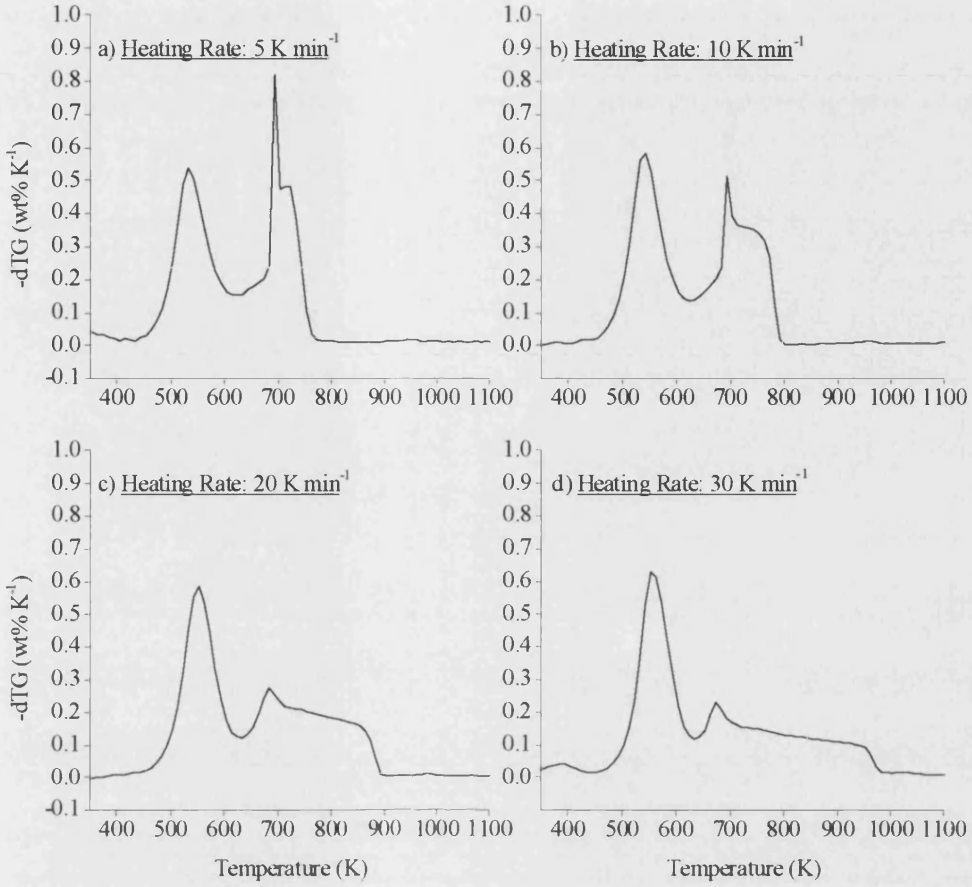

Figure B-2: Rate of weight-loss during oxidation of olive kernels with various heating rates. (β: 5, 10, 20 or 30 K min^{-1}; w_0: 25-30 mg; air flow: 3 ml min^{-1})

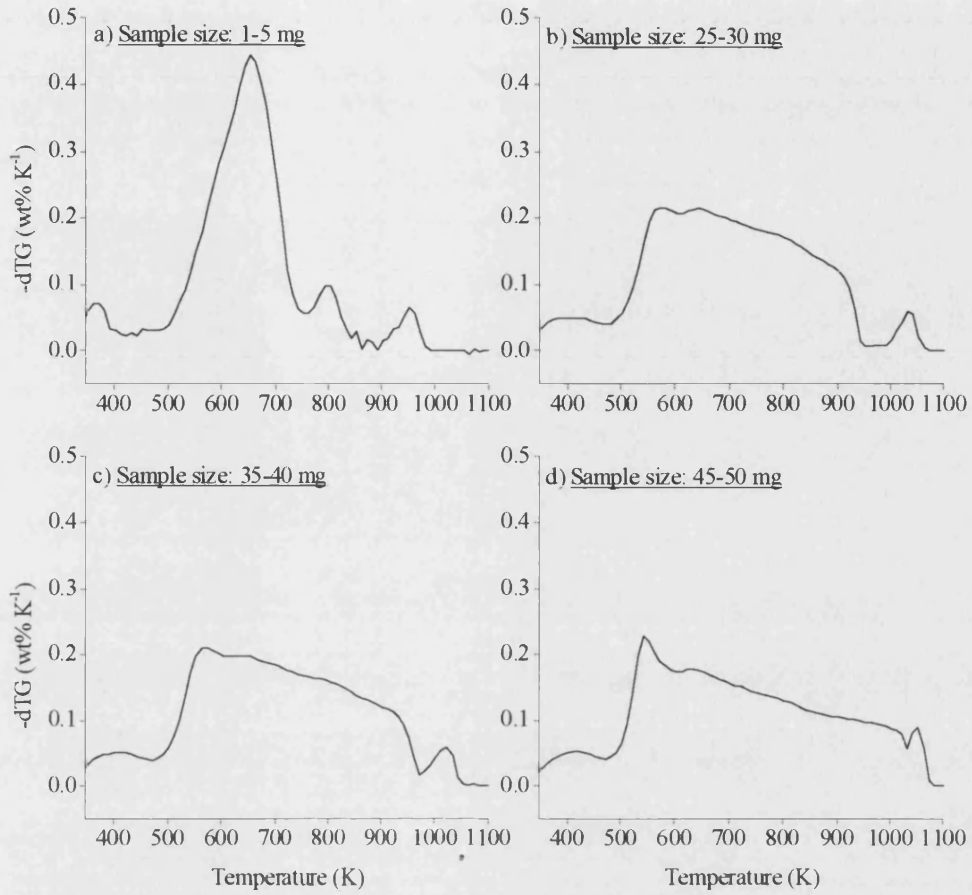

Figure B-3: Rate of weight-loss during oxidation of Ptolemais lignite with various initial sample weights. (β: 20 K min^{-1}; w_0: 1-5, 25-30, 35-40 or 45-50 mg; air flow: 3 ml min^{-1})

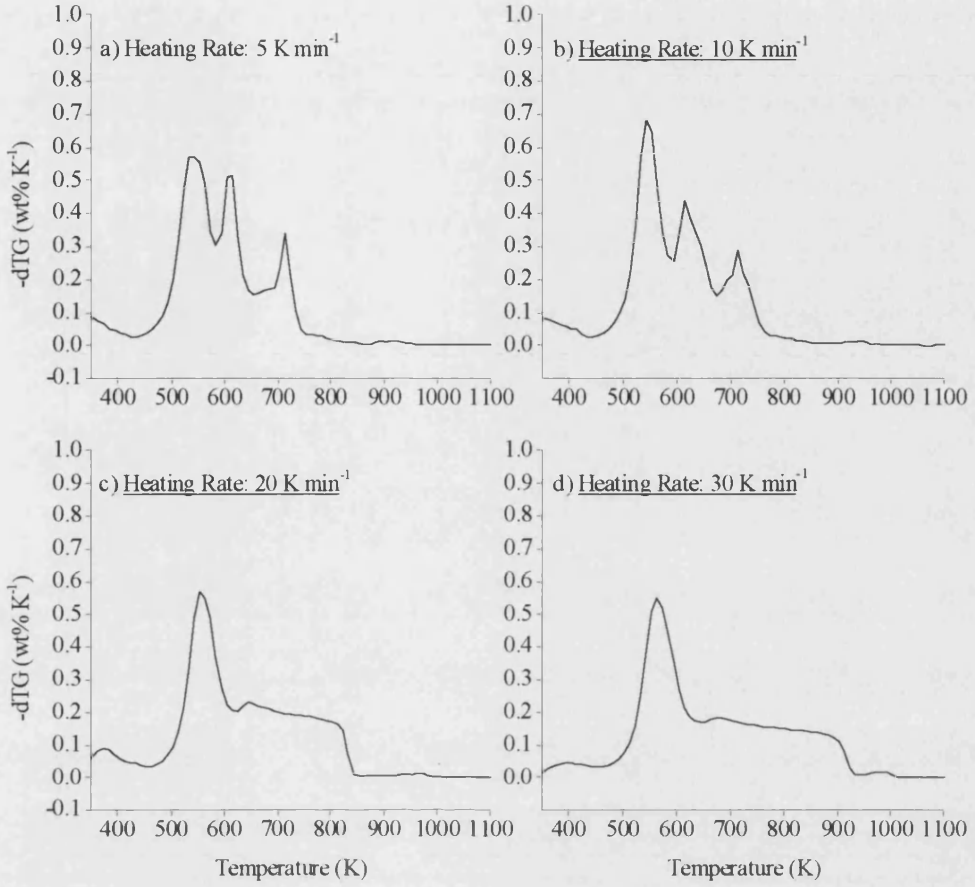

Figure B-4: Rate of weight-loss during oxidation of 60 %wt. olive kernels/Ptolemais lignite blend with various heating rates. (β: 5, 10, 20 or 30 K min^{-1}; w_0: 25-30 mg; air flow: 3 ml min^{-1})

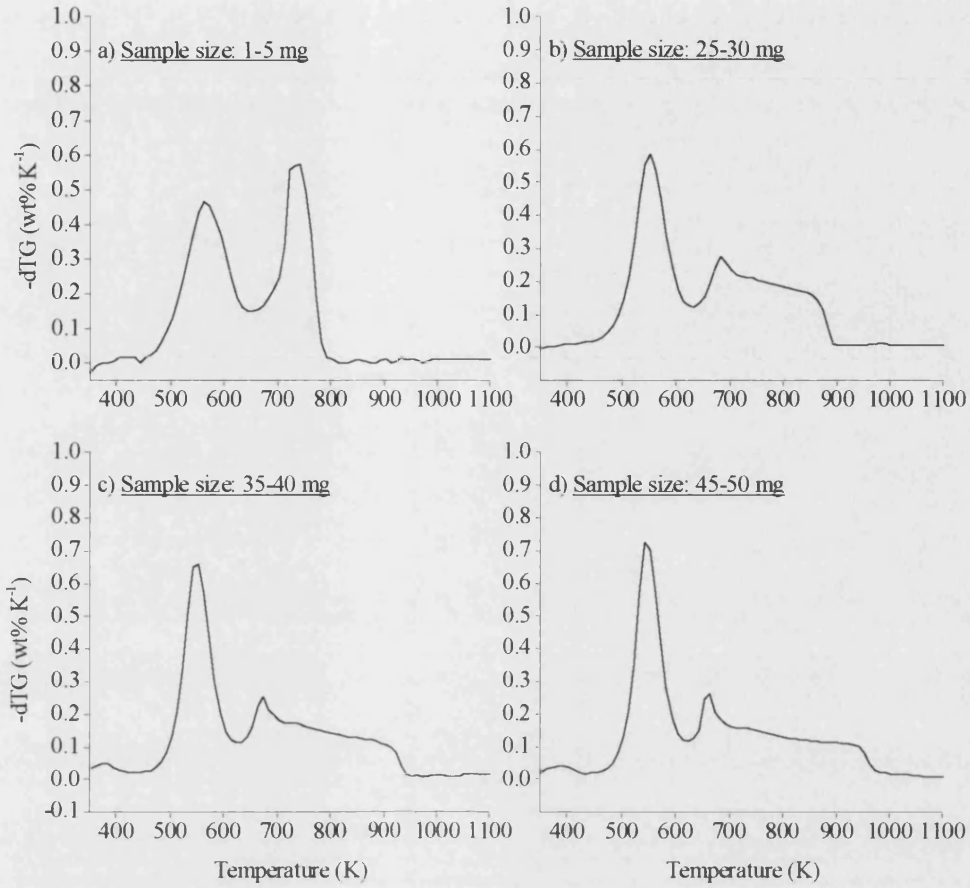

Figure B-5: Rate of weight-loss during oxidation of olive kernels with various initial sample weights. (β: 20 K min^{-1}; w_0: 1-5, 25-30, 35-40 or 45-50 mg; air flow: 3 ml min^{-1})

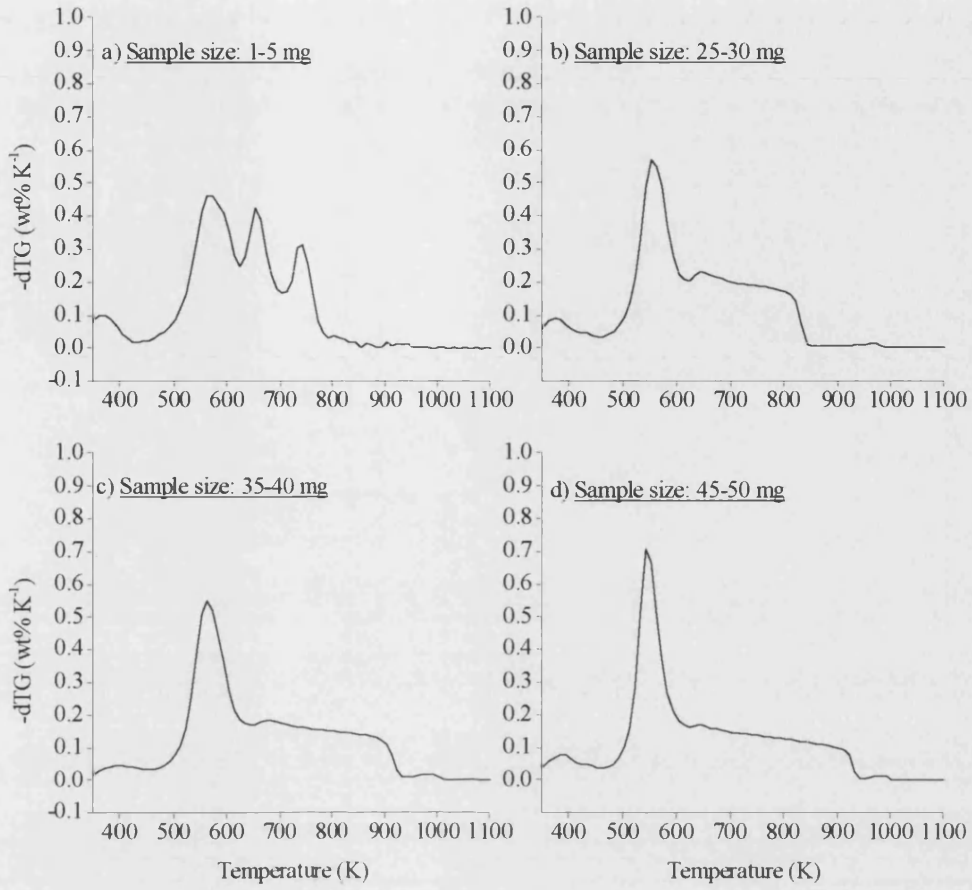

Figure B-6: Rate of weight-loss during oxidation of 60 %wt. olive kernels/Ptolemais lignite blend with various initial sample weights. (β: 20 K min^{-1}; w_0: 1-5, 25-30, 35-40 or 45-50 mg; air flow: 3 ml min^{-1})

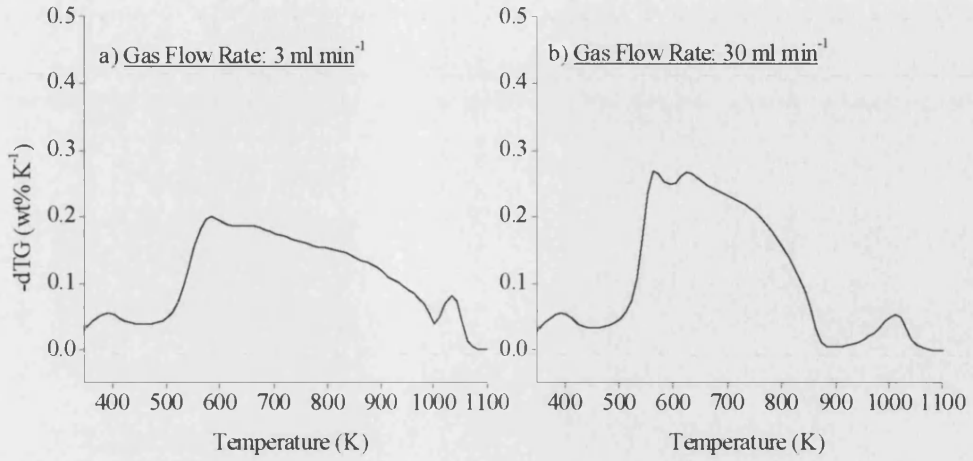

Figure B-7: Rate of weight-loss during oxidation of Ptolemais lignite with various carrier gas flow rates. (β: 20 K min^{-1}; w_0: 25-30 mg; air flow: 3 or 30 ml min^{-1})

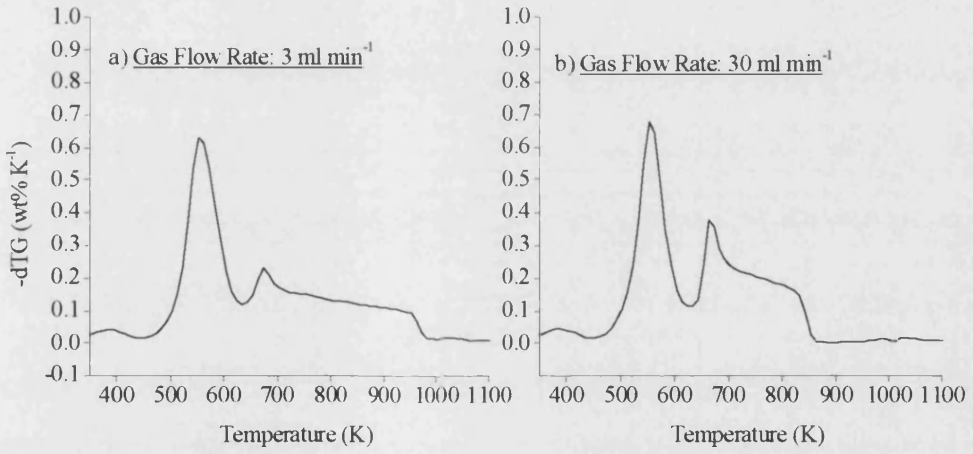

Figure B-8: Rate of weight-loss during oxidation of olive kernels with various carrier-gas flow rates. (β: 20 K min^{-1}; w_0: 25-30 mg; air flow: 3 or 30 ml min^{-1})

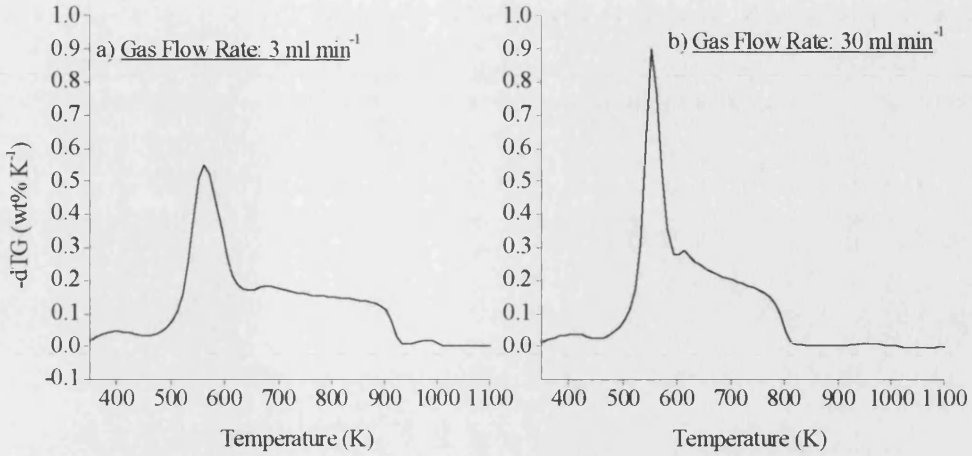

Figure B-9: Rate of weight-loss during oxidation of 60 %wt. olive kernels/Ptolemais lignite blend with various carrier gas flow rates. (β: 20 K min^{-1}; w_0: 25-30 mg; air flow: 3 or 30 ml min^{-1})

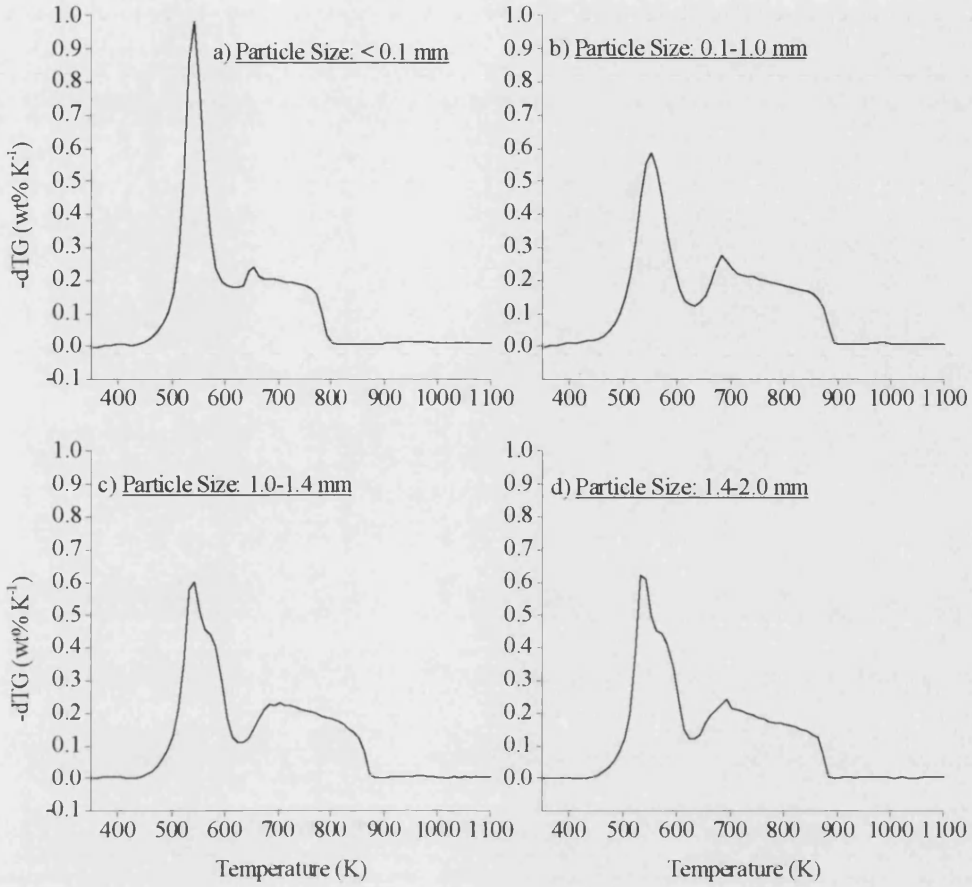

Figure B-10: Rate of weight-loss during oxidation of olive kernels with various particle sizes. (β: 20 K min^{-1}; w_0: 25-30 mg; particle sizes: <0.1, 0.1-1.0, 1.0 – 1.4 and 1.4 – 2.0 mm; air flow: 3 ml min^{-1})

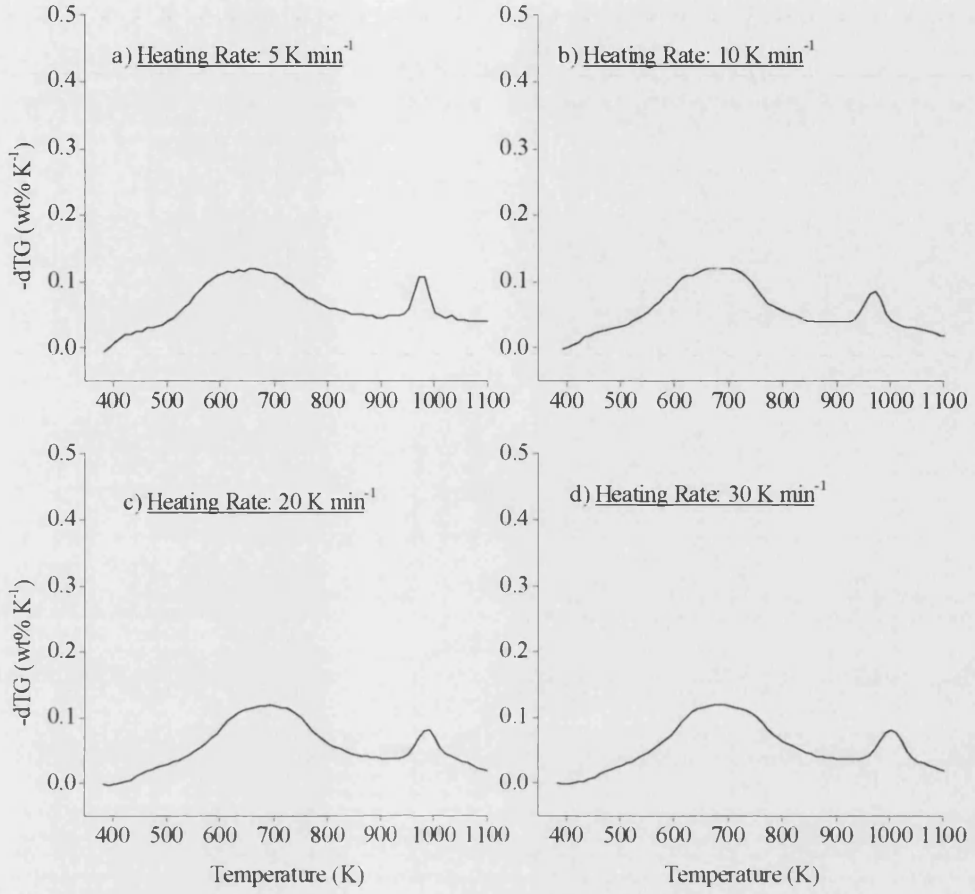

Figure B-11: Rate of weight-loss profiles for pyrolysis of Ptolemais lignite with various heating rates. (β: 5, 10, 20 or 30 K min^{-1}; w_0: 5-10 mg; nitrogen flow rate: 3 ml min^{-1})

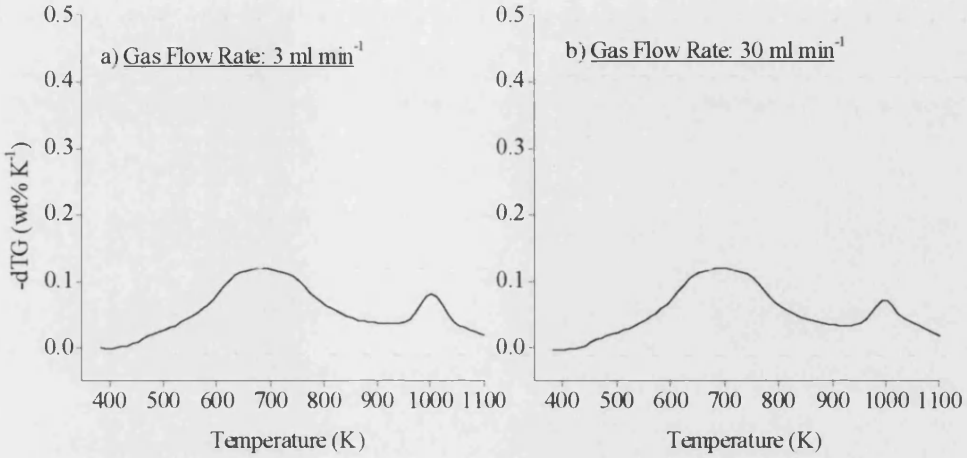

Figure B-12: Rate of weight-loss profiles for pyrolysis of Ptolemais lignite with various carrier gas flow rates. (β: 20 K min^{-1}; w_0: 25-30 mg; nitrogen flow rate: 3 or 30 ml min^{-1})

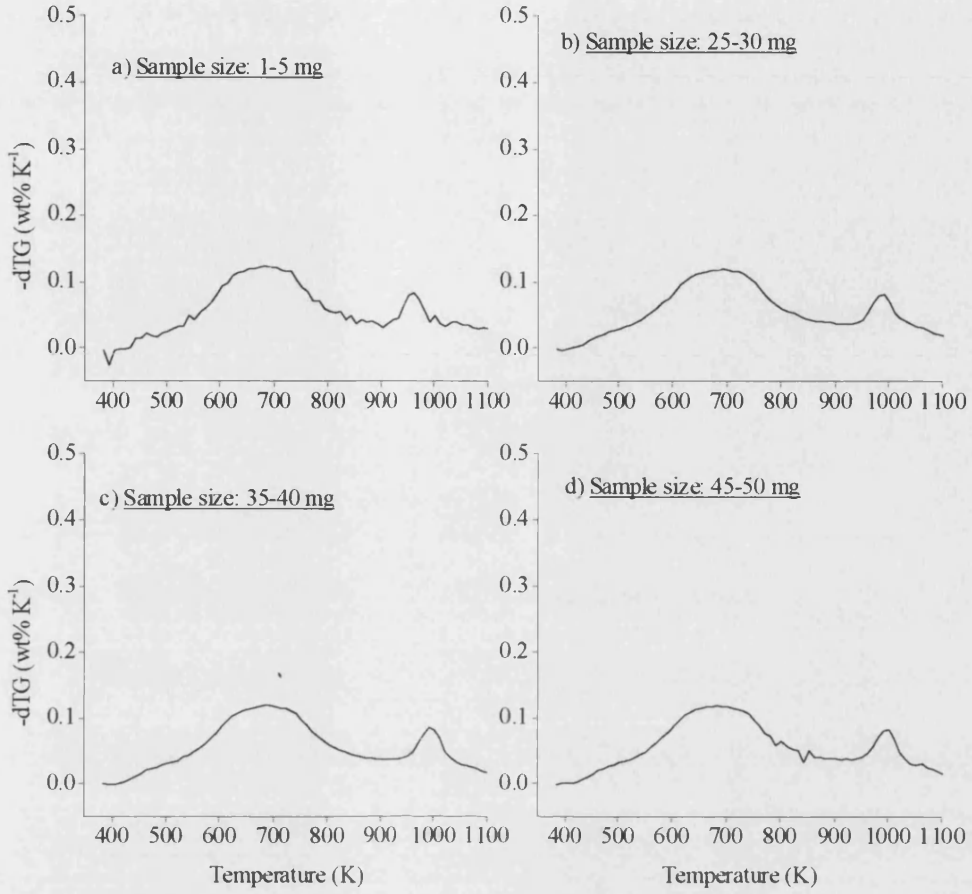

Figure B-13: Rate of weight-loss profiles for pyrolysis of Ptolemais lignite with various initial sample weights. (β: 20 K min^{-1}; w_0: 1-5, 25-30, 35-40 and 45-50 mg; nitrogen flow rate: 3 ml min

Appendix C Dissemination

C.1 Abstract of Lindsey *et al.* [2004]:

There is much interest in adding biomass to coal in energy conversion systems such as pulverised fuel combustion. The environmental advantages of co-combustion are a reduction in the use of coal, a finite resource, and a reduction in new CO2 emissions. However, the impact of co-combustion on energy conversion is not clear. This work is a study using thermogravimetric analysis (TGA) of biomass-coal blends. The main aims are to use TGA data to characterise different blends, and later to understand and predict co-combustion performance. The biomass used in this work is Greek olive kernels (OK) and the coal as a Greek (Ptolemais) lignite (PL) supplied by collaborators. Different blends were made up comprising of 0, 20, 40, 60 80 and 100 dry %wt. OK in PL> A Setaram TG-92 thermogravimetric analyser was used to obtain buoyancy-corrected weight change data for ~50 mg samples of each blend, as they were heated in pure, flowing nitrogen at 5 K min-1 from ambient temperatures to 1200 K. In the above conditions, the samples undergo various carbonisation of charring reactions at different temperatures. These reactions may be identified as different peaks in dTG plots. Here a dTG plot is a graph of temperature T (x-axis) versus the negative of the weight change rate with respect to T, -dW/dT (y-axis), where w is the weight of the sample expressed as a percentage of its origin weight. It was assumed that each dTG peak was represents by a Lorentz function, each characterised by Tmax, the temperature of the maximum of the peak, w, the width of the peak at half its height, and A, the area under the peak. It was assumed that the overall dTG curve was the sum of there Lorentzian profiles. Values of the parameters for all peaks were estimated by non-linear least squares fitting og the summed Lorentzian model with the dTG data. dTG plots for blends were found to comprise of six peaks (Figure 1). Five of these appeared to be common with those in the raw OK material. The peaks for pure PL were apparently modified in the blends. This is contrary to previous studies, which have suggested that the carbonisation of components in biomass-coal blends were important. We are currently exploring the nature of the dTG peaks in both the pure and blended materials.

C.2 Poster Presentations for ICTAC-13 [Lindsey *et al.* 2004]:

THERMOGRAVIMETRIC ANALYSIS OF THE CARBONISATION OF BIOMASS-LIGNITE BLENDS

UNIVERSITY OF BATH

Benjamin K. Lindsey and T.J. Mays

Department of Chemical Engineering, University of Bath, UK

Funded the by European Coal and Steel Community

1. Emissions Benefits of Burning Coal with Biomass

Co-firing biofuels with coal reduces fossil-fuel demands and lower net emissions of CO_2 from power-stations. Undefined interactions between the fuels gives additional reductions in NOx and SOx emissions, disproportionate to levels of fuel-N and S. This poster describes a thermogravimetric method of observing the interaction between the blended fuels, and thus a means of optimising the combustion conditions.

2. Carbonisation of a Fuel

Heating in an absence of O_2 (carbonisation) is the initial stage combustion, and yields volatile materials (VM) and char.

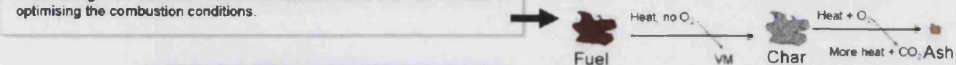

3. Fuel Selection

Olive kernels (OK) and Ptolemais lignite (PL) are commonly available fuels for Southern Europe. Samples of these were ground to < 1-μm and blends in 20, 40, 60, and 80 dry wt.% proportions were produced.

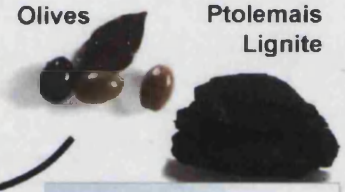

4. Thermogravimetric Analyser

A combined microbalance and furnace

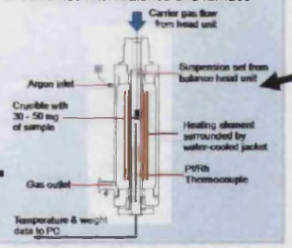

5. Rate of Weight-Loss (-dTG) Profiles

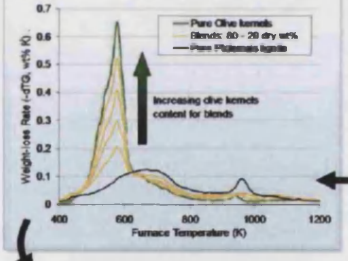

6. Process Peaks in the -dTG Profiles

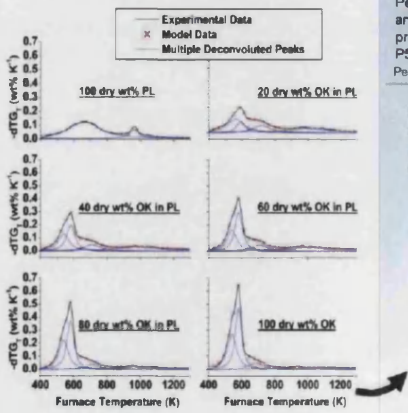

Useful Reference

Varmuza, Kekaras, *et al.* (2003). "Pyrolysis characteristics and kinetics of biomass residuals mixtures with lignite." Fuel 82(15-17): 1949-1960

7. Thermal Processes of the Blends

Peaks within the blend profiles share analogues with those of biomass or lignite profiles (below). Two peaks (combined as P5) could not be resolved.

Peak #	Fuel	Degradation process of:
1	OK	Hemicellulose
2	OK	Cellulose
3	OK	Cellulose
4	PL	Undefined
5	PL & OK	Condensation (PL) & lignin (OK)

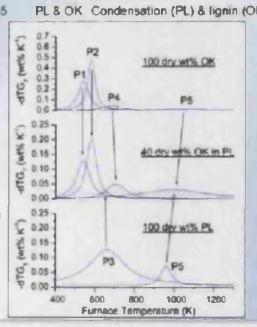

8. Profile Modelling

Equations describing the change in each peaks character with fuel ratio were used to calculate a model profile of weight loss rate for any blend proportion.

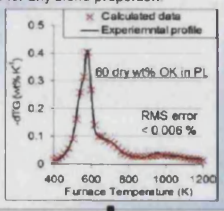

9. Conclusions

- ✓ Thermal process peaks have been isolated from -dTG profiles for the carbonisation of pure and blended fuels.
- ✓ Peaks from pure fuels have analogues in the blends, with positive correlations between the peak properties and the fuel blend ratio.
- ✓ This suggests that carbonisation of the fuels progress along separate pathways.
- ✓ Peak properties can be used to simulate -dTG profiles for new blend combinations.
- ✓ Other work at Bath reveals independent carbonisation occurs for other coal-biomass combinations. This could be important in developing co-fired power stations.

C.3 Abstract of Lindsey *et al.* [2005]:

With one of the many benefits of reduced CO2 emissions from power stations, there is a strong motive for co-firing biomass with coal fuel. However, the impacts of co-firing on other aspects of performance (*e.g.* particle burnout) are not well understood. This study characterise different coal-biomass blends by thermogravimetric analysis (TGA), deriving data to be later correlated with plant performance. Carbonisation of blends of olive kernels in Ptolemais lignite (0–100 dry-%wt.), were performed in a Setaram TG-92 TGA (N_2, 5 K min^{-1}, 400–1200 K), fuels selected as being readily available in Europe. When compared with a rule-of-mixtures type model, the weight loss (TG) profiles revealed linear correlations between biomass content and weight-loss (RMS error < 1.03 %wt.). Weight loss rate (-dTG) data of the blends were deconvoluted using five Lorentzian peaks. Carbonisation of pure olive kernels was fitted with four dTG peaks (T_{max} = 561, 594, 717 and 1058 K) and pure lignite fitted with two peaks (T_{max} = 661 and 1010 K). The blend –dTG profiles retain both of the lignite peaks and three of the kernels peaks; the missing kernel peak being too small to be resolved. The absence of significant additional TG events within the blends strongly suggests that carbonisation of blends two components progress separately. The two sets of experiments support published suggestions that co-carbonisation processes are non-synergistic [Garcia-Perez, Chaala et al. 2001; Kastanaki, Vamvuka et al. 2002] Using the Lorentz peak parameters, a highly accurate model of the blends co-carbonisation –dTG profile was reproduces (RMS error < 0.032 %wt. K^{-1}).

C.4 Poster for 7th World Congress of Chemical Engineering [Lindsey *et al* 2005]:

WCCE 2005, Edinburgh

THERMOGRAVIMETRIC ANALYSIS OF THE CARBONISATION OF BIOMASS-LIGNITE BLENDS

UNIVERSITY OF BATH

Benjamin K. Lindsey and T.J. Mays

Department of Chemical Engineering, University of Bath, UK

Funded the by European Coal and Steel Community

1. Emissions Benefits of Burning Coal with Biomass

Co-firing biofuels with coal reduces fossil-fuel demands and results in lower net emissions of CO_2 from power-stations. Undefined interactions between the fuels gives additional reductions in NOx and SOx emissions, disproportionate to levels of fuel-N and S. This poster describes a thermogravimetric method of observing the interaction between the blended fuels, and thus a means of optimising the combustion conditions.

2. Carbonisation of a Fuel

Heating in an absence of O_2 (carbonisation) is the initial stage combustion, and yields volatile material (VM) and char.

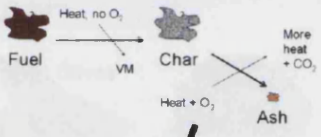

3. Fuel Selection

Olive kernels (OK) and Ptolemais lignite (PL) are commonly available fuels in Southern Europe. Samples were ground to < 1-μm and blends in 20, 40, 60, and 80 dry wt.% proportions produced.

4. Thermogravimetric Analyser

A combined microbalance and furnace

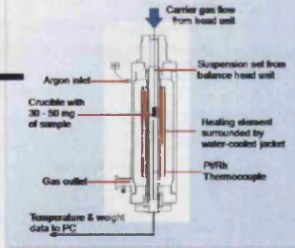

5. Rate of Weight-Loss (-dTG) Profiles

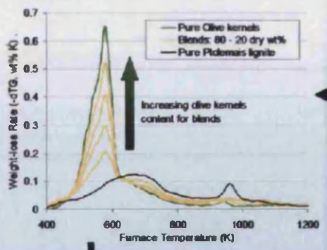

6. Deconvolution of the -dTG Profiles

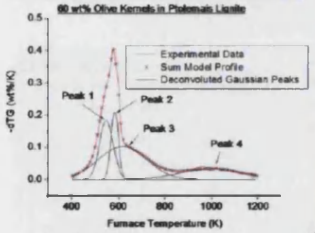

Gaussian Profile:

$$-dTG_i = \left(\frac{\gamma_i}{w_i\sqrt{\pi/2}}\right)\exp\left(-2\frac{(T_f - T_{max,i})^2}{w_i^2}\right)$$

Where for peak i:

γ = Peak area (wt%)

w = Peak width at half - height (K)

T_f = Furnace temperature (K)

T_{max} = Peak temperature (K)

7. Comparison of Peak Trends

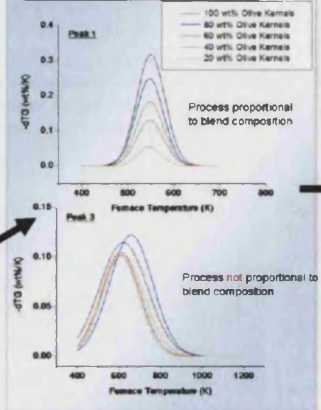

8. Conclusions

- ✓ Peaks representing discrete thermal processes have been isolated from the dTG profiles of pure and blended fuels.
- ✓ Peaks of the pure fuel appear in the blends, allowing changes in the carbonisation process to be observed with changing blend ratio.
- ✓ Peaks at 550 and 680 K coincide with initial pyrolysis of holocellulose components of biomass, and vary proportionally to blend ratio.
- ✓ Peaks at 620 and 980 K coincide with biomass lignin and coal pyrolysis thermal events. Variation of these is independent of biomass content.
- ✓ Other work at Bath reveals independent carbonisation occurs for other coal-biomass combinations. This could be important in developing co-fired power stations.

Useful Reference

Vamvuka, Kakaras, *et al.* (2003). "Pyrolysis characteristics and kinetics of biomass residuals mixtures with lignite." Fuel 82(15-17): 1949-1960

C.5 Poster for SET Award Final 2005:

Thermogravimetric Analysis of Olive Kernel-Ptolemais Lignite Blends

Funded the by ECSC (Project № 7220-PR-131)

B.K. Lindsey and T.J. Mays
Department of Chemical Engineering, University of Bath, UK

Interactions during the Co-firing of Biomass and Lignite

- *Co-firing agricultural waste with coal, originally to reduce the fossil-fuel intake, is also shown to reduce NO_x and SO_2 emissions from power-stations by up to 20%.*
- *However emissions and performance are not directly proportional to fuels ratio.*
- *The implied coal-biomass interactions are poorly understood.*

Materials

Olive kernels (OK) and Ptolemais lignite (PL) are common available fuels for much of Southern Europe.

Proximate Analysis	Olive Kernels	Ptolemais Lignite
Moisture (wt.%)	~ 18.0	~ 45.0
VM (dry wt%)	64.39	40.79
FC (dry wt%)	18.15	36.56
Ash (dry wt%)	13.12	22.65

Samples were ground to < 1-μm. Blends of 20, 40, 60, and 80 wt.% proportions were then produced from pre-dried samples.

The Setaram TG-92 Furnace

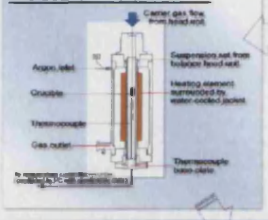

The Thermal Programme

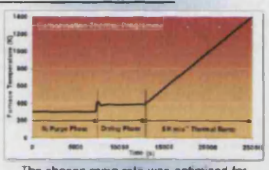

The chosen ramp rate was optimised for peak-resolution vs. experiment time limitations

Profile Deconvolution

Multiple Lorentz-peak fittings of dTG data were performed using non-linear methods:

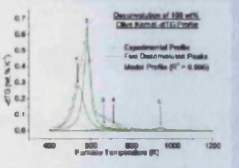

Lorentz curve equation:

$$-dTG_i = \frac{2A_i}{\pi}\left(\frac{w_i}{4\left[T_f - T_{max,i}\right]^2 + w_i^2}\right)$$

$-dTG_i$ = Weight-loss rate of peak i (wt.% K^{-1})
A_i = Peak area (wt.%)
w_i = Peak width at half height (K)
$T_{max,i}$ = Modal temperature (K)
T_f = Furnace temperature (K)

	№ of Peaks	R^2
Olive Kernels	5	0.996
Fuel Blends	7	~0.994
Ptolemais Lignite	4	0.998

Profile Modelling

Grouped peaks parameters are plotted against biomass content (Y), e.g. T_{max}:

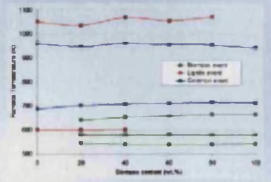

gives a linear equation for each peak in terms of Y:

$$T_{max,i} = m_{i,Y}Y + c_{i,Y}$$

Insert this, along with analogous calculations of each peak area and width, into the Lorentz equation. Combining all peaks gives a dTG profile for any PL-OK blend proportion:

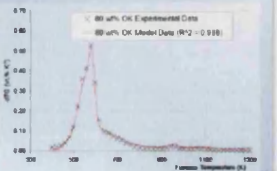

Fuel Character Continuation in Blends

All peaks assigned to either biomass or lignite are observed to continue into the blends, often through the entire series. OK and PL respectively contribute three and two unique peaks to the blend profiles, and two common ones, the latter illustrated below in blue.

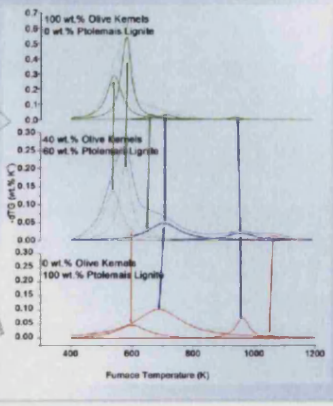

Conclusions

The dTG profiles of a biomass-lignite blend series have been deconvoluted into a total of seven thermal events. Tracking these events through the blends allows a model of the materials decomposition to be formed, revealing the extent of biomass-lignite interaction during carbonisation. The assumption of linear correlations between peak parameters and OK content is crude, but gives accurate results. Equivalent work covering the oxidation of PL-OK blends, as well as other fuel combinations continues at University of Bath.

Key References:

1. Hein and Feldmann (1998) "EU clean coal technology: co-combustion of coal and biomass." Fuel Processing Technology 54(1-3): 159-169.
2. Varma et al. (2003) "Pyrolysis characteristics and kinetics of biomass residuals mixtures with lignite." Fuel 82(15-17): 1949-1960.
3. Liu, Zhang, et al. (2002) "Reduction of N_2O and NO emissions by co-combustion of coal and biomass." Journal of the Institute of Energy 75(504): 81-84.